



TECHNISCHE
UNIVERSITÄT
WIEN

Dissertation

Enhancing Selectivity and Sensitivity of Vibrational Spectroscopy Through Nanoscale Materials: from Nanoparticles to Mesopores

A thesis submitted for the degree of
Doctor of Technical Sciences (Dr. techn.)

at

Technische Universität Wien
Faculty of Technical Chemistry
Institute of Chemical Technologies and Analytics

under supervision of

Univ.Prof. Dr. Bernhard Lendl

defended by

Dipl.-Ing. Felix Frank

Mat. Nr. 01327511



Vienna, 16.12.2024

"The greatness of a mind is determined by the depth of its suffering."

- Hayao Miyazaki

Abstract

Keywords: Mid-Infrared Spectroscopy • Surface-Enhanced Raman Spectroscopy • Liquid-Phase Analysis • Gas-Phase Analysis • Mesoporous Oxides • Metal-Organic Frameworks

This thesis was performed in the scope of the H2020 project HYDROPTICS, aiming to improve processes in the petrochemical industry. To answer the research questions defined in the description of action, the use of nanoscale materials to enhance selected vibrational spectroscopy techniques was explored. This involved the use of porous materials such as mesoporous oxides and metal-organic frameworks, which were coated onto internal reflection elements (IREs) to enhance the sensitivity and selectivity of evanescent field infrared sensing techniques, but also the use of silver nanoparticles for performing surface enhanced Raman spectroscopy.

For the detection of ortho-phosphates, which are used as scale inhibitors in industrial water, a method to coat a thin film of titania onto IREs was developed to use the high affinity of titania towards phosphates for sensing purposes. The interaction between phosphates and titania was studied by in-situ spectroscopy looking at the dependence of pH and concentration, as well as the kinetics of the adsorption process. This concept was further expanded towards organic phosphates and, by functionalisation of the titania surface, also towards the analysis of hydrocarbon contaminants in water streams. Using this technique, sub-ppm limits of detection (LODs) for ortho-phosphates (0.36 mg L^{-1}), glyphosate (0.73 mg L^{-1}), and benzonitrile (0.27 mg L^{-1}) could be reached.

In parallel, a method using metal-organic frameworks (MOFs) as sensing material for ortho-phosphates in water was developed. For this means, a protocol for the repeatable application of a film-like coverage of IREs with adhered MOF crystals was devised to overcome the challenge of the chemisorbed phosphates which could not be removed from the sensing surface easily. Using this combination of MOF and attenuated total reflection infrared spectroscopy (ATR-IR), an automated sensing protocol was developed, reaching limits of detection of 0.57 mg L^{-1} phosphate in water. By applying a single point calibration, differences in sensing layer application could be balanced out, leading to an improved re-

peatability of 94 % (as compared to 74 % without the calibration). Additional experiments were performed to study the use of different MOFs for in-situ spectroscopy of adsorption processes, for instance using a larger pore MOF for the adsorption of hydrocarbons for aqueous solutions and exploring post-synthetic modification to show the versatility of MOFs.

For the detection of cationic surfactants, which are used as film forming corrosion inhibitors in industrial pipelines, surface-enhanced Raman spectroscopy (SERS) was explored. First, the interaction of these surfactants with silver nanoparticles (AgNPs) was studied, showing a strong influence of the surfactant concentration on the aggregation behaviour of AgNPs. Using this knowledge, a sensing protocol was developed for cationic surfactants in water utilising the competitive adsorption of the surfactant and a tracer molecule (methylene blue) to quantify the concentration as a function of the quenching of the tracer signal, which can be applied to concentrations as low as 0.15 mg L^{-1} .

Additionally, ultrasound particle manipulation was employed for an on-line liquid handling module that moved suspended particles present in process streams into the focal plane of a hyperspectral imaging spectrograph. This module was tested and shipped to be integrated in the final prototype of the HYDROPTICS project which was developed for the simultaneous determination of oil-in-water and total suspended particles in a process water stream.

Finally, using the technology of mesoporous materials, another project was pursued during this thesis, which aimed to advance the concept of mid-IR photonic integrated circuits (PICs) based on a germanium-on-silicon platform. In this project under the umbrella of the H2020 project ACTPHAST4R, the benefit of the use of microlenses for the alignment tolerances (increased by a factor of 5x) was demonstrated. Additionally, multi-gas VOC sensing for PICs was pursued as a use-case demonstration for these PICs coated with mesoporous silica, showing high enrichment factors up to 22,000 and sub-ppmv LODs for three model VOCs (toluene, p-xylene, and 1,2,4-trimethylbenzene).

Kurzfassung

Schlagworte: Mittlere Infrarotspektroskopie • Oberflächenverstärkte Ramanspektroskopie • Flüssigphasenanalyse • Gasphasenanalyse • Mesoporöse Oxide • Metallorganische Gerüste

Diese Dissertation wurde im Rahmen des H2020-Projekts HYDROPTICS durchgeführt, das auf die Optimierung von Prozessen in der petrochemischen Industrie abzielte. Zur Beantwortung der Forschungsfragen wurde der Einsatz nanoskaliger Materialien zur Verbesserung ausgewählter Schwingungsspektroskopietechniken untersucht. Dazu gehörte die Verwendung poröser Materialien wie mesoporöser Oxide und metallorganischer Gerüste (MOFs), die auf Oberflächen interner Reflexionselemente (IREs) aufgebracht wurden, um die Empfindlichkeit und Selektivität infrarotspektroskopischer Methoden im evaneszenten Feld zu verbessern. Auch die Verwendung von Silber-Nanopartikeln zur Oberflächenverstärkung des Raman-Effekts wurde untersucht.

Für den Nachweis von ortho-Phosphaten, die als Kesselsteininhibitoren in Industrierwasser verwendet werden, wurde eine Methode zur Beschichtung von IREs mit einem dünnen Film aus Titandioxid entwickelt. Durch die Kombination mit IREs konnte die hohe Affinität von Titandioxid zu Phosphaten für Sensorzwecke genutzt werden. Die Wechselwirkung zwischen Phosphaten und Titandioxid wurde durch in-situ Spektroskopie untersucht, um die Abhängigkeit der Spektren von pH-Wert und Konzentration sowie die Kinetik des Adsorptionsprozesses zu ermitteln. Dieses Konzept wurde auf organische Phosphate und, durch Funktionalisierung der Titandioxid-Oberfläche, auch auf den Nachweis von Kohlenwasserstoff-Verunreinigungen in Wasserströmen ausgeweitet. Mit dieser Technik konnten sub-ppm Nachweisgrenzen von ortho-Phosphaten (0.36 mg L^{-1}), Glyphosat (0.73 mg L^{-1}), und Benzonitril (0.27 mg L^{-1}) erreicht werden.

Parallel dazu wurde eine Methode entwickelt, die MOFs als Sensormaterial für ortho-Phosphate in Wasser verwendet. Ein Protokoll für die wiederholbare Aufbringung einer filmartigen Schicht von elektrostatisch gebundenen MOF Kristallen auf IREs, welche nach jeder Messung einfach entfernt werden konnten, wurde entwickelt, um die Herausforderung

der chemisorbierten Phosphate zu überwinden. Mit dieser Kombination aus MOF und abgeschwächter Totalreflexions-Infrarotspektroskopie wurde ein automatisches Messprotokoll entwickelt, womit Nachweisgrenzen von 0.57 mg L^{-1} erreicht werden konnten. Durch eine Ein-Punkt-Kalibrierung konnten Unterschiede beim Schichtauftrag ausgeglichen werden, was zu einer verbesserten Wiederholbarkeit von 94 % führte (im Vergleich zu 74 % ohne Kalibrierung). Weitere Experimente untersuchten die Verwendung verschiedener MOFs für die in-situ Spektroskopie von Adsorptionsprozessen, wie die Adsorption von Kohlenwasserstoffen in wässrigen Lösungen und die post-synthetische Modifikation zur Demonstration der Vielseitigkeit von MOFs.

Für den Nachweis von kationischen Tensiden, die als filmbildende Korrosionsinhibitoren in industriellen Rohrleitungen eingesetzt werden, wurde der Einsatz oberflächenverstärkter Raman-Spektroskopie (SERS) untersucht. Die Wechselwirkung dieser Tenside mit Silbernanopartikeln (AgNPs) zeigte einen starken Einfluss der Tensidkonzentration auf das Aggregationsverhalten der AgNPs. Basierend auf diesen Erkenntnissen wurde eine Messmethode für kationische Tenside in Wasser entwickelt, die die kompetitive Adsorption des Tensids und eines Tracermoleküls (Methylenblau) nutzt, um die Konzentration in Abhängigkeit von der Auslöschung des Tracersignals zu quantifizieren.

Weiters wurde Ultraschallpartikelmanipulation in ein Online-Flüssigkeitshandhabungsmodul integriert, die Prozessströme suspendierte Partikel in die Fokusebene eines Hyperspektralbildspektrographen bewegte. Dieses Modul wurde getestet und in den endgültigen Prototyp des HYDROPTICS-Projekts integriert, der zur gleichzeitigen Bestimmung vom Gesamt-Öl in Wasser Gehalt und der Menge and suspendierten Partikeln in einem Prozessstrom entwickelt wurde.

Schließlich wurde unter Nutzung mesoporöser Materialtechnologie ein weiteres Projekt verfolgt, welches die Weiterentwicklung des Konzepts von integrierten photonischen Bauteilen basierend auf einem Germanium-auf-Siliciumsystem für den mittleren Infrarotbereich zum Ziel hatte. In diesem Projekt, welches als Subprojekt unter dem H2020 Projekt ACTPHAST4R geführt wurde, wurden die Vorzüge von Mikrolinsen für verbesserte Toleranzen in der optischen Ausrichtung (Verbesserung um einen Faktor von 5x) demonstriert. Außerdem wurde das Detektieren von mehreren volatilen organischen Kontaminanten als use-case für diese Sensoren, die mit mesoporöser Silika besichtet wurden, demonstriert, wobei eine Anreicherung von bis zu 22.000 und sub-ppmv Nachweisgrenzen für die drei Modellkontaminanten (Toluen, p-Xylen, und 1,2,4-Trimethylbenzen) erreicht werden konnten.

Acknowledgments

Abbreviations

| | |
|---|---------|
| attenuated total reflection | ATR |
| Cambridge structural database | CSD |
| covalent organic framework | COF |
| degree of freedom | DOF |
| distributed feedback quantum cascade laser | DFB-QCL |
| dynamic light scattering | DLS |
| electrical impedance spectroscopy | EIS |
| electromagnetic | EM |
| evaporation-induced self-assembly | EISA |
| external cavity quantum cascade laser | EC-QCL |
| Fourier-transform | FT |
| germanium-on-silicon | GOS |
| grazing-incidence small angle x-ray scattering | GI-SAXS |
| infrared | IR |
| internal reflection element | IRE |
| limit of detection | LOD |
| localised surface plasmon resonance | LSPR |
| mercury cadmium telluride | MCT |
| metal-organic framework | MOF |
| micro-opto-electro-mechanical system | MOEMS |
| multivariate curve resolution - alternating least squares | MCR-ALS |
| parts-per-billion volume parts | ppbv |
| photonic integrated circuits | PIC |
| post-synthetic modification | PSM |
| quantum cascade laser | QCL |
| reactive ion etching | RIE |
| secondary building unit | SBU |
| sequential injection analysis | SIA |
| silicon-on-insulator | SOI |

| | |
|-------------------------------------|--------|
| silver nanoparticle | AgNP |
| small-angle x-ray diffraction | SA-XRD |
| surface-enhanced Raman spectroscopy | SERS |
| thermogravimetric analysis | TGA |
| total suspended solid | TSS |
| ultrasound | US |
| ultraviolet | UV |
| visible | VIS |
| volatile organic contaminant | VOC |
| zeolitic imidazolate framework | ZIF |

Symbols

| | |
|--|---------------------|
| absorbance | A |
| absorption coefficient | κ |
| acoustic contrast | Φ |
| amount of adsorbed molecules at certain time | q_t |
| anharmonicity factor | γ_i |
| Avogadro constant | N_A |
| black body radiation | $B(\nu, T)$ |
| complex refractive index | \hat{n} |
| compressibility | $\tilde{\kappa}$ |
| concentration | c |
| concentration vector | \mathbf{c} |
| coverage of evanescent field | S |
| critical angle | θ_c |
| depth of penetration | d_p |
| detectivity | D^* |
| displacement | x |
| displacement of vibrating bond | D |
| dynamic viscosity | η |
| effective path length | d_e |
| electrical field | E |
| electrophoretic mobility | U_E |
| elementary charge | q |
| Elovich model constants | α_e, β_e |
| enthalpy | H |
| equilibrium coverage concentration in adsorption | q_e |
| force constant | K |
| free surface sites | θ_s |
| frequency | ν |
| Freundlich scaling constants | K_F, n_F |

| | |
|---|--------------------|
| full monolayer surface coverage concentration | q_m |
| Gibbs free potential | G |
| Henry factor | $f(\kappa a)$ |
| incident angle | θ_1 |
| induced dipole moment | p |
| Langmuir constant | K_L |
| mass | m |
| molar decadic absorption coefficient | ε |
| number of active reflections | N |
| number of dipole moments | N_p |
| optical path length | d |
| particle density | $\tilde{\rho}$ |
| Planck constant | h |
| polarisability | α |
| polarisation | P |
| rate constant for adsorption kinetic modeling | k_1, k_2, k_{id} |
| rate constant in adsorption/desorption | k_{ads}, k_{des} |
| reduced mass | μ |
| refracted angle | θ_2 |
| refractive index | n |
| relative permittivity | ε_r |
| residual vector | R |
| resonance length of a resonator | l_{res} |
| spectral matrix | \mathbf{S}^T |
| speed of sound | v_{ac} |
| surface area | A_{surf} |
| surface tension | σ |
| temperature | T |
| time | t |
| transmittance | $\frac{I}{I_0}$ |
| vacuum light speed | c_0 |
| vacuum permittivity | ε_0 |
| vacuum wavelength | λ_0 |
| vacuum wavenumber | $\tilde{\nu}_0$ |
| vibrational energy states | E_i |
| vibrational quantum number | n_i |

| | |
|----------------|----------|
| wave frequency | ω |
| wave vector | k |
| Zeta potential | ζ |

Contents

| | |
|--|------------|
| Abstract | ii |
| Kurzfassung | iv |
| Acknowledgements | vi |
| Abbreviations | vii |
| Symbols | ix |
| | |
| I. Framework of this thesis | 1 |
| 1.1. The HYDROPTICS Project | 2 |
| 1.2. The ACTPHAST4R Project | 3 |
| | |
| II. Theoretical part | 5 |
| 2.1. Introduction | 6 |
| 2.2. Mid-Infrared Spectroscopy | 6 |
| 2.2.1. Fundamentals in Infrared Spectroscopy | 6 |
| 2.2.2. Transmission Infrared Spectroscopy | 9 |
| 2.2.3. Mid-Infrared Light Sources and Spectrometers | 12 |
| 2.2.4. Attenuated Total Reflection Infrared Spectroscopy | 15 |
| 2.2.5. Evanescent Field Infrared Spectroscopy Based on Photonic Waveguides | 18 |
| 2.3. Raman Spectroscopy | 20 |
| 2.3.1. Fundamentals in Raman Scattering | 20 |
| 2.3.2. Differences between Raman and mid-IR Spectroscopy | 22 |
| 2.3.3. Modern Raman Instrumentation | 23 |
| 2.3.4. Surface-Enhanced Raman Scattering | 25 |
| 2.4. Introduction to Mesoporous Materials | 27 |
| 2.4.1. Mesoporous Oxides | 27 |
| 2.4.2. Metal-Organic Frameworks | 30 |

| | | |
|--------|--|----|
| 2.5. | Fundamentals of Adsorption Processes in Porous Materials | 34 |
| 2.5.1. | Adsorption Thermodynamics and Kinetics | 34 |
| 2.5.2. | Adsorption Processes in Porous Materials | 38 |
| 2.6. | Fundamentals of Ultrasound Particle Manipulation | 40 |
| 2.6.1. | The Acoustic Radiation Force | 41 |
| 2.6.2. | Operation of an Ultrasound Particle Manipulation Device | 42 |

III. Experimental methods 43

| | | |
|--------|---|----|
| 3.1. | Infrared Setups | 44 |
| 3.1.1. | Preparation of Internal Reflection Elements | 44 |
| 3.1.2. | Performance Considerations for Different Internal Reflection Elements | 44 |
| 3.1.3. | Passivation of Germanium Internal Reflection Elements | 45 |
| 3.1.4. | Optical Setups for Attenuated Total Reflection Infrared Spectroscopy | 46 |
| 3.1.5. | Fabrication of mid-Infrared Photonic Integrated Circuits | 46 |
| 3.1.6. | Optical Setup for the Characterisation of Photonic Waveguides . . . | 47 |
| 3.2. | Vis/Raman Setup | 48 |
| 3.2.1. | Flowcell Design | 48 |
| 3.2.2. | Method Development for Vis/SERS Coupling | 48 |
| 3.3. | Dynamic Light Scattering | 50 |
| 3.3.1. | Particle Size Measurements | 50 |
| 3.3.2. | Zeta Potential Measurements | 50 |
| 3.4. | Ultrasound Enhanced Particle Imaging | 51 |
| 3.4.1. | Design of the Ultrasound Enhanced Particle Imaging System | 51 |
| 3.4.2. | Characterisation of an Acoustofluidic Device | 52 |
| 3.4.3. | Operation of an Acoustofluidic Device | 52 |
| 3.5. | Sampling | 52 |
| 3.5.1. | Liquid Sampling | 53 |
| 3.5.2. | Automated Sampling Methods | 54 |
| 3.5.3. | Gas Sampling and Calibration of Gas Mixtures | 55 |
| 3.6. | Synthesis and Characterisation of Mesoporous Materials | 57 |
| 3.6.1. | Chemicals | 57 |
| 3.6.2. | Synthesis of Mesoporous Oxides | 58 |
| 3.6.3. | Surface Functionalisation of Mesoporous Oxides | 58 |
| 3.6.4. | Characterisation of Mesoporous Oxides | 59 |
| 3.6.5. | Synthesis of Metal-Organic Frameworks | 60 |
| 3.6.6. | Post-Synthetic Modification of Metal-Organic Frameworks | 61 |

| | |
|---|----|
| 3.6.7. Characterisation of Metal-Organic Frameworks | 61 |
|---|----|

| | |
|--|------------|
| IV. Mesoporous Oxides for Studying Surface Interactions and Trace Analysis | 63 |
| 4.1. Optimisation of Synthesis of Mesoporous Titania | 64 |
| 4.2. Theoretical and Practical Considerations of Mesoporous Titania for Sensing Purposes | 69 |
| 4.3. Enrichment of Phosphate Species | 72 |
| 4.4. Enrichment of Hydrocarbons from the Aqueous Phase | 73 |
| 4.5. Enrichment of Volatile Organic Contaminants from the Gas Phase | 76 |
| V. Metal-Organic Frameworks for Adsorption Screening and Trace Analysis | 77 |
| 5.1. Optimisation of Metal-Organic Framework Synthesis | 78 |
| 5.2. Post-Synthetic Modification of Metal-Organic Frameworks | 80 |
| 5.3. Preparation of an Enrichment Film for Phosphates in Water | 82 |
| 5.4. Enrichment of Hydrocarbons from the Aqueous Phase | 82 |
| VI. Surface-Enhanced Raman Scattering for Simulating Corrosion Inhibition | 85 |
| 6.1. Preliminary Results for Surface-Enhanced Raman Scattering of Surfactants | 86 |
| VII. Ultrasound Particle Manipulation for the Imaging of Suspended Solids in Water Treatment | 88 |
| 7.1. Optimisation of the Ultrasound Flow Cell | 89 |
| 8. Conclusions and Outlook | 93 |
| Bibliography | 102 |
| A. Appendix | 113 |
| A.1. Publication I: Metal-organic frameworks combined with mid-infrared spectroscopy for the trace analysis of phosphates in water | 114 |
| A.2. Publication II: Integrated optics waveguides and mesoporous oxides for the monitoring of volatile organic compound traces in the mid-infrared | 123 |

| | |
|---|-----|
| A.3. Publication III: Experimental Demonstration of the high alignment-tolerant Behavior of a mid-Infrared Waveguide Platform for evanescent Field Sensing | 140 |
| A.4. Publication IV: In-situ study of the interactions between metal surfaces and cationic surfactant corrosion inhibitors by surface-enhanced Raman spectroscopy coupled with visible spectroscopy | 148 |
| A.5. Publication V: In-situ study of the adsorption of phosphate species and phosphate derivates in the confined spaces of mesoporous titania | 158 |
| A.6. Publication VI: Development of a particle analysis system for the process water of the petrochemical industry using hyperspectral imaging, white-light imaging, and fluorescence imaging | 168 |
| A.7. Curriculum Vitae | 177 |

Part I.

Framework of this thesis

1.1. The HYDROPTICS Project

This thesis was performed within the scope of the European Union's Horizon 2020 project HYDROPTICS. The broad and ambitious objective of the project was to develop a sensor platform that performs a wide range of monitoring activities in the petrochemical industry. The sensing platform was planned to exploit novel photonic technologies, enabling reliable, accurate, and cost-effective monitoring of the water quality in industrial plants.

The project could be broken down into the following goals:

- **The development of a new on-line oil-in-water analyser for the oil industry:**
In the HYDROPTICS oil-in-water analyser, a novel continuous extraction of the oil from the water stream should be combined with new laser technology to account for residual water in the extraction liquid to move towards a better recyclability of the extraction liquid.
- **The development of a hyperspectral particle analyser for the detection of total suspended solids in industrial water:**
In the HYDROPTICS particle analyser, a high-speed, high-resolution hyperspectral imaging spectrograph should be combined with a ultrasound-assisted flow cell, improving the optical contrast by moving all particles into the focal plane of the spectrograph. This should enable an on-line particle analysis in process water.
- **The development of new mid-IR sensing technologies:**
New technologies in mid-IR sensings should be developed for this project, including the use of mesoporous materials for corrosion inhibitor and oil-in-water analysis, Mach-Zehnder-Interferometers to move towards dispersion spectroscopy, and polarimetric balanced detection schemes to improve the technology readiness level (TRL) of these technologies for practical applications.
- **The development of a digital twin of a crucial process in the water treatment of the petrochemical industry:**
By simulating the key processes in a digital twin, process optimisations can be performed more efficiently and also used to define the optimal positions for the sensors developed in this project.
- **The development of new laser technologies to further the innovation of mid-IR lasers:**
A new on-chip dual-DFB-QCL should be developed to enable better background measurements in recycled cyclohexane. Additionally, dual frequency comb spectrometers should be developed and benchmarked with the more established technology.

For this project, a multinational consortium cooperated consisting of ten partners from five countries: **QuantaRed Technologies** (Austria) was tasked with the development of the analysers by using the technologies developed in this project. After the dissolution of QuantaRed Technologies during the project, this task was shared by **TU Wien** (Austria) and **Silicon Austria Labs** (Austria). TU Wien and Silicon Austria Labs cooperated for the technologies to be integrated in the particle analyser. TU Wien was further tasked with the development of the new mid-IR sensing technologies and the digital twinning, making use of interuniversity synergies. **Alpes Lasers** (Switzerland), **IR-Sweep** (Switzerland), and **imec** (Belgium) were tasked with the development of the new laser technologies. **TUPRAS** (Turkey) and **OMV** (Austria) were the hosts of the pilot testings of the analysers. **NTUA** (Greece) helped with data processing. **DBC Europe** (Belgium) helped with ensuring ethics and by providing a crude business plan for the exploitation of the sensing platform.

In this thesis, parts of the work carried out by TU Wien are featured, with a special focus on the exploration of new sensing schemes for the detection of corrosion inhibitors, phosphates, and oil-in-water, as well as the development of the liquid handling module for the particle analyser.

1.2. The ACTPHAST4R Project

Building on the advances made in the use of mesoporous materials for sensing, another project combining the technology with mid-IR photonic integrated circuits (PICs) was pursued. For that purpose, a proposal was submitted to the ACTPHAST4R board to perform experiments on a platform that has been developed in an earlier cooperation with imec-UGent. The ACTPHAST4R project is another European Union's Horizon 2020 project that aims to support accelerated deployment of cutting-edge photonics technologies. This was done by granting financial support to smaller projects, offering researchers in the chance to turn their scientific concepts into industrially relevant demonstrators.

The project that evolved out the ACTPHAST4R umbrella had the following goals:

- Design a new platform based on germanium-on-silicon technology to move the wavelength region to 8-10 μm .
- Perform a thorough characterisation of the alignment tolerances of the existing design to demonstrate its viability for practical applications.
- Demonstrate a use case for the use of coated PICs and show the capabilities of the mid-IR platform.

The project was carried out in cooperation with imec-UGent and involved a two week research stay at their premises. During this stay, a fabrication run of the PICs, the development of an optical setup for the demonstration of the alignment tolerances, and the measurements of the alignment tolerant behaviour of the PICs were performed.

Part II.

Theoretical part

2.1. Introduction

In this part, several different techniques are introduced covering the scientific path of this thesis. It is divided into four main topics: The first two sections (2.2 and 2.3) will focus on the fundamentals of vibrational spectroscopy, which were the foundation of the research conducted. To better differentiate between the two techniques making up vibrational spectroscopy, section 2.2 will focus on mid-IR spectroscopy, while section 2.3 will give an overview of Raman spectroscopy. In the mid-IR section, a special focus will be placed on evanescent field techniques such as attenuated total reflection and the waveguide technology employed in the ACTPHAST4R project. The next two sections (2.4 and 2.5) are meant to be an introduction to porous materials (section 2.4) and their role in adsorption processes (section 2.5) for mid-infrared sensing. Finally, the work on ultrasound particle manipulation performed in the HYDROPTICS project is featured in section 2.6.

2.2. Mid-Infrared Spectroscopy

Mid-infrared (IR) spectroscopy is a potent analytical technique with the ability to give both qualitative and quantitative information of samples by probing their unique molecular vibrations, resulting in distinctive spectral features commonly regarded as fingerprint. Further, it can also give information on inter- and intramolecular interactions and in complex samples, chemometrics can be used to do latent variable analysis to uncover hidden spectral features. Mid-IR spectroscopy can be used for solid, liquid, and gaseous samples for fast, non-destructive, and label-free measurements.

This section will introduce the fundamentals of the interaction of mid-IR radiation with matter and related phenomena based on literature,^{[1][2]} with a special emphasis on evanescent field sensing techniques which are prominently featured in the experimental part. Beyond that, further information on additional techniques can be found in the literature.^{[1][2]}

2.2.1. Fundamentals in Infrared Spectroscopy

Spectroscopy is based on the interaction of electromagnetic (EM) waves with matter. In general, spectroscopy looks at the dependency of the interaction on the energy of the light quanta. This energy is further related to the frequency ν (or the vacuum wavenumber $\tilde{\nu}_0$) via the Planck constant h and the vacuum light speed c_0 in the Einstein-Planck (2.1) relation.

$$E = h \cdot \nu = h \cdot c_0 \cdot \tilde{\nu}_0 \quad (2.1)$$

Table 2.1.: Different regions of the EM spectrum and the transitions excited by the respective EM waves.

| Wavelength | EM region | Interactions |
|---------------------------------------|---------------------------|--|
| 1 pm - 100 pm | Gamma rays | Nuclear energy transitions |
| 10 pm - 10 nm | X-rays | Core electron transitions |
| 10 nm - 350 nm | Ultraviolet (UV) | Valence electron transitions |
| | radiation | |
| 350 nm - 750 nm | Visible (VIS) | Valence electron transitions |
| | radiation | |
| 750 nm - 100 μm | Infrared radiation | Vibrational and ro-vibrational molecule transitions |
| 100 μ m - 1 mm | Terahertz radiation | Rotational transitions in gas molecules |
| 1 cm - 1 m | Microwaves | Electron spin transitions |
| 1 m - 100 m | Radiowaves | Nuclei spin transitions |

Depending on the energy of the light, different interactions (Table 2.1) are possible, which are studied in the respective branches of spectroscopy.

The practical work in this thesis mainly focused on the mid-IR region, which is a sub-region in the IR region located between 2.5 and 25 μ m. In this part of the EM spectrum, fundamental vibrational transitions are induced. Beyond that, the combination of fundamental modes or their overtones can be found in the near-IR region (located between 750 nm and 2.5 μ m), while rotational transitions and lattice vibrations of crystalline samples can be excited in the far-IR region, which overlaps with the Terahertz radiation and is located between 25 μ m and 100 μ m.

For a better comprehension of infrared spectra, it is important to understand the origin of the transitions between different vibrational energy states and their correlation with the symmetry of the molecules. In a first simple approximation, one can look at the bonds of molecules as undamped springs which can be described by a harmonic oscillator. For this simplified model and considering quantisation of energy levels in molecules, the vibrational modes can be described by their harmonic vibrational energy states E_i in (2.2).

$$E_i = h \cdot \nu_i \left(n_i + \frac{1}{2} \right) \quad (2.2)$$

In this equation, n_i is the vibrational quantum number of the i -th mode ($i = 0, 1, 2, \dots$), while ν_i is the corresponding fundamental frequency of this vibrational mode. For this

model, the vibrational frequency can be described similarly to classical mechanics (2.3).

$$\nu = \frac{1}{2\pi} \sqrt{K \left(\frac{1}{m_1} + \frac{1}{m_2} \right)} \quad (2.3)$$

In this model, m_1 and m_2 correspond to the atomic mass of the atoms, while K corresponds to the force constant, which can be correlated to the bonding strength. Applying this model to the respective bonds of the probed molecule, one can estimate the vibrational transition frequencies for specific functional groups, illustrating the chemical selectivity of IR spectroscopy.

Expanding this model to account for their symmetry, one receives a multitude of single vibrational modes in respect to their degree of freedom (Figure 2.1). For a molecule with N atoms, $3N$ degrees can be made out, while three of them correspond to translational motion in all three dimensions, and two (for linear molecules) or three of them (for non-linear molecules) to rotations around these axes. The remaining $3N-5$ (for linear molecules) or $3N-6$ (for non-linear molecules) correspond to the possible vibrational modes that can be described with (2.2). However, not all of these modes are IR-active: For a vibrational mode, a change in dipole moment needs to be induced in order to be excited by IR radiation. This leads to symmetrical degeneracies, with the actual number of vibrational modes observed in an IR spectrum generally being less than the theoretical amount.

Finally, when looking at transitions of higher order, our initial model of the harmonic oscillator gets increasingly inaccurate. Thus, the vibrational modes are best described with an anharmonic potential function (2.4) with the added anharmonicity factor γ_i , with the deviations shown in Figure 2.1. This assumption also has the added benefit that selection rules for the transitions are more relaxed, as a harmonic oscillator only allows transitions for $\Delta n = \pm 1$ (which would forbid the excitation of overtone vibrations from the ground state).

$$E_i = h \cdot \nu_i \left(n_i + \frac{1}{2} \right) - h \cdot \nu_i \cdot \gamma_i \left(n_i + \frac{1}{2} \right) \quad (2.4)$$

In the mid-IR range, specific information related to most functional groups can be found. For more information regarding the correlation of spectral features to functional groups, a comprehensive guideline can be found in the literature.^[3] Below 1500 cm^{-1} , the information density is the highest, often resulting in significant overlaps. The resulting spectral patterns are unique for each molecule, which is why this region is often called fingerprint region.

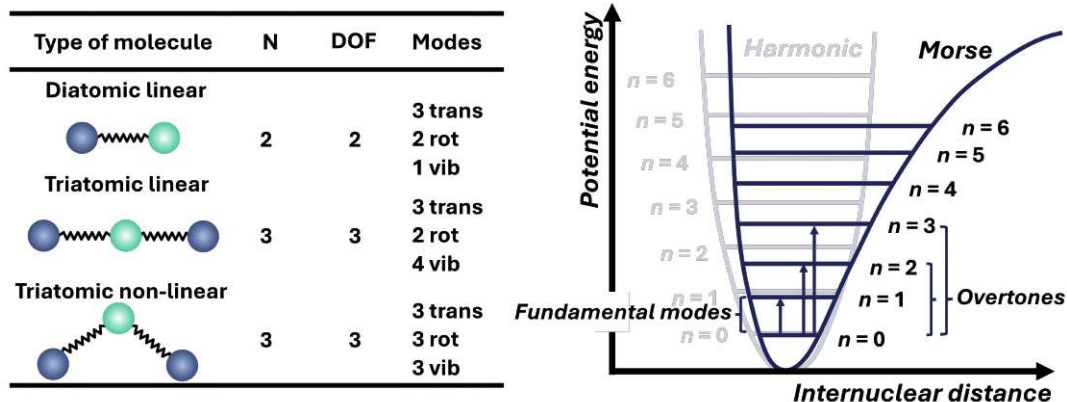


Figure 2.1.: Left: Correlation of simple molecule symmetry with their degrees of freedom (DOF) and the corresponding modes. Right: Harmonic (light blue) and Morse (dark blue) potential functions, describing vibrational energy levels of molecules. All vibrational modes are referenced to the vibrational ground state ($n=0$) with modes with a $\Delta n=1$ referring to the fundamental modes and modes with $\Delta n>1$ referring to the overtones.

2.2.2. Transmission Infrared Spectroscopy

Beyond the qualitative information from fingerprinting the unique spectra and comparing the spectral shape with standard components, also quantitative information can be gathered from an IR spectrum. This is based on the findings from Bouguer, Lambert, and Beer.^{[4] [5] [6]} In their works, they describe the exponential attenuation of light propagating in an absorbing medium, which culminated in the Bouguer-Beer-Lambert law (2.5) well-known to spectroscopists today.

$$A = -\log_{10} \left(\frac{I}{I_0} \right) = \varepsilon(\tilde{\nu}) \cdot c \cdot d \quad (2.5)$$

In this law, A stands for the absorbance, which is the negative decadic logarithm of the transmittance $\frac{I}{I_0}$. The molar decadic absorption coefficient depending on the wavenumber (i.e. the vibrational transitions leading to absorption) is denoted by $\varepsilon(\tilde{\nu})$, while c and d stand for the concentration of the absorbing species and the optical path length, respectively.

For an electromagnetic derivation, which can be found in more detail in literature^{[7] [8] [9] [10]}, we have to start by combining our initial anharmonic oscillator model with the definition of an electromagnetic plane wave $E = E_0 e^{-i\omega t}$, receiving a differential equation for the displacement x of a charged mass (μ denotes the reduced mass and q denotes

the elementary charge) in the time domain t with a wave frequency of ω :

$$\mu \frac{d^2 x}{dt^2} + \mu \gamma \frac{dx}{dt} + \omega_0^2 x = q E_0 e^{-i\omega t} \quad (2.6)$$

In this equation, γ denotes the damping constant (related to the anharmonicity of the oscillator), while ω_0 stands for the eigenfrequency of the oscillator. For the differential equation in (2.6), a solution for $x(t)$ is $x_0 \cdot e^{-\omega t}$. Solving the equation for x_0 leads to the following term for $x(t)$:

$$x(t) = \frac{q}{\mu(\omega_0^2 - \omega^2 - i\omega\gamma)} E_0 e^{-i\omega t} \quad (2.7)$$

As the excitation of vibrational states is closely linked to induced dipoles, we multiply by q to get the induced dipole moment p . Using the definition of the polarisation being $P = p \cdot N_p = \varepsilon_0(\varepsilon_r - 1)E$, with N_p being the number of dipole moments per volume and ε_0 being the vacuum permittivity, we get the following function for the relative permittivity ε_r :

$$\varepsilon_r = 1 + \frac{N_A}{\mu\varepsilon_0} \frac{q^2}{\omega_0^2 - \omega^2 - i\omega\gamma} \cdot c \quad (2.8)$$

Next, deriving the relation $n = \varepsilon_r' = (\varepsilon_r' + i\varepsilon_r'')^2$ from the Maxwell equation and defining the complex refractive index $\hat{n} = n + i\kappa$, we get the relation $\varepsilon_r'' = 2n\kappa$. If we now separate the real and imaginary parts, and solve for the absorption coefficient κ , we get the following form:

$$\kappa = \frac{q^2 N_A}{2n\mu\varepsilon_0} \frac{\omega\gamma}{(\omega_0^2 - \omega^2) + \omega^2\gamma^2} \cdot c \quad (2.9)$$

Finally, adding in the definition of the absorbance, we end up with the following equation, which we can simplify to the Bouguer-Beer-Lambert law in 2.5.

$$A = \frac{2\pi \log_{10}(e) q^2 N_A}{n\mu\varepsilon_0 \lambda_0} \frac{\omega\gamma}{(\omega_0^2 - \omega^2) + \omega^2\gamma^2} \cdot c \cdot d \quad (2.10)$$

As a consequence of the Bouguer-Beer-Lambert law, we can assume $\varepsilon(\tilde{\nu})$ as a molecule-specific constant in a defined analytical system. Thus, this leaves us with a linear dependence of an absorption spectrum defined by this constant scaled linearly by the concentration c and path length d , which is true for most setups, with the model coming to its limits at higher concentrations due to scattering losses and increased intramolecular interactions at higher concentrations.^[8]

For smaller concentrations, however, this model enables us to optimise our spectroscopic setups in regards to the interaction lengths for our devised purpose. For the measurement

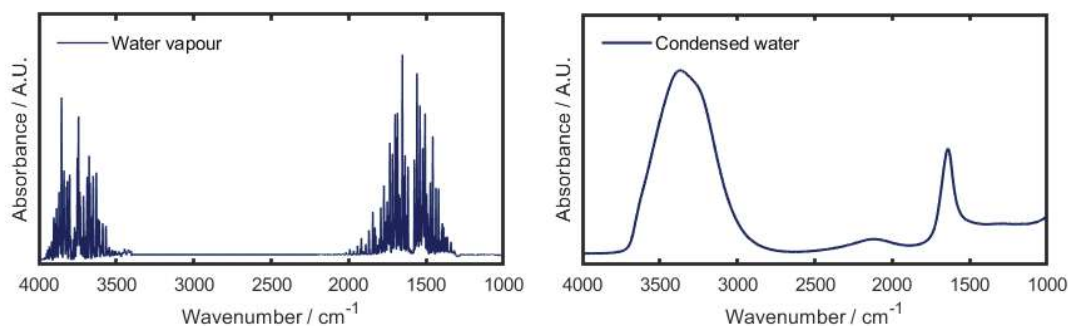


Figure 2.2.: Mid-IR absorbance spectra of water vapour (left) and condensed water (right), respectively.

of gaseous analytes, multi-pass cells can be designed, with meter-long interactions in a reasonable form factor for ppbv (parts-per-billion volume parts) applications. In a similar fashion, transmission flow cells with different thicknesses can be fabricated for the analysis of liquid matrix analytes. For evanescent field methods such as ATR (attenuated total reflection) and photonic waveguides, an increase in path length can also be achieved by designing the internal reflection element (IRE) to have an increased amount of active reflections or by tuning waveguide length or the confinement factor (evanescent field methods are explained in detail in sections 2.2.4 and 2.2.5).

Although it seems like a trivial task to increase the sensitivity of your method by just increasing the path length, the inherent absorptions of the matrix components, especially in liquid phase analysis, makes the implementation of infrared schemes for trace analysis a challenging task. One culprit for this is water, which absorbs strongly in the entirety of the mid-IR regime. For gas measurements, many water vapour absorption lines are found in the range of 5–8 μm or 2000–1250 cm^{-1} (Figure 2.2-left), which may obstruct the analyte signal. Here, well resolved spectra or drying agents may help to clear the interferences. However, for aqueous samples, this luxury does not exist and the strong absorption of water limiting the path length (and, thus, the sensitivity) can only be mitigated with preconcentration schemes (which can also be used to transfer the analyte into a less absorbing solvent, enabling higher path lengths) or by increasing the power of the incident beam (by means of mid-IR lasers or synchrotron radiation). Local preconcentration schemes by combining tunable porous materials with evanescent field methods can also be performed and are a major focus of this thesis (a detailed introduction into this approach is featured in sections 2.2.5 and 2.5.2).

Another way of dealing with complex matrices overlapping with the analyte signal is the use of chemometrics. For non-interacting mixtures, their absorption coefficients are linearly

independent. Thus, the resulting absorption spectra can be seen as a linear combination of their single spectra. In (2.11), the Bouguer-Beer-Lambert law is formulated for this case:

$$A_{mix}(\tilde{\nu}) = (\mathbf{c} \cdot \mathbf{S}^T(\tilde{\nu})) \cdot d + (R) \quad (2.11)$$

In this equation, the $\varepsilon \cdot c$ term is formulated as the product of the concentration vector \mathbf{c} with the spectral matrix $\mathbf{S}S^T$. In case of real spectra, this concept is expanded by the residual vector R , which corresponds to the noise added to the measurement. In the case of known pure component spectra, this approach can be combined with least squares regression to deconvolute the spectrum and solve for the analyte concentrations. In case of unknown pure component spectra or interacting (reacting) mixtures, this is not as simple. Here, more powerful algorithms such as multivariate curve resolution paired with alternating least squares (MCR-ALS) may be employed.^[11] MCR-ALS is a soft-modeling technique that does not require exact knowledge of the spectral system, which can deliver accurate results even for the time-resolved observation of interacting mixtures (i.e. chemical reaction monitoring).^[12] By iteratively improving the initial estimates for C and S with ALS, MCR-ALS proved to be a powerful tool for many complex applications such as the monitoring of thermal protein denaturation in water.^{[13][14]}

2.2.3. Mid-Infrared Light Sources and Spectrometers

Historically, the following parts were needed to record an IR spectrum of an absorbing sample: a thermal IR source, a dispersive grating, an aperture to determine the spectral resolution, and a detector. Due to several reasons, this was a very inefficient approach: First, the black body radiation spectrum (2.12) peaks in the VIS range for typical operation temperatures T (see Figure 2.3). This leads to a generally low intensity of the IR source and, as a result, longer measurement times, especially for the fingerprint range. Additionally, by using a dispersive grating and an aperture (determining the spectral resolution), most of the radiation is filtered out for each grating position (equivalent to a centre wavenumber), making measurements tediously slow, especially for larger spectral ranges and/or higher resolutions.

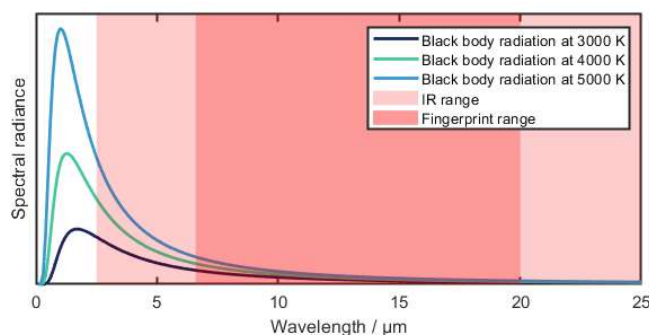


Figure 2.3.: Calculated black body radiation spectra for three different temperatures (3000 K, 4000 K, and 5000 K). The mid-IR range is marked in light red, and the fingerprint region marked in dark red.

$$B(\nu, T) = \frac{2h\nu^3}{c^2} \frac{1}{e^{h\nu/kT} - 1} \quad (2.12)$$

To improve the performance of IR spectrometers, two approaches are obvious: utilising a higher percentage of the IR radiation than for the dispersive approach, and increasing the intensity of the IR source. The first problem has been solved by the introduction of interferometric IR spectrometers. Nowadays, the most frequently employed type of IR spectrometers comprises a Michelson interferometer, which splits the beam into two parts, one being reflected by a fixed mirror while the other one is reflected by a movable mirror (a configuration of such a spectrometer shown in Figure 2.5). Moving the mirror introduces a temporal coherence depending on the retardation caused by the movement of the mirror, where for each wavelength, a different retardation leads to constructive/destructive interference. The resulting superposition beat note of all wavelengths is called interferogram (Figure 2.4), which can be Fourier transformed into an intensity spectrum, hence, such a spectrometer is called a Fourier-transform infrared (FT-IR) spectrometer. This approach has three key advantages compared to traditional dispersive IR spectroscopy:

- As the whole wavelength region can be measured simultaneously, the spectral acquisition is much quicker, with the time advantage directly proportional to the number of resolution elements. (Fellgett advantage)
- As the spectral resolution is not determined by the aperture of the slit as in a dispersive spectrometer but rather by the maximum retardation of the movable mirror, the full circular cross section of the beam can be used. (Jacquinot advantage)
- By using a reference laser (most frequently a HeNe laser), a reference interferogram can be sampled. By correlating the IR interferogram with the reference interferogram,

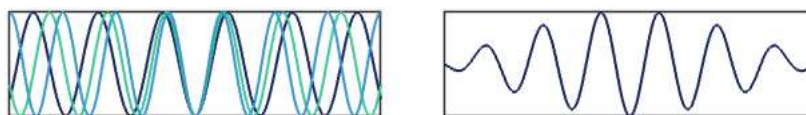


Figure 2.4.: Left: Light wave functions for three different wavelengths, centred at the point of zero retardation. Right: Interferogram for these three wavelengths.

the wavenumber precision can be improved significantly compared to a dispersive spectrometer. (Connes advantage)

On the other front, much effort has been put into improving IR sources. To date, thermal IR sources are still most widely featured in commercial instruments. Here, SiC heating rods (commonly known as Globars, basic design shown in Figure 2.5) are the preferred choice due to their robust and stable broadband operation. They are heated up to temperatures around 1500 K and behave as a homogeneous black body emitter. However, their spectral power measured inside a sample compartment of a standard FT-IR spectrometer is rather low (in the $\mu\text{W}/\text{cm}^{-1}$ range) and is neither focused nor coherent.

Here, stimulated emission as theoretically predicted by Einstein^[15] and experimentally proven by Kopfermann and Ladenburg^[16] promised to provide a new technology for high-brightness IR sources. The first IR laser technology showing promising results were lead salt diode lasers, with broadband emission and higher spectral power densities, however, they required cryogenic cooling and their beam profiles showed astigmatism and divergent behaviour.^{[17][18]} Newer technologies include broadband supercontinuum lasers^[19] and quantum cascade lasers (QCLs)^[20], with QCLs being especially promising due to their high power (>100 mW, even outperforming synchrotron radiation) and their emission in the fingerprint region. They emit from a layer structure of different semiconductor materials by utilising inter-subband transitions of electrons, rendering the band gaps of the semiconductor materials irrelevant. This enables flexible laser design by tuning the layered structure rather than engineering the band gap of the semiconductors of the materials. Beyond their high power, which can be used to improve IR sensing schemes in regard to their sensitivity, they also emit inherently coherent and polarised light, opening up new opportunities for IR spectroscopy. For example, the coherent emission of QCLs can be used to enable phase sensitive measurements in dispersion spectroscopy^[21], while the polarised nature of the emitted light can be used for designing high-performance vibrational circular dichroism spectrometers^[22].

The two most commonly used types of QCLs are distributed feedback (DFB) QCLs^[23] and external cavity (EC) QCLs.^[24] DFB-QCLs employ a Bragg grating on the QCL chip (basic design shown in Figure 2.5), with a single mode emission set by the grating period.

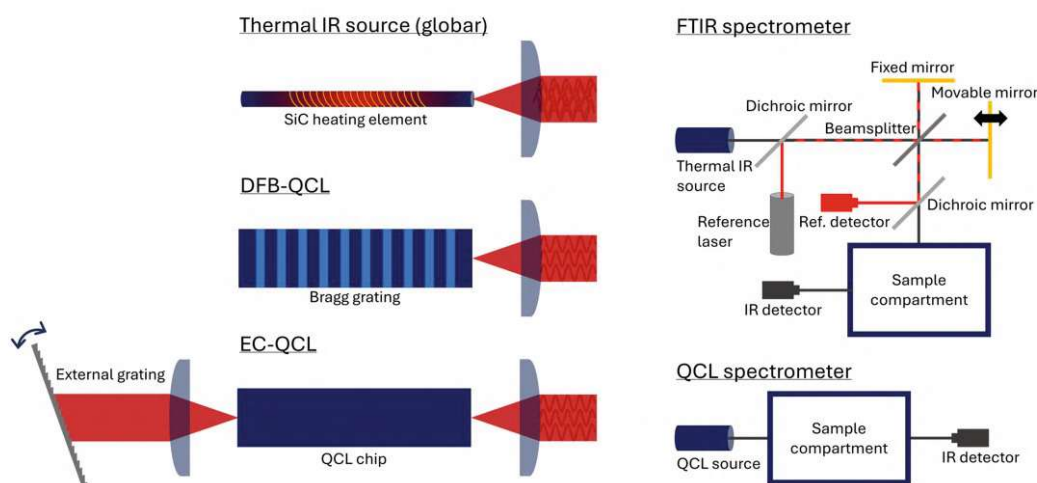


Figure 2.5.: Left: Three different mid-IR sources, a thermal IR source (globar, top), a DFB-QCL (middle), and an EC-QCL (bottom). Right: Two different technologies of mid-IR spectrometers: An FT-IR spectrometer (top, schematically shown for a Michelson interferometer), and a QCL spectrometer (bottom).

This mode can be tuned narrowly by changing the refractive index of the grating, but this tunability usually does not exceed a couple of wavenumbers. Thus, they are frequently used for gas sensing applications due to the sharp gas absorption bands either as single-gas sensors or multi-gas sensors using DFB-QCL arrays.^[25] On the other hand, EC-QCLs offer the same high intensity single-mode emission as DFB-QCLs combined with a broad tunability. This tunability is achieved by adding an external diffraction grating with an adjustable angle (basic design shown in Figure 2.5). This configuration allows for short measurement times (up to several hundred cm^{-1}s) and tuning ranges over several hundred wavenumbers without the need for interferometric components (shown in Figure 2.5 for a sample QCL spectrometer). Although QCLs offer cutting-edge performance in a reasonable form factor, they are much more expensive than thermal IR sources, and may suffer from pulse-to-pulse intensity fluctuations or wavelength drifts.^[26] Nonetheless, recent reports proved that QCL based spectroscopy can outperform even high-end FT-IR spectrometers by compensating the laser intensity noise with balanced detection approaches.^[27]

2.2.4. Attenuated Total Reflection Infrared Spectroscopy

Alongside transmission IR spectroscopy, ATR-IR spectroscopy is the most popular way of recording IR spectra. Especially in routine analysis, the use of diamond ATR units allows for quick, easy, and robust measurements of all kinds of samples (e.g. solids, liquids, slurries, gels) without the need of extensive sample preparation (in the most cases). It

is based on total internal reflection, a phenomenon that occurs when an electromagnetic wave is reflected at the boundary of two media with different refractive indices. This can only occur at angles larger than the critical angle θ_c for a transition from an optical denser medium to an optical rarer medium ($n_1 > n_2$), at smaller angles, refraction following Snell's law (2.13) takes place. Following this equation, θ_c is defined as the limit of refraction (2.14), at which the refracted light cannot leave the incident medium and travels parallel to the boundary ($\theta_2 = 90^\circ$). At angles $\theta_1 > \theta_c$, total internal reflection takes place, and the incident beam is reflected at the same angle from the boundary of the two media. In Figure 2.6, the three cases for a transition from an optical denser to an optical rarer medium (refraction, critical refraction, and total internal reflection) are illustrated.

$$n_1 \cdot \sin(\theta_1) = n_2 \cdot \sin(\theta_2) \quad (2.13)$$

$$\theta_c = \arcsin\left(\frac{n_2}{n_1}\right) \quad (2.14)$$

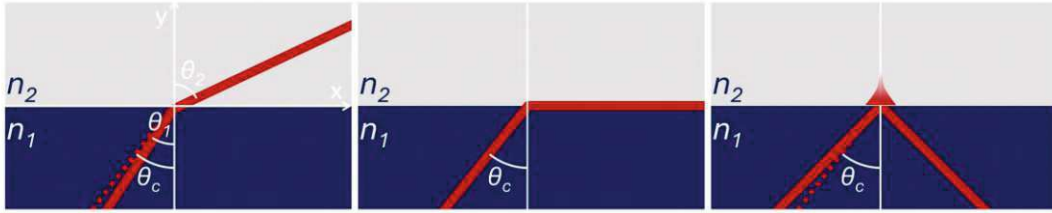


Figure 2.6.: Interaction of a light beam on the boundary of two dielectric media with different refractive indices ($n_1 > n_2$): refraction (left, for $\theta < \theta_c$), critical refraction (middle, for $\theta = \theta_c$), and total reflection (right, for $\theta > \theta_c$).

When a wave is totally reflected, an evanescent field is formed at the interface between the two dielectric media. This is a result of the boundary conditions of the Maxwell equations, which necessitate an electromagnetic field at both sides of the interface. For the plane of incidence (defined as x-y plane), the wave vector k of the imaginary transmitted wave function can be split up into the two components of the x-y plane, leading to:

$$E(x, t) = E_0 e^{i(k_x x + k_y y - \omega t)} \quad (2.15)$$

Taking $k_x = k \cdot \sin(\theta_t)$ and $k_y = k \cdot \cos(\theta_t)$ and using Snell's law to convert θ_t to the angle of incidence θ , we get:

$$E(x, t) = E_0 e^{ix\left(\frac{k}{n_2} n_1 \sin(\theta)\right)} e^{-iy\left(\frac{k}{n_2} \sqrt{n_1^2 \sin^2(\theta) - n_2^2}\right)} e^{-i\omega t} \quad (2.16)$$

Finally, replacing $\frac{k}{n_2}$ with $\frac{2\pi}{\lambda_0}$, with λ_0 denoting the vacuum wavelength, and only looking at the spatial domain ikx , we get the following equation for the electric field, with E'_x denoting the x-component of the wave function and E'_y denoting the y-component of the evanescent field perpendicular to the interface.

$$E(x) = E_0 E'_x E'_y = E_0 e^{ix \left(\frac{2\pi}{\lambda_0} n_1 \sin(\theta) \right)} e^{-iy \left(\frac{2\pi}{\lambda_0} \sqrt{n_1^2 \sin^2(\theta) - n_2^2} \right)} \quad (2.17)$$

Looking at the nature of the E'_x and the E'_y terms, it is obvious that the electrical field exponentially decays in y direction. The amount of this decay is commonly described with the parameter of depth of penetration d_p , which is arbitrarily defined as the distance in y direction, at which the electrical field has decayed to $\frac{1}{e}$ of its original value. Solving (2.17) for this leads to the equation for d_p :

$$d_p = \frac{\lambda_0}{2\pi \sqrt{n_1^2 \sin^2(\theta) - n_2^2}} \quad (2.18)$$

Although we now have a description of the decaying evanescent wave that can be used for absorption measurements, the direct application of the interactions observed for transmission configuration is not as straightforward as it may seem. Starting off, the interaction path lengths as defined for the Bouguer-Beer-Lambert law are not set by the geometry of the transmission cell, but depend on the strength of the electric field. As this strength changes for the polarisation of the light as described in the Fresnel equations, a polarisation dependent expression needs to be added. In an approximation for weakly absorbing samples and bulk dielectric media (i.e. the whole evanescent wave is confined in the optical rarer medium), the following equations ($n_{21} = n_2/n_1$) can be used for this effective path length d_e for parallel ($d_{e,p}$, electric field of the incident wave parallel to plane of incidence) and senkrecht ($d_{e,s}$, electric field of the incident wave perpendicular to plane of incidence) polarisations:^[28]

$$d_{e,p} = \frac{\lambda_0}{n_1} \frac{n_{21} \cos(\theta) [2 \sin^2(\theta) - n_{21}^2]}{\pi (1 - n_{21}^2) [(1 + n_{21}^2) \sin^2(\theta) - n_{21}^2] \sqrt{\sin^2(\theta) - n_{21}^2}} \quad (2.19)$$

$$d_{e,s} = \frac{\lambda_0}{n_1} \frac{n_{21} \cos(\theta)}{\pi (1 - n_{21}^2) \sqrt{\sin^2(\theta) - n_{21}^2}} \quad (2.20)$$

The nature of these equations further lead to some difficulties when trying to compare IR spectra recorded in transmission and ATR configurations, respectively. This is due to the dependence of the effective path length on the wavelength λ_0 and the refractive index of the sample medium n_2 . Comparing an ATR spectrum with a transmission spectrum of the same sample, the wavelength dependence of d_e leads to stronger absorbances at higher wavelengths for two bands with equal absorption coefficients, while the presence of

anomalous dispersion caused by the real part of the permittivity function (2.8) leads to a peak shift towards higher wavelengths in the ATR spectrum.^[29] Using equations (2.19) and (2.20) (for non-polarised light, $d_e = (d_{e,p} + d_{e,s})/2$ is valid), it is also apparent that the interaction length can be tuned by material selection in terms of the refractive index of the IRE as well as the angle of incidence. This allows for narrow tuning up to an effective path length in the small μm range. For larger interaction lengths, multi-bounce IREs (transmission configuration compared with single-bounce and multi-bounce ATR configuration in Figure 2.7) can be employed due the additive nature of light intensity attenuation at each reflection.^[30]

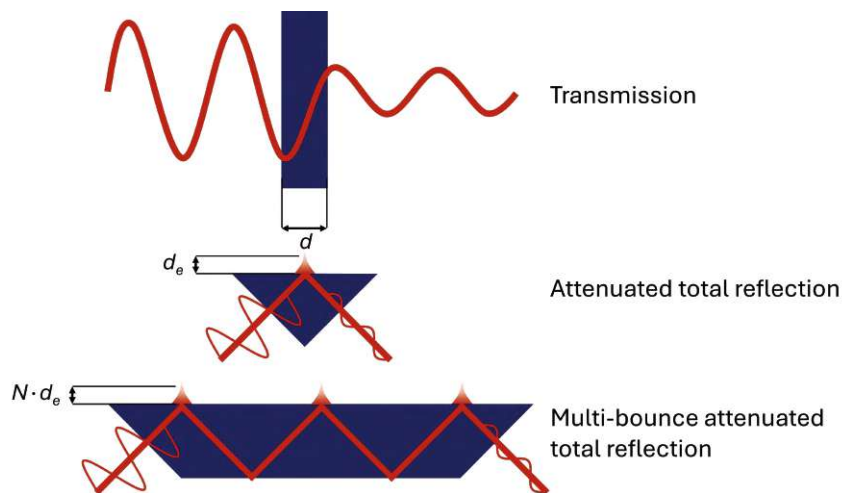


Figure 2.7.: Schematic depiction of the differences between transmission probing in infrared spectroscopy and attenuated total reflection probing (in the case of single and multi-bounce internal reflection elements).

Expressing the Bouguer-Beer-Lambert law for the case of multi-bounce IREs (N denotes the number of active reflections), one gets:

$$A_{ATR} = \varepsilon(\tilde{\nu}) \cdot c \cdot N \cdot d_e \quad (2.21)$$

2.2.5. Evanescent Field Infrared Spectroscopy Based on Photonic Waveguides

To improve the sensitivity of ATR-based sensing methods, the effective pathlength of an IRE can be increased by increasing the number of reflections of the IRE. A straightforward way of doing that is tuning the geometry towards thinner and longer IREs, with achievable pathlengths in the range of 20-40 μm . However, this number of reflections is limited, as the IREs get more fragile (for thinner chips) and bulky (for longer chips), or add scattering

losses, which at some point outweigh the benefit of the increased pathlength.

In the last decades, photonic integrated circuits (PICs) have experienced a development boom, with applications in optical interfacing for telecommunications, as polarisation elements or as optical sensors.^[31] For the mid-infrared, silicon photonics particularly offers a lot of potential,^[32] with the most promising platforms being silicon-on-insulator (SOI)^[33] and germanium-on-silicon (GOS)^[34] in regards to their transparency and optical properties. For evanescent field sensing, PICs are made up by the following components: Light source - optical interface - waveguide - optical interface - detector. For the light source, typically mid-IR lasers are employed, as waveguides are still accompanied by relatively high losses. For basic designs aiming at high throughput fabrication, all components are connected with free space optics, however, also fully integrated systems featuring all components on a chip have been reported.^[35]

In this thesis, a GOS-based trenched rib waveguide platform with monolithically integrated microlenses for back-side coupling is used. In Figure 2.8, a schematic showing the concept of the used waveguides is shown:

- In Figure 2.8-A, the basic concept of rib waveguides is shown. As for most waveguides, it is a high refractive index material that is surrounded by two cladding dielectric materials with lower refractive indices (ideally $n_2 > n_1 < n_3$). In the shown case, the high index material is only used for the waveguides, however, it can also extend into an intermediate layer between the waveguide and substrate to improve confinement properties and losses.
- In Figure 2.8-B,C, the difference of rib and trenched rib waveguides is shown. Trenched rib waveguides have been employed in order to improve the coating behaviour of the waveguides.
- In Figure 2.8-D,E, two possible interfacing strategies are shown. The butt (or edge) coupling strategy is the easiest to implement, as the IR beam can be focused directly onto the interface. It also combines a high bandwidth with relatively efficient coupling. Grating (or vertical) coupling often struggles to achieve both these features, however, it opens up new possibilities in the fabrication, as the gratings can be positioned anywhere on the chip. Also, by implementing microlenses to direct the beam onto the gratings, vertical coupling offers larger alignment tolerances (which was also experimentally demonstrated in this thesis, see chapter 4.5).

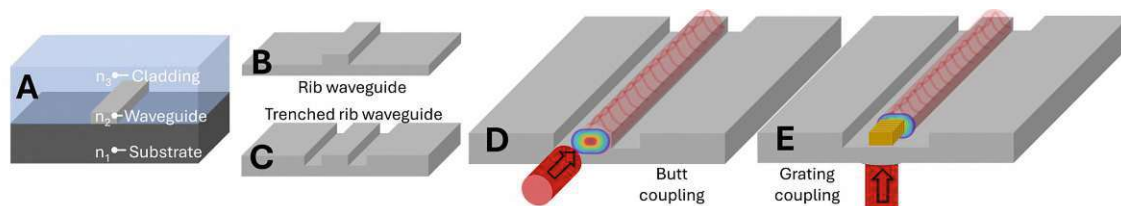


Figure 2.8.: Schematic description of waveguide technology and terminology for the photonic integrated circuits applied in this thesis: A: Basic concept of rib waveguides with a high index waveguide material grown on a substrate and surrounded by the cladding, which are both lower index materials. B-C: Example of a rib (B) and trenched rib (C) waveguide geometry. D-E: Schematic depiction of two different interfacing strategies, butt (or edge) coupling (D) and grating (or vertical) coupling (E).

2.3. Raman Spectroscopy

Raman spectroscopy is another way of probing the molecular vibrations of samples with information complementary to mid-IR spectroscopy. It is also a non-destructive and chemically specific method and is often used as process monitoring tool in aqueous environments^[36]^[37] or for imaging of biological samples^[38] or graphene surfaces^[39] making use of its superior spatial resolution compared to mid-IR imaging techniques as well as information only found in Raman spectra.

This section will introduce the fundamentals of inelastic Raman scattering and the additional information that can be retrieved in Raman spectra, with a special emphasis on surface-enhanced Raman scattering and nanoparticles with a short digression to visible spectroscopy. Beyond the short introduction in this section, additional information on Raman scattering and its applications can be found in the literature.^[40]

2.3.1. Fundamentals in Raman Scattering

When electromagnetic radiation with higher energy than needed for vibrational transitions (in case of Raman spectroscopy visible or near-IR radiation), no direct vibrational mode can be excited. Rather, the electrons are excited to higher states (illustrated in Figure 2.9-left): Usually, a monochromatic light source is used for excitation, which interacts with the electrons and temporarily polarises the molecule, creating a virtual excited state. Going from there, the relaxation can happen in two ways, either returning back to the vibrational ground state, emitting light of the same energy as the incident beam in the process (Rayleigh scattering, elastic), or returning to an excited vibrational state (Stokes scattering, inelastic). Similarly, electrons of a molecule already occupying an excited vibrational

mode can be excited to such a virtual energy state. For this excitation, the electrons can likewise either return to the same vibrational state (Rayleigh) or the ground state (anti-Stokes scattering, inelastic). A relaxation to a higher vibrational mode is theoretically also possible, leading to Stokes scattering, albeit statistically improbable and, thus, does not contribute significantly to the scattered light. As the shift of the wavelength of the scattered light compared to the incident light is directly related to the energy needed for the excitation of vibrational mode, Raman scattering gives molecular information similar to mid-IR spectroscopy.

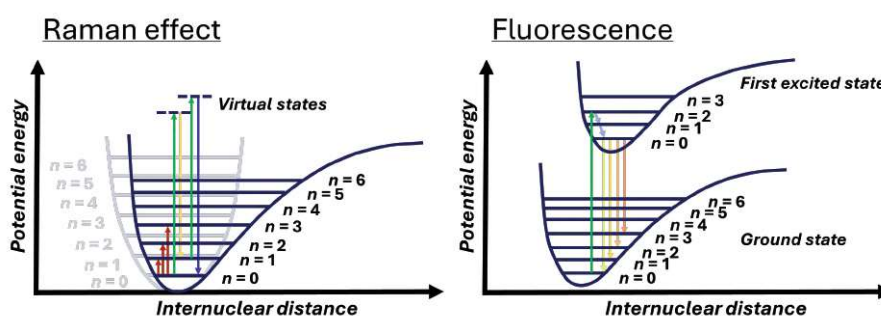


Figure 2.9.: Relevant potential functions for Raman scattering (left) and fluorescence (right). The different colours refer to the red (Stokes) and blue (anti-Stokes) shifts of the scattered (left) or emitted light (right).

Other than these scattering effects, there is also the possibility of fluorescence taking place (illustrated in Figure 2.9-right). For that, the molecules are usually excited electronically and vibrationally, after which the molecules relax vibrationally to the lowest vibrational energy level on the excited state. Afterwards, during electronic relaxation (which can happen either to the vibrational ground state of the electronic ground state, or to a higher vibrational mode), a lower energy light quantum is emitted. As the energy difference between the excitation beam and the emitted fluorescence light is also caused by vibrational transitions, fluorescence often interferes with the Raman spectra. Fluorescence interference is characterised by a broad band (caused by the wide range of possible energy transitions accompanied by absorption, relaxation and emission), leading to an elevated baseline of the Raman spectrum and a lower effective Raman intensity in case of detector saturation.

If we look at the origin of vibrations induced by Raman scattering, we start with the electric field function (E) of a monochromatic light source:

$$E = E_0 e^{-i\omega_0 t} \quad (2.22)$$

Going from there, we look at a simple diatomic molecule that interacts with the incident light, which creates an oscillating dipole moment p . This dipole moment correlates with the incident electric field with a factor α , which is defined as the polarisability of the molecule:

$$p = \alpha E = \alpha E_0 e^{-i\omega_0 t} \quad (2.23)$$

We can expand this polarisability as a function of the displacement of the vibrating bond $D = D_0 - D_r$, stopping at the linear function due to the negligible impact of higher order functions:

$$\alpha = \alpha_0 + \frac{d\alpha}{dD} D \quad (2.24)$$

For a vibrational mode with the frequency ω_r , we can write the displacement of the vibrating bond D as a function of this mode:

$$D = D_0 e^{-i\omega_r t} \quad (2.25)$$

Finally, we can substitute the polarisability with its expanded function and get the following equation:

$$\begin{aligned} p &= \left(\alpha_0 + \frac{d\alpha}{dD} D_0 e^{-i\omega_r t} \right) E_0 e^{-i\omega_0 t} \\ &= \alpha_0 E_0 e^{-i\omega_0 t} + \frac{d\alpha}{dD} D_0 E_0 e^{-i(\omega_0 + \omega_r)t} \end{aligned} \quad (2.26)$$

In this equation, we can now separate the elastic ($e^{-i\omega_0 t}$) and inelastic ($e^{-i(\omega_0 + \omega_r)t}$) parts, which directly correlate to Rayleigh (elastic), Stokes ($\omega_r > 0$) and anti-Stokes ($\omega_r < 0$) scattering.

2.3.2. Differences between Raman and mid-IR Spectroscopy

For molecular vibrations to be excited by IR radiation or inelastic scattering, certain criteria have to be met. For instance, they are IR-active, when $\left(\frac{dp}{dD} \right)_0 \neq 0$, i.e. there is a change in dipole moment for the excited state. For a Raman-active vibrational mode, the condition $\left(\frac{d\alpha}{dD} \right)_0 \neq 0$ has to be met, i.e. there is a change in polarisability in the excited mode. These conditions are not generally mutually exclusive, so most vibrations can both be excited by IR radiation or Raman scattering. However, in the case of centrosymmetric molecules, this is not valid, as molecular symmetry forbids the existence of both IR-active and Raman-active modes. One prominent example here is the carbon dioxide molecule (Figure 2.10), whose symmetric mode leads to a change in polarisability, whereas the dipole moment

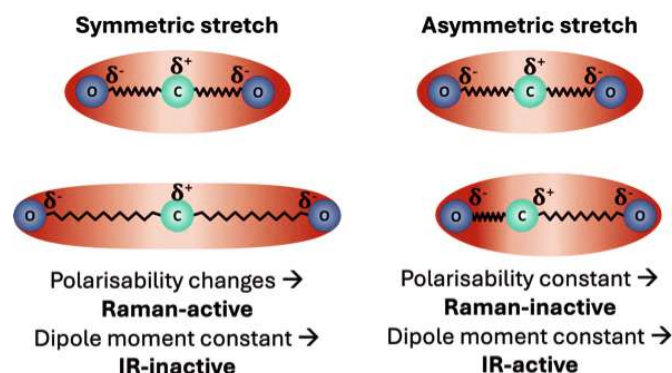


Figure 2.10.: Schematic depiction of the symmetric and asymmetric stretching vibrations of carbon dioxide in regard to their change in polarisability and dipole moment.

of the whole molecule does not change. Conversely, its asymmetric stretching vibration constitutes a change in the dipole moment, whereas the polarisability stays constant.

Other than that, there can be a significant difference in the molar absorption coefficient and the Raman scattering cross section of the matrix in process analysis, as observed for water (high absorption coefficient, weak Raman scatterer). This makes Raman spectroscopy the preferred spectroscopy method for process monitoring in aqueous media. On the other hand, fluorescence does not happen in IR spectroscopy. This gives access to strongly fluorescent samples, which are difficult to measure with Raman spectroscopy.

2.3.3. Modern Raman Instrumentation

Modern Raman spectrometers (schematically shown in Figure 2.11 for a backscattered setup) typically use a laser for excitation, with the most commonly used light sources being green lasers at 532 nm or red lasers at 785 nm. After excitation, the scattered light is focused onto the entry slit, which influences the spectral resolution: Smaller slits lead to a higher spectral resolution (at the cost of intensity). The light is then collimated onto a grating which also has an impact on the spectral resolution as well as the spectral range, depending on the groove density. Finally, the dispersed light hits the array detector (whose pitch also influences the spectral resolution), and the Raman shifts are correlated to the spatial information of the detector element.

The excitation wavelength choice usually depends on three factors:

- **Intensity:** The Raman cross-section is proportional to the fourth power of the wavenumber. Thus, a higher excitation wavelength directly correlates with a much decreased intensity of the Raman scattering spectrum. As a result, the laser power is

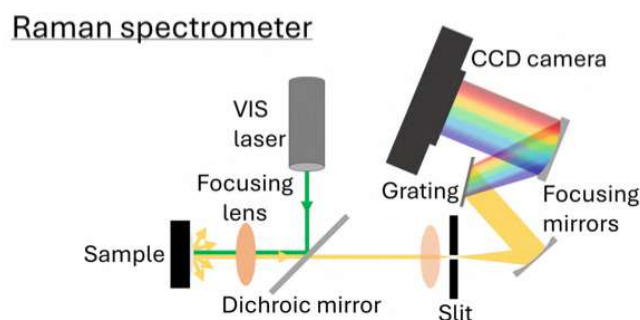


Figure 2.11.: Schematic depiction of a dispersive Raman spectrometer.

commonly higher for higher wavelength excitation, which in turn can lead to sample damage.

- **Fluorescence:** As mentioned before, fluorescence interference is a serious problem for Raman spectroscopy. As electronic transitions are more likely to be caused by higher energy excitation, lower wavelength lasers may result in high fluorescence backgrounds. As a result, 785 nm is still the most widely used laser as a compromise between intensity and low fluorescence interferences. However, some dyes may necessitate even higher wavelengths larger than 1000 nm to avoid fluorescence.
- **Cost:** Longer wavelength near-IR excitation lasers offer excellent properties to avoid high fluorescence interferences. However, the silicon CCD detectors used for visible excitation lasers cannot be used for these higher wavelengths, which require the less sensitive and more expensive InGaAs alternatives.

As Raman spectroscopy is very well suited for the analysis of aqueous samples, it is of interest for process monitoring, e.g. for biotechnologic applications. For inline monitoring, Raman fibre probes can be used as they can be integrated into existing reactors relatively easily.^[41] Their working principle is based on the scheme shown in Figure 2.11, with the excitation laser being coupled into a fibre integrated in the probe. For the interfacing optics between the fibre and the analyte, there are multiple approaches described in literature^{[42][43]}, which are all based on the concept shown in Figure 2.12: Here, the excitation laser exits the optical interface, interacting with the analyte molecules. The backscattered light is then collected by the same optics and is coupled into collection fibres, which guide the light towards the dispersive grating and the detector.

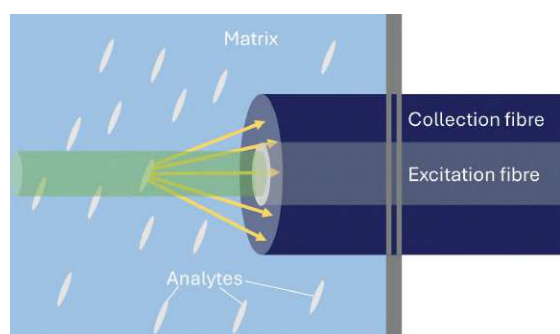


Figure 2.12.: Schematic depiction of a Raman fibre probe for inline process monitoring. Light is emitted from an excitation fibre, while the backscattered light is collected by an array of collection fibres.

2.3.4. Surface-Enhanced Raman Scattering

In 1974, the paper 'Raman spectra of pyridine adsorbed at a silver electrode' by *Fleischmann et al.* was published, looking at the adsorption of pyridine at a roughened silver electrode.^[44] However, the high sensitivity of the Raman signal did not correlate with classical Raman theory, which hinted at some kind of before unknown surface enhancement.^[45]

In the following decades, the field of surface-enhanced Raman spectroscopy (SERS) building on this pioneering work has boomed in popularity. It is now understood that the mechanism of the enhancement is due to the excitement of localised surface plasmon resonances (LSPR) on the metal nanostructures (which, in the first reports, had been the surface roughness of the silver electrode).^[46] These LSPRs occur when light resonantly excites delocalised electrons in the conduction band, while the resonance frequencies (plasmons) of these oscillations depend on the material of the nanostructure. For silver and gold, which are the two most prevalent materials for SERS substrates, their LSPRs are observed in the visible range, making them optimal for the use with the Raman excitation lasers.

Surface enhancement of the Raman signal caused by such LSPRs is typically a two-step process. First, the incident light interacts with the surface, leading to an enhancement of the elastically scattered light off the nanostructure. This light then interacts with the analyte, and is inelastically scattered back to the metal surface. Here, the Raman scattered light is once again enhanced and scattered back to the detector, which records the (typically by multiple orders of magnitude) enhanced Raman signal. The strength of the SERS enhancement (often called SERS effect) is determined by two factors, the strength of the surface enhancement on the metal, and the distance of the analyte to the LSPRs. The effect of the distance between metal surface and molecule depends on the

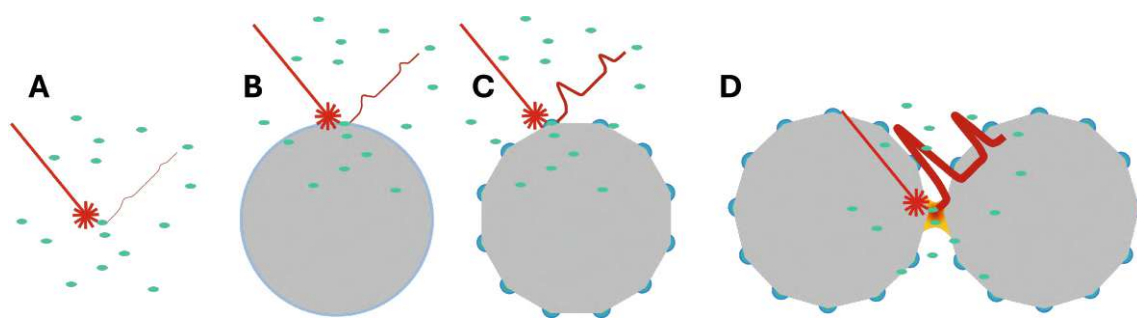


Figure 2.13.: A: Regular Raman scattering for a sample molecule. B: Surface enhanced Raman scattering for a sample molecule adsorbed on a spherical particle. C: Surface enhanced Raman scattering for a sample molecule adsorbed on a roughened particle. D: Surface enhanced Raman scattering for a sample molecule adsorbed in the hotspot between two roughened particles.

strength of the excited dipolar electric field scaling with the distance ($E(r) \propto r^{-3}$) and the approximation of the SERS intensity ($I_{SERS} = |E^4|$), which leads to a dependence of the SERS intensity on the distance of $I_{SERS} \propto r^{-12}$. On the other hand, the magnitude of the surface enhancement depends on the strength of the electric field that is excited by the LSPRs. Here, the shape of the nanostructures plays a big role in the enhancement. For single nanoparticles, the excitement is not significant, especially if their shape is spherical. However, for aggregated particles, around the area where the particles are in contact or in very close proximity (so-called hotspots), the electrical field greatly increases, which in combination with the aforementioned E^4 relation leads to SERS enhancements up to $10^{10} - 10^{11}$.^[47] In Figure 2.13, the SERS effect for different particles and a particle aggregate is schematically shown. Similar hotspots can be artificially created on single particles by designing nanostructures with inherently high plasmon resonances such as nanorods (with the ends acting as 'nanoantennas') or nanostars (where each tip acts as a 'nanoantenna').

Despite this, spherical-like nanoparticles are still used extensively due to their easy and scalable synthesis, which can also be performed in-situ. Here, the Leopold-Lendl method^[48] or the Lee-Meisel method^[49] are two prominent examples for the synthesis of spherical-like silver particles, with precise control over their size by controlling the synthesis parameters. However, for these particles, the surface cannot be controlled well, which makes their quality control very important. Here, visible spectroscopy can be used, as LSPRs can be seen in the extinction spectra as a combined effect of absorbance and scattering.

The scattering of light by nanoparticles is described by the Rayleigh and Mie theories, which describe how spherical particles scatter electromagnetic radiation. According to

these theories, the size of the nanoparticle relative to the wavelength of the incident light plays a critical role. When the diameter of the nanoparticle is much smaller than the wavelength of light, Rayleigh scattering occurs, where the intensity of scattered light is inversely proportional to the fourth power of the wavelength. This means that smaller nanoparticles scatter shorter wavelengths more efficiently than longer wavelengths.

As the diameter of the nanoparticles increases and becomes comparable to the wavelength of light, the scattering behaviour transitions from Rayleigh scattering to Mie scattering. In this regime, the scattering is more complex and depends on both the size and the refractive index of the nanoparticles. Larger nanoparticles can scatter light more efficiently across a broader range of wavelengths, leading to enhanced scattering effects.

Considering this for aggregated particles, extinction spectroscopy can serve as a powerful in-situ quality control tool for spherical-like nanoparticles in SERS applications. This has been experimentally shown in the course of this thesis in publication IV.

2.4. Introduction to Mesoporous Materials

Mesoporous materials (defined as materials with pore sizes of 2-50 nm^[50]) possess many properties that make them attractive for chemical engineering, most prominently their high specific surface area and pore volumes. This has led to the development of different classes of mesoporous materials that can be tailored around their respective application. In the last decades, they have been successfully used in the fields of membranes^[51], catalysis^[52], sensing^[53], or batteries^[54]. In this thesis, mesoporous oxides and metal-organic frameworks have been combined with vibrational spectroscopy, and their theory and synthesis will be introduced in the following pages. For more in-depth information on the materials used in this thesis, the reader is guided to literature for further reading.^{[55] [56] [57] [58] [59]}

2.4.1. Mesoporous Oxides

Mesoporous oxides are the oldest class of mesoporous materials, with the first procedure to synthesise mesoporous silica being patented in the 1960s.^[60] Building on this method, the field of mesoporous oxides exploded in the 1990s, with many new applications and materials being reported by groups all around the world over the following decades.^{[61] [62] [63]} In this thesis, mesoporous silica and titania were used in the experimental work, which are two of the most commonly applied mesoporous oxides due to their versatile properties and transparency in the mid-IR.

Sol-Gel Chemistry

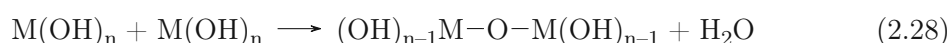
Sol-gel chemistry is a versatile and widely used method for producing solid materials from small molecules. For mesoporous materials, strategies established in sol-gel chemistry have been used successfully, such as the Stöber method for nanoscale particles^[64], which is still a widely used method for the synthesis of mesoporous spheres, although it was developed in the 1960s. The process involves the transition of a system from a liquid 'sol' (a colloidal suspension of particles) into a solid 'gel' phase. As precursors for sol-gel synthesis reactions, typically, metal alkoxides, metal salts or their silicon equivalents are used. Most sol-gel reactions typically are made up of two reaction steps, hydrolysis and polycondensation, which can either happen concurrently or in two separate steps. Hydrolysis is the first step in the sol-gel process, where metal alkoxides ($M(OR)_n$) react with water. This reaction replaces the alkoxide groups (OR) with hydroxyl groups (OH), forming the alcohol (ROH) as byproduct. The general hydrolysis reaction can be represented as:

Hydrolysis

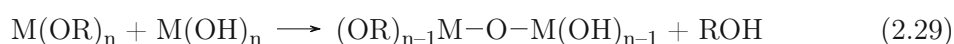


The free hydroxyl groups formed during the hydrolysis can now react during the polycondensation step. Polycondensation involves the linking of these hydroxylated metal species to form a three-dimensional network. This can occur through two main types of reactions: condensation of two hydroxyl groups (dehydration) and condensation of an alkoxide group with a hydroxyl group (dealcoholation). These can be written as:

Dehydration



Dealcoholation



The sol-gel process allows for precise control over the composition and structure of the synthesised material at the molecular level, making it possible to create materials with tailored properties. Especially, the pH value is an important parameter for the synthesis of controlled materials. For sol-gel synthesised silica, an acidic pH value leads to very small scale materials, while an alkaline pH value leads to larger scale condensation products.^[65] For sol-gel synthesised titania, a change in pH value does not lead to such a big change, although some influence on the crystallinity has been reported in literature.^[66]

Materials synthesised by sol-gel processes can range from ceramics and glasses to thin films, fibres, as well as nanoparticles, each with specific applications in fields such as optics, electronics, and catalysis.

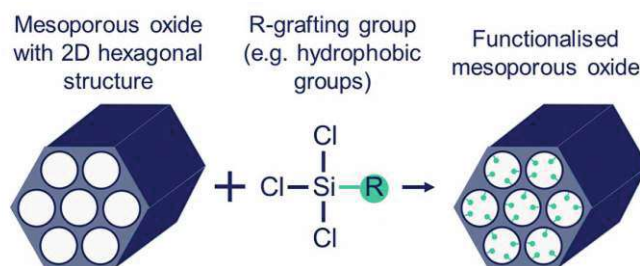


Figure 2.14.: Schematic depiction of the post-synthetic modification of mesoporous oxides.

One of the key advantages of sol-gel chemistry is its ability to produce materials at relatively low temperatures compared to traditional methods. This low-temperature processing is particularly beneficial for creating coatings and films on temperature-sensitive substrates. Additionally, the sol-gel process can be used to incorporate various dopants or functional groups into the material, enhancing its properties for specific applications. For the synthesis of functionalised mesoporous oxides, two strategies can be employed, one being the use of already functionalised precursor materials, which is called direct synthesis, or by the post-synthetic modification route, modifying the surface oxides in the pores by reaction with functional silanes. In the direct synthesis, functional groups are incorporated into the mesoporous structure during the formation process. This method ensures a uniform distribution of functional groups and strong interaction with the oxide framework, leading to enhanced stability and performance. However, this requires precise control over synthesis conditions and can be limited by the compatibility of functional groups with the synthesis environment or a subsequent heat treatment. On the other hand, the post-synthetic modification route (shown in Figure 2.14 for mesoporous oxides) involves introducing functional groups into pre-formed mesoporous oxides. This method offers greater flexibility in choosing functional groups and allows for multiple modifications. Nevertheless, it may result in less uniform distribution and weaker interactions with the oxide framework, which can affect the stability and functionality of the material.^[67]

Self-Assembly for Surfactant Templating

Self-assembly is a spontaneous process where disordered components autonomously form an organised structure due to specific local interactions. This process, termed molecular self-assembly when involving molecules, can be static or dynamic. Static self-assembly leads to an ordered state as the system approaches equilibrium, reducing its free energy. Dynamic self-assembly, often referred to as self-organisation, involves patterns formed by specific local interactions among pre-existing components.

The classic definition of self-assembly explains the formation of a self-assembled system as a spontaneous process where all interactions happen in close proximity to the involved species. This process can be guided by templating agents, enabling the formation of highly organised covalent molecules. Such a process is schematically shown in Figure 2.15-A for the hydrolysis of a sol-gel precursor, forming an oxidic network around the micellar structures in the same solution. After the condensation reaction completes, the micellar structures are removed (which can either happen thermally or with solvents), leaving behind a mesoporous oxide.

That concept is used in this thesis, where a soft-templating method involving self-assembly was employed to synthesise mesoporous metal oxide layers with a defined porosity. This method is called evaporation-induced self-assembly (EISA) and combines sol-gel chemistry and molecular self-assembly to fabricate mesoporous metal oxides through a solution phase synthesis. The EISA process involves the rapid evaporation of solvents, leading to the self-assembly of amphiphilic organic molecules by increasing the surfactant concentration in the solution, moving along the isotherm towards the preferred micellar structure, as shown in Figure 2.15-B.

Two methods that are commonly applied in order to receive well ordered layers are spin-coating and dip-coating. In this thesis, spin-coating was used, and this process is schematically shown in Figure 2.15-C. Here, a defined amount of precursor solution is applied to the coating substrate, either while it is already spinning (dynamic spin coating) or before spinning (static spin coating). During spinning, the solvents in the precursor solution evaporate, while the surfactant concentration in the gel increases, moving along an isotherm in the phase diagram seen in Figure 2.15-B. After all the solvent evaporated, the surfactant phase self-assembles depending on the ratio of solid mass to surfactant, which is a controlled parameter. Finally, after completion of the polycondensation of the oxidic network around the surfactant template, the template is removed, with only the porous oxide remaining.

2.4.2. Metal-Organic Frameworks

Metal-organic frameworks (MOFs) are a novel class of porous materials that have quickly gathered attention since their discovery in the 1990s by Omar Yaghi.^[68] They are composed of metal ions or clusters (called secondary building units or SBUs) coordinated to organic ligands (called linkers), forming 1D, 2D, or 3D networks, shown schematically for one layer of a 3D-MOF made up of iron-based SBUs and an aminoterephthalate linker. The possibility to choose from a variety of different SBUs and linkers makes them highly versatile chemically and structurally, with high porosity, large surface area, and adjustable

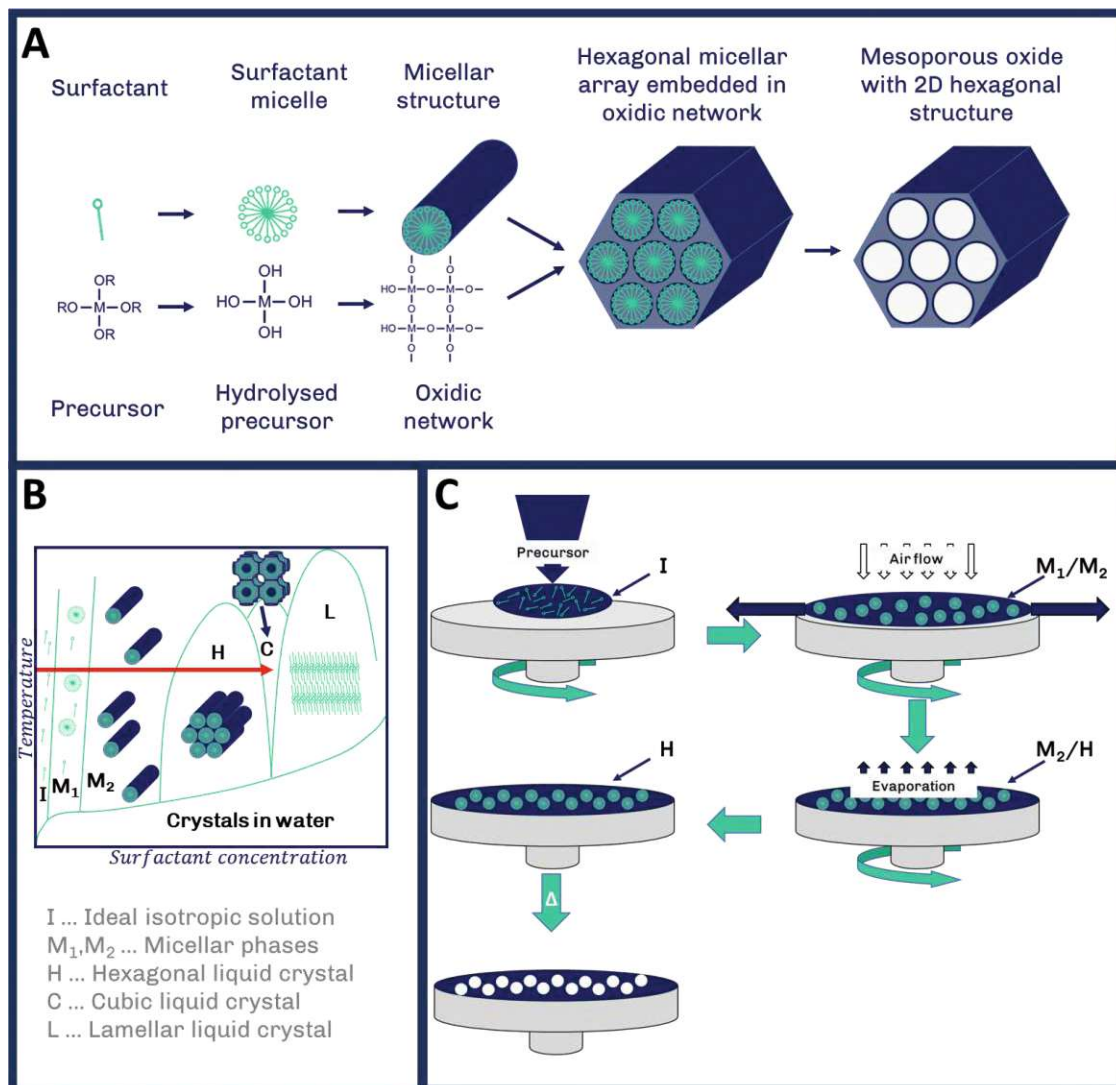


Figure 2.15.: Schematic depiction of an evaporation-induced self-assembly process for the synthesis of mesoporous materials. A: General process: Micellar surfactant structure forming in the same solution as the hydrolysis reaction of the sol-gel mixture. B: Phase diagram for surfactants in water. Isotherm marked in red, the phases in the spin-coating scheme reference to the concentration dependant phases shown in the phase diagram. C: Spin-coating of a precursor solution, evaporation of solvent leads to self-assembly of the surfactant templates.

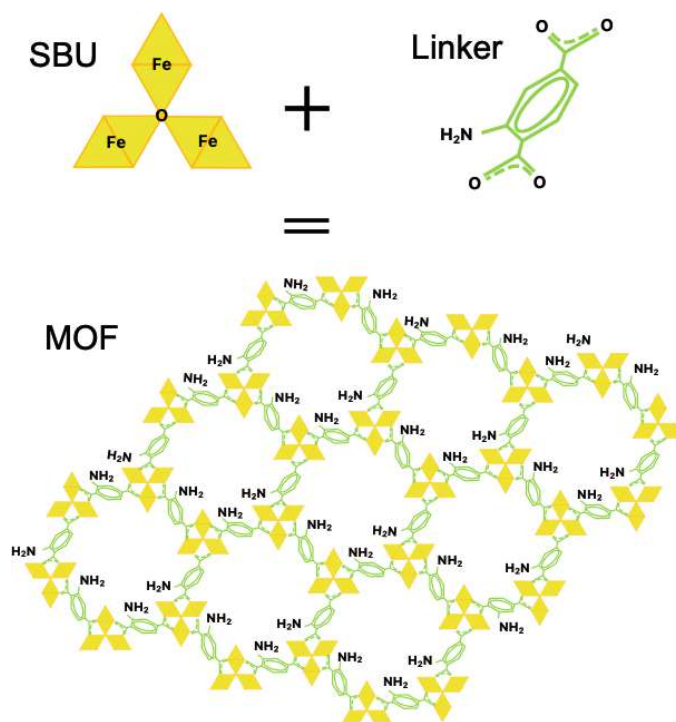


Figure 2.16.: Schematical depiction of MOF structures. Graphic reproduced in part from Publication I^[69] under the CC-BY 4.0 license.

pore sizes, based on the choice of building blocks.

Based on the early works of the Yaghi group and other groups around the world, a new field of reticular chemistry was formed as an umbrella term for MOFs and other similar structural materials such as covalent organic frameworks (COFs), made up entirely of covalent bonds, with bridging elements such as boron or nitrogen and zeolitic imidazolate frameworks (ZIFs), based on imidazolate linkers, forming structures resembling zeolitic networks.^[57]

Reticular synthesis involves the self-assembly of different building blocks under specific conditions, leading to pre-defined structures.^[70] The conditions needed for this self-assembly to take place are typically achieved in solvothermal reactors^[71] or assisted with microwaves^[72], although some MOFs can also be synthesised at room temperature. For MOFs, the choice of metal and organic ligand plays a crucial role in determining the structure and properties of the resulting MOF. For instance, the coordination preferences of the metal ions influence the size and shape of the pores, while the organic linkers play a great role in the coordination structure (using different numbers or positions of the bridging groups) and pore sizes (by using different chain lengths of the linker molecules).

The properties of the resulting MOF can further be tailored to the planned application

by functionalisation of the linker group, introducing specific chemical functionalities to the framework. Here, similar to mesoporous oxides, two strategies can be chosen, a direct approach and post-synthetic modification:

- In the direct approach, linkers with pre-designed functionalities are introduced into the synthesis, leading to a controlled synthesis of functionalised MOFs.^[73] This process can also be extended by adding multiple different functionalities with defined ratios to the process, which leads to multivariate MOFs^[74] exactly tuned to the respective application.
- Post-synthetic modification (PSM) is performed when the direct approach is not feasible, mostly due to the resulting structure not being thermodynamically stable. One example for this is the selective linker removal of multivariate MOFs, which can lead to better accessibility of active regions in catalysis. This is typically done by introducing sacrificial linkers with low thermal stability together with the active linker during synthesis, followed by a thermal removal step.^[75] Another example for the use of PSM in MOF synthesis is for the introduction of functional elements that may inhibit the formation of the pre-defined MOF structure, such as carboxyl groups. Here, methods known from solid-phase peptide synthesis can be used to graft functional groups onto the linkers.^[76]

Based on these properties, MOFs have successfully been used in a variety of applications. For instance, their high surface area and tunable pore sizes enable them to adsorb large amounts of gases, making them suitable candidates for gas storage and separation applications.^{[77][78]} Similarly, they have been used for the removal of pollutants from water, showcasing a potential application in wastewater remediation.^[79]

Beyond gas storage and the removal of pollutants, MOFs have shown high potential in (photo-)catalysis. The metal centers in MOFs can act as classical catalytic sites, or for photoactive MOFs as catalytic sites similar to semiconductor quantum dots. Meanwhile, the organic linkers can be modified to introduce additional functional groups that enhance catalytic activity or the absorption of light in photocatalysis.^[80] Once again, the selection of suitable metal and organic components allows for the tunable design of efficient and selective (photo-)catalysts for a wide range of chemical reactions.

Another promising field for MOFs is drug delivery. Here, the possibility of different release mechanisms and speeds and their relatively good biocompatibility for certain MOFs have been demonstrated in recent years. For instance, directed drug release in pH-responsive MOFs^[81] is a promising new application in cancer immunotherapy, while tuning pore size, functionalisation, and adding co-guests can be used to improve the release

kinetics.^[82]

Last but not least, MOFs can be applied for sensing purposes, which has also been done in experimental work associated to this thesis.^[69] Similar to their application in gas and pollutant removal, their tunable functionalities and pore sizes as well as their recyclable loading and release mechanisms makes the use of MOFs for chemical sensing feasible, which has been demonstrated for fluorescence-based^[83], infrared-based^[84], or electrochemical-based methods.^[85]

2.5. Fundamentals of Adsorption Processes in Porous Materials

For the purpose of using mesoporous materials for sensing, they are often applied to the sensor surface as a sensing layer, making use of their high surface area to achieve a high density of detectable interactions. Therefore, it is important to understand the relevant adsorption processes that guide these interactions. In the following pages, a short introduction to adsorption kinetics and thermodynamics is given based on the following literature recommended for further reading.^[86]^[87]

2.5.1. Adsorption Thermodynamics and Kinetics

Adsorption is a surface phenomenon where molecules from a gas or liquid phase accumulate on the surface of a solid or liquid. This process is fundamental in various scientific and industrial applications, including catalysis^[88], environmental remediation^[89], and material science.^[90] Understanding the thermodynamics and kinetics of adsorption is crucial for optimising these processes and developing new materials with enhanced adsorption properties. In the following pages, the concentration is used as a placeholder for the amount of adsorbate in the phase covering the adsorbent. However, it is important to note that adsorption out of the liquid phase and adsorption out of the gas phase are not fully congruent in nature. This is mostly due to matrix effects, as adsorption is a competitive process and liquid matrices (especially water) tend to play a bigger role in the adsorption process than the mostly inert gas matrices. As a result, adsorption out of the liquid phase is often more complex than out of the gas phase, as more possible parameters need to be considered.^[91] However, for this introduction, all matrices are considered to be inert in order to focus on a phenomenological description of the adsorption process.

Adsorption Thermodynamics

Adsorption is driven by the reduction of the Gibbs free potential G at the adsorption site (or more accurately, the chemical potential), with an exothermic reaction ($\Delta H < 0$) usually being its driver. There are two types of adsorption, physisorption and chemisorption.

Physisorption is based on the physical adsorption of molecules on surfaces by van-der-Waals interactions or other intermolecular attraction forces. These interactions are usually driven by a negative reaction enthalpy ΔH of a few kJ mol^{-1} and low activation energies, leading to a generally reversible behaviour. They also do not lead to the dissociation or formation of chemical bonds in neither the adsorbate (the adsorbed molecules) or the adsorbent (the surface at which adsorption happens). However, due to steric effects or the distortion of the bonds, the electron density of the bonds may be changed locally and reversibly, which leads to a change in the force constant of the bonds and, thus, can be detected by infrared spectroscopy as a shift of the absorption bands (see chapter 2.2.1 for reference).^[92] Additionally, for gas species, a condensed phase forms on the adsorbent, and the resulting IR spectra appear similar to their liquid counterparts.^[93]

Chemisorption is based on the formation of (typically covalent) bonds between the adsorbate and adsorbent. These bonds are much stronger than those formed during physisorption, with negative reaction enthalpies in the range of a few hundreds of kJ mol^{-1} . The strong binding energies of the covalent bonds generally lead to irreversible adsorption. Chemisorption is also highly specific to the adsorbate and the surface, often resulting in a monolayer of adsorbate molecules.

Adsorption typically happens in several stages:

1. Transport of adsorbate molecules: The adsorbate molecules move from the bulk phase to the surface of the adsorbent. In mesoporous materials, this happens by means of diffusion.
2. Adsorption at the surface: The adsorbate molecules adhere to the surface of the adsorbent. This stage can involve either physisorption or chemisorption, depending on the nature of the interaction.
3. Formation of an adsorption layer: Over time, one or more layers of adsorbate molecules form on the surface. In physisorption, multiple layers can form, while chemisorption typically results in a single monolayer.
4. Equilibrium: Eventually, the rate of adsorption equals the rate of desorption, leading to a dynamic equilibrium. At this point, the amount of adsorbate on the surface remains constant.



Figure 2.17.: Schematical depiction of the Langmuir and Freundlich isotherms.

As the free and adsorbed molecules are in a dynamic equilibrium, the concentration (or pressure for gases) of the free molecules determine the extent of the adsorption. These equilibriums can be described by adsorption isotherms, with different models to fit the respective prerequisites for each mechanism. The two most common models are the Freundlich and the Langmuir models.

The Freundlich model is a fully empirical model that was proposed by Freundlich in 1908 that works well for heterogeneous adsorbent surfaces and multi-layer adsorption. The model is described by the following equation, where q_e denotes the equilibrium coverage (can also be described by a concentration or an intensity of an infrared band) at a certain concentration c , with K_F and n being unitless scaling factors:

$$q_e = K_F c^{1/n_F} \quad (2.30)$$

The Langmuir model was the first scientifically derived isotherm that is based on the following three assumptions: a mono-layer adsorption, a completely flat and homogeneous surface, and the adsorption not being dependant on the occupation of neighbouring adsorption sites. Considering this, one can write the dynamic equilibrium of the adsorption reaction as:



Formulating the rate equations of the free surface sites θ_s for adsorption and desorption and solve for equilibrium (adsorption rate equals desorption rate), one gets the following equation:

$$\begin{aligned} \left(\frac{d\theta_s}{dt}\right)_{ads} &= -\left(\frac{d\theta_s}{dt}\right)_{des} \\ k_{ads}c(1 - \theta_s) &= k_{des}\theta_s \end{aligned} \quad (2.32)$$

Going from this, solving for θ_s , simplifying $k_{ads}/k_{des} = K_L$, and adding the concentration as $\theta_s = q_e/q_m$, with q_e being the equilibrium concentration, and q_m being the concentration at full surface coverage, one gets the Langmuir isotherm:

$$q_e = \frac{q_m K_L c}{1 + K_L c} \quad (2.33)$$

Adsorption Kinetics

The most commonly used adsorption kinetic models include the Lagergren first-order model, the pseudo-second-order model, the intraparticle diffusion model, and the Elovich model.^{[94][95]} The Lagergren first-order model is one of the earliest and simplest models used to describe adsorption kinetics. It is based on the assumption that the rate of adsorption is proportional to the number of available adsorption sites. Mathematically, it can be expressed as:

$$\frac{dq_t}{dt} = k_1(q_e - q_t) \quad (2.34)$$

In this model, q_t is the amount of adsorbate adsorbed at time t , q_e is the amount adsorbed at equilibrium, and k_1 is the rate constant of the first-order adsorption. This model is particularly useful for describing the adsorption of solutes from dilute solutions and is often applied in cases where the adsorption process is relatively straightforward.

The pseudo-second-order model is another widely used kinetic model which assumes that the rate of adsorption is proportional to the square of the number of unoccupied sites. This model is expressed as:

$$\frac{dq_t}{dt} = k_2(q_e - q_t)^2 \quad (2.35)$$

Here, k_2 is the rate constant of the pseudo-second-order adsorption. This model is more suitable for systems where the adsorption process involves chemisorption, which includes the sharing or exchange of electrons between the adsorbate and the adsorbent. The pseudo-second-order model often provides a better fit for experimental data compared to the first-order model, especially in cases where the adsorption process is more complex.

The intraparticle diffusion model considers the diffusion of adsorbate molecules within the pores of the adsorbent as the rate-limiting step. This model is particularly relevant for porous materials where the internal surface area plays a significant role in the adsorption process. The intraparticle diffusion model can be described by the equation:

$$q_t = k_{id}t^{1/2} + C \quad (2.36)$$

For this model, k_{id} is the intraparticle diffusion rate constant and C is the integration constant that reflects the thickness of the boundary layer. This model helps in identifying

whether the adsorption process is controlled by surface adsorption or by diffusion within the pores.

The Elovich model is another important kinetic model used to describe adsorption processes, particularly those involving chemisorption on heterogeneous surfaces. This model assumes that the adsorption rate decreases exponentially with the increase in the amount of adsorbed adsorbate, which is characteristic of systems where the activation energy for chemisorption increases as the surface coverage increases. The Elovich equation is expressed as:

$$\frac{dq_t}{dt} = \alpha_E e^{-\beta_E q_t} \quad (2.37)$$

where α_E and β_E are constants. Here, α_E represents the initial adsorption rate, and β_E is related to the extent of surface coverage and activation energy for adsorption. The Elovich model is particularly useful for describing adsorption processes where the adsorbent surface is highly heterogeneous, which usually coincides with systems that can be fitted with the Freundlich isotherm.

2.5.2. Adsorption Processes in Porous Materials

Porous materials are very popular substrates for adsorption processes due to their large specific surface areas. However, adsorption in porous materials is unique compared to bulk adsorption on surfaces as the adsorbate undergoes different grades of confinement depending on the pore structure of the adsorbent.

For certain adsorption systems (depending on pore size and the chemical and physical properties of the adsorbent/adsorbate), this confinement can lead to an increased influence of the surface tension σ of the condensed phase on the Gibbs free energy G .

$$\sigma = \left(\frac{\partial G}{\partial A_{surf}} \right)_{n,v,T} \quad (2.38)$$

At higher concentrations, this leads to an increased adsorption, as a reduction of the surface area A_{surf} inside the pores decreases the free energy of the system, which is called capillary (or pore) condensation. In Figure 2.18, this effect is described schematically.

Similarly, after fully loading the pores, desorption is hindered, as the condensed liquid forms a meniscus as it tries to minimise the surface area, which can lead to a hysteresis in the adsorption/desorption isotherm. Based on this phenomenon, the dependency of the adsorption on the porosity is defined by means of six types of adsorption isotherms by IUPAC. These distinct isotherms are schematically shown in Figure 2.19:

The type I isotherm is typical for microporous materials (pores < 2 nm). It indicates monolayer adsorption, where the adsorbate molecules form a single layer on the surface

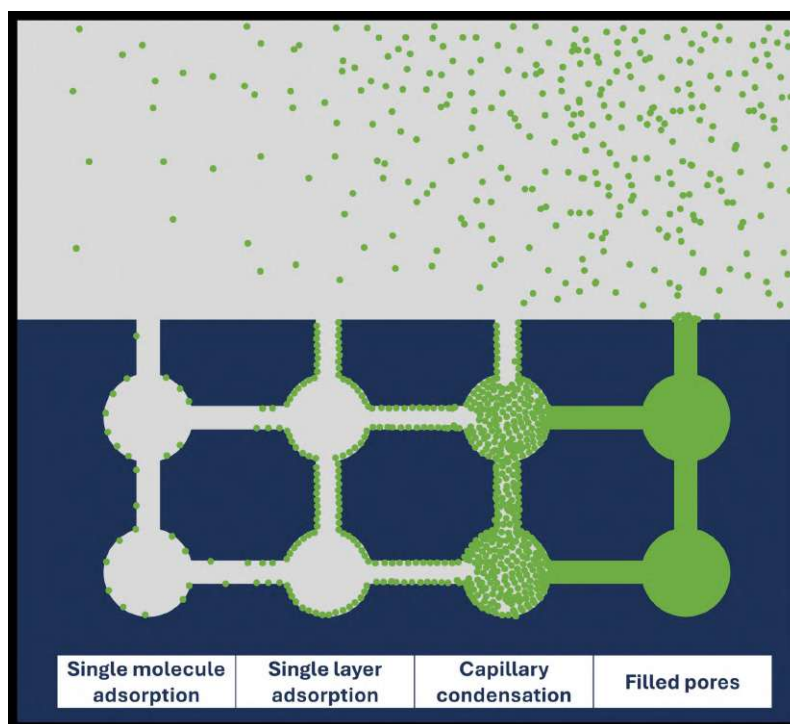


Figure 2.18.: Schematical depiction of capillary condensation in porous materials. The adsorbant concentration increases from left to right.

of the pores. The Langmuir isotherm assumes a finite number of identical sites and no interaction between adsorbed molecules. This behaviour can be described by the Langmuir model and is further divided into two subtypes I(a) and I(b) depending on the broadness of the pore distribution. The type II isotherm is characteristic of non-porous or macroporous materials (pores > 50 nm). It shows an initial monolayer adsorption followed by multilayer adsorption as the pressure increases. The knee of the curve represents the completion of the monolayer coverage. The type III isotherm is less common and indicates weak adsorbate-adsorbent interactions. It is typically observed in non-porous or macroporous materials where multilayer adsorption occurs without a distinct monolayer formation (also called islands). The type IV isotherm is associated with mesoporous materials (pores between 2 nm and 50 nm). It shows an initial monolayer-multilayer adsorption followed by capillary condensation, which is indicated by a hysteresis loop for larger mesopores shown in subtype IV(a). For smaller mesopores, this behaviour is completely reversible, leading to no hysteresis loop as shown in subtype IV(b). The type V is very similar to Type III and indicates weak adsorbate-adsorbent interactions, but rather in mesoporous materials than in non- or macroporous materials. It, therefore, also shows a hysteresis loop due to capillary condensation, which is larger or smaller based on the pore size. The type VI

isotherm represents stepwise multilayer adsorption on a uniform non-porous surface. Each step corresponds to the formation of a new adsorbate layer.

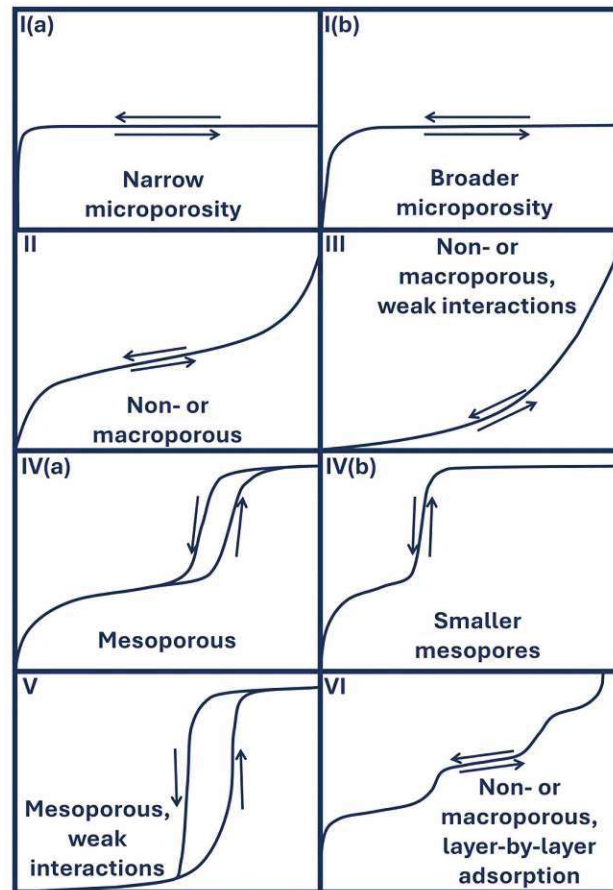


Figure 2.19.: Schematical depiction of the six adsorption isotherm types as classified by IUPAC.^[96] The x-axis always corresponds to the adsorbant concentration, while the y-axis corresponds to the amount of adsorbed material.

2.6. Fundamentals of Ultrasound Particle Manipulation

In the scope of the HYDROPTICS project, another task was the establishment of an on-line particle imaging system in an attempt to improve current total suspended solid (TSS) tests in water treatment. To achieve this, an ultrasound assisted flow cell was designed together with **Stephan Freitag** based on the work performed during his PhD thesis. In the following pages, a quick introduction to ultrasound manipulation and its possible application in imaging and spectroscopy is given based on the literature suggested for further reading.^[97]

2.6.1. The Acoustic Radiation Force

When an acoustic radiation force acts on particles in a suspension, they may orient themselves according to the acoustic field. This can be exploited to manipulate particles by introducing them into an acoustic resonator. In an acoustic resonator, an acoustic wave is created by a transducer and propagates through the medium to the other side of the resonator, where it is reflected back towards the resonator (schematically shown in Figure 2.20). In this thesis, an acoustic resonator was integrated into a microfluidic cell (i.e. an acoustofluidic cell), but there are also other possible applications, such as integrating it with Raman probes or cuvettes.

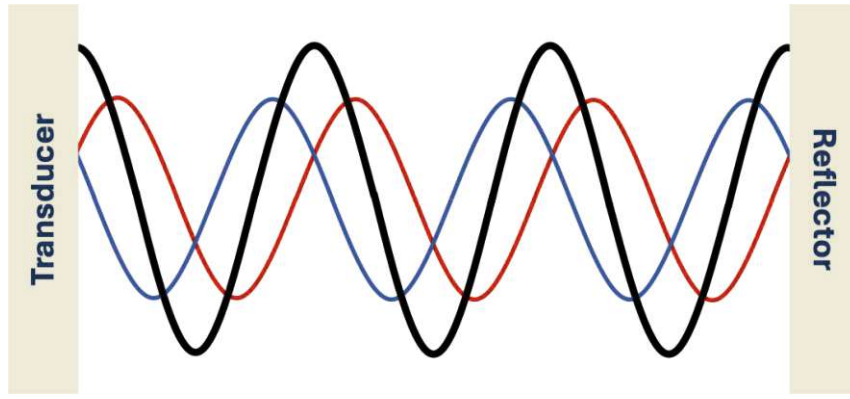


Figure 2.20.: Formation of a standing wave (black) in an acoustic resonator as superposition of incident (red) and reflected (blue) waves.

If the resonance condition of the resonator is met ($l_{res.} = n \cdot \lambda/2$), where n is a positive integer and λ is the wavelength of the acoustic wave, an acoustic standing wave forms. The resulting field is well-defined (2.39) and particles migrate towards the nodal or anti-nodal planes depending on their acoustic contrast $\Phi(\tilde{\kappa}, \tilde{\rho})$ (2.40), as particles with a high compressibility $\tilde{\kappa}$ such as suspended droplets tend to have a negative acoustic contrast, leading to particles moving into anti-nodal planes, while particles with a low compressibility such as polymer beads or sand particles have a positive acoustic contrast, and the particles move into the nodal planes.

$$F_z^{rad} = 4\pi \cdot \Phi(\tilde{\kappa}, \tilde{\rho}) \cdot (kR)^3 \cdot E_{ac} \cdot (2kz) \quad (2.39)$$

$$\Phi(\tilde{\kappa}, \tilde{\rho}) = \frac{1}{3} \left(\frac{5\tilde{\rho} - 2}{2\tilde{\rho} + 1} - \tilde{\kappa} \right) \quad (2.40)$$

2.6.2. Operation of an Ultrasound Particle Manipulation Device

To operate an acoustofluidic cell, several parameters have to be considered. First, the dimensions of the cell need to be defined beforehand, as the resonance frequency is dependant on the distance between the transducer and the reflector. Here, the relation $l_{res.} = n \cdot \lambda/2$ can be used to estimate the dimensions of the cell. For instance, for driving a cell with an aqueous suspension ($v_{ac}(H_2O) \approx 1500 \text{ m/s}$) at a frequency of 2 MHz, multiples of $375 \mu\text{m}$ ($\lambda/2$) may be used to set the distance between the transducer and the reflector. However, this is just a first approximation, as the real value may slightly differ from this theoretical estimation, as slight deviations from the optimal setup (slight angles, manufacturing tolerances, changes in speed of sound due to changing particles concentrations) lead to deviations in the resonance frequency. Therefore, the cell needs to be characterised in advance to determine the correct resonance frequency. This can be done by impedance spectroscopy, as the electrical impedance response of the piezoelectric transducer is in line with the resonance condition of the ultrasound standing wave in the acoustic resonator.

Further, the operation of an acoustic resonator leads to thermal losses that are introduced to the microfluidic cell acting as heat sink. When operated in an optical imaging system, the thermal load further increases by the light source of the optical microscope. As the liquid volume of a microfluidic device is limited and not enough thermal energy can be dissipated by the liquid flow, temperature stabilisation needs to be introduced to the cell. This is typically done by thermoelectric cooling, which has shown to perform very well for this purpose, with temperature fluctuations of below 10 mK when operated at 37 °C.^[98]

Part III.

Experimental methods

3.1. Infrared Setups

In this thesis, different infrared techniques were used, including ATR-FT-IR, and PICs used for evanescent waveguide sensing in a QCL-IR spectrometer. The following section aims to list all experimental infrared setups that have been used in the course of this thesis.

3.1.1. Preparation of Internal Reflection Elements

The Si IREs used in this work (20 mm x 10 mm x 0.5 mm) were cut out of a double-sided-polished Czochralski Silicon wafer. Narrow facets with a defined angle of 45° were polished using a MULTIPREPTM polishing system (ALLIED High Tech Products, USA). Two aluminium oxide discs (15 µm, and 9 µm) were employed, followed by three diamond polishing discs (3 µm, 1 µm, and 0.1 µm). The Ge IREs (20 mm x 10 mm x 0.5 mm) used for coating were diced from undoped double-sided polished wafers and faceted in a manner consistent with the Si.

3.1.2. Performance Considerations for Different Internal Reflection Elements

To choose the best performing IRE for the application, the properties of the materials have to be considered. Here, the optical properties and, especially for liquid phase measurements, the chemical stability of the materials are important. As for the optical properties, the refractive indices are responsible for the depth of penetration (2.18), and, thus, the effective interaction lengths of the IR radiation with the liquid phase (2.19)-(2.20). For Ge, Si and diamond IREs, these values were calculated and are listed in Table 3.1^[9].

Another thing to consider is the inherent IR absorption of the materials. For instance, diamond has a broad IR band between 2700 and 1800 cm⁻¹, making only the region between 1500 and 800 cm⁻¹ accessible when using diamond IREs with the dimensions used in this thesis (20 mm x 10 mm x 0.5 mm). Similarly, the strong IR adsorption of the SiO₂ passivation layer of Si IREs makes the region below 1250 cm⁻¹ inaccessible for spectroscopic purposes. In Figure 3.1, this is shown for IREs made out of the three materials used this thesis.

When using a coated IRE, the chemical stability of the IRE surface towards the sample matrix is important to ensure adhesion of the coating. This needs to be considered for Ge, as its oxidic passivation layer is water soluble, which can lead to delamination of the coating when using it for the measurement of aqueous samples.

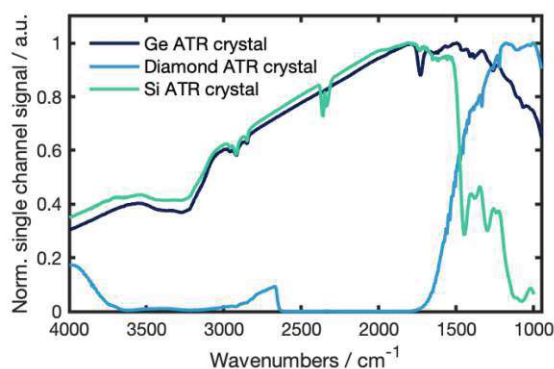


Figure 3.1.: Comparison of the single channel spectrum for IREs made out of three different materials (Ge, Diamond, Si).

Table 3.1.: Optical properties of the used IREs. $1200\text{-}1000\text{ cm}^{-1}$ is relevant for phosphate measurements, $1600\text{-}1400\text{ cm}^{-1}$ is relevant for aromatic hydrocarbons, and $2300\text{-}2200\text{ cm}^{-1}$ is relevant for nitriles, all of which were analytes in this thesis.

| IRE materials | Si | Ge | Diamond |
|---------------------------|-----------------------------------|------------|------------|
| n_1 | 3.42 | 4 | 2.4 |
| n_2 | 1.33 | 1.33 | 1.33 |
| θ | | 45° | 55° |
| | $1200\text{-}1000\text{ cm}^{-1}$ | | |
| $d_{e,avg} / \mu\text{m}$ | 0.70 | 0.46 | 1.30 |
| $d_{p,avg} / \mu\text{m}$ | 0.72 | 0.58 | 1.01 |
| | $1600\text{-}1400\text{ cm}^{-1}$ | | |
| $d_{e,avg} / \mu\text{m}$ | 0.51 | 0.34 | 0.95 |
| $d_{p,avg} / \mu\text{m}$ | 0.53 | 0.43 | 0.74 |
| | $2300\text{-}2200\text{ cm}^{-1}$ | | |
| $d_{e,avg} / \mu\text{m}$ | 0.34 | 0.22 | 0.63 |
| $d_{p,avg} / \mu\text{m}$ | 0.35 | 0.28 | 0.49 |

3.1.3. Passivation of Germanium Internal Reflection Elements

To prevent the delamination of porous enrichment layers on Ge IREs, a protective intermediate layer can be applied. In this thesis, thin sputtered layers of TiO_2 were applied, both to improve adhesion and to protect the GeO_2 layer from the aqueous environment. This process was performed in cooperation with **Mauro David** and **Borislav Hinkov** from the FKE group at the ETIT faculty of TU Wien.

The faceted Ge IREs were sputtered with titanium dioxide (KJ Lesker, 99.9%) on a LS 320 S sputter system (Von Andrenne, Germany). The residual pressure in the chamber prior to the inlet of the argon gas was 8e-5 mbar. During sputtering, the equilibrium chamber pressure was maintained at 2e-5 mbar. Following the cleaning of the samples and of the target, the deposition was performed at a deposition rate of 2.27 nm min⁻¹. The thickness of the deposited film was determined with an alpha-SE ellipsometer and the corresponding CompleteEASE software (J.A. Wollam Co., United States) at an angle of incidence of 70°.

3.1.4. Optical Setups for Attenuated Total Reflection Infrared Spectroscopy

The measurement setup comprises a custom built ATR mount and aluminium flow cell that has been developed by Bettina Baumgartner in a previous project.^[99] The measurement setup is designed for seamless integration into a Vertex 80V FT-IR spectrometer (Bruker, Germany) equipped with a liquid nitrogen cooled mercury cadmium telluride (MCT) detector (InfraRed Associates, $D^* = 4e10 \text{ cm Hz}^{0.5} \text{ W}^{-1}$ at 9.2 μm). After applying the analyte, collection of the spectra was done with the OPUS 8.1 software, which were recorded using a spectral resolution of 4 cm⁻¹ and averaging 32 scans per spectrum (double-sided, backward-forward acquisition mode). During all measurements, the sample compartment was flushed with dry air to remove interference from water vapour.

3.1.5. Fabrication of mid-Infrared Photonic Integrated Circuits

The mid-IR PICs used in this thesis (Publications II and III^[100]) were developed in the H2020 AQUARIUS project, where their concept has been successfully demonstrated. The fabrication of the PICs was not modified for the work performed in this thesis and was done by **Mattias Verstuyft**, **Jeroen Missinne** and **Nuria Teigell Beneitez** at IMEC/UGent.

Following the cleaving of the sample from a 4" germanium-on-silicon wafer, a photoresistive coating (MIR701) was applied via spin coating. The grating coupler and waveguide layout were then patterned into the photoresist using UV-lithography. The pattern was then transferred onto the 2 μm thick germanium layer in a single etch step through reactive ion etching (RIE) with a mixture of CF₄, SF₆, and H₂, resulting in the etching of 1 μm of Ge. The remaining photoresist was subsequently removed by rinsing with acetone, IPA, and deionised water, followed by the use of an oxygen plasma. Another UV-lithography step was employed for a lift-off process, ensuring that a reflective layer of 1 μm of gold, deposited using e-gun evaporation, only covered the grating couplers.

Prior to the definition of the microlenses on the backside, a thick layer of photoresist was applied to the top side for protection. Subsequently, the backside was polished in

order to minimise scattering effects. A thick layer of AZ4562 (12 μm) was applied to the backside and patterned with UV-lithography, leaving cylinders with a diameter of 250 μm . They were reflowed on a hotplate at 150 $^{\circ}\text{C}$, forming nearly spherical structures. These structures were transferred from the photoresist layer into the silicon using RIE with an SF_6 , O_2 gas mixture. Finally a 900 nm thick Si_xN_y antireflective coating was deposited on the structures using plasma-enhanced chemical vapour deposition (PECVD). From the finished chip, the photoresist was removed from the top by rinsing in acetone, IPA, and deionised water, and the surface was freed from any remaining residues using an oxygen plasma.

3.1.6. Optical Setup for the Characterisation of Photonic Waveguides

In Publications II and III,^[100] two different setups were used for mounting the photonic integrated circuits.

In Publication II, a miniaturised cage setup based on the one published in the publication by Teigell Beneitez et al.^[101] was blueprinted by **Bettina Baumgartner** for use with the ChemDetect QCL spectrometer (DRS Daylight Solutions, USA). A schematic depiction of the combined setup and the miniaturised cage setup are shown in Figure 3.2

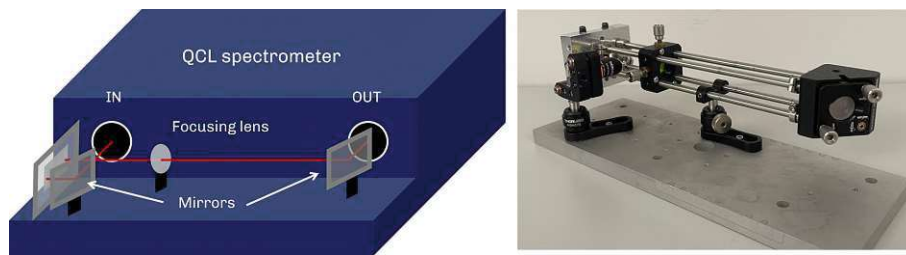


Figure 3.2.: Left: Schematic depiction of the measurement setup used for combining the QCL spectrometer and the waveguide. Right: Picture of the cage setup.

In Publication III,^[100] a setup with three axis control over the waveguide was used to demonstrate the alignment tolerances of the waveguides. This was combined with a micro-opto-electro-mechanical system (MOEMS) external cavity quantum cascade laser (EC-QCL) also developed in the H2020 project AQUARIUS. The laser was operated at a 570 kHz pulse repetition rate and a 100 ns pulse length, emitting between 6.36 and 7.45 μm . The detector integrated in the spectrometer was a thermoelectrically cooled high speed MCT detector integrated ($D^* = 4\text{e}9 \text{ cm Hz}^{0.5} \text{ W}^{-1}$). A schematic and an image of the whole system are depicted in Figure 3.3. This setup was optimised and measurements were performed together with **Mattias Verstuylft** during a research stay at IMEC/UGent.

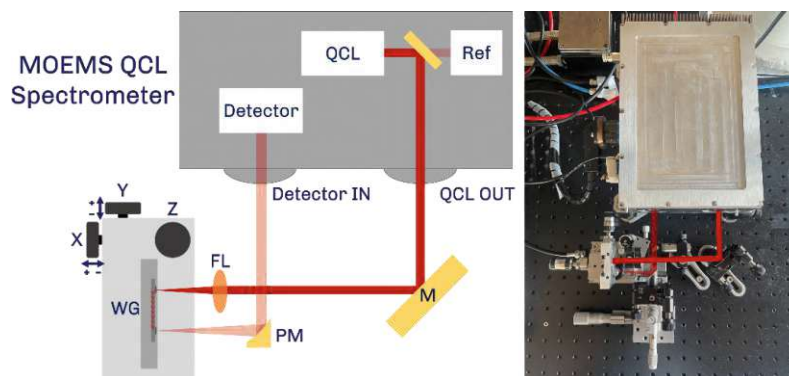


Figure 3.3.: Left: Schematic depiction of the measurement setup with three axis control (WG = waveguide, FL = focusing lens, PM = parabolic mirror, M = mirror). Right: Picture of the actual setup, beam path marked in red. Graphic reproduced from Publication III^[100] under the CC-BY 4.0 license.

3.2. Vis/Raman Setup

This section describes the setups and experimental methods devised for the coupled SERS-Vis study of the interaction of metal surfaces and cationic surfactants used in Publication IV.^[102]

3.2.1. Flowcell Design

To accompany both SERS and Vis spectroscopy, a flow cell was designed to fit into the sample compartment of a UV-Vis spectrometer (Cary 50 Bio, Agilent, USA) while making space for a Raman fibre probe (WP RP 785, Wasatch Photonics, USA) which was connected to the Raman spectrometer (WP 785 Raman spectrometer Wasatch Photonics, USA). The optical pathlength for the extinction measurements was 20 mm being the distance between the two optical grade glass windows glued into the cut-outs of the aluminium body of the flow cell. To ensure a stable suspension of the silver nanoparticles (AgNPs) used for the SERS measurements, a magnetic stirrer was fitted to the bottom of the flow cell (Cimarec i Mini Stirrer Thermo Fisher Scientific, USA). The measurement setup is depicted schematically in Fig. 3.4.

3.2.2. Method Development for Vis/SERS Coupling

The measurements performed with the Vis/SERS system featured in Publication IV^[102] can be divided into two categories: a study of the interaction between AgNPs and cationic surfactants combining Vis spectroscopy and SERS and the quantification of these cationic surfactants using a SERS-based system while using the Vis as an in-built quality con-

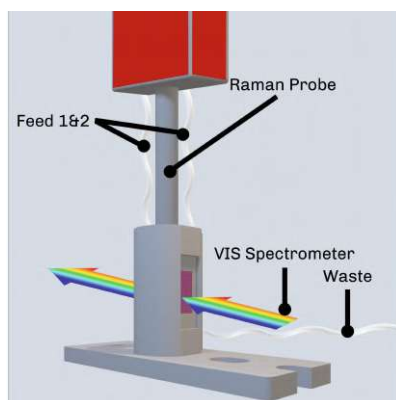


Figure 3.4.: Schematic depiction of the measurement setup accommodating the Raman probe used for SERS inside the sample compartment of the UV-Vis spectrometer. Graphic reproduced from Publication IV^[102] under the CC-BY 3.0 license

trol for the in-situ synthesised AgNPs. For all measurements, the AgNPs were synthesised by injecting aqueous stock solutions of AgNO_3 (1.11mM) and $\text{NH}_2\text{OH} \cdot \text{HCl}$ (15 mM $\text{NH}_2\text{OH} \cdot \text{HCl}$ and 30 mM NaOH) in a volumetric ratio of 9:1.

For the study of the interaction between the AgNPs and the surfactants, four measurement series were carried out, varying the ratios between AgNPs and the surfactant (1:9, 2:8, 5:5, 8:2). These ratios refer to the volumetric ratios of AgNP suspension to the surfactant (BAC-16). The concentrations of the BAC-16 used for each measurement series is listed in Table 3.2, with the concentrations referring to the samples before mixing.

Table 3.2.: Experimental parameters for the Vis-SERS measurements. BAC-16 concentrations refer to the samples before mixing.

| Ratios | c(BAC-16) / mg L^{-1} | | | | | | | |
|--------|--------------------------------|------|-----|-----|---|---|---|--------|
| 1:9 | 0.02 | 0.05 | 0.2 | 0.5 | 1 | 2 | 4 | |
| 2:8 | 0.02 | 0.05 | 0.2 | 0.5 | 1 | 2 | 4 | |
| 5:5 | 0.02 | 0.05 | 0.2 | 0.5 | 1 | 2 | 4 | 10 100 |
| 8:2 | | | 0.2 | 0.5 | 1 | 2 | 4 | 10 100 |

To correlate the experiments with different ratios of AgNPs and the surfactant (Table 3.2), the BAC-16 concentrations were standardised to reflect the number of BAC-16 molecules per AgNP in suspension. To do this, two simplifications regarding the particle size had to be made: First, a particle radius of 53 nm (the median size of the pristine particles) was assumed for all particles as an average for the unimodal particle size distribution. Additionally, for aggregated silver particles, the surface of the particle aggregates equals

the sum of the single particle surfaces.

Using these simplifications, the number of BAC-16 molecules per AgNP (C_{BAC}^*) could be estimated using the BAC-16 concentration before mixing with the AgNP colloid (c_{BAC} , in mol mL^{-1}) and the volumetric ratio ($x : y$) with the following equation:

$$C_{BAC}^* = \frac{c_{BAC} \cdot N_A \cdot y}{c_{AgNP} \cdot x} \quad (3.1)$$

3.3. Dynamic Light Scattering

This section describes the dynamic light scattering procedures used as particle size reference methods for Publication IV.^[102]

3.3.1. Particle Size Measurements

To give further context on the aggregation of the AgNPs, dynamic light scattering (DLS) was performed on the colloid-surfactant system (featured in Publication IV^[102]). For these experiments, 0.5 mL of AgNPs were synthesised as described in chapter 3.2.2. After stirring for 90 s, 4.5 mL of the surfactant solutions (concentrations shown in Table 3.2) were added. The resulting mixture was stirred for another eight minutes. Afterwards, 1 mL of the suspension was injected into the cuvette and mounted into the Litesizer 500 (Anton Paar, Austria). The measurement was subsequently started after temperature stabilisation at 25 °C, with the calibration of the instrument set at 30 s (resulting in a total time of 10 min after particle synthesis for each measurement). The measurement data was transformed into a particle size distribution using ISO 22412^[103] and the narrow analysis model in the Kalliope software package (Anton Paar, Austria).

3.3.2. Zeta Potential Measurements

To compare the surface of the silver particles with the metal surfaces used, Zeta potential measurements were performed on a suspension of pristine AgNPs (featured in Publication IV^[102]). For these experiments, 0.5 mL of AgNPs were synthesised as described in chapter 3.2.2. After stirring for 90 s, 4.5 mL of deionised water was added. The resulting mixture was stirred for another eight minutes. Afterwards, 1 mL of the suspension was injected into a quartz cuvette, the Univette (Anton Paar, Austria) accessory mounted, and the Zeta potential measurement started. The measurement was performed on a Litesizer 500 (Anton Paar, Austria) at 25 °C, with temperature stabilisation and calibration of the instrument set at 30 s (total time after particle synthesis was 10 minutes for each measurement). For the evaluation of the measurements, the Smoluchowski approximation of

the Henry factor $f(\kappa a)$ was used, while using the following equation 3.2 to calculate the Zeta potential ζ . In this equation, η denotes the dynamic viscosity, while U_E denotes the electrophoretic mobility and ε denotes the dielectric constant.

$$\zeta = \frac{3\eta U_E}{2\varepsilon f(\kappa a)} \quad (3.2)$$

3.4. Ultrasound Enhanced Particle Imaging

This section describes the setups and experimental methods used for the demonstration of the particle manipulation system which is part of the particle analyser that has been published in Publication VI.^[104]

3.4.1. Design of the Ultrasound Enhanced Particle Imaging System

The first version of the acoustofluidic flow cell used in this thesis was designed by Stephan Freitag for the H2020 HYDROPTICS project. The full particle manipulation setup was then designed in close cooperation with project partners to fit into their hyperspectral imaging system. This system was then integrated into the pilot prototype for the screening of process water for suspended solids.

The cell has been designed to achieve both a lateral (grey) separation, utilising a height of $375 \mu\text{m}$ (which translates to a half wavelength) and an axial (red) separation, utilising a width of 6 mm (which translates to eight wavelengths). Using this setup, it was possible to separate the different kinds of particles enough to generate a line scan hyperspectral image during moderate flow rates. The proposed measurement setup is shown in Figure 3.5-A. In Figure 3.5-B, the design of the acoustofluidic cell is shown.

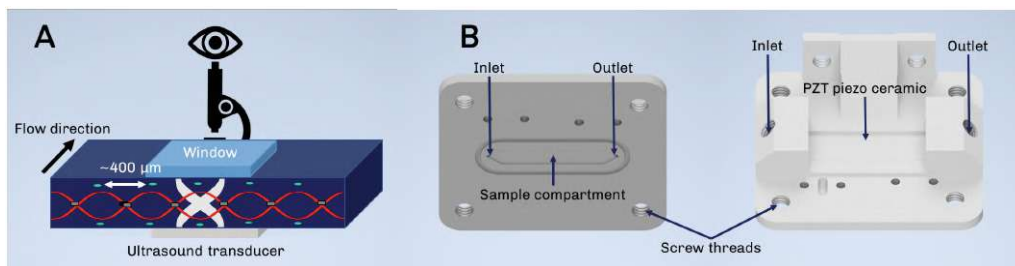


Figure 3.5.: A: Schematic of the ultrasound enhanced particle imaging system. B: Design of the acoustofluidic flow cell.

3.4.2. Characterisation of an Acoustofluidic Device

The cell is in theory designed to resonate at a US frequency of approximately 2 MHz. This value, however, is purely based on the dimensions of the sample compartment, with the optimal resonance frequency situated around the calculated value with a slight deviation. To determine this optimal resonance frequency, electrical impedance spectroscopy (EIS) can be used, where the minima of the amplitude of the electrical impedance can be interpreted as resonance minima. As there are different resonance conditions in a complex system, a multitude of resonance minima has to be expected with absolute and relative minima. For these minima, it is important to not just choose the absolute minimum for the particle manipulation, but to test every single minimum, as the absolute minimum can result from parts of the cell which do not contribute to the particle manipulation in the sample compartment such as the window holder. Just after testing and evaluating the response of every possible minimum, the optimal resonance frequency can be determined. The impedance spectrum was recorded on an ISX-3 electrical impedance spectrometer (sciospec, Germany) in the range of 1.5-2.5 MHz.

3.4.3. Operation of an Acoustofluidic Device

The demonstration of the separation capabilities of the acoustofluidic cell for suspended particles was performed in the laboratory before the liquid handling unit was shipped to the project partner **SAL** for further integration. The testing setup (Figure 3.6) comprised the acoustofluidic cell, on which an optical window was mounted using a 3D-printed window fixture. The piezo was connected to a sonicamp ultrasound driver (usePAT, Austria). Handling of the suspension of red 10 μm polystyrene particles in water was performed using a peristaltic pump (Ismatec, Germany) using a feed of 0.36 mL min^{-1} . The pump was connected to the cell with 1/16" PTFE tubings (O.D. = 1/16", 1 mm I.D., VICI AG, Switzerland). The cell was then placed under a Keyence Digital Microscope (Keyence, Japan) and images recorded using a magnification of 30x.

3.5. Sampling

In this thesis, analytes in different states of matter were measured using various configurations. In order to achieve the best results for each configuration, the sampling techniques were also optimised for the respective purpose.

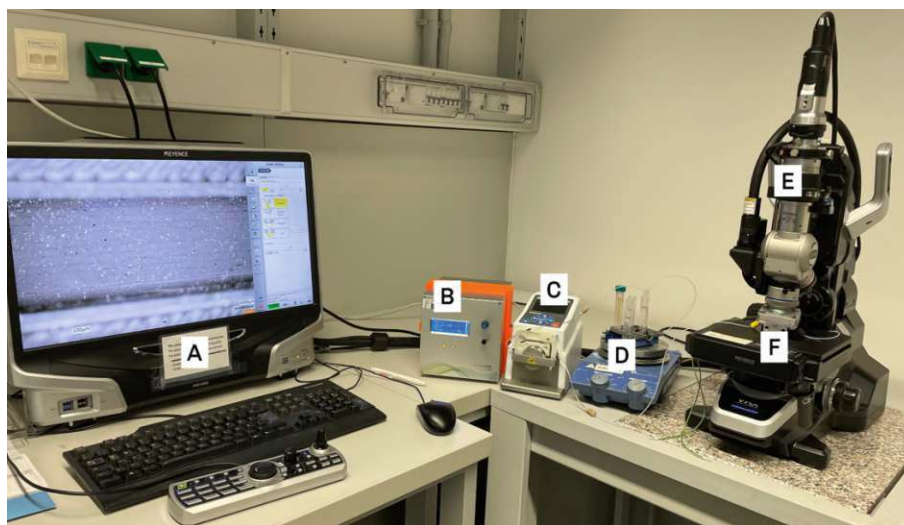


Figure 3.6.: Setup for acoustofluidic cell prototype testing: Keyence PC (A), Ultrasound driver (B), peristaltic pump (C), magnetic stirrer with particle suspension (D), Keyence digital microscope (E), acoustofluidic cell (F).

3.5.1. Liquid Sampling

For the sampling of liquid analytes, three different techniques have been applied in the scope of this thesis:

- For transmission measurements in a benchtop FT-IR spectrometer, 1-2 mL sample (amount depending on the liquid volume of the transmission cell) was injected using disposable syringes (B. Braun, Germany) and using 1/16" PTFE tubings (O.D. = 1/16", 0.75 mm I.D., VICI AG, Switzerland).
- For most measurements in ATR configuration, liquid handling was performed using a peristaltic pump (Ismatec, Germany) and 1/16" PTFE tubings (O.D. = 1/16", 0.75 mm I.D., VICI AG, Switzerland).
- For the measurements of phosphate using metal-organic frameworks (Publication I)^[69], an automated sequential injection analysis (SIA) system modified from the SIA system reported by Freitag et al.^[98] was employed (schematically shown in Figure 3.7). It consisted of a 10-port selection valve (VICI, Switzerland), as well as a Cavro XC syringe pump (Tecan, Switzerland) equipped with a 500 μ L glass syringe (Tecan, Switzerland). The components were connected with PTFE tubing (VICI, Switzerland, O.D. = 1/16", I.D. = 0.75 mm). The SIA setup and the FT-IR spectrometer were controlled by a LabVIEW VI using a server-client program structure.^[105] The sampling method is described in more detail in chapter 3.5.2.

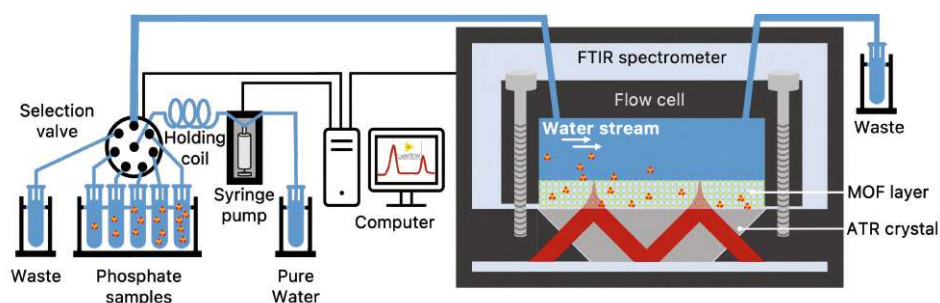


Figure 3.7.: Schematic depiction of the automated sequential injection analysis system used for the measurement of phosphates with MOF covered IREs. Graphic reproduced from Publication I^[69] under the CC-BY 4.0 license.

3.5.2. Automated Sampling Methods

Sequential Injection Analysis

Before performing measurements with the automated SIA system in Publication I,^[69] it had to be calibrated to ensure the correct concentration of the analyte in the flow cell. For this, considerations regarding the liquid volume to be replaced had to be made to optimise the injection volume of the SIA system.

The total dead volume of the system was 98 μL , made up of 20 μL flow cell volume and 78 μL dead volume caused by the tubing (50 cm of PTFE tubing with an I.D. of 0.75 mm). In a first iteration, 300 μL (roughly three times the total volume) was chosen for the sample pulse. To verify the amount of 300 μL pulses needed for a total exchange of the volume in the flow cell, calibration experiments with phosphate tracer solutions (150-1000 mg L^{-1}) using the uncoated IRE were performed, comparing the tracer band height after one and two pulses. For this purpose, the height of the strongest absorption band at 1077 cm^{-1} was chosen. This experiment led to almost identical calibration functions for one and two pulses, which can be seen in Figure 3.8.

In Figure 3.9, a sample SIA sequence for a ortho-phosphate concentration of 25 mg L^{-1} is shown. In each sequence, first an ortho-phosphate standard of 10 mg L^{-1} was measured, followed by the analysis of the actual sample. For each concentration of the ortho-phosphate solutions (5-75 mg L^{-1}), a separate port on the selection valve was used. The whole sequence (shown in Figure 3.9) was made up of three parts: First, the flow cell was flushed with deionised water, followed by a 9 min conditioning step of the MOF in the aqueous sample medium (Figure 3.9-a,b,c). After collecting a background spectrum (denoted with an asterisk in Figure 3.9), 300 μL of the standard was injected at a speed of 100 $\mu\text{L s}^{-1}$ and measured (Figure 3.9-d,e) 63 s after injection. After flushing with deionised water, another

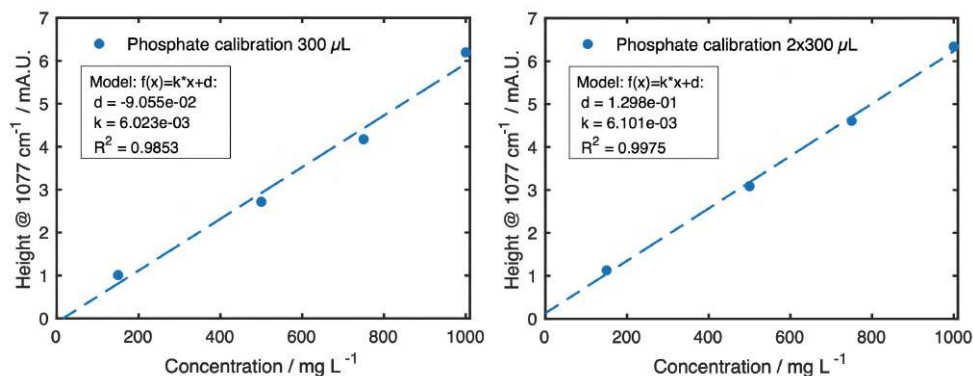


Figure 3.8.: Comparison of the calibration functions of phosphate solutions applying one pulse (300 μL , left) and two pulses (2x300 μL , right) using the same flow cell setup. Graphic reproduced from Publication I^[69] under the CC-BY 4.0 license.

background spectrum was collected (denoted with an asterisk in Figure 3.9). Then, 300 μL of the sample was injected at a speed of $100 \mu\text{L s}^{-1}$ and measured (Figure 3.9-f,g) 63 s after injection.

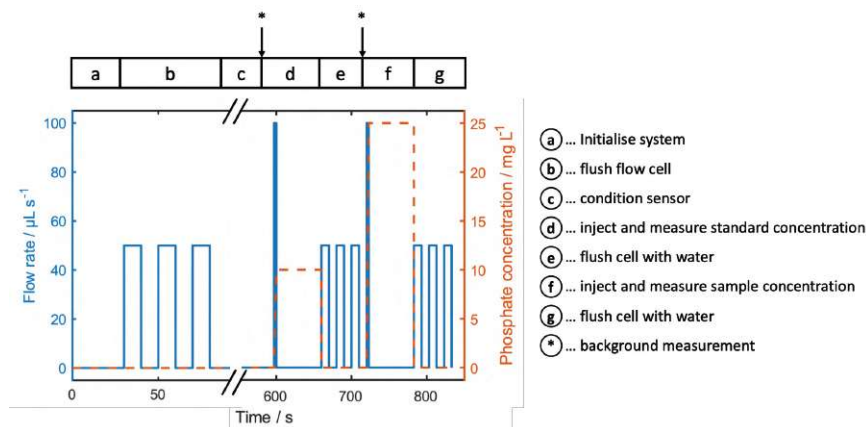


Figure 3.9.: SIA sequence for a sample automated sensor experiment with a standard concentration of 10 mg L^{-1} and a sample concentration of 25 mg L^{-1} . A phosphate concentration of 0 mg L^{-1} at a positive flow rate signifies flushing the flow cell with deionised water. The timing of background measurements is denoted by asterisks. Graphic reproduced from Publication I^[69] under the CC-BY 4.0 license

3.5.3. Gas Sampling and Calibration of Gas Mixtures

The pure gas samples and gas mixtures for the volatile organic contaminant (VOC) analysis with the functionalised silica coated PIC sensors were prepared using an adapted protocol

of the one published by Baumgartner et al.^[106] First, 400-600 μ L of the liquid VOCs were injected into a PTFE tubing connected to an evacuated gas reservoir (2 x 10 L Festo CRVZS Series, connected with stainless steel tubing). This reservoir was filled up to 7 bar using dry pressurised air and connected to an MCQ GB100 gas mixer (MCQ instruments, Italy) via a pressure reducing valve, ensuring a 1.5 bar operating pressure. To the second inlet of the gas mixer, N₂ was connected for the dilution of the gas samples. The whole gas sampling setup is schematically shown in Figure 3.10.

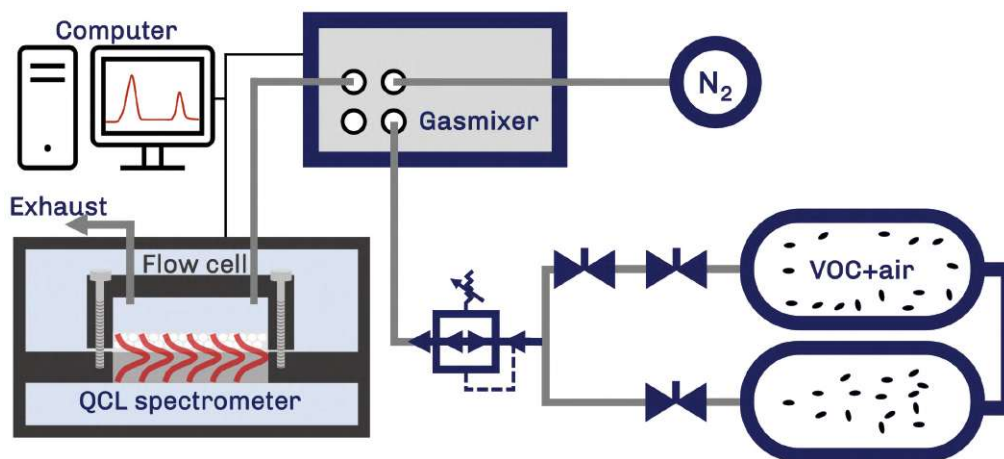


Figure 3.10.: Schematic depiction of the gas sampling system used for the VOC sensing with functionalised silica coated PICs.

To determine the VOC concentrations of the diluted gas samples used for sensor calibration, the gas handling system was connected to a 4 cm gas transmission cell mounted in a Vertex 70V FT-IR spectrometer (Bruker, Germany) equipped with a liquid nitrogen cooled mercury cadmium telluride (MCT) detector (InfraRed Associates, $D^* = 4e10 \text{ cm Hz}^{0.5} \text{ W}^{-1}$ at 9.2 μm). Before the measurements, the transmission cell was flushed with the diluted VOC samples (with 2 % steps between 0 % and 10 % and 10 % steps between 10 % and 100 %). The spectra were collected using the OPUS 8.1 software at a spectral resolution of 2 cm^{-1} , averaging 32 spectra (double-sided, backward-forward acquisition mode). To reduce interferences caused by water vapour, the sample compartment was flushed with dry air at all times. The concentrations of the VOC samples at each gas mixer setting were obtained by deconvolution of the mixed spectra using a MATLAB R2021a toolbox^[107] by applying an MCR-ALS algorithm to the collected spectra. For this, the spectral range of the skeletal vibrations of the aromatic rings of the VOCs between 1400 and 1600 cm^{-1} was used. By multiplication of the loadings with the respective pure spectra and comparison of the areas with reference spectra (1 ppm, 1 m path length) gathered from the PNNL database (for 1,2,4-trimethylbenzene, the spectrum of 1,2,3-trimethylbenzene was used un-

der the assumption of a similar total absorption in the analysed region), the corresponding concentrations could be calculated.

3.6. Synthesis and Characterisation of Mesoporous Materials

3.6.1. Chemicals

Solvents: Ethanol (EtOH, Chem-Lab, 100 % p.a.), chloroform (CHCl₃, VWR, anhydrous ≥ 99.5 % stabilised with iso-amylene), acetone (VWR, ≥ 99.8 %), N,N-dimethylformamide (DMF, Sigma-Aldrich, >99 %), 2-Propanol (IPA, Roth, >99.9 % HPLC grade), absolute acetone (Sigma-Aldrich, 99 %) used for surface functionalisation was dried over molecular sieves. Acetone and IPA for rinsing substrates were used in technical quality. Nitric acid (HNO₃, Sigma-Aldrich, 70 %) was diluted to a 2 M solution with deionised water for cleaning purposes of the SERS/Vis cell.

Precursors for mesoporous oxides or reference materials: titanium(IV)-chloride (TiCl₄, Merck, 97 % p.s.), tetraisopropyl orthotitanate (TTIP, TCI Chemicals), Pluronic F-127 (F-127, Sigma-Aldrich, BioReagent), trichlorophenylsilane (Ph-SiCl₃, TCI, ≥ 98.0 %), titanium oxide (Degussa P25), tetraethoxysilane (TEOS, Sigma-Aldrich 99.5 %), hydrochloric acid (HCl, VWR, 37 %), cetyltrimethylammonium bromide (CTAB, Sigma-Aldrich, 99 %), hexamethyldisilazane (HMDS, TCI Chemicals, >96.0 %), Pluronic P-123 (P-123, Sigma-Aldrich), acetylacetone (AcAc, TCI Chemicals, >99.0 %)

Precursors for metal-organic frameworks or reference materials: Ferric chloride hexahydrate (FeCl₃ · 6 H₂O, Fluka, 99 % p.a.), 2-Aminoterephthalic acid (NH₂-H₂BDC, Sigma-Aldrich, 99 %), iron oxide microparticles (Fe₂O₃ MP, Sigma-Aldrich, <5 μ m, ≥ 96 %), 2-chloro-1-methylpyridinium iodide (Mukaiyama, TCI, 97 %), N,N-diisopropylethylamine (DIEA, Sigma-Aldrich, ≥ 99 %), tert-butyloxycarbonyl protected proline (Boc-Pro-OH, Sigma-Aldrich, ≥ 99 %), biphenyl-4,4'-dicarboxylic acid (H₂BPDC, Sigma-Aldrich, 97 %)

Precursors for the AgNP synthesis: Silver nitrate (AgNO₃, Sigma-Aldrich, >99.0 %), Hydroxylammonium chloride (NH₂OH.HCl, Sigma-Aldrich, 99.999 %), Sodium hydroxide (NaOH, Sigma-Aldrich, >98 % anhydrous)

Analytes: Phosphoric acid (H₃PO₄, 85 % in H₂O, 99.99 % trace metal basis), sodium dihydrogen phosphate (NaH₂PO₄, Fluka, 99 % p.a.), sodium hydrogen phosphate (Na₂HPO₄, Sigma-Aldrich, ≥ 98.0 %), sodium phosphate (Na₃PO₄, Sigma-Aldrich, ≥ 98.0 %), glyphosate (GLP, Sigma-Aldrich, analytical standard), benzonitrile (BN, Sigma-Aldrich, 99 %), toluene (VWR AnalaR NORMAPUR, 99.8 %), p-xylene (Merck, 99 %), 1,2,4-trimethylbenzene (Sigma-Aldrich, p.s.), benzyldimethylhexadecylammonium chloride (BAC-16, Sigma-Aldrich), methylene blue (MB, Sigma-Aldrich, p.a.), sodium sulphate an-

hydrous (Na_2SO_4 , Sigma-Aldrich, >99 %), sodium nitrate (NaNO_3 , Merck, >99 % p.a.)

3.6.2. Synthesis of Mesoporous Oxides

Synthesis of Mesoporous Silica

For the synthesis of mesoporous silica films for the coating of PICs, the protocol established by Bettina Baumgartner^{[99][101]} was used. First, 1.75 g abs. EtOH, 2.08 g TEOS and 0.9 g 0.056 M HCl were added to a round necked flask. This sol-solution was then heated under reflux. At the same time, 0.041 g CTAB were dissolved in 0.4 g abs. EtOH. After 3 h under reflux, 0.5 mL of the sol-solution were added to the CTAB solution and stirred for 10 min. Then, 30 μL of the resulting solution were spin-coated onto the substrates at 2000 rpm and 30 % relative humidity for 25 s. Afterwards, the coated substrates were placed in the oven at 110 °C overnight. This process was repeated two times for the coating of the PICs to ensure that the waveguides were fully covered.

After finishing the coating procedure, the coated PIC was placed in a three neck round flask after the heat treatment and dried for 2 h at 150 °C under vacuum. Then, 20 mL abs. acetone and 0.5 mL HMDS were added and everything heated to reflux for another 4 h. Afterwards, the substrate was removed from the liquid, washed with acetone and dried in the oven overnight at 110 °C.

Synthesis of Mesoporous Titania

The synthesis of the titania layers on the IREs (both the passivated Ge IREs used for phosphate adsorption studies and pristine Si IREs used for hydrocarbon sensing) used for Publication V was performed using a coating solution prepared as follows: First, 0.0766 g of the surfactant Pluronic F-127, 0.38 g deionised water, 1.85 g EtOH and 0.5 g of the prepared titania stock solution were stirred until the surfactant was fully dissolved. The stirring was then continued for another 30 min. 50 μL of the prepared sol was then spin-coated onto the IREs at 2000 rpm and 30 % relative humidity for 25 s. For the passivated Ge IREs, they were gently cleaned with EtOH using a lab wipe in order to not damage the sputtered TiO_2 layer. Annealing of the layer was performed at 60 °C for 1 day, followed by 110 °C, 150 °C and 185 °C for 2 days each. To remove the remaining surfactant, the coated ATR sensors were calcined at 350 °C for 30 min.

3.6.3. Surface Functionalisation of Mesoporous Oxides

Surface functionalisation of mesoporous titania was done in order to increase the affinity of the titania surface towards apolar substances such as hydrocarbons. The surface

functionalisation is based on the procedure published by Wacht et al. for mesoporous zirconia.^[108]

The coated IREs were ultrasonically cleaned in acetone, EtOH, and deionised water for 10 min each. After removing residual solvent with a pressurised air stream, the coated sample was placed in a three-neck round-bottom flask with a reflux cooler and a bubbler, a nitrogen gas inlet, and a vacuum connection, and inertised. Afterwards, the coating was heated to 110 °C for 10 h in an inert atmosphere, followed by a treatment at 150 °C in vacuum for 2 h, after which the flask was filled with nitrogen again. Finally, 20 mL of dried CHCl₃ and 500 μL of (Ph-SiCl₃)₄ were added under a nitrogen stream at ambient temperatures. After reacting with the coated IRE for 24 h, the IRE was removed from the solution and ultrasonically cleaned in deionised water, EtOH, and acetone for 10 min each. Finally, the functionalised sample was placed in an oven at 90 °C overnight to remove residual solvents.

3.6.4. Characterisation of Mesoporous Oxides

Small-angle x-ray diffractometry (SA-XRD) data and grazing-incidence small-angle x-ray scattering (GI-SAXS, featured in Publication V) data were collected using an Empyrean multipurpose diffractometer, equipped with a GalliPIX 3D area detector and the Data Collector software (all from PANalytical, Netherlands). The measurements were conducted in Bragg-Brentano geometry (SA-XRD) and in a standard GI-SAXS configuration, respectively, both with the Cu anode operating at 45 kV and 40 mA. The diffractograms were recorded between 1 and 5° 2θ with a step size of 0.0143° and an integration time of 98 s/step in continuous scan mode. The GI-SAXS measurements were performed in a 2θ range between -3.5 and 3.5°, following the guideline provided by PANalytical. The small-angle x-ray diffractograms were evaluated using the Data Viewer software (PANalytical, Netherlands) whereas the 2D-scattering patterns received in the GI-SAXS experiments were evaluated using the XRD2DScan software (PANalytical, Netherlands).

The layer thickness (featured in Publication V) was determined using a Dektak XTL Stylus profilometer (Bruker, Germany) by measuring the indent of three scratches at different positions.

Contact angles were measured on a DSA 30 contact angle goniometer (Krüss, Germany) equipped with a video camera. For that, 3 μL water droplets were placed on the surface of the sample. The shape of the droplets was analysed by the Young-Laplace method in the software of the goniometer.

3.6.5. Synthesis of Metal-Organic Frameworks

Synthesis of NH₂-MIL-88B(Fe)

The synthesis of NH₂-MIL-88B(Fe) was performed following the report of Bauer et al.^[71]: 2.025 g FeCl₃ · 6 H₂O was dissolved in 25 mL of DMF. In parallel, a solution of 0.675 g NH₂-H₂BDC in 20 mL of DMF was prepared, and the two solutions were subsequently mixed. This mixture was put into a Teflon lined solvothermal reactor and heated for 24 h at 115 °C. After cooling down, the solvent and the brown precipitate were separated by centrifugation for 3 min at 4000 rpm (Rotofix 32 A, Hettich, Germany). The precipitate was washed four times using DMF, twice with deionised water, and twice with EtOH. After the last washing step, the as-synthesised MOF was dispersed in EtOH and put into a crystallising dish to let the solvent evaporate at ambient conditions. Finally, the resulting brown powder was dried at 90 °C for 24 h to remove any remaining traces of EtOH.

Synthesis of NH₂-MIL-101(Fe)

The synthesis of NH₂-MIL-101(Fe) was also performed following the report of Bauer et al.^[71]: 1.013 g FeCl₃ · 6 H₂O was dissolved in 25 mL of DMF. In parallel, a solution of 0.338 g NH₂-H₂BDC in 20 mL of DMF was prepared, and the two solutions were subsequently mixed. This mixture was put into a Teflon lined solvothermal reactor and heated for 24 h at 115 °C. After cooling down, the solvent and the brown precipitate were separated by centrifugation for 3 min at 4000 rpm (Rotofix 32 A, Hettich, Germany). The precipitate was washed four times using DMF, twice with deionised water, and twice with EtOH. After the last washing step, the as-synthesised MOF was dispersed in EtOH and put into a crystallising dish to let the solvent evaporate at ambient conditions. Finally, the resulting brown powder was dried at 90 °C for 24 h to remove any remaining traces of EtOH.

Synthesis of MIL-126(Fe)

The synthesis of NH₂-MIL-88B(Fe) was performed following the report of Bara et al.^[109]: 242 mg H₂BPDC was dissolved in 30 mL of DMF. This process was assisted by ultrasound sonication to achieve full dissolution of the reagent. To this mixture, 540 mg FeCl₃ · 6 H₂O was added and the resulting mixture was poured into a Teflon lined autoclave and heated for 48 h at 120 °C. After cooling down, the solvent and the orange-brown precipitate were separated by centrifugation for 3 min at 4000 rpm (Rotofix 32 A, Hettich, Germany). The precipitate was then washed four times using DMF, and four times with DCM. After the last washing step, the MOF was dispersed in DCM and poured into a crystallising dish.

Finally, the resulting brown powder was dried at 90 °C for 24 h to remove any remaining traces of DCM.

3.6.6. Post-Synthetic Modification of Metal-Organic Frameworks

For the grafting of functional groups onto the amino group of the aminoterephthalate linker, a protocol using a Monowave 50 (Anton Paar, Austria) reactor was devised. For that, 56 mg of the NH₂-MIL-88 B(Fe), 112 μL DIEA, 108 mg of Boc-Pro-OH, and 112 μL of Mukaiyama reagent were dispersed in 5 mL DCM and added to a Monowave reaction vessel. The vessel was mounted in the Monowave 50 reactor and the mixture heated up to 80 °C in 5 min, which was subsequently held for 20 min. After cooling, the precipitate was separated from the solvent by centrifugation for 3 min at 4000 rpm (Rotofix 32 A, Hettich, Germany) and washed three times using DCM. For the removal of the Boc protection group, the washed precipitate was dispersed in 5 mL DCM, once again mounted in the Monowave 50 reactor and heated up to 150 °C in 5 min, which was also held for 20 min. After cooling, the same washing procedure as before was performed, the washed precipitate dispersed in DCM and poured into a crystallising dish. Finally, the resulting brown powder was dried at 90 °C for 24 h to remove any remaining traces of DCM.

3.6.7. Characterisation of Metal-Organic Frameworks

X-ray diffraction patterns were measured on an X'Pert PRO MPD diffractometer, which was equipped with a X'Celerator line scan detector using the Data Collector software (all from PANalytical, Netherlands). All measurements were conducted in Bragg-Brentano geometry, with the Cu anode operating at 45 kV and 40 mA. The diffractograms were recorded between 5° and 25° 2θ at a step size of 0.01° and an integration time of 360 s/step in continuous scan mode. The measured diffractograms were compared to the simulated theoretical diffractograms which were calculated by Rietveld refinement using data^{[71][110]} from the Cambridge Structural Database (CSD). Rietveld refinement was performed in the HighScore Plus platform^[111] (PANalytical, Netherlands). FT-IR-ATR measurements of NH₂-MIL-88B(Fe) (featured in Publication I^[69]) were performed on a Tensor 37 FT-IR spectrometer (Bruker Optics, Germany) equipped with a Platinum ATR unit (Diamond, single-bounce, Bruker Optics, Germany) and a N₂-cooled MCT detector. Spectra were recorded with 4 cm⁻¹ resolution, using the average of 32 scans for each spectrum. To demonstrate the successful synthesis of the NH₂-MIL-88 B(Fe) as a crystalline MOF, scanning electron microscopy (SEM) was performed. The MOFs were prepared by suspending them in IPA with a concentration of 0.03 wt% and stirred for 1 h. This suspension was then drop-casted on a silicon wafer. After evaporation of the solvent, the silicon wafer

was mounted on the SEM sample holder. For better contrast, the sample was coated with a 20 nm sputtered layer of Au. The SEM images were recorded on a FEI QUANTA 200 ESEM scanning electron microscope at magnifications of 30,000x and 160,000x using the secondary electron configuration. Thermogravimetric analysis (TGA) was performed on a STA 449 C Jupiter (NETZSCH, Germany) which was controlled by a TASC 414/4 unit (NETZSCH, Germany). Before the measurement, 30-40 mg of the sample was placed in an aluminium oxide crucible which was mounted in the instrument, which was inertised using a flow of Argon. The sample was then heated at a ramp of 5 K min⁻¹ up to a temperature of 600 °C. During the experiment, a steady flow of 50 mL min⁻¹ of Argon was used to remove gaseous combustion products.

Part IV.

Mesoporous Oxides for Studying Surface Interactions and Trace Analysis

Introduction

This part serves as an introduction to the research on mesoporous oxides, which resulted in Publications II and V. The focus is laid on the preliminary research leading to the results as well as some unpublished results. For more detailed descriptions of the results of the publications, the reader is guided to the Appendix.

4.1. Optimisation of Synthesis of Mesoporous Titania

The optimisation of the synthesis was performed in three steps. First, suitable precursors needed to be found and a basic recipe created. Here, a plethora of different synthesis protocols can be found in literature, however, the many parameters involved in the formation of such a layer that are difficult to fully control (e.g., relative humidity of the lab, temperature fluctuations, hygroscopic precursors) may necessitate slight modifications in the procedure for any given laboratory.

After setting up a basic recipe, the focus was laid on the heat treatment, as the high shrinkage of titania-based sol gel layers makes it crucial to limit the stress on the freshly formed network. Intermediate treatment such as ammonia treatment of coated layers was also explored, which has shown promising results in literature.^{[112] [113]}

Finally, approaches to modify the thickness of the layer were explored, including coating multiple layers or varying the volatile components of the coating solution.

The first step was covered by varying two key parameters: the titanium-containing precursor material and the surfactant. For the titanium-containing precursor, TTIP and an ethanolic stock solution $\text{TiOEt}_{x.y} \text{HCl}$ (further referred to as TiEt_5) following the procedure reported by Faustini et al.^[114] were evaluated. For this stock solution, first, 8.65 g TiCl_4 was slowly added to 8 mL EtOH under stirring in an ice bath. After the fuming stopped, EtOH was added to the solution until it weighed 18.75 g. This procedure resulted in a stock solution of TiCl_4 with a molality of 2.432 mmol Ti per g solution. On the other hand, three different surfactants, two different block-copolymers of the Pluronic family (P-123 and F-127) and cetyltrimethylammonium bromide (CTAB) were used in the experiments.

Comparing the synthesis using TTIP with TiEt_5 , two additional substances were added to the reaction mixture for TTIP, namely HCl (0.9 M) and AcAc. The addition of these substances helped with stabilising the solution, as otherwise, precipitates formed that interfered with the coating. For TiEt_5 , this was not necessary, as the precursor solution was more acidic due to the residual HCl from the reaction of TiCl_4 with EtOH. Therefore, only water was added instead of the HCl and AcAc to improve the hydrolysis of the

Table 4.1.: Recipes for the titania synthesis using TTIP as precursor.

| TTIP | all masses are in g | | | | | |
|-------|---------------------|----------|--------|---------|---------|--------|
| P-123 | m(TTIP) | m(P-123) | m(HCl) | m(AcAc) | m(EtOH) | Φ |
| R1 | 1.5 | 0.313 | 1 | 0.265 | 9 | 37.0 % |
| R2 | 1.5 | 0.425 | 1 | 0.265 | 9 | 44.4 % |
| F-127 | m(TTIP) | m(F-127) | m(HCl) | m(AcAc) | m(EtOH) | Φ |
| R3 | 1.5 | 0.638 | 1 | 0.265 | 9 | 37.0 % |
| R4 | 1.5 | 0.325 | 1 | 0.265 | 9 | 44.4 % |

precursor.

The starting point for all synthesis recipes was based on the procedure published by Yun et al.^[115] as well as the recipe for mesoporous silica established by Bettina Baumgartner in our laboratory.^[99] In Yun’s approach, TTIP was mixed with IPA, and AcAc and stirred for 2 h. Afterwards, P-123 dissolved in IPA was added to the solution, the pH adjusted with HCl and stirred for another 3 h, before spin-coating the substrates for 25 s at 2000 rpm. Before coating, the substrates were cleaned with EtOH in an ultrasonic bath and freed from the residual solvent using a lab wipe. This cleaning step was also done for all other substrates as the method was fine-tuned. The layers were then heat treated for 24 h at 60 °C to help with the formation of the titania network, followed by another heat treatment for 24 h at 110 °C to remove all volatile parts.

In the approach inspired by the recipe for mesoporous silica, TTIP was first hydrolysed *in-situ* by adding water, AcAc and IPA. The pH of water was then set to 1.2 and the solution stirred for 3 h at room temperature. Afterwards, a defined amount of the hydrolysed titania was added to a solution of the P-123 in IPA, stirred for another 10 min, and then, spin-coated onto the cleaned substrates at 2000 rpm and the respective relative humidity for 25 s.

In Table 4.1, the recipes for the samples prepared with TTIP using these two approaches are shown. The procedures described above were not changed when using F-127 instead of P-123. For the approach inspired by the procedure for mesoporous silica, the layers cracked immediately after coating, and the approach was no longer followed.

The formation of cracks in the layer also posed to be a problem for the procedure inspired by Yun’s approach, albeit at a lower rate. Ultimately, it was found that the cracking could be brought under control when using the TiEt_5 precursor,^[114] even when reducing the reaction time of the hydrolysis. This resulted in an optimised procedure for the synthesis of the coating solution: First, TiEt_5 , water, EtOH, and the surfactant were mixed and

Table 4.2.: Recipes for the titania synthesis using TiEt_5 as precursor.

| TiEt_5 | all masses are in g | | | | |
|-----------------|----------------------|----------|---------------------------|---------|--------|
| P-123 | m(TiEt_5) | m(P-123) | m(H_2O) | m(EtOH) | Φ |
| R5 | 1 | 0.092 | 0.76 | 3.7 | 27.3 % |
| R6 | 1 | 0.152 | 0.76 | 3.7 | 38.2 % |
| F-127 | m(TiEt_5) | m(F-127) | m(H_2O) | m(EtOH) | Φ |
| R7 | 1 | 0.092 | 0.76 | 3.7 | 27.3 % |
| R8 | 1 | 0.152 | 0.76 | 3.7 | 38.2 % |
| R9 | 1 | 0.223 | 0.76 | 3.7 | 47.6 % |
| CTAB | m(TiEt_5) | m(CTAB) | m(H_2O) | m(EtOH) | Φ |
| R10 | 1 | 0.092 | 0.76 | 3.7 | 27.3 % |
| R11 | 1 | 0.152 | 0.76 | 3.7 | 38.2 % |

stirred vigorously until the surfactant was dissolved completely. The stirring was then continued for another 30 min. 50 μL of the prepared solution was then spin-coated onto the cleaned substrates at 2000 rpm and the respective relative humidities for 25 s. The layers were then heat treated for 24 h at 60 $^\circ\text{C}$, followed by another heat treatment for 24 h at 110 $^\circ\text{C}$. In Table 4.2, the recipes for the samples prepared with TiEt_5 are shown.

For this first procedure leading to a successful coating, the coatings prepared using F-127 as template led to the best results, while the coatings prepared with P-123 and CTAB still occasionally cracked after the heat treatment, especially after thermally removing the template for 4 h at 400 $^\circ\text{C}$ after the initial heat treatment.

In the next step, the heat treatment was optimised to improve the layer quality, trying to receive crack-free layers for all templates. Trying to treat the layers with gaseous ammonia after coating, which has been reported in literature^{[112][113]} to improve the layer quality, did not work for the system used in this thesis. Beyond the synthesis of intact layers, another aspect to be considered in this stage was to receive ordered mesoporosity, as connected mesoporous systems lead to faster diffusion in the pores. The presence of ordered mesoporosity was confirmed using SA-XRD, which was performed for all samples in this optimisation step (SA-XRD of the first intact layer with ordered mesoporosity, a layer with the optimised synthesis and heat treatment and the pyrolysed layer in Figure 4.1). Using this data, also the pore size could be approximated by using the Bragg d-spacing as a measure for the pore size (while disregarding the wall thickness). Starting with the recipes shown in Table 4.2, the samples prepared with F-127 showed some sharp peaks in the diffractogram hinting at ordered porosity, while the samples prepared with P-123 only

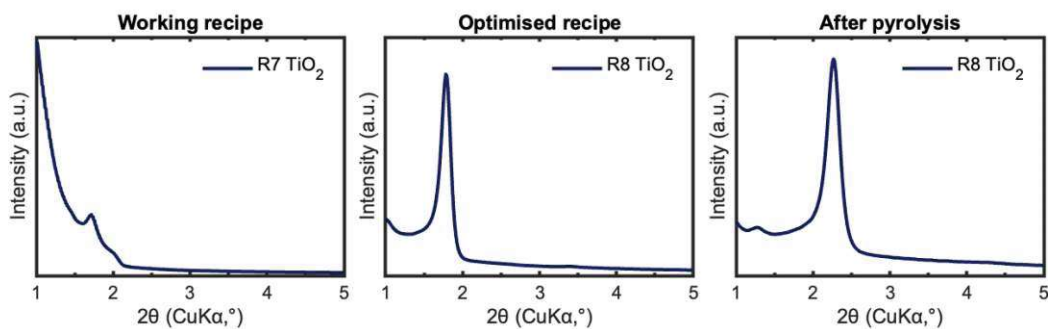


Figure 4.1.: Left: SA-XRD of the first intact layer with ordered mesoporosity (synthesised with R7). Middle: SA-XRD of the layer after optimisation of synthesis and heat treatment (synthesised with R8). Right: SA-XRD of the pyrolysed layer after optimisation of synthesis and heat treatment (synthesised with R8).

showed diffuse signals hinting at non-ordered wormlike pores, and the samples prepared with CTAB showed no porosity at all. The absence of pores in the CTAB samples can probably be attributed to the pores collapsing during the strong shrinking of titania during the heat treatment combined with the small size of CTAB micelles.

As both the relative humidity (%RH) during the coating and the sol:surfactant ratio have shown to influence the order of the porous structure, studies have been performed varying the %RH at the different sol:surfactant ratios listed in Table 4.2, with %RH = 40-50 % leading to the sharpest peaks in the diffractograms, while a %RH below 20 % had a negative impact on the intactness of the layer. No change in porous structure could be observed when varying the %RH.

Looking at the impact of the heat treatment durations, shorter heat treatment was found to lead to more cracks, while a longer heat treatment at 110 °C of 48 h led to less cracking. This behaviour could be further improved by adding two more heat treatments at 150 °C and 185 °C, which already removed some of the template ($T_b(\text{F-127}) = 150\text{ °C}$) and, thus, allowed to reduce the pyrolysis time to 30 min while still removing most of the template. Another study was performed looking at the influence of the temperature of the pyrolysis on the porous structure using temperature-controlled SA-XRD (shown in Figure 4.2), showing that at higher temperatures up to 450 °C, the pore size can be controlled. At higher temperatures, the pore size no longer decreases (shown by a constant d-spacing), but rather, the pore volume decreases (shown by a decrease in the area below the peak).

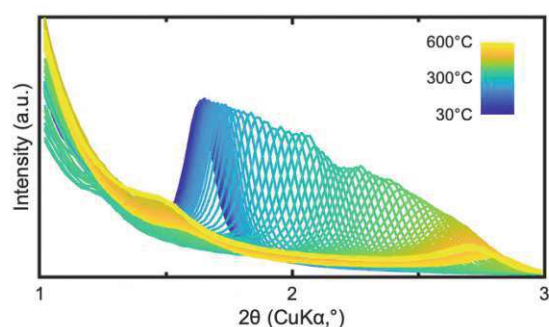


Figure 4.2.: Dependence of the pyrolysis temperature on the pore size (approximated by the d-spacing).

As a last step, the control of the layer thickness was explored by changing the volatile component of the coating solution (i.e. the EtOH content). By doing this, the layer thickness could be varied between 150 nm and 300 nm. Although a thicker layer would be beneficial for the sensitivity of an adsorption-based sensing concept, as more of the evanescent field would be covered by the sensing layer, a recipe resulting in a layer thickness of 200 nm was finally chosen for the coating of the IREs, as the thicker layers were once again prone to cracking.

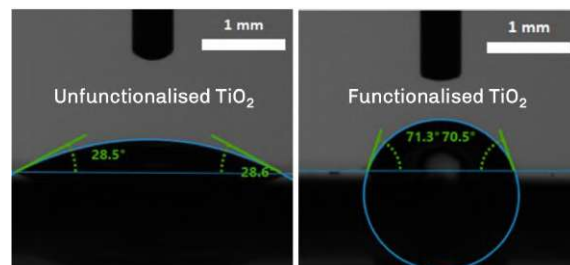


Figure 4.3.: Left: Wetting behaviour with water of a pyrolysed unfunctionalised mesoporous titania layer. Right: Wetting behaviour with water of a pyrolysed functionalised mesoporous titania layer.

After establishing this recipe for the synthesis of mesoporous titania, the functionalisation of the titania surface was explored. Here, two approaches were followed: A concurrent removal of the template during the functionalisation process inspired by the protocol established by Bettina Baumgartner,^[99] and a functionalisation of the pyrolysed titania layers with silanes, based on the protocol published by Dominik Wacht.^[108] In the concurrent approach, the coated substrate was placed in a three neck round flask after the heat treatment and dried for 2 h at 185 °C under vacuum. Then, 20 mL abs. acetone and 0.5 mL HMDS were added and everything heated to reflux for another 4 h. Afterwards, the sub-

strate was removed from the liquid, washed with acetone and dried in the oven overnight at 110 °C. Due to the template being significantly larger than the CTAB molecules, whose micelles can be broken up more easily than the polymer chain of the Pluronic F-127, the first approach did not appear to be feasible. In the post pyrolysis functionalisation, the coated IREs were first immersed and ultrasonically treated in acetone, ethanol and deionised water for 10 min each to activate the surface oxides. After drying the chip for 2 h at 150 °C under vacuum, the flask was cooled down to ambient temperature, inertised with nitrogen and the chip immersed in 20 mL of abs. chloroform. Afterwards, 0.5 mL of Ph-SiCl₃ was added and kept under inert conditions for 24 h. Afterwards, the coating was cleaned with acetone, ethanol and deionised water and dried at 90 °C overnight. The successful functionalisation was confirmed by looking at the wetting behaviour of the surface with water, which is shown in Figure 4.3. Comparing the wetting angles of the functionalised and the unfunctionalised titania, it is apparent that the functionalisation has increased the hydrophobicity significantly, which enables the use of mesoporous titania for the enrichment of apolar contaminants in water.

4.2. Theoretical and Practical Considerations of Mesoporous Titania for Sensing Purposes

For quantitative analysis using mid-IR spectroscopy using ATR configuration, usually the Boguer-Beer-Lambert law (2.21) is used. To maximise the sensitivity of the method, a compromise between the incident light I_0 and the interaction length d_e needs to be found. For ATR spectroscopy, also the inherent absorptivity of the IRE has to be considered as shown in the single channel spectra (i.e. I_0 for the respective IREs) in Figure 3.1. If adding an enrichment layer to enhance the sensitivity, also the absorptivity of the layer has to be considered. In Figure 4.4, the single channel spectra for a pristine Ge IRE, a Ge IRE coated with a mesoporous TiO₂ layer, and a Ge IRE coated with a functionalised mesoporous TiO₂ layer are compared. In this spectrum, the TiO₂ absorption is responsible for the transparency at lower wavenumbers (for this purpose described as the wavenumber at which $I/I_{max} < 0.1$) moving from 800 cm⁻¹ to 970 cm⁻¹. Adding a surface functionalisation further shifts the lower wavenumber transparency up to 1140 cm⁻¹ due to the Si-O-Ti band. Considering this, the added benefit of a broader IR transparency when using Ge IREs in the place of Si IREs is eliminated if using it in combination with functionalised mesoporous titania. Therefore, coated Si IREs were used for the sensing of hydrocarbons in the aqueous phase.

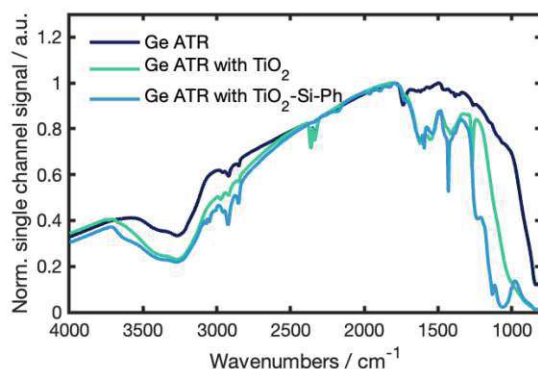


Figure 4.4.: Comparison of the single channel spectra for a pristine Ge IRE (navy), a Ge IRE coated with a mesoporous TiO_2 layer (green), and a Ge IRE coated with a functionalised mesoporous TiO_2 layer (light blue).

Another aspect to consider when using adsorption-based enrichment is that due to the enrichment layer covering (parts of) the evanescent field, the optical properties of these layers need to be included in the calculation of the theoretical effective pathlength. As the evanescent field decays exponentially in the direction perpendicular to the interface (2.17), a simple equation (4.1) can be set up to calculate the percentage S of the field being covered by the porous enrichment layer with a thickness of l . Using this value of S , the effective path length inside the layer $d_{e,film}$ can be calculated (4.2).

$$S = 1 - e^{\frac{-2 \cdot l}{d_p}} \quad (4.1)$$

$$d_{e,film} = d_e \cdot N \cdot S \quad (4.2)$$

With these equations, the effective pathlength in the films can be calculated for each analyte region for the used IREs. In Table 4.3, these values are calculated for the used Ge and Si IREs and in Figure 4.5, the effective pathlengths are visualised as a function of the wavenumbers.

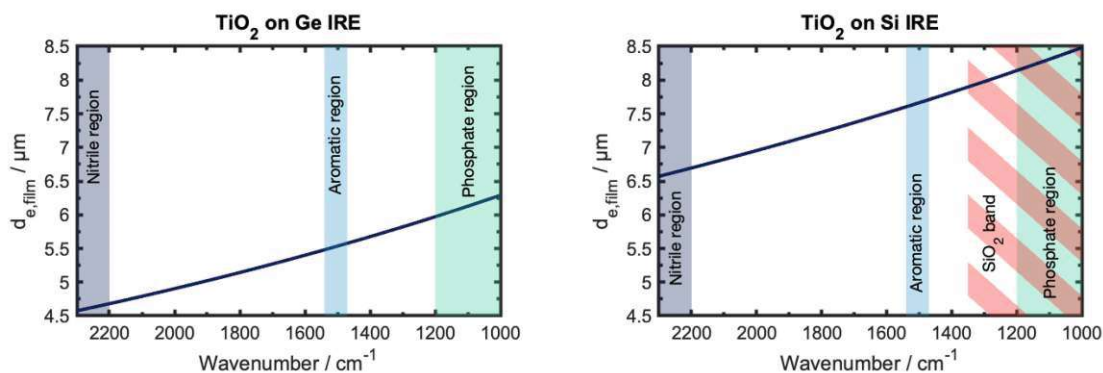


Figure 4.5.: Left: Illustrated calculated values of the effective pathlength in the titania film coated on a Ge IRE depending on the wavelength of the light. Relevant absorbance regions of the analytes marked in different colours. Right: Illustrated calculated values of the effective pathlength in the titania film coated on a Si IRE depending on the wavelength of the light. Relevant absorbance regions of the analytes and the native SiO₂ passivation layer marked in different colours.

Table 4.3.: Calculated values for the optical parameters of the used IREs at the relevant wavenumbers for the detecting nitriles (2230 cm⁻¹), aromatic hydrocarbons (1500 cm⁻¹), and phosphates (1100 cm⁻¹). All values are assumed for a titania layer with a thickness of 200 nm and a refractive index of 1.623.

| | $\tilde{\nu}_0 / \text{cm}^{-1}$ | $d_p / \mu\text{m}$ | $d_e / \mu\text{m}$ | S / a.u. | $d_{e, \text{film}} / \mu\text{m}$ |
|--------|----------------------------------|---------------------|---------------------|----------|------------------------------------|
| Ge IRE | 2230 | 0.309 | 0.320 | 0.73 | 4.65 |
| | 1500 | 0.459 | 0.476 | 0.58 | 5.54 |
| | 1100 | 0.626 | 0.649 | 0.47 | 6.13 |
| Si IRE | 2230 | 0.402 | 0.528 | 0.63 | 6.66 |
| | 1500 | 0.597 | 0.785 | 0.49 | 7.66 |
| | 1100 | 0.814 | 1.070 | 0.39 | 8.31 |

Using these values for $d_{e, \text{film}}$, the experimental values of the ATR measurements can be compared with transmission measurements and an estimation of the amount of adsorbed analyte in the layer can be made. However, it should be noted that this is just a first approximation as for this model, four simplified assumptions were made:

- First, it does not consider the shift of the band due to anomalous dispersion near an absorbance band.
- Second, it assumes the refractive index of the layer to be constant between 2300

and 1000 cm^{-1} , with values retrieved from literature ($n_{mp\text{TiO}_2}=1.623$).^[116] Mid-IR ellipsometry as performed for mesoporous ZrO_2 by Wacht et al.^[108] was explored, but did not deliver meaningful results for the titania layers.

- Third, it uses the middle of the absorbance peak (region) for the calculation. This disregards the non-linear change of the effective path length as a function of the wavenumber, but is a good approximation.
- Finally, the amount of analyte in the matrix above the layer is disregarded, as this concentration is negligible assuming enrichment factors of >1000 .

4.3. Enrichment of Phosphate Species

In Publication V, a comprehensive study of the adsorption of different phosphate species in mesoporous titania was conducted, looking at both the thermodynamic as well as the kinetic perspectives of the adsorption. Additionally, the dependence of the IR spectrum of adsorbed phosphate species on the pH value was explored, and the band shapes were compared with literature spectra for phosphates adsorbed onto bulk titania.^{[117][118]} By doing this, it could be confirmed that all phosphate was bound by chemisorption forming a bridging bidentate surface complex rather than through electrostatic interactions.

Leading up to the results of this publication, some optimisations regarding the intermediate layers were necessary, as for a direct coating of mesoporous titania onto the Ge IREs, there was an insufficient stability towards the aqueous media of the phosphate solutions, leading to a delamination of the titania layer as the water soluble GeO_2 passivation layer of the Ge IRE made contact with the liquid phase. To circumvent this, two approaches were explored. In previous projects, the use of a sputtered layer of SiO_2 greatly improved the stability of the Ge IRE in aqueous media. However, the strong Si-O-Si band led to very noisy spectra (see Figure 4.6).

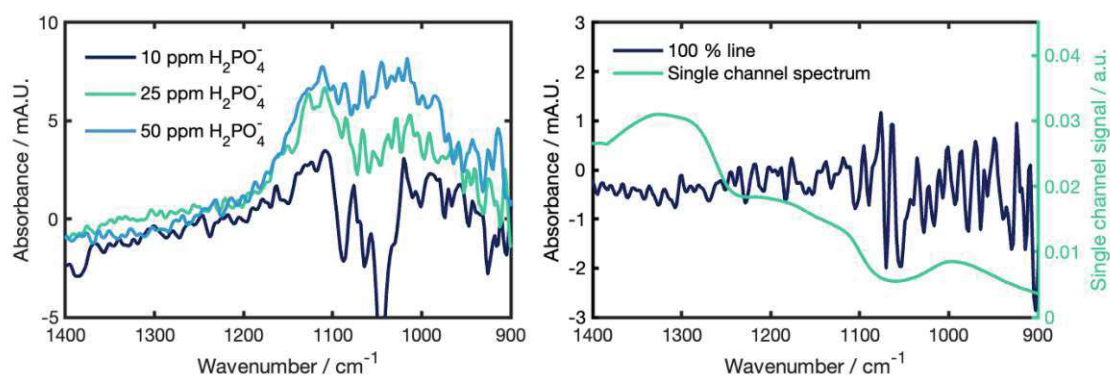


Figure 4.6.: Left: Sample phosphate spectra acquired on a mesoporous TiO_2 coated Ge IRE with a SiO_2 protection layer. Right: 100 % line (blue) and single channel spectrum (green) of the mesoporous TiO_2 coated Ge IRE with a SiO_2 protection layer.

Based on the incompatibility of a SiO_2 intermediate layer for phosphate measurements, a new approach had to be devised. Here, together with Mauro David and Borislav Hinkov from the FKE group at TU Wien, a thin (20 nm thick) sputtered TiO_2 layer was applied to the pristine Ge IRE. By doing that, a protective intermediate layer could be applied while enhancing the adhesion between the IRE and the mesoporous layer and being transparent even below 1000 cm^{-1} .

4.4. Enrichment of Hydrocarbons from the Aqueous Phase

To study the adsorption behaviour of organic contaminants, seven different concentrations between 10 and 200 mg L^{-1} of benzonitrile as a model substance in water were applied to a phenyl functionalised mesoporous titania layer coated onto a Si IRE. Sampling was performed by a continuous flow of the analyte using a peristaltic pump. To determine the optimal time for sampling, adsorption/desorption cycles were performed, with 3 min of time for each step. In Figure 4.7, an exemplary cycle for a concentration of 75 mg L^{-1} is shown. Looking at the data in this cycle, the fast response of adsorption-based enrichment can be seen, as 90 % of the equilibrium concentration is adsorbed after just 70 s. Desorption is equally fast, with 90 % of the equilibrium concentration being desorbed after 80 s.

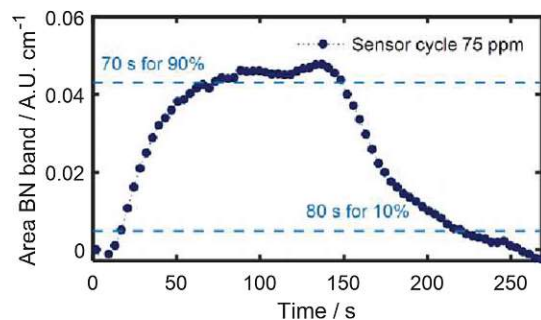


Figure 4.7.: Adsorption/desorption cycle for benzonitrile in a phenyl functionalised mesoporous titania layer. Blue dashed lines show 10% and 90% of the band area of the equilibrium concentration of adsorbed benzonitrile.

Table 4.4.: Adsorption data collected for BN in mesoporous titania for equilibrium sampling. Band heights are averaged for 4 independent samples. Fits were performed for the averaged band heights.

| $c / \text{mg L}^{-1}$ | $A / \text{A.U.}$ |
|--|---------------------------------------|
| 10 | $7.30\text{e-}04 \pm 2.65\text{e-}05$ |
| 29 | $1.50\text{e-}03 \pm 3.79\text{e-}05$ |
| 50 | $2.13\text{e-}03 \pm 9.29\text{e-}05$ |
| 75 | $2.73\text{e-}03 \pm 2.83\text{e-}05$ |
| 100 | $2.97\text{e-}03 \pm 5.13\text{e-}05$ |
| 150 | $3.72\text{e-}03 \pm 1.37\text{e-}04$ |
| 200 | $4.31\text{e-}03 \pm 3.79\text{e-}05$ |
| $K_F / \text{A.U.cm}^{-1}[\text{L mg}^{-1}]^{1/n}$ | $2.54\text{e-}4$ |
| n_F | 1.863 |
| χ_F^2 | $3.64\text{e-}05$ |

Building onto this, the equilibrium concentration was determined for each benzonitrile solution using the signal of four independent runs. In Table 4.4, the adsorption data collected for benzonitrile is displayed. In this table, A stands for the averaged band heights for equilibrium adsorption, which are shown together with the standard deviation of the four samples. In line with the perceived mechanism of multilayer adsorption caused by hydrophobic interactions, the adsorption data was described with the Freundlich model to establish a calibration function. For that, the averaged band heights were fitted using the Freundlich equation (2.30) and the fitting parameters q_e and K_F shown in Table 4.4 as

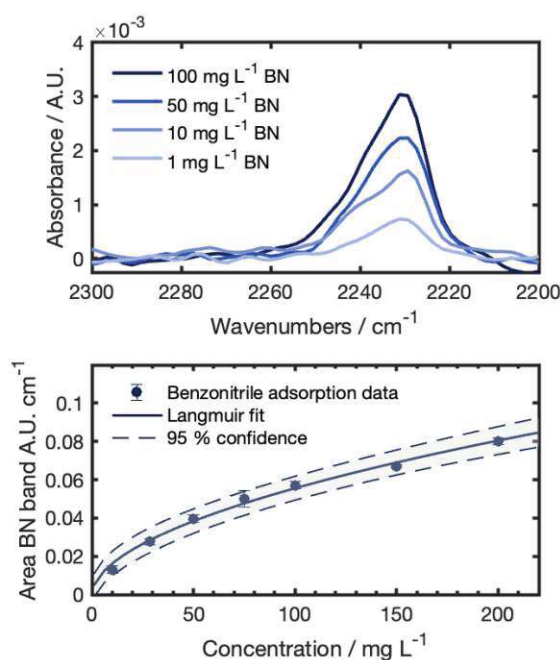


Figure 4.8.: Top: Exemplary spectra of different concentrations of adsorbed benzonitrile. The background spectrum was recorded of deionised water on the mesoporous film. Bottom: Freundlich fit for the data set received for benzonitrile with 95 % confidence interval of the fit function represented by the grey area. Error bars show standard deviations for 4 independent measurements.

well as the error of the fit χ_F^2 were received. The fit (with 95 % confidence intervals of the fit function) can also be seen in Figure 4.8 together with exemplary spectra of the nitrile band of different concentrations of benzonitrile.

The sensitivity can be described by two parameters: the limit of detection (LOD) and the enrichment factor n_{Enrich} . Evaluating the sensing system regarding its LOD uses the fitting parameters as calibration function. Applying the standard definition of the LOD^{[119][120]} to the sensing system, it can be calculated by the concentration equivalent to a band area 3 times the noise floor of the sensing system, which is equivalent to a significance of 99 % for the signal in comparison to the noise floor. The resulting equation is shown in (4.3) for a Freundlich fit. In this equation, σ is denoting the noise, which is calculated from the 100 % lines in the peak area (2300-2200 cm⁻¹ for the benzonitrile measurements).

$$LOD = \left(\frac{3s}{K_F} \right)_F^n \quad (4.3)$$

Using this equation and a RMS noise of 4.22e-5, a LOD of 0.27 mg L⁻¹ could be calculated. For the enrichment factor, the peak areas were compared with a calibration

acquired in a transmission measurement of benzonitrile. As opposed to the LOD determination, where the peak heights were used due to a more accurate noise definition, the peak areas are more accurate at lower concentrations where the enrichment factor is the largest and were, thus, used for the calculation of the enrichment factors. For transmission configuration, an absorption coefficient ϵ of $2.22\text{e-}3 \text{ A.U. cm}^{-2} \text{ mg}^{-1} \text{ L}$ was determined. Comparing the expected peak area with the actual peak areas \bar{A} (4.4) then resulted in an enrichment factor of 126 ± 19 at 10 mg L^{-1} , which decreased to 39 ± 1 at 200 mg L^{-1} due to the non-linear nature of the adsorption enhancement.

$$n_{\text{Enrich}} = \frac{\bar{A}}{\epsilon \cdot c \cdot d_{e,\text{film}}} \quad (4.4)$$

4.5. Enrichment of Volatile Organic Contaminants from the Gas Phase

In Publication II, the use of mid-IR PICs for multi-gas VOC sensing was explored. Applying PICs in the mid-IR is a relatively new research field that offers a lot of promise due to the possibility of designing fully integrated sensors and combining the light source, a waveguide sensor, and the detector on a single chip. Another approach can be the fabrication of cheap disposable sensor chips with highly alignment tolerant interfaces. This approach was chosen in this thesis, where in cooperation with **Mattias Verstuyft** and **Nuria Teigell Beneitez** from imec/UGent such chips were fabricated. The alignment tolerant interfaces were demonstrated in Publication III, showing in-plane 1 dB alignment tolerances of $\pm 16 \mu\text{m}$, and out-of-plane 1 dB alignment tolerances larger than $150 \mu\text{m}$. For the VOC sensing, the PIC was coated with three layers of mesoporous silica, fully covering the evanescent field of the mid-IR waveguide. This led to sub-ppmv limits of detection and a maximum signal enhancement of 22,000 due to the adsorption-based enrichment.

Part V.

Metal-Organic Frameworks for Adsorption Screening and Trace Analysis

Introduction

This part serves as an introduction to the research on metal-organic frameworks (MOFs), which resulted in Publication I. The focus of this part is laid on the preliminary research leading to the published results as well as some unpublished results. For more detailed descriptions of the results of the publication, the reader is guided to the Appendix.

5.1. Optimisation of Metal-Organic Framework Synthesis

MOFs are a very versatile group of materials with the potential to efficiently tailor their structure to accommodate guest molecules by varying the linkers and SBUs. In this thesis, this was performed for sensing purposes, targeting phosphates and hydrocarbons as analytes in aqueous matrices. Therefore, a crucial factor for choosing MOFs for their planned application as sensing material was their water stability.

The MIL-101 (Fe) family (based on terephthalate linkers and iron oxide clusters as SBUs) has been effectively used for the removal of phosphate from aqueous solutions, with the best performing MOF from this family using an amino-substituted terephthalic acid as linker ($\text{NH}_2\text{-MIL-101 (Fe)}$).^[121] Additionally, $\text{NH}_2\text{-MIL-88 B(Fe)}$, a flexible counterpart of the aminoterephthalate MOF family of $\text{NH}_2\text{-MIL-101 (Fe)}$, was synthesised as some reports have stated it to be the more thermodynamically stable MOF. In order to also expand towards oil-in-water applications, also MIL-126 (Fe), substituting the aminoterephthalate linker with a larger bipyridine dicarboxylate linker to accommodate the larger hydrocarbons, was synthesised as well.

To find an optimal synthesis procedure for the MOFs, three different approaches were tested: a classical synthesis approach at room pressure, a solvothermal approach using sealed PTFE lined reactors,^{[71][121]} and a microwave assisted approach, which has shown some very short reaction times and high yields in literature.^{[122][123]} In the end, the solvothermal approach resulted in the most crystalline MOFs. To verify the successful synthesis, powder XRDs of the MOFs were acquired and compared with the simulated diffractograms calculated by Rietveld refinement using their cif files available in literature.^{[71][110]} For the aminoterephthalate MOFs $\text{NH}_2\text{-MIL-88 B(Fe)}$ and $\text{NH}_2\text{-MIL-101 (Fe)}$, diffractograms of the synthesised MOFs showed that the synthesis protocols needed to be adjusted from literature,^[71] as especially for the $\text{NH}_2\text{-MIL-101 (Fe)}$, a mixture of $\text{NH}_2\text{-MIL-101 (Fe)}$ and $\text{NH}_2\text{-MIL-88 B(Fe)}$ was obtained. In Figure 5.1, powder diffractograms of the MOFs prepared with their optimised synthesis protocol and their respective Rietveld refined simulated diffractograms are shown, showing good accordance with literature.^{[71][110]} In Figure 5.2, SEM images of $\text{NH}_2\text{-MIL-88 B(Fe)}$ crystals are displayed,

showing the crystallinity of the synthesised material.

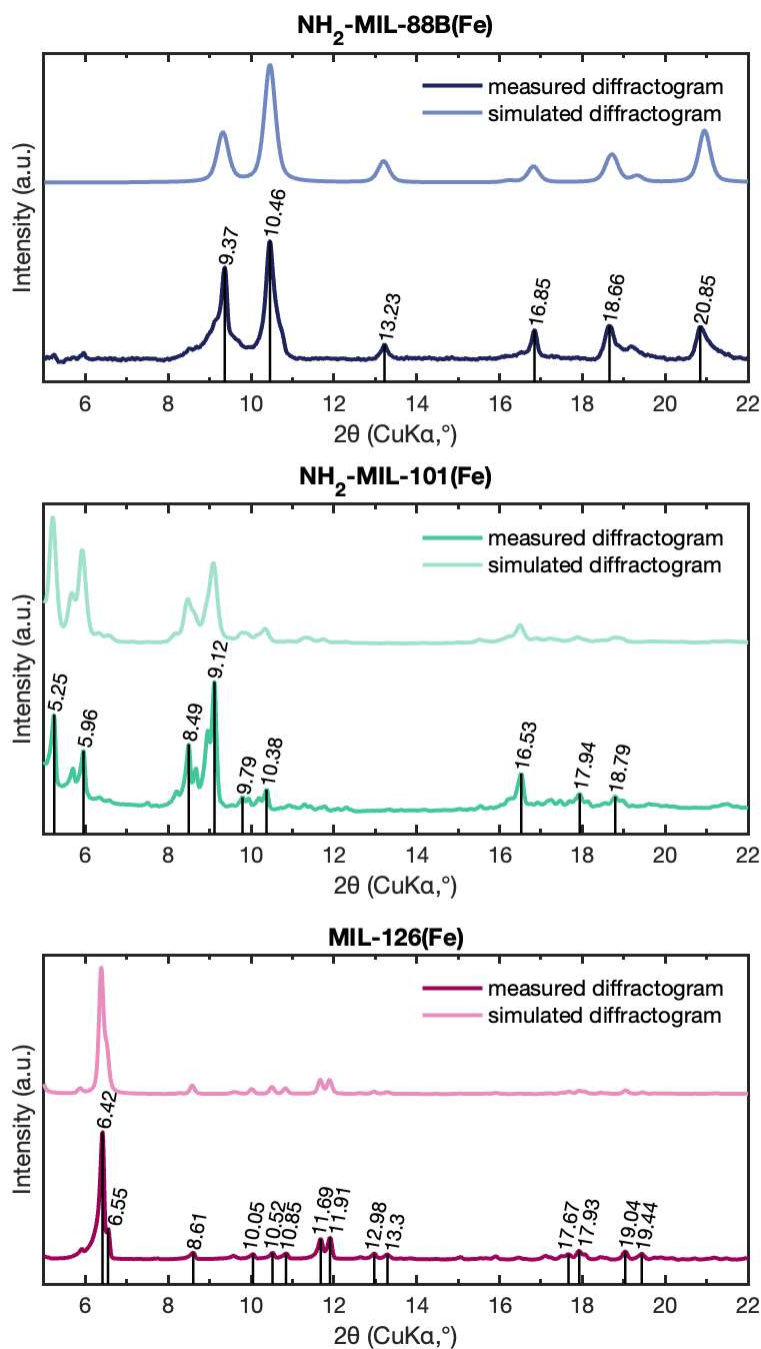


Figure 5.1.: Measured and Rietveld refined diffractograms of NH₂-MIL-88 B(Fe) (top), NH₂-MIL-101 (Fe) (middle), and MIL-126 (Fe) (bottom).

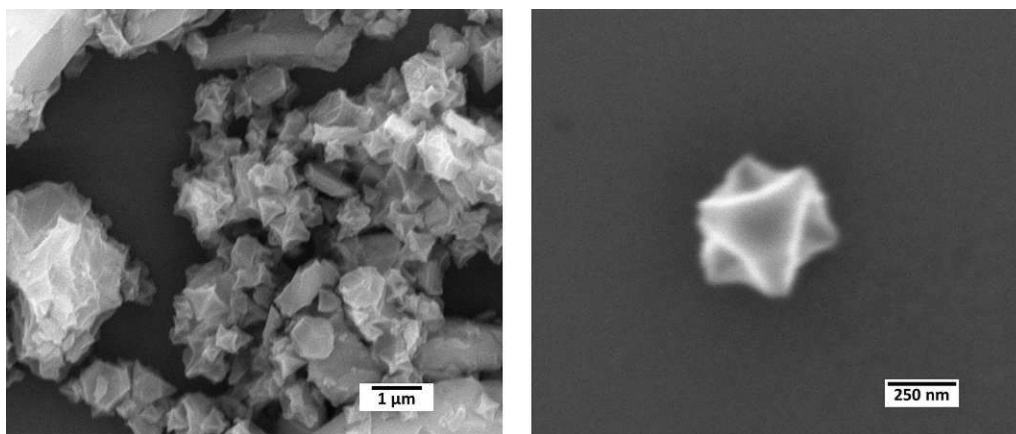


Figure 5.2.: Scanning electron microscopy images of isolated $\text{NH}_2\text{-MIL-88B(Fe)}$ crystals with magnifications of 30,000x (left) and 160,000x (right). Graphic reproduced from the electronic supporting information of Publication I^[69] under the CC-BY 4.0 license

5.2. Post-Synthetic Modification of Metal-Organic Frameworks

Another method explored to potentially improve the sensitivity of MOFs towards certain analytes was post-synthetic modification. One possible application here was the introduction of chiral groups such as amino acids to move towards chiral sensitive adsorption of guest molecules. Here, solid phase peptide synthesis,^[124] a method known from peptide chemistry was used. Usually, the amide coupling works in two steps: First, the amide bond between the free amino group of the peptide (or in the case of iron aminoterephthalate MOFs the free amino group of the linker) and the carboxy group of the amino acid (whose amino group is protected to stop cross-reactions) is formed. Then, the protective group is removed to reveal the free amino group that can be used for the coupling of the next amino acid. In Figure 5.3-left, IR spectra of all stages are displayed, showing the successful conversion by the growth of the amide bands at 1682 cm^{-1} and 1524 cm^{-1} as well as the removal of the Boc protection group at 1624 cm^{-1} . In the thermogravimetric analysis (TGA) curves in Figure 5.3-right, the thermolability of the Boc protection group can be clearly seen by the first onset at $150\text{ }^\circ\text{C}$, while the inclusion of an amino acid seems to shift the first onset of the modified $\text{Fe}(\text{NH}_2\text{BDC})$ from $250\text{ }^\circ\text{C}$ to $280\text{ }^\circ\text{C}$.

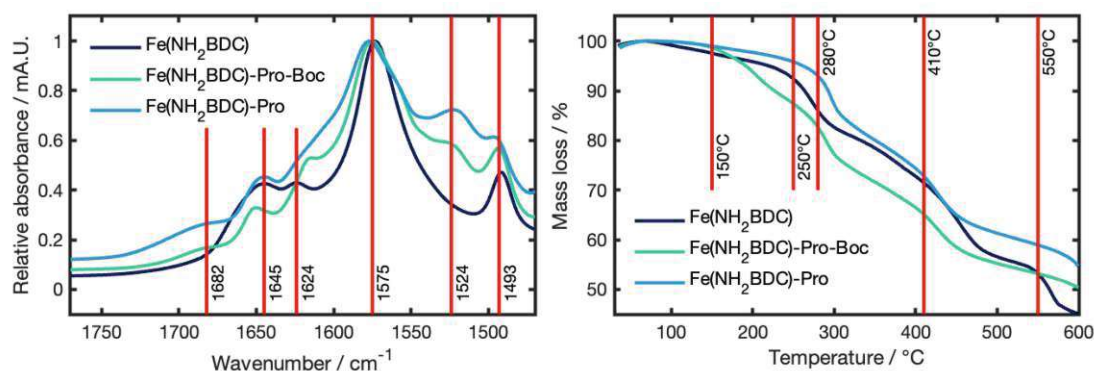


Figure 5.3.: Left: IR spectra of the Amide region for a unmodified Fe(NH₂BDC) (navy), a modified Fe(NH₂BDC) before protective group removal (green), and a modified Fe(NH₂BDC) after protective group removal (blue). Right: TGA curves of the same MOFs, onsets marked with red lines.

Looking at the mass loss in the first step of the thermal decomposition (i.e. the removal of the Boc group), the yield of the PSM reaction (i.e. the percentage of modified amino groups in the linkers) can be estimated. As the difference between the masses of the unprotected and protected modified MOF (reference mass was not taken from before onset to account for the desorption of residual solvents) was 6.2% (see Figure 5.4), one can use the molar masses of the pure components ($M(\text{Fe}(\text{NH}_2\text{BDC}))=720.92 \text{ g mol}^{-1}$, $M(\text{Boc-Pro})=215.25 \text{ g mol}^{-1}$, $M(\text{Boc})=100.12 \text{ g mol}^{-1}$) and the amount of NH₂ groups per molar mass unit of the MOF (i.e. 3) to come up with the following equation (5.1). Entering the values for the mass losses and molar masses into the equation leads to a yield of 17.2% for the PSM reaction.

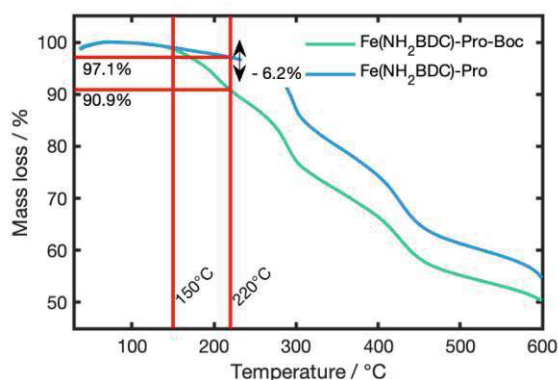


Figure 5.4.: TGA curves of the modified MOFs focusing on the first decomposition step.

$$\%(\text{NH}_2\text{-Pro}) = \frac{M(\text{MOF}) \cdot \%(\Delta m)}{3(M(\text{Boc}) - \%(\Delta m)) \cdot M(\text{Boc-Pro})} \quad (5.1)$$

5.3. Preparation of an Enrichment Film for Phosphates in Water

For sensing applications using an adsorptive material on an IR probe (IREs, ATR fibres, PICs), a well-defined enrichment film is important to guarantee reproducible measurements. However, the deposition of well-defined MOF layers onto substrates is challenging and limited to a selected few classes of MOFs, an alternative strategy was devised that encompassed the use of a suspension of small MOF crystals for spin coating in IPA, leading to a layer-like coverage of substrates by MOFs bound by weak interaction forces. After a subsequent activation at elevated temperatures, the coated sensors could be mounted in the FT-IR spectrometer, while after the measurement, the film could easily be wiped off and another film applied to the sensor. By performing a single point calibration with a defined standard before sample measurement, reproducible results could be achieved. In Publication I, this concept was applied for phosphate sensing in water, showing similar enrichment performances as mesoporous oxides and sub-mg L⁻¹ LODs, with a reproducibility of 94 %.

5.4. Enrichment of Hydrocarbons from the Aqueous Phase

To study the adsorption behaviour of organic contaminants, six different concentrations between 25 and 766 mg L⁻¹ of benzonitrile as a model substance in water were applied to a layer-like film of MIL-126(Fe) coated onto a Si IRE. Sampling was performed by a continuous flow of the analyte using a peristaltic pump. To determine the optimal time for sampling, adsorption/desorption cycles were performed, with 1 min of time for each step. In Figure 5.5, an exemplary cycle for a full calibration run is shown. Looking at the data in this run, the fast response of adsorption-based enrichment can be seen, as full adsorption and desorption respectively is done in less than a minute, and a faster response than the one with the mesoporous titania was obtained.

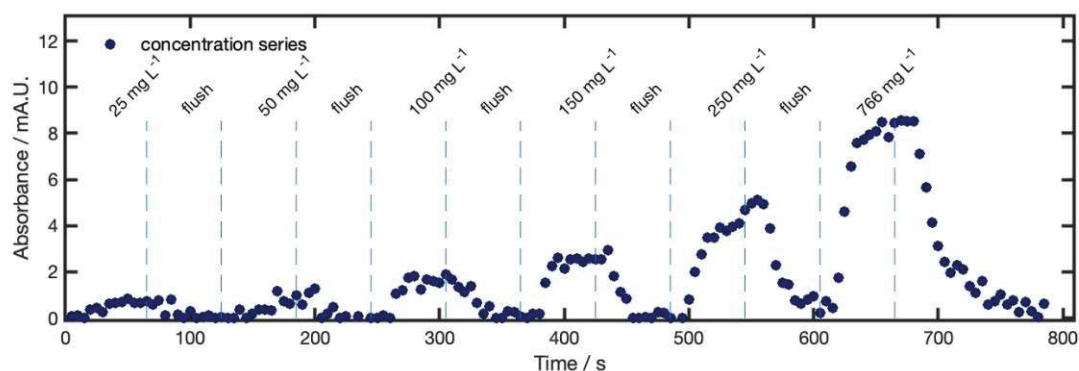


Figure 5.5.: Full calibration run of the BN adsorption in MIL-126(Fe).

In the same manner as for the mesoporous oxides, the equilibrium signal for each concentration was determined for each benzonitrile solution using the signal of three independent sampling runs. As already mentioned in chapter 5.3, a new film was applied for each measurement run. In Table 5.1, the adsorption data collected for benzonitrile is displayed. In this table, A stands for the averaged band heights for equilibrium adsorption, which are shown together with the standard deviation of the three samples. Once again, the adsorption data was described with the Freundlich model to obtain a calibration curve. For that, the averaged band heights were fitted using the Freundlich equation (2.30) and the fitting parameters q_e and K_F shown in Table 5.1 as well as the error of the fit χ_F^2 were received. The fit (with 95% confidence intervals of the fit function) can also be seen in Figure 5.6 together with exemplary spectra of the nitrile band of different concentrations of benzonitrile.

Describing the sensitivity in the same manner as for the mesoporous oxides, the LOD can be calculated using the same equation (4.3). Considering a higher noise floor (which can probably be attributed to fluctuations caused by the MOF) of 3.05×10^{-4} , a LOD of 18.0 mg L^{-1} can be calculated. As for the enrichment factor, an accurate estimation cannot be made due to the irregular coating, making it impossible to calculate $d_{e, \text{film}}$. However, comparing the noise floors and the LODs of the enrichments in mesoporous titania films and MIL-126, respectively, the enrichment factors can be estimated to be around 6 times lower for MIL-126 compared to the mesoporous titania.

Table 5.1.: Adsorption data collected for BN on MIL-126(Fe) for equilibrium sampling. Band heights are averaged for 3 independent samples. Fits were performed for the averaged band heights.

| $c / \text{mg L}^{-1}$ | $A / \text{A.U.}$ |
|--|---------------------------------------|
| 25 | $8.90\text{E-}04 \pm 3.02\text{E-}04$ |
| 50 | $1.63\text{E-}03 \pm 5.03\text{E-}04$ |
| 100 | $2.54\text{E-}03 \pm 6.47\text{E-}04$ |
| 150 | $3.49\text{E-}03 \pm 8.51\text{E-}04$ |
| 250 | $5.14\text{E-}03 \pm 9.58\text{E-}04$ |
| 766 | $9.53\text{E-}03 \pm 1.02\text{E-}03$ |
| $K_F / \text{A.U.cm}^{-1}[\text{L mg}^{-1}]^{1/n}$ | 1.48E-4 |
| n_F | 1.590 |
| χ_F^2 | 9.24E-05 |

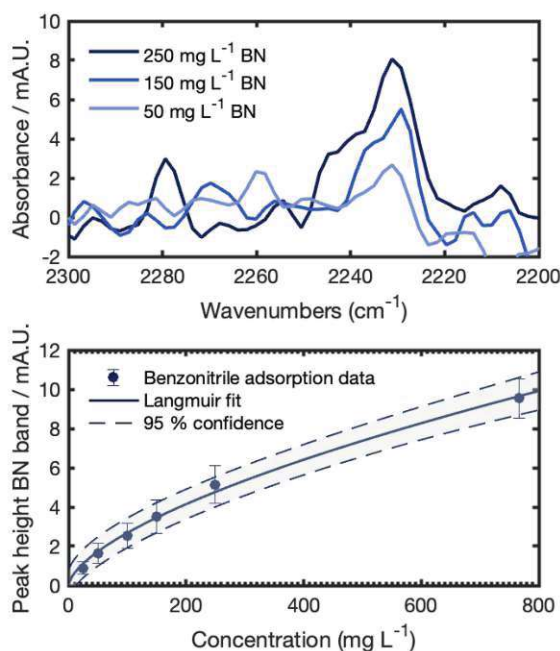


Figure 5.6.: Top: Exemplary spectra of different concentrations of adsorbed benzonitrile. The background spectrum was recorded of deionised water on the MIL-126(Fe). Bottom: Freundlich fit for the data set received for benzonitrile with 95 % confidence interval of the fit function represented by the grey area. Error bars show standard deviations for 3 independent measurements.

Part VI.

**Surface-Enhanced Raman
Scattering for Simulating Corrosion
Inhibition**

Introduction

This part serves as an introduction to the research on surface-enhanced Raman scattering for studying the interactions between metal surfaces and cationic surfactants, which resulted in Publication IV.^[102] The focus of this part is laid on the preliminary research leading to the published results and a basic description of the results. For more detailed results of the publication, the reader is guided to the Appendix.

6.1. Preliminary Results for Surface-Enhanced Raman Scattering of Surfactants

Usually, the strategy to set up a SERS system is to find nanoparticles that share an extinction maximum with the excitation wavelength of the Raman laser. For AgNPs, the extinction maximum usually is situated around 430 nm,^[125] making blue lasers optimal, while AuNPs show an extinction maximum around 520 nm,^[126] encouraging the use of green lasers. However, the active component in the corrosion inhibitor studied in this thesis was a benzalkonium chloride (BAC-16) that is prone to fluorescence interference due to the presence of the benzyl group near the active centre. Therefore, a 785 nm laser needed to be used, which does not overlap with any LSPR region of neither AuNPs nor AgNPs, making direct sensing measurements not really feasible. However, the presence of surfactants in a nanoparticle emulsion usually influences the aggregation behaviour of the nanoparticles. This, as a consequence, changes the scattering properties of the emulsion as described in Mie theory. As the extinction maximum and, thus, the LSPR of the nanoparticles strongly depend on the size of the scattering centre, this aggregation behaviour can be used to study the interaction of the particles with the surfactants.

To better control the amount of particles, the in-situ synthesis method proposed by Leopold and Lendl was used.^[48] Although AuNPs have an inherently higher extinction maximum, the scalability and easy handling of the AgNP synthesis outweighed the advantage of the better fit with the excitation wavelength. The pristine AgNPs synthesised had a median particle radius of 53 nm and an extinction maximum of 430 nm.^[102]

In order to be independent from the concentration of BAC-16, different surfactant/AgNP ratios were measured. In Figure 6.1, these preliminary results are shown. The SERS signal here describes the height of the overlapping aromatic C-H in plane deformation of the benzyl group and C-N deformation of the quaternary amine at 1003 cm^{-1} , referenced to the height of the sapphire band of the Raman probe.

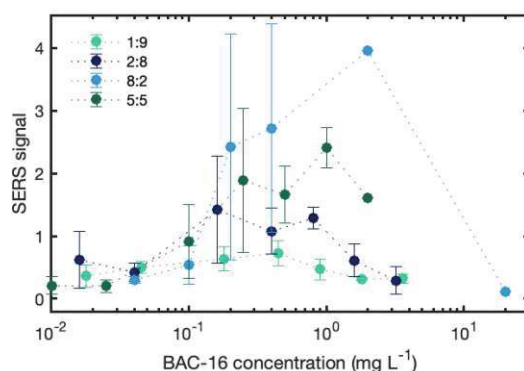


Figure 6.1.: Unscaled results of the SERS measurements.

Looking at the dependence of the SERS signal on the BAC-16 concentrations in Figure 6.1, two points could be made out. First, by referencing the BAC-16 concentration with the surfactant/AgNP ratios and standardising the heights, the results for all ratios were comparable. Building on that, an estimation for the number of BAC-16 molecules in suspension was made and used for further referencing. The second point was that the results seemed unintuitive from a classical standpoint, as the SERS signal usually increases at higher analyte concentrations. However, the nature of measurement system being dependent not only on the analyte concentration but also on the surface enhancement made it possible to correlate the SERS results with additional methods to show the aggregation of the AgNPs induced by the interaction with BAC-16. By designing a flow cell to accommodate the Raman probe in the sample compartment of a UV-VIS spectrometer, a nearly concurrent measurement of the extinction spectrum was possible, which could be used both to show the aggregation-induced shift of the extinction maximum and also as an in-built quality control tool for the synthesised AgNPs. To finally correlate the shift of the extinction maximum and the surface enhancement to aggregation, ex-situ DLS experiments were performed. By doing this, a comprehensive picture of the interactions of AgNPs with surfactants could be shown, which can serve as model particle system to better describe film forming corrosion inhibition.

Additionally, these insights were employed to develop a sensing protocol for BAC-16 in aqueous solutions. This involved utilising the particle shielding at elevated BAC-16 concentrations for the SERS quenching of a methylene blue tracer. The indirect protocol enabled the quantification of BAC-16 in a wide concentration range by modifying the ratio of sample to water in the assay.

Part VII.

Ultrasound Particle Manipulation for the Imaging of Suspended Solids in Water Treatment

Introduction

This part serves as an introduction to the research on ultrasound particle manipulation, which resulted in Publication VI. The focus of this part is laid on the preliminary research leading to the published results. For more detailed descriptions of the results of the publication, the reader is guided to the Appendix.

7.1. Optimisation of the Ultrasound Flow Cell

Going from the original design of the flow cell (Figure 3.5), the cell was adapted slightly going through the testing stages:

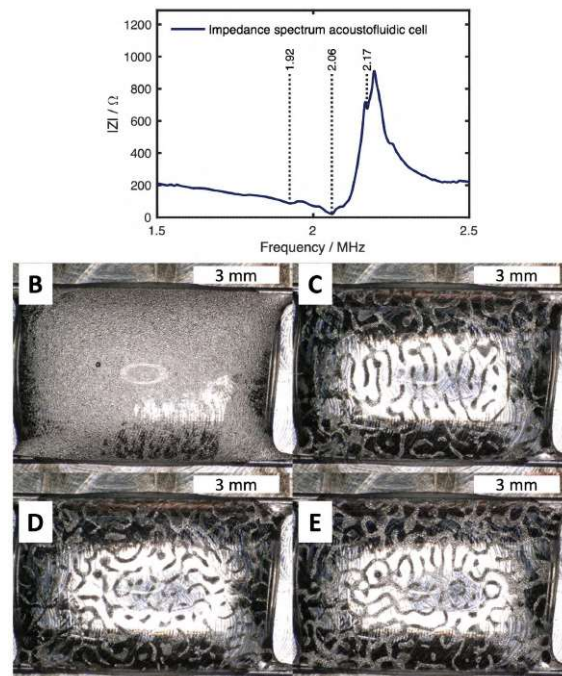


Figure 7.1.: A: Impedance spectrum of the acoustofluidic cell. B-E: Acoustofluidic cell with starch suspension. B: Cell operated at non-ideal frequency > 2.5 MHz. C: Cell operated at 1.92 MHz. D: Cell operated at 1.92 MHz. E: Cell operated at 1.92 MHz.

In the first stage, the cell was characterised using impedance spectroscopy in order to find the optimal operation frequency. As can be seen in Figure 7.1-A, three local minima at 1.92 MHz, 2.06 MHz, and 2.17 MHz can be found in the impedance spectrum between 1.8 and 2.2 MHz (the minima beyond that were not considered, as the frequency normally only varies by a few kHz compared to the calculated value). Using these frequencies, the operation of the acoustofluidic cell was tested using a suspension of starch particles in

water. In Figure 7.1-B, operation at a non-ideal frequency is demonstrated, where some movement of the particles but no complete pattern formation can be observed. In all relative minima shown in Figure 7.1-C,D,E, the particles are being clearly reorientated by the ultrasound field.

In the next stage, the cell was mounted below a Keyence digital microscope with a moderately strong light source. For this setup, no external cooling was necessary as the thermal input of the light source did not impair the particle manipulation. With this setup, the working principle of the US manipulation module could be proven. From now on, the cell was operated at 2.06 MHz, which showed the most stable performance when guiding particles. In Figure 7.2, a photo of the working principle is shown. Looking at the distances separating each nodal plane, it can be seen that the values are all situated around the target value of 375 μm , with a mean of 373.6 μm , proving the fact that the particles can be pushed into the nodal planes reliably. Additionally, the relatively large fluctuation did not matter due to the targeted particle being between 10 and 50 μm .

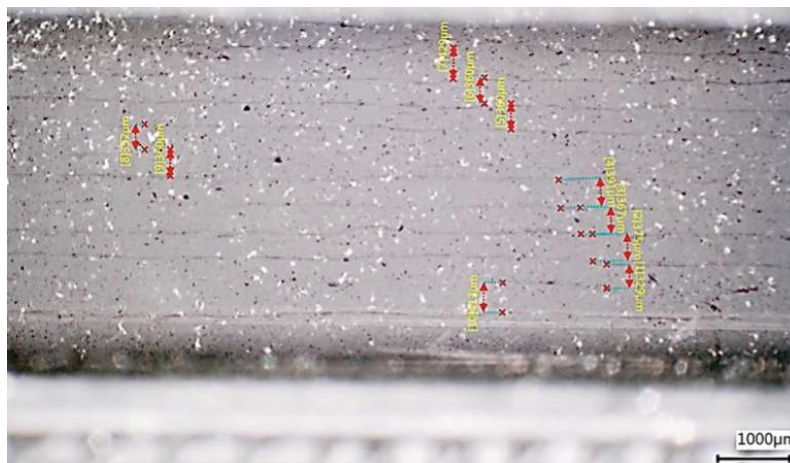


Figure 7.2.: Acoustofluidic cell with guided 10 μm PS beads. Photos shot with the Keyence Digital microscope, digital measurements performed with the Keyence software.

As the resolution was not sufficient to resolve the particles in the flow both temporally and spatially for this imaging solution, a bright light source and fast spectrograph was needed which were developed by **Thomas Arnold** and **Martin de Biasio** at Silicon Austria Labs in Villach, Austria. This, however, led to new challenges, as the increased brightness of the light source resulted in a significant thermal input. Additionally, the higher magnification required a shorter distance of the imaging camera and the flow cell, necessitating a new design including temperature stabilisation and a thinner window.

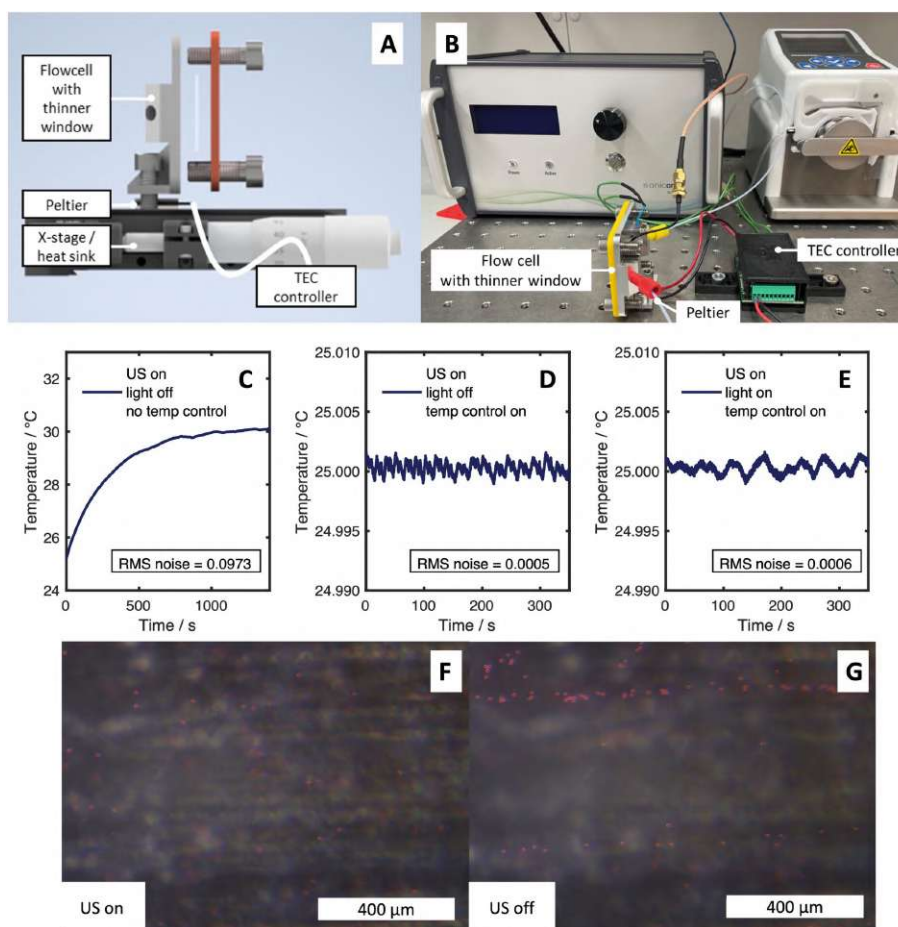


Figure 7.3.: A: Rendered image of the upgraded setup for the US manipulation. B: Upgraded setup for the US manipulation mounted on a breadboard. C: Temperature curve of the setup with turned on US manipulation without the optimised light source. D: Temperature curve of the temperature stabilised setup with turned on US manipulation without the optimised light source. E: Temperature curve of the temperature stabilised setup with turned on US manipulation with the optimised light source turned on. F: Image of the flow cell with 10 μm polystyrene beads without active particle manipulation. G: Image of the flow cell with 10 μm polystyrene beads with active particle manipulation.

In Figure 7.3-A,B, these upgrades are shown, with the temperature control being done thermoelectrically using a TEC-1091 controller (Meerstetter, Switzerland) and a suitable peltier element. First experiments even without temperature control (temperature graph shown in Figure 7.3-C) showed some promising results concerning the resolution of the particles (Figure 7.3-F,G), although the stability of the particle manipulation sharply decreased over time. Adding the temperature stabilisation (temperature graphs for the flow cell with active particle manipulation with and with the light source on are shown in Fig-

ure 7.3-D,E) improved the long-term performance greatly while still delivering the same results. This setup was then delivered to our project partners from Silicon Austria Labs, who fully integrated the cell into the prototype that was used for the pilot testing within the HYDROPTICS research project.

8. Conclusions and Outlook

The research presented in this thesis has been conducted and developed out of the research goals of the European Union H2020 project HYDROPTICS. In this interdisciplinary research project, a platform was developed to improve on-line analysis tools for monitoring a produced water treatment process in the petrochemical industry. The work was split into the development of a particle analyser and an on-line oil-in-water analyser. Beyond this, novel technologies were researched within the scope of the project to also measure other key parameters such as the oil-in-water content as well as the concentration of corrosion inhibitors.

In this thesis, nanoscale materials (mesoporous oxides, metal-organic frameworks, and nanoparticles) were used to improve the sensitivity of vibrational spectroscopic techniques. This led to the following key results connected to the HYDROPTICS project:

- Advances in the use of mesoporous oxides for trace sensing of contaminants in the liquid phase:

In the research leading to Publication V, a workflow for the deposition of mesoporous titania layers for the use in adsorption-enhanced attenuated total reflection mid-infrared spectroscopy was established. The use of mesoporous titania led to an increase in IR transparency compared to other sensing materials such as mesoporous silica. This could be exploited to enrich (organic and inorganic) phosphate species out of aqueous solutions, studying the adsorption thermodynamics and kinetics and also showing their potential for sensing applications. Beyond the results presented in publication V, a method for the functionalisation of the mesoporous titania surfaces was developed and demonstrated for the enrichment of benzonitrile out of aqueous solutions.

- A method for the trace analysis of phosphates in water using metal-organic frameworks:

In the research leading to Publication I, a workflow for the deposition of single-use enrichment layers based on $\text{NH}_2\text{-MIL-88 B(Fe)}$ was established and combined with an automated flow system to measure aqueous phosphate solutions. An internal referencing to compensate for variation in MOF film depositions made it possible to

increase the reproducibility of phosphate analysis from 74% to 94%. This resulted in sensitive measurements with an LOD of 0.18 mg L^{-1} phosphorus in water.

This also laid the groundwork for using infrared spectroscopy as a tool to quickly study the adsorption capabilities of metal-organic frameworks, as demonstrated for the adsorption of benzonitrile in aqueous solutions into MIL-126(Fe).

- An in-situ study of the interactions between metal surfaces and corrosion inhibitors: In the research leading to Publication IV, the interactions of benzalkonium chloride (which is used as an active ingredient in corrosion inhibitors) and silver nanoparticles (which have a similar surface charge as stainless steel) were studied using surface-enhanced Raman spectroscopy. For that, a flow cell was developed to allow nearly concurrent probing by Raman spectroscopy and VIS spectroscopy. Using these two complimentary techniques and ex-situ particle analysis, it was possible to show the threshold concentration for bilayer formation of the corrosion inhibitor on the surface of the nanoparticles breaking up the aggregates formed at lower corrosion inhibitor concentrations.
- The development of a liquid handling system for the use in the particle analyser: In the research leading to Publication VI, a liquid handling system including was optimised to be integrated into the particle analyser. Using temperature stabilisation, the thermal load of the strong light source needed to perform microparticle imaging could be compensated. Optimisation of the ultrasound particle manipulation also made it possible to direct all particles into the focal plane of the imaging spectrograph, increasing the optical contrast of the imaging.

Building on the advances in mesoporous material technology, a second project could be performed in the scope of the H2020 project ACTPHAST4R, a platform enabling young researchers to have access to novel photonic technologies. This project enabled my stay at imec/UGent and the fabrication of new photonic integrated circuits designed for the use as evanescent field waveguide sensors in the mid-IR developed in an earlier H2020 project for new applications. The work with these photonic integrated circuits led to the following key results connected to the ACTPHAST4R project:

- Demonstration of the alignment tolerances of the photonic integrated circuits: In the research leading to Publication III, the alignment tolerances of mid-IR germanium-on-silicon PICs employing monolithically integrated microlenses were studied in axial and horizontal directions. It could be demonstrated that the use of microlenses improved the 1 dB alignment tolerances by a factor of 5 while also stabilising the transmission spectra for the full PICs.

- Photonic integrated circuits as tools for multi-gas contaminant sensing:

In the research leading to Publication II, the PICs were coated with functionalised mesoporous silica and combined with a state-of-the-art mid-IR laser spectrometer to show the capabilities of the concept for multi-gas VOC sensing. The sensing capabilities were demonstrated using a mixture of three aromatic volatile organic contaminants, whose spectra were deconvoluted using chemometric tools, revealing sub-ppmv LODs and enrichment factors up to 20,000.

Building on the research performed in this thesis, several interesting fields can be pursued for follow-up research, further advancing the developed technologies.

For instance, further developments of the titania layers to receive crystalline titania is a promising way of studying photocatalytic processes using mid-IR spectroscopy: Further, the enrichment film technology can be expanded as a tool for high-throughput evaluation of the adsorption potential of MOFs towards different contaminants, gathering not only raw information of the adsorbed material quantity, but also collecting in-situ chemical information of the adsorption processes. Finally, the high effective pathlength of the mid-IR PICs compared to IREs of the same dimensions offers an intriguing possibility to increase the sensitivity of evanescent field sensing. Here, two possible directions can be pursued, one being the improvement of the waveguide design to move towards lower-noise measurements, while new surface functionalisations can be used to open up the concept towards a more diverse field of potential analytes.

List of Figures

| | |
|---|----|
| 2.1. Left: Correlation of simple molecule symmetry with their degrees of freedom (DOF) and the corresponding modes. Right: Harmonic (light blue) and Morse (dark blue) potential functions, describing vibrational energy levels of molecules. All vibrational modes are referenced to the vibrational ground state ($n=0$) with modes with a $\Delta n=1$ referring to the fundamental modes and modes with $\Delta n>1$ referring to the overtones. | 9 |
| 2.2. Mid-IR absorbance spectra of water vapour (left) and condensed water (right), respectively. | 11 |
| 2.3. Calculated black body radiation spectra for three different temperatures (3000 K, 4000 K, and 5000 K). The mid-IR range is marked in light red, and the fingerprint region marked in dark red. | 13 |
| 2.4. Left: Light wave functions for three different wavelengths, centred at the point of zero retardation. Right: Interferogram for these three wavelengths. | 14 |
| 2.5. Left: Three different mid-IR sources, a thermal IR source (globar, top), a DFB-QCL (middle), and an EC-QCL (bottom). Right: Two different technologies of mid-IR spectrometers: An FT-IR spectrometer (top, schematically shown for a Michelson interferometer), and a QCL spectrometer (bottom). | 15 |
| 2.6. Interaction of a light beam on the boundary of two dielectric media with different refractive indices ($n_1 > n_2$): refraction (left, for $\theta < \theta_c$), critical refraction (middle, for $\theta = \theta_c$), and total reflection (right, for $\theta > \theta_c$). | 16 |
| 2.7. Schematic depiction of the differences between transmission probing in infrared spectroscopy and attenuated total reflection probing (in the case of single and multi-bounce internal reflection elements). | 18 |

| | |
|---|----|
| 2.8. Schematic description of waveguide technology and terminology for the photonic integrated circuits applied in this thesis: A: Basic concept of rib waveguides with a high index waveguide material grown on a substrate and surrounded by the cladding, which are both lower index materials. B-C: Example of a rib (B) and trenched rib (C) waveguide geometry. D-E: Schematic depiction of two different interfacing strategies, butt (or edge) coupling (D) and grating (or vertical) coupling (E). | 20 |
| 2.9. Relevant potential functions for Raman scattering (left) and fluorescence (right). The different colours refer to the red (Stokes) and blue (anti-Stokes) shifts of the scattered (left) or emitted light (right). | 21 |
| 2.10. Schematic depiction of the symmetric and asymmetric stretching vibrations of carbon dioxide in regard to their change in polarisability and dipole moment. | 23 |
| 2.11. Schematic depiction of a dispersive Raman spectrometer. | 24 |
| 2.12. Schematic depiction of a Raman fibre probe for inline process monitoring. Light is emitted from an excitation fibre, while the backscattered light is collected by an array of collection fibres. | 25 |
| 2.13. A: Regular Raman scattering for a sample molecule. B: Surface enhanced Raman scattering for a sample molecule adsorbed on a spherical particle. C: Surface enhanced Raman scattering for a sample molecule adsorbed on a roughened particle. D: Surface enhanced Raman scattering for a sample molecule adsorbed in the hotspot between two roughened particles. | 26 |
| 2.14. Schematic depiction of the post-synthetic modification of mesoporous oxides. | 29 |
| 2.15. Schematic depiction of an evaporation-induced self-assembly process for the synthesis of mesoporous materials. A: General process: Micellar surfactant structure forming in the same solution as the hydrolysis reaction of the sol-gel mixture. B: Phase diagram for surfactants in water. Isotherm marked in red, the phases in the spin-coating scheme reference to the concentration dependant phases shown in the phase diagram. C: Spin-coating of a precursor solution, evaporation of solvent leads to self-assembly of the surfactant templates. | 31 |
| 2.16. Schematic depiction of MOF structures. Graphic reproduced in part from Publication I ^[69] under the CC-BY 4.0 license. | 32 |
| 2.17. Schematic depiction of the Langmuir and Freundlich isotherms. | 36 |
| 2.18. Schematic depiction of capillary condensation in porous materials. The adsorbant concentration increases from left to right. | 39 |

| | |
|---|----|
| 2.19. Schematical depiction of the six adsorption isotherm types as classified by IUPAC. ^[96] The x-axis always corresponds to the adsorbant concentration, while the y-axis corresponds to the amount of adsorbed material. | 40 |
| 2.20. Formation of a standing wave (black) in an acoustic resonator as superposition of incident (red) and reflected (blue) waves. | 41 |
| 3.1. Comparison of the single channel spectrum for IREs made out of three different materials (Ge, Diamond, Si). | 45 |
| 3.2. Left: Schematic depiction of the measurement setup used for combining the QCL spectrometer and the waveguide. Right: Picture of the cage setup. . . | 47 |
| 3.3. Left: Schematic depiction of the measurement setup with three axis control (WG = waveguide, FL = focusing lens, PM = parabolic mirror, M = mirror). Right: Picture of the actual setup, beam path marked in red. Graphic reproduced from Publication III ^[100] under the CC-BY 4.0 license. | 48 |
| 3.4. Schematic depiction of the measurement setup accommodating the Raman probe used for SERS inside the sample compartment of the UV-Vis spectrometer. Graphic reproduced from Publication IV ^[102] under the CC-BY 3.0 license | 49 |
| 3.5. A: Schematic of the ultrasound enhanced particle imaging system. B: Design of the acoustofluidic flow cell. | 51 |
| 3.6. Setup for acoustofluidic cell prototype testing: Keyence PC (A), Ultrasound driver (B), peristaltic pump (C), magnetic stirrer with particle suspension (D), Keyence digital microscope (E), acoustofluidic cell (F). | 53 |
| 3.7. Schematic depiction of the automated sequential injection analysis system used for the measurement of phosphates with MOF covered IREs. Graphic reproduced from Publication I ^[69] under the CC-BY 4.0 license. | 54 |
| 3.8. Comparison of the calibration functions of phosphate solutions applying one pulse (300 μL , left) and two pulses (2x300 μL , right) using the same flow cell setup. Graphic reproduced from Publication I ^[69] under the CC-BY 4.0 license. 55 | 55 |
| 3.9. SIA sequence for a sample automated sensor experiment with a standard concentration of 10 mg L^{-1} and a sample concentration of 25 mg L^{-1} . A phosphate concentration of 0 mg L^{-1} at a positive flow rate signifies flushing the flow cell with deionised water. The timing of background measurements is denoted by asterisks. Graphic reproduced from Publication I ^[69] under the CC-BY 4.0 license | 55 |
| 3.10. Schematic depiction of the gas sampling system used for the VOC sensing with functionalised silica coated PICs. | 56 |

| | | |
|------|--|----|
| 4.1. | Left: SA-XRD of the first intact layer with ordered mesoporosity (synthesised with R7). Middle: SA-XRD of the layer after optimisation of synthesis and heat treatment (synthesised with R8). Right: SA-XRD of the pyrolysed layer after optimisation of synthesis and heat treatment (synthesised with R8). | 67 |
| 4.2. | Dependence of the pyrolysis temperature on the pore size (approximated by the d-spacing). | 68 |
| 4.3. | Left: Wetting behaviour with water of a pyrolysed unfunctionalised mesoporous titania layer. Right: Wetting behaviour with water of a pyrolysed functionalised mesoporous titania layer. | 68 |
| 4.4. | Comparison of the single channel spectra for a pristine Ge IRE (navy), a Ge IRE coated with a mesoporous TiO ₂ layer (green), and a Ge IRE coated with a functionalised mesoporous TiO ₂ layer (light blue). | 70 |
| 4.5. | Left: Illustrated calculated values of the effective pathlength in the titania film coated on a Ge IRE depending on the wavelength of the light. Relevant absorbance regions of the analytes marked in different colours. Right: Illustrated calculated values of the effective pathlength in the titania film coated on a Si IRE depending on the wavelength of the light. Relevant absorbance regions of the analytes and the native SiO ₂ passivation layer marked in different colours. | 71 |
| 4.6. | Left: Sample phosphate spectra acquired on a mesoporous TiO ₂ coated Ge IRE with a SiO ₂ protection layer. Right: 100 % line (blue) and single channel spectrum (green) of the mesoporous TiO ₂ coated Ge IRE with a SiO ₂ protection layer. | 73 |
| 4.7. | Adsorption/desorption cycle for benzonitrile in a phenyl functionalised mesoporous titania layer. Blue dashed lines show 10 % and 90 % of the band area of the equilibrium concentration of adsorbed benzonitrile. | 74 |
| 4.8. | Top: Exemplary spectra of different concentrations of adsorbed benzonitrile. The background spectrum was recorded of deionised water on the mesoporous film. Bottom: Freundlich fit for the data set received for benzonitrile with 95 % confidence interval of the fit function represented by the grey area. Error bars show standard deviations for 4 independent measurements. | 75 |
| 5.1. | Measured and Rietveld refined diffractograms of NH ₂ -MIL-88 B(Fe) (top), NH ₂ -MIL-101 (Fe) (middle), and MIL-126 (Fe) (bottom). | 79 |

| | | |
|------|--|----|
| 5.2. | Scanning electron microscopy images of isolated $\text{NH}_2\text{-MIL-88 B(Fe)}$ crystals with magnifications of 30,000x (left) and 160,000x (right). Graphic reproduced from the electronic supporting information of Publication I ^[69] under the CC-BY 4.0 license | 80 |
| 5.3. | Left: IR spectra of the Amide region for a unmodified $\text{Fe(NH}_2\text{BDC)}$ (navy), a modified $\text{Fe(NH}_2\text{BDC)}$ before protective group removal (green), and a modified $\text{Fe(NH}_2\text{BDC)}$ after protective group removal (blue). Right: TGA curves of the same MOFs, onsets marked with red lines. | 81 |
| 5.4. | TGA curves of the modified MOFs focusing on the first decomposition step. | 81 |
| 5.5. | Full calibration run of the BN adsorption in MIL-126(Fe) | 83 |
| 5.6. | Top: Exemplary spectra of different concentrations of adsorbed benzonitrile. The background spectrum was recorded of deionised water on the MIL-126(Fe) . Bottom: Freundlich fit for the data set received for benzonitrile with 95 % confidence interval of the fit function represented by the grey area. Error bars show standard deviations for 3 independent measurements. | 84 |
| 6.1. | Unscaled results of the SERS measurements. | 87 |
| 7.1. | A: Impedance spectrum of the acoustofluidic cell. B-E: Acoustofluidic cell with starch suspension. B: Cell operated at non-ideal frequency > 2.5 MHz. C: Cell operated at 1.92 MHz. D: Cell operated at 1.92 MHz. E: Cell operated at 1.92 MHz. | 89 |
| 7.2. | Acoustofluidic cell with guided $10\ \mu\text{m}$ PS beads. Photos shot with the Keyence Digital microscope, digital measurements performed with the Keyence software. | 90 |
| 7.3. | A: Rendered image of the upgraded setup for the US manipulation. B: Upgraded setup for the US manipulation mounted on a breadboard. C: Temperature curve of the setup with turned on US manipulation without the optimised light source. D: Temperature curve of the temperature stabilised setup with turned on US manipulation without the optimised light source. E: Temperature curve of the temperature stabilised setup with turned on US manipulation with the optimised light source turned on. F: Image of the flow cell with $10\ \mu\text{m}$ polystyrene beads without active particle manipulation. G: Image of the flow cell with $10\ \mu\text{m}$ polystyrene beads with active particle manipulation. | 91 |

List of Tables

| | |
|---|----|
| 2.1. Different regions of the EM spectrum and the transitions excited by the respective EM waves. | 7 |
| 3.1. Optical properties of the used IREs. 1200-1000 cm^{-1} is relevant for phosphate measurements, 1600-1400 cm^{-1} is relevant for aromatic hydrocarbons, and 2300-2200 cm^{-1} is relevant for nitriles, all of which were analytes in this thesis. | 45 |
| 3.2. Experimental parameters for the Vis-SERS measurements. BAC-16 concentrations refer to the samples before mixing. | 49 |
| 4.1. Recipes for the titania synthesis using TTIP as precursor. | 65 |
| 4.2. Recipes for the titania synthesis using TiEt_5 as precursor. | 66 |
| 4.3. Calculated values for the optical parameters of the used IREs at the relevant wavenumbers for the detecting nitriles (2230 cm^{-1}), aromatic hydrocarbons (1500 cm^{-1}), and phosphates (1100 cm^{-1}). All values are assumed for a titania layer with a thickness of 200 nm and a refractive index of 1.623. . . . | 71 |
| 4.4. Adsorption data collected for BN in mesoporous titania for equilibrium sampling. Band heights are averaged for 4 independent samples. Fits were performed for the averaged band heights. | 74 |
| 5.1. Adsorption data collected for BN on MIL-126(Fe) for equilibrium sampling. Band heights are averaged for 3 independent samples. Fits were performed for the averaged band heights. | 84 |

Bibliography

- [1] P.R. Griffiths and J.A. de Haseth. *Fourier Transform Infrared Spectrometry*. John Wiley & Sons, 2nd edition, 2006.
- [2] P.J. Larkin. *Infrared and Raman Spectroscopy, Principles and Spectral Interpretation*. Elsevier, 2nd edition, 2018.
- [3] G. Socrates. *Infrared and Raman Characteristic Group Frequencies: Tables and Charts*. John Wiley & Sons, 2004.
- [4] P. Bouguer. *Essai D'Optique, Sur La Gradation De La Lumiere*. C. Jombert, 1729.
- [5] J.H. Lambert. *Photometria sive de mensura et gradibus luminis, colorum et umbrae*. Klett, 1760.
- [6] A. Beer. Bestimmung der Absorption des rothen Lichts in farbigen Flüssigkeiten. *Annalen der Physik*, 162(5):78–88, 1852.
- [7] T.G. Mayerhöfer, S. Pahlow, and J. Popp. The Bouguer-Beer-Lambert Law: Shining Light on the Obscure. *ChemPhysChem*, 21(18):2029–2046, 2020.
- [8] T.G. Mayerhöfer and J. Popp. Beer's Law - Why Absorbance Depends (Almost) Linearly on Concentration. *ChemPhysChem*, 20(4):511–515, 2019.
- [9] G. Ramer and B. Lendl. *Attenuated Total Reflection Fourier Transform Infrared Spectroscopy*. John Wiley & Sons, 2013.
- [10] G.A. Reider. *Photonik: eine Einführung in die Grundlagen*. Springer-Verlag, 2013.
- [11] A. de Juan, J. Jaumot, and R. Tauler. Multivariate Curve Resolution (MCR). Solving the mixture analysis problem. *Analytical Methods*, 6(14):4964–4976, 2014.
- [12] A. de Juan, E. Casassas, and R. Tauler. *Soft Modeling of Analytical Data*. John Wiley & Sons, 2006.
- [13] S. Vijayakumar, J. Rowlette, A. Schwaighofer, and B. Lendl. Laser-Based Mid-Infrared Spectroscopy for Monitoring Temperature-Induced Denaturation of Bovine Serum Albumin and De-/Stabilization Effects of Sugars. *Analytical Chemistry*, 95(15):6441–6447, 2023.
- [14] M.R. Alcaráz, A. Schwaighofer, H. Goicoechea, and B. Lendl. Application of MCR-ALS to reveal intermediate conformations in the thermally induced α - β transition of poly-L-lysine

monitored by FT-IR spectroscopy. *Spectrochimica Acta Part A: Molecular and Biomolecular Spectroscopy*, 185:304–309, 2017.

- [15] A. Einstein. Zur Quantentheorie der Strahlung. *Phys. Z.*, 18:121–128, 1917.
- [16] H. Kopfermann and R. Ladenburg. Experimental Proof of 'Negative Dispersion.'. *Nature*, 122(3073):438–439, 1928.
- [17] F.K. Tittel, D. Richter, and A. Fried. *Mid-Infrared Laser Applications in Spectroscopy*, pages 458–529. Springer Berlin Heidelberg, Berlin, Heidelberg, 2003.
- [18] M. Tacke. New developments and applications of tunable IR lead salt lasers. *Infrared Physics & Technology*, 36(1):447–463, 1995.
- [19] I. Zorin, P. Gattinger, A. Ebner, and M. Brandstetter. Advances in mid-infrared spectroscopy enabled by supercontinuum laser sources. *Optics Express*, 30(4):5222–5254, 2022.
- [20] J. Faist, F. Capasso, D.L. Sivco, C. Sirtori, A.L. Hutchinson, and A.Y. Cho. Quantum cascade lasers. *Science*, 264(5158):553–556, 1994.
- [21] A. Dabrowska, S. Lindner, A. Schwaighofer, and B. Lendl. Mid-IR dispersion spectroscopy - A new avenue for liquid phase analysis. *Spectrochimica Acta Part A: Molecular and Biomolecular Spectroscopy*, 286:122014, 2023.
- [22] D.-R. Hermann, G. Ramer, M. Kitzler-Zeiler, and B. Lendl. Quantum Cascade Laser-Based Vibrational Circular Dichroism Augmented by a Balanced Detection Scheme. *Analytical Chemistry*, 94(29):10384–10390, 2022.
- [23] J. Faist, C. Gmachl, F. Capasso, C. Sirtori, D.L. Sivco, J.N. Baillargeon, and A.Y. Cho. Distributed feedback quantum cascade lasers. *Applied Physics Letters*, 70(20):2670–2672, 1997.
- [24] A. Hugi, R. Maulini, and J. Faist. External cavity quantum cascade laser. *Semiconductor Science and Technology*, 25(8):083001, 2010.
- [25] A. Genner, P. Martín-Mateos, H. Moser, and B. Lendl. A Quantum Cascade Laser-Based Multi-Gas Sensor for Ambient Air Monitoring. *Sensors*, 20(7), 2020.
- [26] M. Brandstetter, C. Koch, A. Genner, and B. Lendl. Measures for optimizing pulsed EC-QC laser spectroscopy of liquids and application to multi-analyte blood analysis. In *Proc.SPIE*, volume 8993, page 89931U, 2014.
- [27] C.K. Akhgar, G. Ramer, M. Žbik, A. Trajnerowicz, J. Pawluczyk, A. Schwaighofer, and B. Lendl. The Next Generation of IR Spectroscopy: EC-QCL-Based Mid-IR Transmission Spectroscopy of Proteins with Balanced Detection. *Analytical Chemistry*, 92(14):9901–9907, 2020.
- [28] M. Milosevic. *Internal Reflection and ATR Spectroscopy*. John Wiley & Sons, Inc., 2012.

- [29] T.G. Mayerhöfer and J. Popp. Understanding Advanced Attenuated Total Reflection Correction: The Low Absorbance Assumption. *Applied Spectroscopy*, Online First version, 2024.
- [30] W.N. Hansen. Expanded formulas for attenuated total reflection and the derivation of absorption rules for single and multiple ATR spectrometer cells. *Spectrochimica Acta*, 21(4):815–833, 1965.
- [31] P. Dong, Y.-K. Chen, G.-H. Duan, and D.T. Neilson. Silicon photonic devices and integrated circuits. *Nanophotonics*, 3(4-5):215–228, 2014.
- [32] R. Soref. Mid-infrared photonics in silicon and germanium. *Nature Photonics*, 4(8):495–497, 2010.
- [33] Y. Chen, H. Lin, J. Hu, and M. Li. Heterogeneously Integrated Silicon Photonics for the Mid-Infrared and Spectroscopic Sensing. *ACS Nano*, 8(7):6955–6961, 2014.
- [34] M. Nedeljkovic, J.S. Penades, V. Mittal, G.S. Murugan, A.Z. Khokhar, C. Littlejohns, L.G. Carpenter, C.B.E. Gawith, J.S. Wilkinson, and G.Z. Mashanovich. Germanium-on-silicon waveguides operating at mid-infrared wavelengths up to 8.5 μm . *Optics Express*, 25(22):27431–27441, 2017.
- [35] B. Hinkov, F. Pilat, L. Lux, P.L. Souza, M. David, A. Schwaighofer, D. Ristanić, B. Schwarz, H. Detz, A.M. Andrews, B. Lendl, and G. Strasser. A mid-infrared lab-on-a-chip for dynamic reaction monitoring. *Nature Communications*, 13(1):4753, 2022.
- [36] K. Wieland, M. Masri, J. von Poschinger, T. Brück, and C. Haisch. Non-invasive Raman spectroscopy for time-resolved in-line lipidomics. *RSC Adv.*, 11:28565–28572, 2021.
- [37] D.I. Ellis, R. Eccles, Y. Xu, J. Griffen, H. Muhamadali, P. Matousek, I. Goodall, and R. Goodacre. Through-container, extremely low concentration detection of multiple chemical markers of counterfeit alcohol using a handheld SORS device. *Scientific reports*, 7(1):12082, 2017.
- [38] H. Abramczyk and B. Brozek-Pluska. Raman Imaging in Biochemical and Biomedical Applications. Diagnosis and Treatment of Breast Cancer. *Chemical Reviews*, 113(8):5766–5781, 2013.
- [39] D. Graf, F. Molitor, K. Ensslin, C. Stampfer, A. Jungen, C. Hierold, and L. Wirtz. Raman imaging of graphene. *Solid State Communications*, 143(1):44–46, 2007.
- [40] P.R. Griffiths. *Introduction to the Theory and Instrumentation for Vibrational Spectroscopy*. John Wiley & Sons, 2001.
- [41] I. Latka, S. Dochow, C. Krafft, B. Dietzek, and J. Popp. Fiber optic probes for linear and nonlinear Raman applications - Current trends and future development. *Laser & Photonics Reviews*, 7(5):698–731, 2013.

- [42] Z. Huang, H. Zeng, I. Hamzavi, D.I. McLean, and H. Lui. Rapid near-infrared Raman spectroscopy system for real-time in vivo skin measurements. *Optics letters*, 26(22):1782–1784, 2001.
- [43] A. Mahadevan-Jansen, M.F. Mitchell, N. Ramanujam, U. Utzinger, and R. Richards-Kortum. Development of a fiber optic probe to measure NIR Raman spectra of cervical tissue in vivo. *Photochemistry and photobiology*, 68(3):427–431, 1998.
- [44] M. Fleischmann, P.J. Hendra, and A.J. McQuillan. Raman spectra of pyridine adsorbed at a silver electrode. *Chemical Physics Letters*, 26(2):163–166, 1974.
- [45] D.L. Jeanmaire and R.P. Van Duyne. Surface raman spectroelectrochemistry: Part I. Heterocyclic, aromatic, and aliphatic amines adsorbed on the anodized silver electrode. *Journal of Electroanalytical Chemistry and Interfacial Electrochemistry*, 84(1):1–20, 1977.
- [46] S. Schlücker. Surface-Enhanced Raman Spectroscopy: Concepts and Chemical Applications. *Angewandte Chemie International Edition*, 53(19):4756–4795, 2014.
- [47] E.C. Le Ru, E. Blackie, M. Meyer, and P.G. Etchegoin. Surface Enhanced Raman Scattering Enhancement Factors: A Comprehensive Study. *The Journal of Physical Chemistry C*, 111(37):13794–13803, 2007.
- [48] N. Leopold and B. Lendl. A New Method for Fast Preparation of Highly Surface-Enhanced Raman Scattering (SERS) Active Silver Colloids at Room Temperature by Reduction of Silver Nitrate with Hydroxylamine Hydrochloride. *The Journal of Physical Chemistry B*, 107(24):5723–5727, 2003.
- [49] P.C. Lee and D. Meisel. Adsorption and surface-enhanced Raman of dyes on silver and gold sols. *The Journal of Physical Chemistry*, 86(17):3391–3395, 1982.
- [50] J. Rouquerol, D. Avnir, C.W. Fairbridge, D.H. Everett, J.M. Haynes, N. Pernicone, J.D.F. Ramsay, K.S.W. Sing, and K.K. Unger. Recommendations for the characterization of porous solids (Technical Report). *Pure and Applied Chemistry*, 66(8):1739–1758, 1994.
- [51] T. Konegger, C.-C. Tsai, H. Peterlik, S.E. Creager, and R.K. Bordia. Asymmetric polysilazane-derived ceramic structures with multiscalar porosity for membrane applications. *Microporous and Mesoporous Materials*, 232:196–204, 2016.
- [52] A. Taguchi and F. Schüth. Ordered mesoporous materials in catalysis. *Microporous and Mesoporous Materials*, 77(1):1–45, 2005.
- [53] T. Wagner, S. Haffer, C. Weinberger, D. Klaus, and M. Tiemann. Mesoporous materials as gas sensors. *Chem. Soc. Rev.*, 42:4036–4053, 2013.
- [54] A. Eftekhari. Ordered mesoporous materials for lithium-ion batteries. *Microporous and Mesoporous Materials*, 243:355–369, 2017.

- [55] G.J. de A.A. Soler-Illia, C. Sanchez, B. Lebeau, and J. Patarin. Chemical strategies to design textured materials: from microporous and mesoporous oxides to nanonetworks and hierarchical structures. *Chemical reviews*, 102(11):4093–4138, 2002.
- [56] D. Fattakhova-Rohlfing, A. Zaleska, and T. Bein. Three-dimensional titanium dioxide nanomaterials. *Chem. Rev.*, 114(19):9487–558, 2014.
- [57] O.M. Yaghi, M. J. Kalmutzki, and C.S. Diercks. *Introduction to reticular chemistry*. John Wiley & Sons, 2019.
- [58] X.H. Bu, M.J. Zaworotko, and Z. Zhang, editors. *Metal-organic framework: From Design to Application*. Springer, 2020.
- [59] S. Kaskel, editor. *The Chemistry of Metal-Organic Frameworks Synthesis, Characterization, and Applications*, volume 1. John Wiley & Sons, 2016.
- [60] M. Le Page, R. Beau, and J. Duchene. Porous silica particles containing a crystallized phase and method. US Patent: 3493341A, January 1967.
- [61] D. Zhao, J. Feng, Q. Huo, N. Melosh, G.H. Fredrickson, B.F. Chmelka, and G.D. Stucky. Triblock Copolymer Syntheses of Mesoporous Silica with Periodic 50 to 300 Angstrom Pores. *Science*, 279(5350):548–552, 1998.
- [62] Y. Deng, J. Wei, Z. Sun, and D. Zhao. Large-pore ordered mesoporous materials templated from non-Pluronic amphiphilic block copolymers. *Chem Soc Rev*, 42(9):4054–70, 2013.
- [63] P.C.A. Alberius, K.L. Frindell, R.C. Hayward, E.J. Kramer, G.D. Stucky, and B.F. Chmelka. General Predictive Syntheses of Cubic, Hexagonal, and Lamellar Silica and Titania Mesostructured Thin Films. *Chem. Mater.*, 14(8):3284–3294, 2002.
- [64] W. Stöber, A. Fink, and E. Bohn. Controlled growth of monodisperse silica spheres in the micron size range. *Journal of Colloid and Interface Science*, 26(1):62–69, 1968.
- [65] Z.V. Faustova and Y.G. Slizhov. Effect of solution pH on the surface morphology of sol-gel derived silica gel. *Inorganic Materials*, 53:287–291, 2017.
- [66] W. Zhang, S. Chen, S. Yu, and Y. Yin. Experimental and theoretical investigation of the pH effect on the titania phase transformation during the sol-gel process. *Journal of Crystal Growth*, 308(1):122–129, 2007.
- [67] F. das C.M. da Silva, M.J. dos S. Costa, L.K.R. Da Silva, A.M. Batista, and G.E. da Luz Jr. Functionalization methods of SBA-15 mesoporous molecular sieve: A brief overview. *SN Applied Sciences*, 1(6):654, 2019.
- [68] O.M. Yaghi, G. Li, and H. Li. Selective binding and removal of guests in a microporous metal-organic framework. *Nature*, 378(6558):703–706, 1995.

- [69] F. Frank, B. Baumgartner, and B. Lendl. Metal-organic frameworks combined with mid-infrared spectroscopy for the trace analysis of phosphates in water. *Sens. Actuators B Chem.*, 399:134778, 2024.
- [70] O.M. Yaghi, M. O’Keeffe, N.W. Ockwig, H.K. Chae, M. Eddaoudi, and J. Kim. Reticular synthesis and the design of new materials. *Nature*, 423:705–714, 2003.
- [71] S. Bauer, C. Serre, T. Devic, P. Horcajada, J. Marrot, G. Férey, and N. Stock. High-Throughput Assisted Rationalization of the Formation of Metal Organic Frameworks in the Iron(III) Aminoterephthalate Solvothermal System. *Inorg. Chem.*, 47(17):7568–7576, 2008.
- [72] Y. Dong, T. Hu, M. Pudukudy, H. Su, L. Jiang, S. Shan, and Q. Jia. Influence of microwave-assisted synthesis on the structural and textural properties of mesoporous MIL-101(Fe) and NH₂-MIL-101(Fe) for enhanced tetracycline adsorption. *Materials Chemistry and Physics*, 251, 2020.
- [73] H. Guo, B. Niu, X. Wu, Y. Zhang, and S. Ying. Effective removal of 2,4,6-trinitrophenol over hexagonal metal-organic framework NH₂-MIL-88B(Fe). *Appl. Organometal. Chem.*, 33(1):e4580, 2019.
- [74] M. Mon, R. Bruno, E. Tiburcio, M. Viciano-Chumillas, L.H.G. Kalinke, J. Ferrando-Soria, D. Armentano, and E. Pardo. Multivariate Metal-Organic Frameworks for the Simultaneous Capture of Organic and Inorganic Contaminants from Water. *Journal of the American Chemical Society*, 141(34):13601–13609, 2019.
- [75] S. Naghdi, A. Cherevan, A. Giesriegl, R. Guillet-Nicolas, S. Biswas, T. Gupta, J. Wang, T. Haunold, B.C. Bayer, G. Rupprechter, M.C. Toroker, F. Kleitz, and D. Eder. Selective ligand removal to improve accessibility of active sites in hierarchical MOFs for heterogeneous photocatalysis. *Nature Communications*, 13(1):282, 2022.
- [76] J. Bonnefoy, A. Legrand, E.A. Quadrelli, J. Canivet, and D. Farrusseng. Enantiopure Peptide-Functionalized Metal-Organic Frameworks. *Journal of the American Chemical Society*, 137(29):9409–9416, 2015.
- [77] Q. Qian, P.A. Asinger, M.J. Lee, G. Han, K. Mizrahi Rodriguez, S. Lin, Francesco M. Benedetti, A.X. Wu, W.S. Chi, and Z.P. Smith. MOF-Based Membranes for Gas Separations. *Chemical Reviews*, 120(16):8161–8266, 2020.
- [78] S. Choi, T. Watanabe, T.-H. Bae, D.S. Sholl, and C.W. Jones. Modification of the Mg/DOBDC MOF with Amines to Enhance CO₂ Adsorption from Ultradilute Gases. *J. Phys. Chem. Lett.*, 3(9):1136–1141, 2012.
- [79] Z.U. Zango, K. Jumbri, N.S. Sambudi, N.H. Hanif Abu Bakar, N.A. Fathihah Abdullah, C. Basheer, and B. Saad. Removal of anthracene in water by MIL-88(Fe), NH₂-MIL-88(Fe), and mixed-MIL-88(Fe) metal-organic frameworks. *RSC Adv.*, 9(71):41490–41501, 2019.

- [80] Q. Wang, Q. Gao, A.M. Al-Enizi, A. Nafady, and S. Ma. Recent advances in MOF-based photocatalysis: environmental remediation under visible light. *Inorganic Chemistry Frontiers*, 7(2):300–339, 2020.
- [81] F. Duan, X. Feng, X. Yang, W. Sun, Y. Jin, H. Liu, K. Ge, Z. Li, and J. Zhang. A simple and powerful co-delivery system based on pH-responsive metal-organic frameworks for enhanced cancer immunotherapy. *Biomaterials*, 122:23–33, 2017.
- [82] N. Kaur, P. Tiwari, K.S. Kapoor, A.K. Saini, V. Sharma, and S.M. Mobin. Metal-organic framework based antibiotic release and antimicrobial response: an overview. *CrystEngComm*, 22(44):7513–7527, 2020.
- [83] D. Zhao, X. Wan, H. Song, L. Hao, Y. Su, and Y. Lu. Metal-organic frameworks (MOFs) combined with ZnO quantum dots as a fluorescent sensing platform for phosphate. *Sens. Actuators B Chem.*, 197:50–57, 2014.
- [84] H. Zhou, X. Hui, D. Li, D. Hu, X. Chen, X. He, L. Gao, He Huang, C. Lee, and X. Mu. Metal-Organic Framework-Surface-Enhanced Infrared Absorption Platform Enables Simultaneous On-Chip Sensing of Greenhouse Gases. *Advanced Science*, 7(20):2001173, 2020.
- [85] S. Achmann, G. Hagen, J. Kita, I.M. Malkowsky, C. Kiener, and R. Moos. Metal-Organic Frameworks for Sensing Applications in the Gas Phase. *Sensors*, 9(3):1574–1589, 2009.
- [86] S.J. Gregg and K.S.W. Sing. *Adsorption, Surface Area, & Porosity*. Academic Press, 2nd edition, 1982.
- [87] P. Atkins and J. de Paula. *Physical Chemistry*. Oxford University Press, 9th edition, 2010.
- [88] C.M. Friend and B. Xu. Heterogeneous Catalysis: A Central Science for a Sustainable Future. *Accounts of Chemical Research*, 50(3):517–521, 2017.
- [89] P. Samanta, A.V. Desai, S. Let, and S.K. Ghosh. Advanced Porous Materials for Sensing, Capture and Detoxification of Organic Pollutants toward Water Remediation. *ACS Sustainable Chemistry & Engineering*, 7(8):7456–7478, 2019.
- [90] S. Haukka and T. Suntola. Advanced Materials Processing by Adsorption Control. *Interface Science*, 5(2):119–128, 1997.
- [91] N. Cherkasov. Liquid-phase adsorption: Common problems and how we could do better. *Journal of Molecular Liquids*, 301:112378, 2020.
- [92] P. Hollins. The influence of surface defects on the infrared spectra of adsorbed species. *Surface Science Reports*, 16(2):51–94, 1992.
- [93] B. Baumgartner, J. Hayden, J. Loizillon, S. Steinbacher, D. Grosso, and B. Lendl. Pore Size-Dependent Structure of Confined Water in Mesoporous Silica Films from Water Adsorption/Desorption Using ATR-FTIR Spectroscopy. *Langmuir*, 35(37):11986–11994, 2019.

- [94] E.D. Revellame, D.L. Fortela, W. Sharp, R. Hernandez, and M.E. Zappi. Adsorption kinetic modeling using pseudo-first order and pseudo-second order rate laws: A review. *Cleaner Engineering and Technology*, 1:100032, 2020.
- [95] F.-C. Wu, R.-L. Tseng, and R.-S. Juang. Characteristics of Elovich equation used for the analysis of adsorption kinetics in dye-chitosan systems. *Chemical Engineering Journal*, 150(2):366–373, 2009.
- [96] M. Thommes, K. Kaneko, A.V. Neimark, J.P. Olivier, F. Rodriguez-Reinoso, J. Rouquerol, and K.S.W. Sing. Physisorption of gases, with special reference to the evaluation of surface area and pore size distribution (IUPAC Technical Report). *Pure and Applied Chemistry*, 87(9-10):1051–1069, 2015.
- [97] T. Laurell and A. Lenshof, editors. *Microscale Acoustofluidics*. The Royal Society of Chemistry, 2014.
- [98] S. Freitag, B. Baumgartner, S. Radel, A. Schwaighofer, A. Varriale, A. Pennacchio, S. D’Auria, and B. Lendl. A thermoelectrically stabilized aluminium acoustic trap combined with attenuated total reflection infrared spectroscopy for detection of Escherichia coli in water. *Lab Chip*, 21(9):1811–1819, 2021.
- [99] B. Baumgartner, J. Hayden, A. Schwaighofer, and B. Lendl. In Situ IR Spectroscopy of Mesoporous Silica Films for Monitoring Adsorption Processes and Trace Analysis. *ACS Appl. Nano Mater.*, 1(12):7083–7091, 2018.
- [100] F. Frank, M. Verstuyft, N.T. Beneitez, J. Missinne, G. Roelkens, D. van Thourhout, and B. Lendl. Experimental Demonstration of the High Alignment-Tolerant Behavior of a Mid-Infrared Waveguide Platform for Evanescent Field Sensing. *ACS Applied Optical Materials*, 2024.
- [101] N. T. Beneitez, B. Baumgartner, J. Missinne, S. Radosavljevic, D. Wacht, S. Hugger, P. Leszcz, B. Lendl, and G. Roelkens. Mid-IR sensing platform for trace analysis in aqueous solutions based on a germanium-on-silicon waveguide chip with a mesoporous silica coating for analyte enrichment. *Opt. Express*, 28(18):27013–27027, 2020.
- [102] F. Frank, D. Tomasetig, P. Nahrungbauer, W. Ipsmiller, G. Mauschitz, K. Wieland, and B. Lendl. In situ study of the interactions between metal surfaces and cationic surfactant corrosion inhibitors by surface-enhanced Raman spectroscopy coupled with visible spectroscopy. *Analyst*, 2024.
- [103] ISO 22412:2017 Particle size analysis-Dynamic light scattering (DLS), International Organization for Standardization, 2017.
- [104] T. Arnold, M. De Biasio, T. Bereczki, B. Oliveira, F. Frank, S. Freitag, and B. Lendl. Development of a particle analysis system for the process water of the petrochemical industry

using hyperspectral imaging, white-light imaging, and fluorescence imaging. *Proc.SPIE*, 12519:125190I, 2023.

- [105] C. Wagner, A. Genner, G. Ramer, and B. Lendl. *Advanced Total Lab Automation System (ATLAS)*, book section 1. IntechOpen, Rijeka, 2011.
- [106] B. Baumgartner, J. Hayden, and B. Lendl. Mesoporous silica films for sensing volatile organic compounds using attenuated total reflection spectroscopy. *Sens. Actuators, B.*, 302:127194, 2020.
- [107] J. Jaumot, A. de Juan, and R. Tauler. MCR-ALS GUI 2.0: New features and applications. *Chemometrics and Intelligent Laboratory Systems*, 140:1–12, 2015.
- [108] D. Wacht, M. David, B. Hinkov, H. Detz, A. Schwaighofer, B. Baumgartner, and B. Lendl. Mesoporous Zirconia Coating for Sensing Applications Using Attenuated Total Reflection Fourier Transform Infrared (ATR FT-IR) Spectroscopy. *Appl. Spectrosc.*, 76(1):141–149, 2021.
- [109] D. Bara, C. Wilson, M. Mörtel, M.M. Khusniyarov, S. Ling, B. Slater, S. Sproules, and R.S. Forgan. Kinetic Control of Interpenetration in Fe-Biphenyl-4,4'-dicarboxylate Metal-Organic Frameworks by Coordination and Oxidation Modulation. *Journal of the American Chemical Society*, 141(20):8346–8357, 2019.
- [110] M. Dan-Hardi, H. Chevreau, T. Devic, P. Horcajada, G. Maurin, G. Férey, D. Popov, C. Riekkel, S. Wuttke, J.-C. Lavalley, A. Vimont, T. Boudewijns, D. de Vos, and C. Serre. How Interpenetration Ensures Rigidity and Permanent Porosity in a Highly Flexible Hybrid Solid. *Chemistry of Materials*, 24(13):2486–2492, 2012.
- [111] T. Degen, M. Sadki, E. Bron, U. König, and G. Nénert. The HighScore suite. *Powder Diffr.*, 29(S2):S13–S18, 2014.
- [112] K. Zimny, T. Roques-Carmes, C. Carteret, M.J. Stébé, and J.L. Blin. Synthesis and photoactivity of ordered mesoporous titania with a semicrystalline framework. *The Journal of Physical Chemistry C*, 116(11):6585–6594, 2012.
- [113] I. Naboulsi, B. Lebeau, L. Michelin, C. Carteret, M. Bonne, and J.L. Blin. Influence of crystallization conditions and of gaseous ammonia treatment on mesoporous tio2 properties. *Microporous and Mesoporous Materials*, 262:1–12, 2018.
- [114] M. Faustini, A. Grenier, G. Naudin, R. Li, and D. Grosso. Ultraporous nanocrystalline TiO₂-based films: synthesis, patterning and application as anti-reflective, self-cleaning, superhydrophilic coatings. *Nanoscale*, 7(46):19419–25, 2015.
- [115] H.S. Yun, K. Miyazawa, I. Honma, H. Zhou, and M. Kuwabara. Synthesis of semicrystallized mesoporous TiO₂ thin films using triblock copolymer templates. *Materials Science and Engineering C*, 23:487–494, 2003.

- [116] S. Abdellatif, P. Sharifi, K. Kirah, R. Ghannam, A. S. G. Khalil, D. Erni, and F. Marlow. Refractive index and scattering of porous TiO₂ films. *Microporous and Mesoporous Materials*, 264:84–91, 2018.
- [117] W. Gong. A real time in situ ATR-FTIR spectroscopic study of linear phosphate adsorption on titania surfaces. *Int. J. Miner. Process.*, 63(3):147–165, 2001.
- [118] P.A. Connor and A.J. McQuillan. Phosphate Adsorption onto TiO₂ from Aqueous Solutions: An in Situ Internal Reflection Infrared Spectroscopic Study. *Langmuir*, 15(8):2916–2921, 1999.
- [119] G.L. Long and J.D. Winefordner. Limit of detection. A closer look at the IUPAC definition. *Anal. Chem.*, 55(7):712A–724A, 1983.
- [120] J. Mocak, A.M. Bond, S. Mitchell, and G. Scollary. A statistical overview of standard (IUPAC and ACS) and new procedures for determining the limits of detection and quantification: Application to voltammetric and stripping techniques. *Pure Appl. Chem.*, 69(2):297–328, 1997.
- [121] Q. Xie, Y. Li, Z. Lv, H. Zhou, X. Yang, J. Chen, and H. Guo. Effective Adsorption and Removal of Phosphate from Aqueous Solutions and Eutrophic Water by Fe-based MOFs of MIL-101. *Sci. Rep.*, 7(1):3316, 2017.
- [122] Y. Dong, T. Hu, M. Pudukudy, H. Su, L. Jiang, S. Shan, and Q. Jia. Influence of microwave-assisted synthesis on the structural and textural properties of mesoporous MIL-101(Fe) and NH₂-MIL-101(Fe) for enhanced tetracycline adsorption. *Materials Chemistry and Physics*, 251, 2020.
- [123] M. Ma, A. Bétard, I. Weber, N.S. Al-Hokbany, R.A. Fischer, and N. Metzler-Nolte. Iron-Based Metal-Organic Frameworks MIL-88B and NH₂-MIL-88B: High Quality Microwave Synthesis and Solvent-Induced Lattice "Breathing". *Crystal Growth & Design*, 13(6):2286–2291, 2013.
- [124] I. Coin, M. Beyermann, and M. Bienert. Solid-phase peptide synthesis: from standard procedures to the synthesis of difficult sequences. *Nature Protocols*, 2(12):3247–3256, 2007.
- [125] A. Amirjani, F. Firouzi, and D.F. Haghshenas. Predicting the Size of Silver Nanoparticles from Their Optical Properties. *Plasmonics*, 15(4):1077–1082, 2020.
- [126] L. B. Scaffardi, N. Pellegrini, O. de Sanctis, and J. O. Tocho. Sizing gold nanoparticles by optical extinction spectroscopy. *Nanotechnology*, 16(1):158, 2005.

Appendix

A. Appendix

In this part, the full scientific publications making up this cumulative thesis are presented. The contributions to the respective publications are categorised into low (x), medium (xx), and high (xxx).

| | Publications | | | | | |
|--------------------|--------------|-----|-----|-----|-----|----|
| | I | II | III | IV | V | VI |
| Setup development | xxx | xx | xx | xxx | xxx | xx |
| Data acquisition | xxx | xxx | xxx | xx | xxx | xx |
| Data analysis | xxx | xxx | xxx | xxx | xxx | x |
| Interpretation | xxx | xxx | xxx | xxx | xxx | x |
| Manuscript writing | xxx | xxx | xxx | xxx | xxx | xx |

A.1. Publication I: Metal-organic frameworks combined with mid-infrared spectroscopy for the trace analysis of phosphates in water



Contents lists available at ScienceDirect

Sensors and Actuators: B. Chemical

journal homepage: www.elsevier.com/locate/snb

Metal-organic frameworks combined with mid-infrared spectroscopy for the trace analysis of phosphates in water

Felix Frank^a, Bettina Baumgartner^{a,b}, Bernhard Lendl^{a,*}

^a Research Division of Environmental Analytics, Process Analytics and Sensors, Institute of Chemical Technologies and Analytics, TU Wien, Getreidemarkt 9, 1060 Vienna, Austria

^b Inorganic Chemistry and Catalysis group, Debye Institute for Nanomaterials Science, Utrecht University, Universiteitsweg 99, 3584 CG Utrecht, the Netherlands

ARTICLE INFO

Keywords:

Mid-IR spectroscopy
Metal-organic frameworks
Sensing
Functional coating
Phosphate
Trace analysis

ABSTRACT

Detecting traces of phosphates in water is critical for monitoring water quality in aquatic ecosystems. Mid-infrared techniques are effective for label-free and quick measurements in at-line or in-line applications, but sensitivity is limited due to high water absorption. To combat this, preconcentration schemes combined with evanescent field spectroscopy can be used to enrich the analyte in the probed volume and thereby increasing sensitivity. Metal-organic frameworks (MOFs) are versatile materials with defined porosity and tuneable chemistry, which make them ideal for selective adsorption of target molecules. In this study, an NH₂-MIL-88B (Fe) (= Fe₃O(NH₂-BDC)₃) MOF-based enrichment layer was prepared on a diamond attenuated total reflection (ATR) crystal for in situ Fourier transform infrared (FTIR) spectroscopic measurements of ortho-phosphates in water. A workflow for single-use enrichment layers was established, and an automated flow system was used to apply aqueous phosphate solutions. Using internal referencing and compensating for variation in MOF film depositions, phosphate analysis reproducibility increased from 74% to 94%. The Langmuir adsorption model was used to derive a limit of detection (LOD) of 0.18 mg L⁻¹ phosphorus in water. Overall, this work demonstrates the effectiveness of NH₂-MIL-88B(Fe) MOFs as enrichment layers for aqueous phosphate sensing. Our results provide a promising avenue for the development of sensitive and selective sensors for environmental and biomedical applications.

1. Introduction

Phosphorus is an essential element for the development and survival of life. Besides the use as fertilisers in agriculture, phosphates are also prominently used in detergents, accounting for a worldwide phosphate production of 220 million tons in 2021 [1]. The excessive use of phosphates led to an accumulation of nutrients in aquatic ecosystems around the world. This resulted in the eutrophication of several aquatic ecosystems, creating algal and cyanobacterial mats, reduced oxygen concentrations in affected waters and, as a consequence, a severe loss of biodiversity [2,3]. As preventive measures, the US environmental protection agency and the European environmental agency recommend a maximal phosphorus concentration between 0.05 and 0.1 mg L⁻¹ in flowing waters. In recent years, point source water pollution due to industrial sewage has been reduced by strict regulations and mitigation schemes, making non-point sources such as agricultural runoff, construction sites or other seasonal events the main contributors to the

continuing problem of phosphate eutrophication. As these non-point sources are difficult to monitor, constant surveillance of nutrient concentration is essential in vulnerable waters in order to preserve the quality of drinking water and aquatic ecosystems [4–6]. To date, the standard method to determine trace amounts of phosphates is based on a colorimetric assay, which detects the presence of the blue phosphomolybdate complex by means of spectrophotometry [7]. This method allows for an application range between 0.5 mg L⁻¹ and 5 mg L⁻¹ and very accurate measurements [8], but involves an off-line multi-step sample preparation, additional chemical reagents (yielding toxic chemical waste) and generally either narrow detection ranges or high limits of detection [9].

Fourier transform infrared (FTIR) spectroscopy is a widely used technique for analysing liquid samples in the food and beverage industry, such as soft-drinks, milk, wine, beer, and edible oils, as well as in biotechnological applications for process monitoring and control [10–15]. This spectroscopic technique provides molecular-specific

* Corresponding author.

E-mail address: bernhard.lendl@tuwien.ac.at (B. Lendl).

<https://doi.org/10.1016/j.snb.2023.134778>

Received 19 May 2023; Received in revised form 14 September 2023; Accepted 11 October 2023

Available online 12 October 2023

0925-4005/© 2023 The Authors. Published by Elsevier B.V. This is an open access article under the CC BY license (<http://creativecommons.org/licenses/by/4.0/>).

information by probing characteristic vibrational transitions. FTIR spectroscopy has further shown promise for the surveillance of both natural and process water streams, for instance in the detection of bacteria in eutrophic lakes and the analysis of oil in water content in process water streams [16,17].

The analysis of concentrations greater 0.1 g L^{-1} of phosphate in non-sweetened soft-drinks and biotechnology has also been demonstrated using FTIR spectroscopy, based on specific IR absorption bands of phosphates in the mid-IR region between 1200 and 1000 cm^{-1} [18,19]. Using this approach, fast and direct quantification can be achieved without requiring the use of toxic reagents such as phosphomolybdate, which is needed for spectrophotometric phosphate analysis. However, the high water absorption in the characteristic fingerprint region, thus, also in the spectral region of the phosphate bands, limits the sensitivity of IR spectroscopic techniques in aqueous samples. To combat this, preconcentration schemes can be employed, boosting the achievable limits of detection (LODs) from the high mg mL^{-1} range to the sub- mg L^{-1} range [20,21], enabling analysis of trace amounts of phosphates in flowing waters.

For evanescent field sensing, this can be realised by enrichment coatings, which help in accumulation the analyte in the volume probed by the evanescent field. Early works used polymer-coated ATR elements or fibres to extract and preconcentrate hydrophobic analytes such as

chlorinated hydrocarbons present in water [22]. However, their response time is long due to slow diffusion of the analyte into the polymer enrichment films. The use of porous oxides such as silica and zirconia improves on this concept by providing a faster sensor response based on adsorption. The introduction of surface functionalities such as hydrophobic groups or ion exchange sites enables further fine-tuning of the layer towards respective analytes such as organic contaminants, volatile organic compounds, or nitrates [23–28].

The strong absorption bands of silica and zirconia overlap with the phosphate bands around 1100 cm^{-1} , which impede their application as a phosphate enrichment layer. Polymers lack mechanical stability due to swelling in water and show long response times, although almost full recovery after phosphate adsorption into polymer-based anion-exchange membranes has been reported [29,30]. Therefore, selecting a material for phosphate enrichment requires a compromise between stability, affinity, and capability to regenerate, and new materials beyond polymers and oxides need to be considered.

In metal-organic frameworks (MOFs), organic linkers coordinate to single metal ions or metal-oxide clusters (secondary building units, SBUs), yielding crystalline materials with high specific surface areas and tuneable porosity and functionality. The chemical affinity of MOFs can be modified by linker and cluster design towards various target molecules including CO_2 , VOCs and BTX [31–34]. This makes MOFs

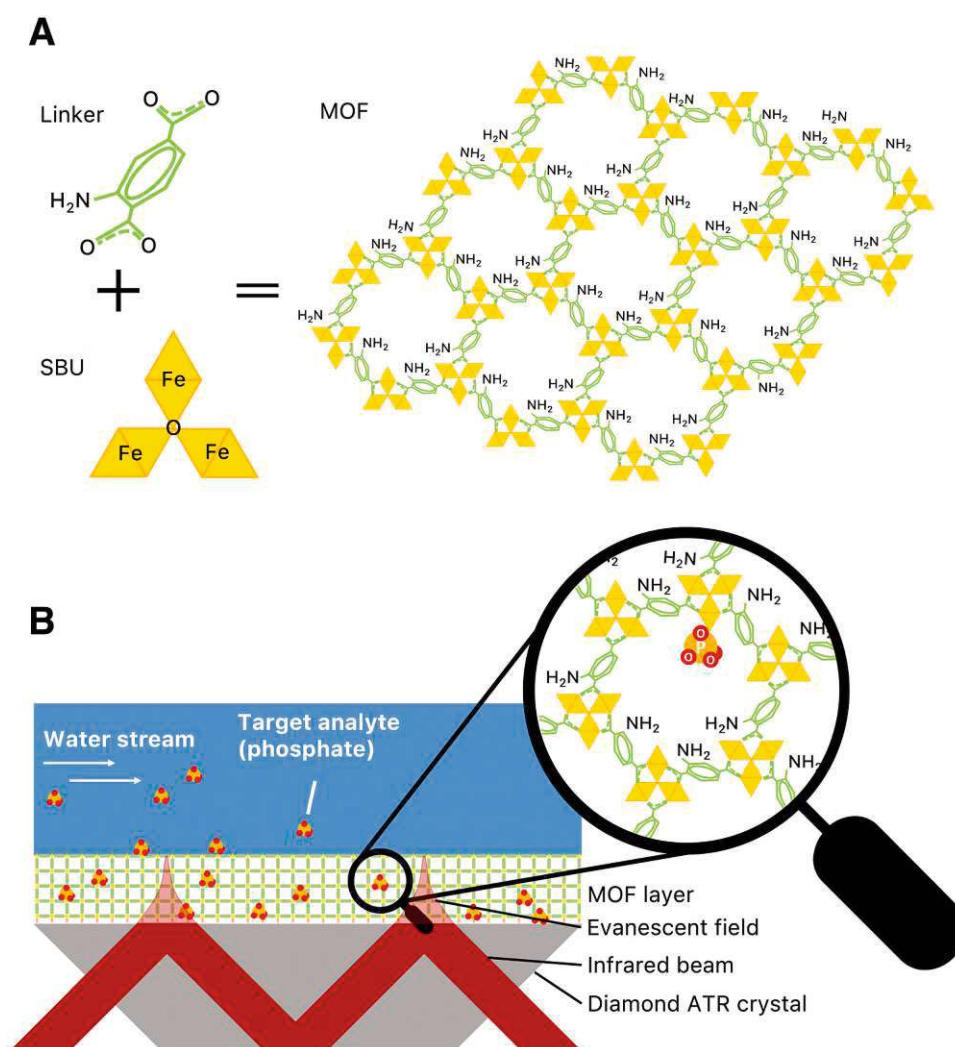


Fig. 1. A: Structure of $\text{NH}_2\text{-MIL-88B(Fe)}$, SBUs shown in light yellow, aminoterephthalate linker shown in green. B: Schematic of the measurement principle: Phosphate (dark yellow and red) is enriched from the aqueous phase into the MOF film, which covers the evanescent field (light red) of the infrared beam (dark red) passing through the diamond ATR crystal (grey), leading to specific absorption in the mid-IR region.

attractive materials for the adsorptive removal of pollutants [35,36] and adsorption-based sensing schemes [37,38]. Most MOF-based sensors rely on changes in the capacity, fluorescence or luminescence of the MOF or hosted species such as quantum nanodots upon interaction with the analyte [39–42]. Thereby, phosphates can be detected at concentrations as low as 0.005 mg L^{-1} . However, additional chemical substrates and an incubation time of 40 min are required and the sensing material cannot be regenerated [43].

In this contribution, we combine the concept of preconcentration in the evanescent field in ATR-FTIR spectroscopy with the high adsorption capacity of MOFs (Fig. 1) for direct liquid-phase phosphate sensing without the need of additional substrates. The employed $\text{NH}_2\text{-MIL-88B (Fe)}$ (Fig. 1-A) is a member of the water-stable iron(III) aminoterephthalate family, which has shown high phosphate affinity [44]. The MOF was synthesised according to literature [45] and characterised with X-ray diffraction and FTIR spectroscopy.

We aimed for a highly reproducible and fast method of preparing single-use powder-based enrichment layers. For this, we spin-coated an $\text{NH}_2\text{-MIL-88B(Fe)}$ suspension onto a diamond ATR crystal, yielding MOF covered ATR crystals, which are further denoted as 'MOF films'. The sensing performance of MOF films was investigated and compared to an enrichment film made of non-porous iron oxide powder with similar particle size to prove the advantageous properties of the highly porous materials. These results demonstrate the high potential of MOFs for mid-IR liquid phase sensing.

2. Materials and methods

Ferric chloride hexahydrate ($\text{FeCl}_3 \cdot 6 \text{ H}_2\text{O}$, Fluka, 99% p.a.), 2-Aminoterephthalic acid ($\text{NH}_2\text{-H}_2\text{BDC}$, Sigma-Aldrich, 99%), N,N-Dimethylformamide (DMF, Sigma-Aldrich, >99%), 2-Propanol (IPA, Roth, >99.9% HPLC grade), Ethanol (EtOH, Chem-Lab, 100% p.a.), Sodium dihydrogen phosphate (NaH_2PO_4 , Fluka, 99% p.a.), Sodium sulphate anhydrous (Na_2SO_4 , Sigma-Aldrich, >99%), Sodium nitrate (NaNO_3 , Merck, >99% p.a.), Iron oxide microparticles (Fe_2O_3 MP, Sigma-Aldrich, <5 μm , $\geq 96\%$) were used as received.

2.1. Synthesis of $\text{NH}_2\text{-MIL-88B(Fe)}$

The synthesis of $\text{NH}_2\text{-MIL-88B(Fe)}$ was performed following the report of Bauer et al. [45]: 2.025 g $\text{FeCl}_3 \cdot 6 \text{ H}_2\text{O}$ was dissolved in 25 mL of DMF. To this solution, a solution of 0.675 g $\text{NH}_2\text{-H}_2\text{BDC}$ in 20 mL of DMF was added. The reaction mixture was poured into a Teflon lined autoclave and heated for 24 h at 115 °C. After cooling down, the brown precipitate was separated from the solvent via centrifugation for 3 min at 4000 rpm (Rotofix 32 A, Hettich, Germany). The as-synthesised MOF was then washed four times using DMF, twice with deionised water, and twice with EtOH. After the last step, the MOF was dispersed in EtOH and poured into a crystallising dish. After evaporation of the EtOH at ambient conditions, the brown powder was dried at 90 °C for 24 h to remove any remaining trace of solvent.

2.2. Characterisation of $\text{NH}_2\text{-MIL-88B(Fe)}$

X-ray diffraction patterns were collected with an X'Pert PRO MPD diffractometer, equipped with a X'Celerator line scan detector and the Data Collector software (all from PANalytical, Netherlands). The measurements were conducted in Bragg-Brentano geometry, with the Cu anode operating at 45 kV and 40 mA. The diffractograms were recorded between 5° and 25° 2θ with a step size of 0.01° and an integration time of 360 s/step in continuous scan mode. Simulation of the theoretical diffractogram was done by Rietveld refinement using data [45] from the Cambridge Structural Database (CSD). Rietveld refinement was performed using HighScore Plus [46] (PANalytical, Netherlands). FTIR-ATR measurements for the characterisation of $\text{NH}_2\text{-MIL-88B(Fe)}$ were performed using a Tensor 37 FTIR spectrometer (Bruker Optics,

Germany) equipped with a Platinum ATR unit (Diamond, single-bounce, Bruker Optics, Germany) and a N_2 -cooled MCT detector. Spectra were recorded with 4 cm^{-1} resolution, averaging 32 scans per spectrum.

2.3. Preparation of enrichment film

The coating suspension was prepared by dispersing the dried MOF or Fe_2O_3 MP in IPA, resulting in a mixture with 3.5 wt% solid. The liquid was continuously stirred using a magnetic stir bar to maintain the homogeneity of the suspension. The enrichment film was then spin-coated onto the ATR element at a spinner velocity of 1150 rpm and subsequently annealed for 15 min at 110 °C.

2.4. Optical setup for FTIR spectroscopy

MOF films were coated onto a diamond ATR crystal ($20 \times 10 \times 0.5 \text{ mm}^3$, facets with an angle of 55° (Diamond Materials, Germany)). This geometry resulted in 14 active bounces (N) at a total effective pathlength ($d_{e,tot} = d_e N$) of $18.1 \mu\text{m}$ at 1100 cm^{-1} ($n_{dia} = 2.4$, $n_{sample} = n_{water} = 1.33$) and a depth of penetration (d_p) of $1 \mu\text{m}$ [47]. The measurement setup comprised a custom built ATR mount and an aluminium flow cell previously reported by Freitag et al. [48] and Baumgartner et al. [23], which allowed the integration into the sample compartment of a Vertex 70 v FTIR spectrometer (Bruker, Germany). Spectra were collected with OPUS 8.1 software using a spectral resolution of 4 cm^{-1} , 32 scans per spectrum (double sided, forward-backward acquisition mode). During all measurements, the sample compartment was flushed with dry air. The noise floor of the sensor was determined by evaluating the RMS noise of 100% lines, measured in a stopped flow environment of the water background, yielding an RMS noise of 1.85×10^{-4} A.U. between 1000 and 1200 cm^{-1} .

2.5. Data processing and spectra evaluation

The evaluation of the spectra collected during the sensing experiments was done using an in-house MATLAB R2021a script. Spectra were baseline corrected by a two-point linear algorithm between 1195 cm^{-1} and 920 cm^{-1} . The band heights were then determined at the peak maximum of the baseline corrected spectra situated at 1025 cm^{-1} .

2.6. Liquid handling and automation

The automated sequential injection analysis (SIA) system is schematically shown in Fig. 2. It is modified from the SIA system previously reported by Freitag et al. [48], and consisted of a 10-port selection valve (VICI, Switzerland), as well as a Cavo XC syringe pump (Tecan, Switzerland) equipped with a 500 μL glass syringe (Tecan, Switzerland). The components were connected with PTFE tubing (VICI, Switzerland, O.D. = 1/16 in., I.D. = 0.75 mm). Each concentration of the sample phosphate solutions (ortho-phosphate, pH = 5.15–5.75, 5–75 mg L^{-1}) was fed to a separate port on the selection valve. The SIA setup and the FTIR spectrometer were controlled by a LabVIEW VI using a server-client program structure [49].

The SIA sequence used for the automated sensor experiments is shown in Fig. 3 (characterisation of SIA system in ESI). It consisted of first measuring a phosphate standard followed by analysis of the actual sample. The whole sequence comprised three parts:

- 1) flushing the flow cell, followed by a 9 min conditioning step of the MOF in the aqueous sample medium (a-c in Fig. 3),
- 2) measurement of the standard with a concentration of 10 mg L^{-1} of ortho-phosphate in water (d-e in Fig. 3) and
- 3) the actual measurement of the sample at the end of each measurement cycle (f-g in Fig. 3).

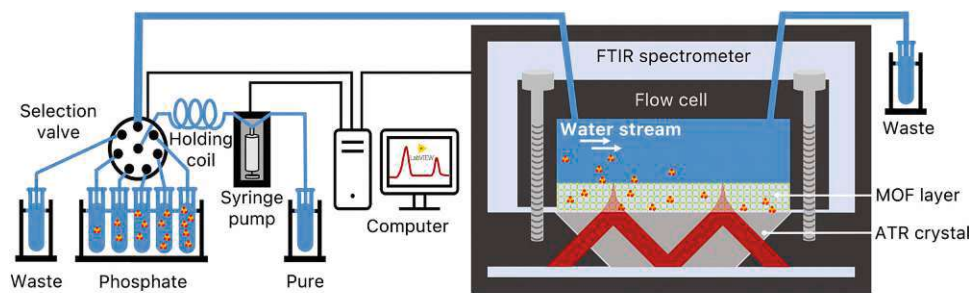


Fig. 2. Schematic depiction of the automated sequential injection analysis system.

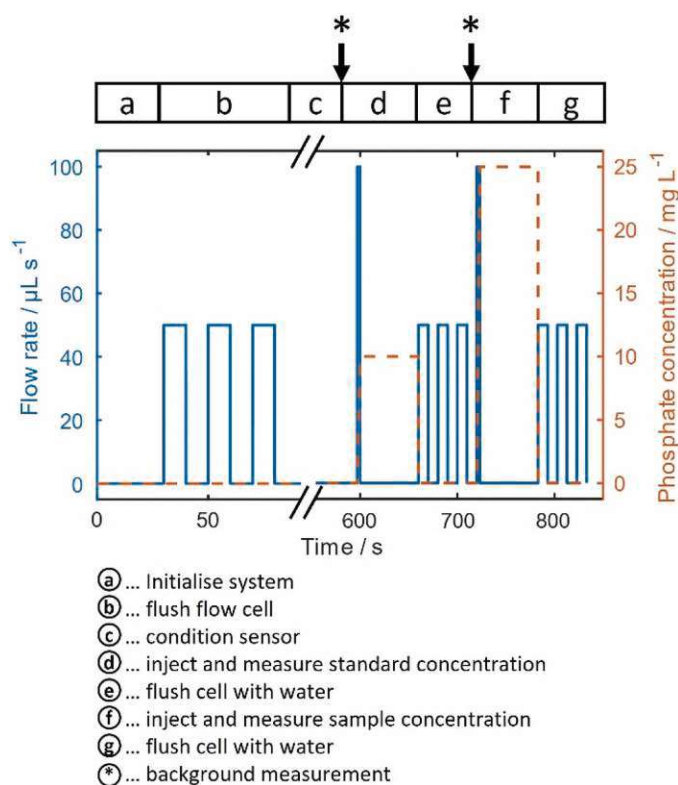


Fig. 3. SIA sequence for a sample automated sensor experiment with a standard concentration of 10 mg L^{-1} and a sample concentration of 25 mg L^{-1} . A phosphate concentration of 0 mg L^{-1} at a positive flow rate signifies flushing the flow cell with deionised water. The timing of background measurements is denoted by asterisks.

Furthermore, intermittent washing steps using deionised water were employed after each measurement step. This procedure allowed to acquire the data needed to account for slightly different sensitivities of the individually prepared sensing films. Each measurement step (both standard and sample) consisted of a background measurement (denoted with asterisks in Fig. 3), followed by the injection of $300 \mu\text{L}$ orthophosphate solution at a speed of $100 \mu\text{L s}^{-1}$ and 7 sample channel measurements with 10 s between each of them, equating to a total duration of 63 s.

2.7. Evaluation of sensor performance

The sensor performance was evaluated by executing the measurement sequence as shown in Fig. 3 in triplicate for each concentration (5 mg L^{-1} , 10 mg L^{-1} , 25 mg L^{-1} , 50 mg L^{-1} , and 75 mg L^{-1}), with new films for each measurement. Each film was prepared following the procedure described in Section 2.3, while the ATR crystal was cleaned

between each loop by wiping the film off with a clean room wipe, followed by ultrasonication for 3 min in EtOH. All sensor experiments were performed at $22 \text{ }^\circ\text{C}$ and standard pressure.

To assess the influence of interfering ions, 25 mg L^{-1} of sulphate and nitrate were added to phosphate samples of the aforementioned concentrations. These measurements were carried out in a manner consistent with the methodology described in 2.6, with two replicates for each sample. The standard measurements for these samples containing the interfering ions were also done with a 10 mg L^{-1} pure phosphate standard to ensure comparability with the pure phosphate measurements.

3. Results and discussion

3.1. Characterisation of $\text{NH}_2\text{-MIL-88B(Fe)}$

ATR-FTIR spectroscopy and powder X-ray diffraction of the as-synthesised $\text{NH}_2\text{-MIL-88B(Fe)}$ confirmed the MOF structure and presence of the incorporated amino-moiety. The ATR-FTIR spectra of the as-synthesised $\text{NH}_2\text{-MIL-88B(Fe)}$ and the commercially available Fe_2O_3 MPs are shown in Fig. 4-A. Bands corresponding to the aminoterephthalate linker were assigned as the asymmetric and symmetric NH_2 stretching vibrations at 3460 cm^{-1} and 3329 cm^{-1} , two intense asymmetric and symmetric $\text{C}=\text{O}$ bands at 1574 cm^{-1} and 1379 cm^{-1} [50], a differently coordinated $\text{C}=\text{O}$ band at 1425 cm^{-1} [51], the skeletal $\text{C}=\text{C}$ vibration band at 1493 cm^{-1} [50], the C-N vibration mode at 1254 cm^{-1} [50], and the aromatic C-H bending vibration band at 766 cm^{-1} [52]. The band at 517 cm^{-1} corresponds to O-Fe-O vibration seen in the ATR-FTIR spectrum of the Fe_2O_3 MP and confirms the formation of the coordination network of the MOF [50,53].

The powder X-ray diffractogram of $\text{NH}_2\text{-MIL-88B(Fe)}$ as well as the simulated diffractogram obtained by Rietveld refinement of the powder refraction data using the literature CIF file 647646 [45] are shown in Fig. 4-B. The characteristic reflections (hkl) of $\text{NH}_2\text{-MIL-88B(Fe)}$ are visible at 9.37° (002), 10.46° (101), 13.23° (102), 16.85° (103), 18.66° (200), 19.18° (201), and 20.85° (202). Further characterisation of $\text{NH}_2\text{-MIL-88B(Fe)}$ including scanning electron microscopy images, nitrogen physisorption and a thermogravimetric study can be found in the ESI and were in line with literature [50,54,55].

3.2. Evaluation of sensing performance

The phosphate enrichment experiments were performed using the automated SIA sequence described in Section 2.6 with five different concentrations (5 mg L^{-1} , 10 mg L^{-1} , 25 mg L^{-1} , 50 mg L^{-1} , and 75 mg L^{-1}) for both the MOF and the Fe_2O_3 MP films (with higher concentrations added due to lower enrichment), respectively. The enrichment was monitored using the absorbance maximum of the phosphate band at 1025 cm^{-1} .

The sensor response was determined first to find the right compromise between response time and sensitivity (Fig. 5-A). As can be seen in Fig. 5-B, it took 9 min to reach 90% of the equilibrium signal for a phosphate solution with a concentration of 25 mg L^{-1} , while 43% can be

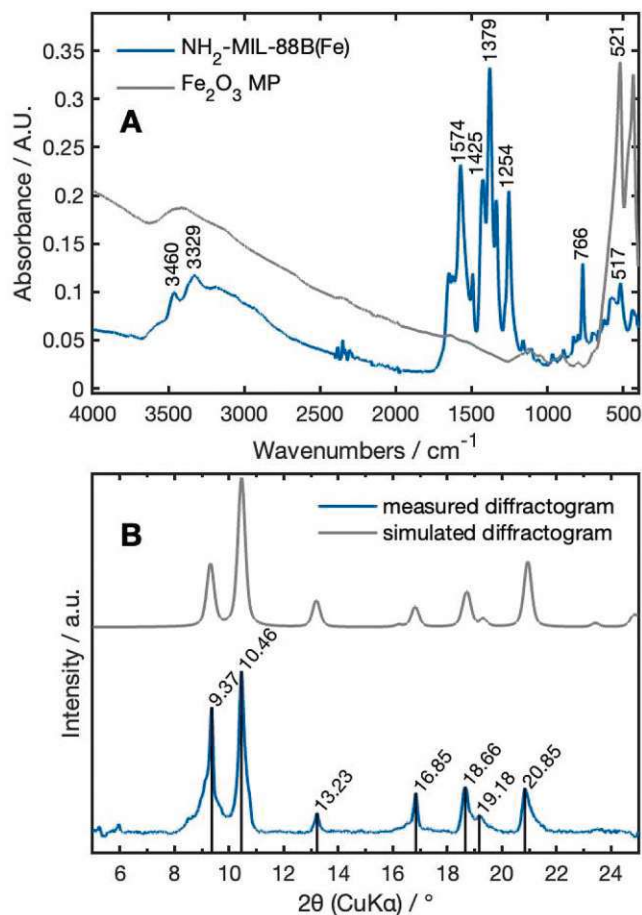


Fig. 4. A: ATR-FTIR spectra of as-synthesised $\text{NH}_2\text{-MIL-88B(Fe)}$ (blue) and the commercially available Fe_2O_3 MPs (grey). B: Powder X-ray diffractogram of as synthesised $\text{NH}_2\text{-MIL-88B(Fe)}$ (blue). Simulated powder X-ray diffractogram obtained by Rietveld refinement of the literature data (grey).

achieved in 1 min. In order to present a fast yet sensitive method of sensing phosphates, an enrichment time of 1 min (63 s, as 3 s are needed for sample injection) was chosen. This enrichment time can, however, be extended in order to increase sensitivity at the cost of response time. A sample phosphate enrichment profile for this enrichment time is depicted in Fig. 5-B*.

Recorded phosphate spectra with an enrichment time of 63 s used for calibration as well as a 100% line as noise reference are shown in Fig. 6. The broad absorption band between 1160 cm^{-1} and 950 cm^{-1} seen in the phosphate spectra can be explained by overlapping P-O vibrations similar to other oxidic adsorbents [56].

The band heights obtained after 63 s of enrichment (Section 2.6 for description of the measurement steps) were normalised by the band heights obtained from the initially recorded standard spectrum. The normalised data were used to establish the calibration function, which is given in Fig. 7. The unavoidable difference between the spin-coated enrichment films, which were prepared for each sample measurement, required such normalisation, as already mentioned in Section 2.6. By employing the normalisation, an increase of the repeatability from 74% to 94% could be observed (see ESI for unreferenced data and discussion of errors).

The better quality of the fit (see ESI) of the Langmuir adsorption model (1) over the multi-layer Freundlich model further suggests the expected single-site adsorption of phosphate into the MOF [23]. As a result, the Langmuir model (1) was used as the calibration function. In this equation, q_e (unitless) denotes the relative band height for the adsorbed analyte referenced with the band height for the standard

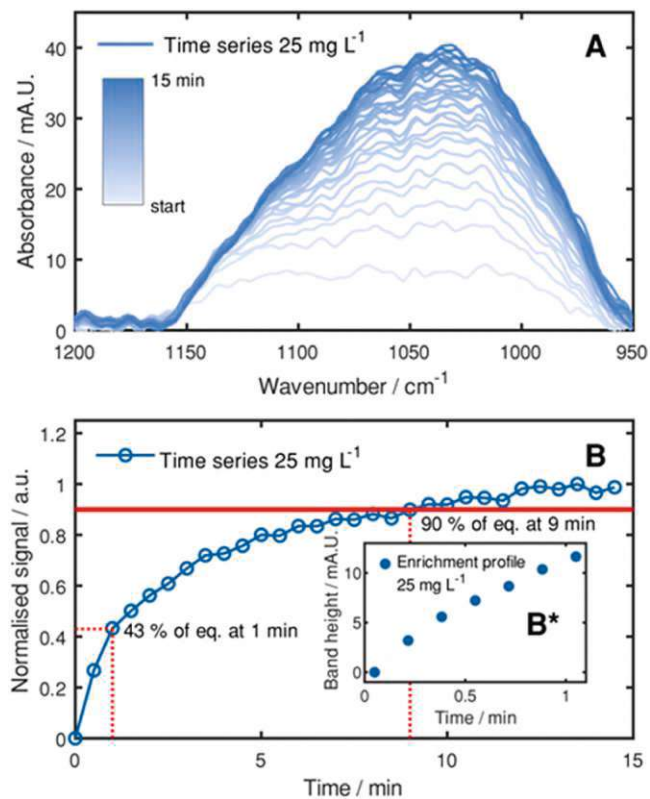


Fig. 5. A: Development of the spectrum of the enriched phosphate until equilibrium is reached. B: Normalised peak area over enrichment time. B* : Phosphate enrichment profile for a phosphate concentration of 75 mg L^{-1} as a function of time.

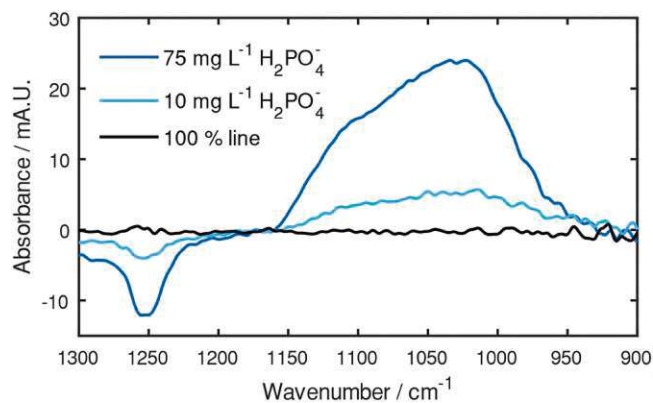


Fig. 6. Spectra of the enriched sample phosphate (75 mg L^{-1} , dark blue), the standard phosphate (10 mg L^{-1} , light blue), both as used for sensor calibration, and the 100% RMS line (black) for noise evaluation.

concentration, with q_m (unitless) being the maximum relative band height associated to the adsorbed analyte, and K_L (L mg^{-1}) being the Langmuir constant.

$$q_e = \frac{q_m K_L c}{1 + K_L c} \quad (1)$$

The calibration function fitted with the Langmuir equation shown in Fig. 7 revealed a theoretical maximum relative band height q_m of 7.55 and a K_L of 0.0183. Using K_L and q_m and the noise floor of 1.85×10^{-4} A. U. (as mentioned in Section 2.4) allowed the calculation of a theoretical limit of detection (LOD) for the sensor. The LOD was determined as three times the relative band height above the referenced noise floor (2) [57,

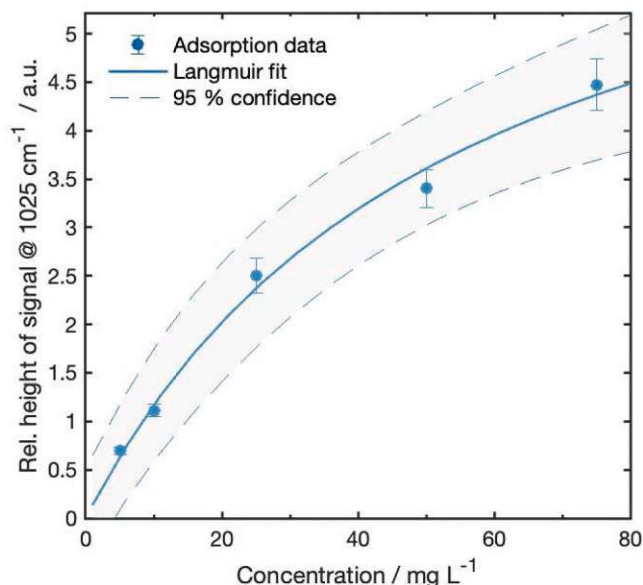


Fig. 7. Referenced phosphate band heights as function of the applied concentration. The band height was referenced to the standard concentration of 10 mg L^{-1} . Error bars show the standard deviation for each concentration ($n = 3$ for each respective concentration). Data points were fitted with the Langmuir equation (solid line) with a 95% confidence of the fit (dashed line).

[58]. The noise floor was referenced with the mean band height ($s_{rel} = 2.61 \times 10^{-2}$) of the phosphate standard. This equates to a theoretical LOD of 0.57 mg L^{-1} phosphate in water (equivalent to 0.18 mg L^{-1} phosphorus in water). The limit of quantification (LOQ, defined as nine times the relative band height above the referenced noise floor) equates to 1.72 mg L^{-1} phosphate in water (equivalent to 0.55 mg L^{-1} phosphorus in water) [58].

$$LOD = \frac{3s_{rel}}{(q_m - 3s_{rel})K_L} \quad (2)$$

Identical experiments were performed using Fe_2O_3 MP films. The lower specific surface area of Fe_2O_3 MP compared to the MOF did not allow for significant phosphate loading, making the referencing and, thus, a reproducible sensing assessment, impossible (see ESI). This finding justifies the use of the highly porous $\text{NH}_2\text{-MIL-88B(Fe)}$ for phosphate enrichment.

3.3. Phosphate sensing with interfering ions

In order to account for sample solutions closer to environmental applications and to simulate the presence of interfering ions in natural waters, experiments in the presence of sulphate and nitrate ions with a fixed concentration of 25 mg L^{-1} each were performed. Comparing the relative band intensities with and without interfering ions (Fig. 8) shows a negligible influence of the interfering ions at lower phosphate concentrations ($c < 10 \text{ mg L}^{-1}$), as the measured values are within or close to the margin of errors at the respective concentrations. At larger concentrations, however, the calibration curve flattens significantly compared to the pure phosphate samples, impeding the quantification of unknown phosphate concentrations in the presence of sulphate and nitrate. This can most probably be attributed to competitive adsorption effects, which increase with total ion concentrations. Similar effects have been observed for phosphates and sulphates on goethite, albeit with lower interferences [59], and can be attributed to the lack of equivalent surface sites for the adsorption above a certain threshold concentration.

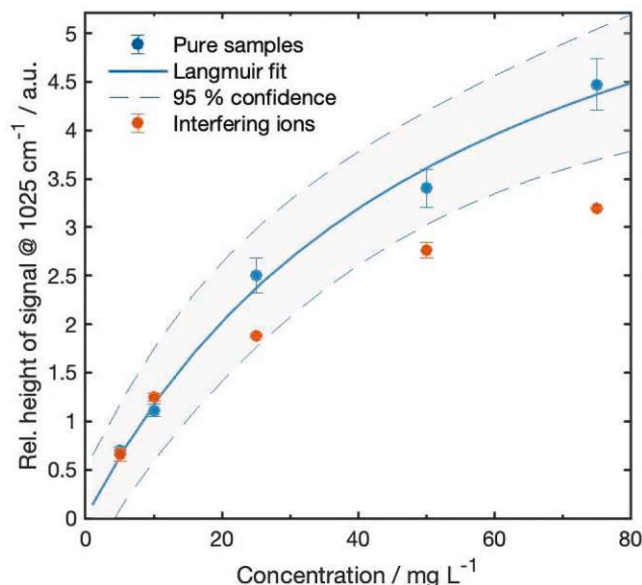


Fig. 8. Relative heights of the phosphate bands of the pure phosphate samples referenced to the standard concentration (10 mg L^{-1}) as function of the applied concentration (blue). Relative heights of the phosphate bands of samples with added interfering ions (25 mg L^{-1} , orange). Error bars for the samples with interfering ions show the standard deviation for each concentration ($n = 2$).

4. Conclusion

In this work, we introduced a phosphate sensor comprising a MOF as enrichment film combined with liquid-phase, ATR-FTIR spectroscopy. The MOF $\text{NH}_2\text{-MIL-88B(Fe)}$ was chosen as enrichment material as it offers a good compromise between stability, affinity, and enrichment capability. The successful synthesis of $\text{NH}_2\text{-MIL-88B(Fe)}$ was confirmed through FTIR spectroscopy, X-ray diffraction, N_2 sorption, and scanning electron microscopy. We established a facile and reproducible procedure for spin-coating $\text{NH}_2\text{-MIL-88B(Fe)}$ films onto a diamond ATR. The MOF powder films acted as enrichment layer, effectively preconcentrating phosphate from water within the volume probed by the evanescent wave of the ATR crystal. The sensing performance of the system was evaluated using an automated SIA system coupled with an FTIR spectrometer, measuring concentrations ranging between 5 mg L^{-1} and 75 mg L^{-1} with a measurement time of 1 min. By referencing the sample measurement with an internal reference point at a concentration of 10 mg L^{-1} , we showed that measurement errors due to variations in the film application could be compensated, improving the repeatability from 74% to 94%. The data from a concentration series was described with the Langmuir adsorption model, which also served as the sensor's calibration function. An LOD of 0.18 mg L^{-1} phosphorus in water was determined. Adsorption studies in the presence of interfering ions showed a good sensing performance below a phosphate concentration of 10 mg L^{-1} , with more interferences at higher phosphate concentrations.

Regarding speed, sensitivity, and reproducibility, the use of MOF-based enrichment films represents a good compromise for phosphate sensing. Further, the combination of MOFs with ATR spectroscopy is not limited to phosphates and paves the way for porous enrichment layers with tuneable affinities towards various pollutants. To enhance the performance of the enrichment layers, future work will focus on tuning the material to allow for full regeneration. Additionally, further studies will be performed to better understanding the competitive adsorption of different ions in MOFs.

CRediT authorship contribution statement

Felix Frank: Conceptualization, Methodology, Investigation,

Software, Validation, Writing – Original Draft, Visualization. **Bettina Baumgartner**: Methodology, Validation, Writing – review & editing, Visualization. **Bernhard Lendl**: Validation, Writing – review & editing, Funding acquisition, Supervision.

Declaration of Competing Interest

The authors declare that they have no known competing financial interests or personal relationships that could have appeared to influence the work reported in this paper.

Data availability

Data will be made available on request.

Acknowledgments

This work is part of the HYDROPTICS project, which has received funding from the European Union's Horizon 2020 research and innovation program under the grant agreement No. 871529. This project is an initiative of the Photonics Public Private Partnership. X-ray diffraction was performed at the interfaculty X-ray centre of TU Wien. B.B. acknowledges funding from the Austrian Science Fund (FWF, grant number J4607-N). Fruitful discussions with Felix Eder on the topic of X-ray diffraction methods are acknowledged. The help of Eva Szoldatits, Karin Föttinger, Nevzat Yigit, and Johannes Graf for the characterisation of the MOFs is greatly appreciated.

Appendix A. Supporting information

Supplementary data associated with this article can be found in the online version at [doi:10.1016/j.snb.2023.134778](https://doi.org/10.1016/j.snb.2023.134778).

References

- [1] Mineral commodity summaries 2022, U.S. Geological Survey, Reston, VA, (2022) 1–202, (<https://doi.org/10.3133/mcs2022>).
- [2] D.L. Correll, The role of phosphorus in the eutrophication of receiving waters: a review, *J. Environ. Qual.* 27 (1998) 261–266, (<https://doi.org/10.2134/jeq1998.00472425002700020004x>).
- [3] P.H. Abelson, A potential phosphate crisis, *Science* 283 (1999) 2015, (<https://doi.org/10.1126/science.283.5410.2015>).
- [4] S.R. Carpenter, Eutrophication of aquatic ecosystems: Bistability and soil phosphorus, *Proc. Natl. Acad. Sci.* 102 (2005) 10002–10005, (<https://doi.org/10.1073/pnas.0503959102>).
- [5] S.R. Carpenter, N.F. Caraco, D.L. Correll, R.W. Howarth, A.N. Sharpley, V.H. Smith, Nonpoint pollution of surface waters with phosphorus and nitrogen, *Ecol. Appl.* 8 (1998) 559–568, ([https://doi.org/10.1890/1051-0761\(1998\)008\[0559:NPOSWW\]2.0.CO;2](https://doi.org/10.1890/1051-0761(1998)008[0559:NPOSWW]2.0.CO;2)).
- [6] J.P. Gustafsson, A. Renman, G. Renman, K. Poll, Phosphate removal by mineral-based sorbents used in filters for small-scale wastewater treatment, *Water Res* 42 (2008) 189–197, (<https://doi.org/10.1016/j.watres.2007.06.058>).
- [7] C.H. Fiske, Y. Subbarow, The colorimetric determination of phosphorus, *J. Biol. Chem.* 66 (1925) 375–400, ([https://doi.org/10.1016/S0021-9258\(18\)84756-1](https://doi.org/10.1016/S0021-9258(18)84756-1)).
- [8] S. Ganesh, F. Khan, M.K. Ahmed, P. Velavendan, N.K. Pandey, U. Kamachi Mudali, Spectrophotometric determination of trace amounts of phosphate in water and soil, *Water Sci. Technol.* 66 (2012) 2653–2658, (<https://doi.org/10.2166/wst.2012.468>).
- [9] M.A.P. Mahmud, F. Ejeian, S. Azadi, M. Myers, B. Pejčić, R. Abbassi, A. Razmjou, M. Asadnia, Recent progress in sensing nitrate, nitrite, phosphate, and ammonium in aquatic environment, *Chemosphere* 259 (2020), 127492, (<https://doi.org/10.1016/j.chemosphere.2020.127492>).
- [10] H. LeThanh, B. Lendl, Sequential injection Fourier transform infrared spectroscopy for the simultaneous determination of organic acids and sugars in soft drinks employing automated solid phase extraction, *Anal. Chim. Acta* 422 (2000) 63–69, ([https://doi.org/10.1016/S0003-2670\(00\)01019-9](https://doi.org/10.1016/S0003-2670(00)01019-9)).
- [11] C.K. Akhgar, V. Nürnberger, M. Nadvornik, V. Ramos-Garcia, I. Ten-Doménech, J. Kuligowski, A. Schwaighofer, E. Rosenberg, B. Lendl, Fatty acid determination in human milk using attenuated total reflection infrared spectroscopy and solvent-free lipid separation, *Appl. Spectrosc.* 76 (2022) 730–736, (<https://doi.org/10.1177/00037028211065502>).
- [12] A. Edelmann, J. Diewok, J.R. Baena, B. Lendl, High-performance liquid chromatography with diamond ATR–FTIR detection for the determination of carbohydrates, alcohols and organic acids in red wine, *Anal. Bioanal. Chem.* 376 (2003) 92–97, (<https://doi.org/10.1007/s00216-003-1879-0>).
- [13] I.F. Duarte, A. Barros, C. Almeida, M. Spraul, A.M. Gil, Multivariate analysis of NMR and FTIR data as a potential tool for the quality control of beer, *J. Agric. Food Chem.* 52 (2004) 1031–1038, (<https://doi.org/10.1021/jf030659z>).
- [14] B. Muik, B. Lendl, A. Molina-Diaz, M. Valcarcel, M.J. Ayora-Cañada, Two-dimensional correlation spectroscopy and multivariate curve resolution for the study of lipid oxidation in edible oils monitored by FTIR and FT-Raman spectroscopy, *Anal. Chim. Acta* 593 (2007) 54–67, (<https://doi.org/10.1016/j.aca.2007.04.050>).
- [15] H. Tiernan, B. Byrne, S.G. Kazarian, ATR-FTIR spectroscopy and spectroscopic imaging for the analysis of biopharmaceuticals, *Spectrochim. Acta A Mol. Biomol. Spectrosc.* 241 (2020), 118636, (<https://doi.org/10.1016/j.saa.2020.118636>).
- [16] D.C. Sigeo, A. Dean, E. Levado, M.J. Tobin, Fourier-transform infrared spectroscopy of *Pediastrum duplex*: characterization of a micro-population isolated from a eutrophic lake, *Eur. J. Phycol.* 37 (2002) 19–26, (<https://doi.org/10.1017/S0967026201003444>).
- [17] ASTM Standard D7678–11, Standard Test Method for Total Oil and Grease (TOG) and Total Petroleum Hydrocarbons (TPH) in Water and Wastewater with Solvent Extraction using Mid-IR Laser Spectroscopy, ASTM International, West Conshohocken, PA, 2011, (<https://doi.org/10.1520/D7678-17>).
- [18] R. Vonach, B. Lendl, R. Kellner, Modulation of the pH in the determination of phosphate with flow injection and fourier transform infrared detection, *Analyst* 122 (1997) 525–530, (<https://doi.org/10.1039/A608540G>).
- [19] S. Dzurenova, B. Zimmermann, A. Kohler, V. Tafintseva, O. Slany, M. Certik, V. Shapaval, Microcultivation and FTIR spectroscopy-based screening revealed a nutrient-induced co-production of high-value metabolites in oleaginous *Mucoromycota* fungi, *PLoS One* 15 (2020), e0234870, (<https://doi.org/10.1371/journal.pone.0234870>).
- [20] S. Garrigues, T. Vidal, M. Gallignani, M. de la Guardia, On-line preconcentration and flow analysis-fourier transform infrared determination of carbaryl, *Analyst* 119 (1994) 659–664, (<https://doi.org/10.1039/AN9941900659>).
- [21] D. Perez-Guaita, Z. Richardson, P. Héraud, B. Wood, Quantification and identification of microproteinuria using ultrafiltration and ATR-FTIR spectroscopy, *Anal. Chem.* 92 (2020) 2409–2416, (<https://doi.org/10.1021/acs.analchem.9b03081>).
- [22] R. Krska, E. Rosenberg, K. Taga, R. Kellner, A. Messina, A. Katzir, Polymer coated silver halide infrared fibers as sensing devices for chlorinated hydrocarbons in water, *Appl. Phys. Lett.* 61 (1992) 1778–1780, (<https://doi.org/10.1063/1.108424>).
- [23] B. Baumgartner, J. Hayden, A. Schwaighofer, B. Lendl, In situ IR spectroscopy of mesoporous silica films for monitoring adsorption processes and trace analysis, *ACS Appl. Nano Mater.* 1 (2018) 7083–7091, (<https://doi.org/10.1021/acsam.8b01876>).
- [24] Y. Lu, L. Han, C.J. Brinker, T.M. Niemczyk, G.P. Lopez, Chemical sensors based on hydrophobic porous sol-gel films and ATR-FTIR spectroscopy, *Sens. Actuators B Chem.* 36 (1996) 517–521, ([https://doi.org/10.1016/S0925-4005\(97\)80122-0](https://doi.org/10.1016/S0925-4005(97)80122-0)).
- [25] Q. Qin, Y. Xu, Enhanced nitrobenzene adsorption in aqueous solution by surface silylated MCM-41, *Microporous Mesoporous Mater.* 232 (2016) 143–150, (<https://doi.org/10.1016/j.micromeso.2016.06.018>).
- [26] D. Wacht, M. David, B. Hinkov, H. Detz, A. Schwaighofer, B. Baumgartner, B. Lendl, Mesoporous zirconia coating for sensing applications using attenuated total reflection fourier transform infrared (ATR FT-IR) spectroscopy, *Appl. Spectrosc.* 76 (2021) 141–149, (<https://doi.org/10.1177/00037028211057156>).
- [27] B. Baumgartner, J. Hayden, B. Lendl, Mesoporous silica films for sensing volatile organic compounds using attenuated total reflection spectroscopy, *Sens. Actuators B Chem.* 302 (2020), 127194, (<https://doi.org/10.1016/j.snb.2019.127194>).
- [28] B. Baumgartner, S. Freitag, C. Gasser, B. Lendl, A pocket-sized 3D-printed attenuated total reflection-infrared filterometer combined with functionalized silica films for nitrate sensing in water, *Sens. Actuators B Chem.* 310 (2020), 127847, (<https://doi.org/10.1016/j.snb.2020.127847>).
- [29] T. Nur, M.A.H. Johir, P. Loganathan, T. Nguyen, S. Vigneswaran, J. Kandasamy, Phosphate removal from water using an iron oxide impregnated strong base anion exchange resin, *J. Ind. Eng. Chem.* 20 (2014) 1301–1307, (<https://doi.org/10.1016/j.jiec.2013.07.009>).
- [30] R. Lu, B. Mizaikoff, W.-W. Li, C. Qian, A. Katzir, Y. Raichlin, G.-P. Sheng, H.-Q. Yu, Determination of chlorinated hydrocarbons in water using highly sensitive mid-infrared sensor technology, *Sci. Rep.* 3 (2013) 2525, (<https://doi.org/10.1038/srep02525>).
- [31] O.M. Yaghi, G. Li, H. Li, Selective binding and removal of guests in a microporous metal-organic framework, *Nature* 378 (1995) 703–706, (<https://doi.org/10.1038/378703a0>).
- [32] S. Choi, T. Watanabe, T.-H. Bae, D.S. Sholl, C.W. Jones, Modification of the Mg/DOBDC MOF with amines to enhance CO₂ adsorption from ultradilute gases, *J. Phys. Chem. Lett.* 3 (2012) 1136–1141, (<https://doi.org/10.1021/jz300328j>).
- [33] K. Yang, F. Xue, Q. Sun, R. Yue, D. Lin, Adsorption of volatile organic compounds by metal-organic frameworks MOF-177, *J. Environ. Chem. Eng.* 1 (2013) 713–718, (<https://doi.org/10.1016/j.jece.2013.07.005>).
- [34] R. El Osta, A. Carlin-Sinclair, N. Guillou, R.I. Walton, F. Vermoortele, M. Maes, D. de Vos, F. Millange, Liquid-phase adsorption and separation of xylene isomers by the flexible porous metal-organic framework MIL-53(Fe), *Chem. Mater.* 24 (2012) 2781–2791, (<https://doi.org/10.1021/cm301242d>).
- [35] N.A. Khan, Z. Hasan, S.H. Jung, Adsorptive removal of hazardous materials using metal-organic frameworks (MOFs): A review, *J. Hazard. Mater.* 244–245 (2013) 444–456, (<https://doi.org/10.1016/j.jhazmat.2012.11.011>).
- [36] S.H. Jung, J.H. Lee, J.W. Yoon, C. Serre, G. Férey, J.S. Chang, Microwave synthesis of chromium terephthalate MIL-101 and its benzene sorption ability, *Adv. Mater.* 19 (2007) 121–124, (<https://doi.org/10.1002/adma.200601604>).

- [37] X. Fang, B. Zong, S. Mao, Metal-organic framework-based sensors for environmental contaminant sensing, *Nano Micro Lett.* 10 (2018) 64, <https://doi.org/10.1007/s40820-018-0218-0>.
- [38] M.R. Tchalala, P.M. Bhatt, K.N. Chappanda, S.R. Tavares, K. Adil, Y. Belmabkhout, A. Shkurenko, A. Cadiou, N. Heymans, G. De Weireld, G. Maurin, K.N. Salama, M. Eddaoudi, Fluorinated MOF platform for selective removal and sensing of SO₂ from flue gas and air, *Nat. Commun.* 10 (2019) 1328, <https://doi.org/10.1038/s41467-019-09157-2>.
- [39] H.-Y. Li, S.-N. Zhao, S.-Q. Zang, J. Li, Functional metal-organic frameworks as effective sensors of gases and volatile compounds, *Chem. Soc. Rev.* 49 (2020) 6364–6401, <https://doi.org/10.1039/C9CS00778D>.
- [40] M.Y. Zorainy, M. Gar Alalam, S. Kaliaguine, D.C. Boffito, Revisiting the MIL-101 metal-organic framework: design, synthesis, modifications, advances, and recent applications, *J. Mater. Chem. A* 9 (2021) 22159–22217, <https://doi.org/10.1039/D1TA06238G>.
- [41] W.P. Lustig, S. Mukherjee, N.D. Rudd, A.V. Desai, J. Li, S.K. Ghosh, Metal-organic frameworks: functional luminescent and photonic materials for sensing applications, *Chem. Soc. Rev.* 46 (2017) 3242–3285, <https://doi.org/10.1039/C6CS00930A>.
- [42] P. Kumar, A. Deep, K.-H. Kim, Metal organic frameworks for sensing applications, *Trends Anal. Chem.* 73 (2015) 39–53, <https://doi.org/10.1016/j.trac.2015.04.009>.
- [43] D. Zhao, X. Wan, H. Song, L. Hao, Y. Su, Y. Lv, Metal-organic frameworks (MOFs) combined with ZnO quantum dots as a fluorescent sensing platform for phosphate, *Sens. Actuators B Chem.* 197 (2014) 50–57, <https://doi.org/10.1016/j.snb.2014.02.070>.
- [44] Q. Xie, Y. Li, Z. Lv, H. Zhou, X. Yang, J. Chen, H. Guo, Effective adsorption and removal of phosphate from aqueous solutions and eutrophic water by Fe-based MOFs of MIL-101, *Sci. Rep.* 7 (2017) 3316, <https://doi.org/10.1038/s41598-017-03526-x>.
- [45] S. Bauer, C. Serre, T. Devic, P. Horcajada, J. Marrot, G. Férey, N. Stock, High-throughput assisted rationalization of the formation of metal organic frameworks in the iron(III) aminoterephthalate solvothermal system, *Inorg. Chem.* 47 (2008) 7568–7576, <https://doi.org/10.1021/ic800538r>.
- [46] T. Degen, M. Sadki, E. Bron, U. König, G. Nénert, The highscore suite, *Powder Diffr.* 29 (2014) S13–S18, <https://doi.org/10.1017/S0885715614000840>.
- [47] G. Ramer, B. Lendl, Attenuated total reflection fourier transform infrared spectroscopy, in: R.A. Meyers, R.A. Meyers (Eds.), *Encyclopedia of Analytical Chemistry*, John Wiley & Sons, 2013.
- [48] S. Freitag, B. Baumgartner, S. Radel, A. Schwaighofer, A. Varriale, A. Pennacchio, S. D'Auria, B. Lendl, A thermoelectrically stabilized aluminium acoustic trap combined with attenuated total reflection infrared spectroscopy for detection of *Escherichia coli* in water, *Lab Chip* 21 (2021) 1811–1819, <https://doi.org/10.1039/D0LC01264E>.
- [49] C. Wagner, A. Genner, G. Ramer, B. Lendl, Advanced total lab automation system (ATLAS), in: R.D. Asmundis (Ed.), *Modeling, Programming and Simulations Using LabVIEW™ Software*, IntechOpen, 2011.
- [50] L. Shao, Z. Yu, X. Li, X. Li, H. Zeng, X. Feng, Carbon nanodots anchored onto the metal-organic framework NH₂-MIL-88B(Fe) as a novel visible light-driven photocatalyst: Photocatalytic performance and mechanism investigation, *Appl. Surf. Sci.* 505 (2020), 144616, <https://doi.org/10.1016/j.apsusc.2019.144616>.
- [51] C.C.R. Sutton, G. daSilva, G.V. Franks, Modeling the IR spectra of aqueous metal carboxylate complexes: correlation between bonding geometry and stretching mode wavenumber shifts, *Chem. Eur. J.* 21 (2015) 6801–6805, <https://doi.org/10.1002/chem.201406516>.
- [52] T.A. Vu, G.H. Le, H.T. Vu, K.T. Nguyen, T.T.T. Quan, Q.K. Nguyen, H.T.K. Tran, P. T. Dang, L.D. Vu, G.D. Lee, Highly photocatalytic activity of novel Fe-MIL-88B/GO nanocomposite in the degradation of reactive dye from aqueous solution, *Mater. Res. Express* 4 (2017), 035038, <https://doi.org/10.1088/2053-1591/aa6079>.
- [53] T.K. Mahto, A.R. Chowdhuri, B. Sahoo, S.K. Sahu, Polyaniline-functionalized magnetic mesoporous nanocomposite: A smart material for the immobilization of lipase, *Polym. Compos.* 37 (2016) 1152–1160, <https://doi.org/10.1002/pc.23278>.
- [54] Z.U. Zango, K. Jumbri, N.S. Sambudi, N.H. Hanif Abu Bakar, N.A. Fathihah Abdullah, C. Basheer, B. Saad, Removal of anthracene in water by MIL-88(Fe), NH₂-MIL-88(Fe), and mixed-MIL-88(Fe) metal-organic frameworks, *RSC Adv.* 9 (2019) 41490–41501, <https://doi.org/10.1039/C9RA08660A>.
- [55] H. Guo, B. Niu, X. Wu, Y. Zhang, S. Ying, Effective removal of 2,4,6-trinitrophenol over hexagonal metal-organic framework NH₂-MIL-88B(Fe), *Appl. Organo Chem.* 33 (2019), e4580, <https://doi.org/10.1002/aoc.4580>.
- [56] P.A. Connor, A.J. McQuillan, Phosphate adsorption onto TiO₂ from aqueous solutions: an in situ internal reflection infrared spectroscopic study, *Langmuir* 15 (1999) 2916–2921, <https://doi.org/10.1021/la980894p>.
- [57] G.L. Long, J.D. Winefordner, Limit of detection. A closer look at the IUPAC definition, *Anal. Chem.* 55 (1983) 712A–724A, <https://doi.org/10.1021/ac00258a001>.
- [58] J. Mocak, A.M. Bond, S. Mitchell, G. Scollary, A statistical overview of standard (IUPAC and ACS) and new procedures for determining the limits of detection and quantification: Application to voltammetric and stripping techniques, *Pure Appl. Chem.* 69 (1997) 297–328, <https://doi.org/10.1351/pac199769020297>.
- [59] J.S. Geelhoed, T. Hiemstra, W.H. Van Riemsdijk, Phosphate and sulfate adsorption on goethite: Single anion and competitive adsorption, *Geochim. Cosmochim. Acta* 61 (1997) 2389–2396, [https://doi.org/10.1016/S0016-7037\(97\)00096-3](https://doi.org/10.1016/S0016-7037(97)00096-3).

Felix Frank holds an MSc in technical chemistry specialised on high performance materials from TU Wien in 2020. During his master thesis he worked on microporous networks in polymer derived ceramics, tailored for gas permeation. He is now an early-stage researcher working on his PhD in the Lendl lab. In his research, he focuses on the combination of porous materials with photonic technologies.

Bettina Baumgartner holds a MSc in technical chemistry specialized on applied synthetic chemistry from TU Wien (2016). In December 2019, she completed her PhD from TU Wien supervised by Prof. Bernhard Lendl, where she combined porous materials with IR spectroscopy to gain insights into chemical and physical processes within these materials. In 2020, she joined Prof. Masahide Takahashi's group at Osaka Prefecture University, Japan, as a JSPS research fellow, where she worked on in situ investigations of MOF growth mechanisms and adsorption phenomena into MOFs. Since 2021, Bettina is a FWF Schrödinger research fellow in the group of Prof. Bert M. Weckhuysen at Utrecht University, The Netherlands, where she works on operando spectroscopy of photoactive MOFs.

Prof. Dr. Bernhard Lendl received his PhD degree in Technical Chemistry from TU Wien in 1996. In 2001 he became associate professor at TU Wien. Since 2011 he heads the research division on Environmental and Process Analytical Chemistry at TU Wien where he was also appointed full professor for Vibrational Spectroscopy in 2016. His research focuses on advancing analytical sciences through the development of novel analytical techniques and instrumentation based on infrared and Raman spectroscopy and their application to environmental and process analytical chemistry, material characterization as well as bio-medical diagnostics. Lendl is recipient of the Norman Sheppard Award from the IRDG (2022), the Agilent Thought Leader Award (2021), the Anton Paar Research Award (2018), the Robert Kellner Lecture DAC (EuChemS) in 2015, the FACSS Innovation Award in 2011 and the Dr. Wolfgang Houska Award (B&C foundation) in 2008.

A.2. Publication II: Integrated optics waveguides and mesoporous oxides for the monitoring of volatile organic compound traces in the mid-infrared

This accepted publication was still in production process at the time of submitting this thesis, therefore, the submitted document without journal formatting is included.

Integrated optics waveguides and mesoporous oxides for the monitoring of volatile organic compound traces in the mid-infrared

Felix Frank¹, Bettina Baumgartner^{1,2}, Mattias Verstuyft³, Nuria Teigell Beneitez³, Jeroen Missinne⁴, Dries Van Thourhout³, Gunther Roelkens³, and Bernhard Lendl^{1*}.

¹ Research Division of Environmental Analytics, Process Analytics and Sensors, Institute of Chemical Technologies and Analytics, TU Wien, Getreidemarkt 9, 1060 Vienna, Austria

² Van't Hoff Institute for Molecular Sciences, University of Amsterdam, Science Park 904, 1098 XH Amsterdam, The Netherlands

³ Photonics Research Group, Ghent University-imec, Technologiepark-Zwijnaarde 126, 9052 Gent, Belgium

⁴ Center for Microsystems Technology, Ghent University-imec, Technologiepark-Zwijnaarde 126, 9052 Gent, Belgium

Corresponding Author(s):

* E-Mail: bernhard.lendl@tuwien.ac.at

Postal address: Institute of Chemical Technologies and Analytics, TU Wien, Getreidemarkt 9/164-UPA, 1060 Vienna, Austria

Abstract:

Volatile organic compounds (VOCs) are an ever-growing hazard for health and environment due to their increased emissions and accumulation in the air. Quantum-cascade laser-based infrared (QCL-IR) sensors hold significant promise for gas monitoring, thanks to their compact, rugged design, high laser intensity, and high molecule-specific detection capabilities within the mid-infrared (mid-IR) spectrum's fingerprint region. In this work, tunable external-cavity QCLs were complemented by an innovative germanium-on-silicon integrated optics waveguide sensing platform with integrated microlenses for efficient back-side optical interfacing for the tunable laser spectrometer. The waveguide chip was coated with a mesoporous silica coating, thereby increasing the signal by adsorptive enhancement of volatile organic compounds (VOCs) while at the same time limiting water vapor interferences. Different least square fitting methods were explored to deconvolute the resulting spectra, showing sub-ppmv limits of detection and enrichment factors of up to 22,000 while keeping the footprint of the setup small (29x23x11 cm³). Finally, a use-case simulation for the continuous detection of VOCs in a process analytical technology (PAT) environment confirmed the high potential of the technique for the monitoring of contaminants. By successfully demonstrating the use of photonic waveguides for the monitoring of VOCs, this work offers a promising avenue for the further development of fully integrated sensors on a chip.

Keywords: Mid-IR spectroscopy, mesoporous materials, functional coating, integrated optics sensing, volatile organic compounds

Introduction

Volatile organic compounds (VOCs) are a class of organic compounds with high vapor pressure at atmospheric conditions. Anthropogenic VOC emissions are formed during combustion processes, in the paint and ink industry, the generation of fossil fuels, and farming. They account for total global emissions of 100 Mt per year. ¹ Many of those show harmful effects on humans, animals, and plants alike and are

classified as environmental contaminants.² Therefore, it is important to continuously monitor their concentrations, especially in high exposure environments such as gas stations, industry, and indoors. Here, concentrations can peak into the ppmv-range.^{3,4} The increasing need for environmental protection and personal safety has driven the development of a wide range of VOC sensors,⁵ among them (electro)chemical VOC sensors,⁶ gravimetric sensors,⁷ or non-targeted approaches using gas chromatography coupled with mass spectrometry (GC-MS).⁸ However, these sensors suffer from limitations such as lack of selectivity, interference with other compounds in the air (e.g., water vapor), or high cost and bulkiness, as is the case with GC-MS. Consequently, detecting low concentrations of VOCs from a complex atmosphere remains a significant challenge.

Mid-infrared (mid-IR) spectroscopy probes the characteristic ro-vibrational modes of molecules and shows great promise to selectively detect volatile organic compounds (VOCs) in complex atmospheres.⁹ Going beyond traditional Fourier transform infrared (FT-IR) spectroscopy, quantum cascade lasers (QCL) or interband cascade lasers (ICL) can be employed, making use of their inherently high intensity to enable higher sensitivities.¹⁰ However, to reach the high sensitivities needed for trace gas analysis in absorption mid-IR spectroscopy, long interaction lengths are needed. These are typically realized by employing bulky and expensive multi-pass cells, also necessitating high sample volumes.¹¹

For more compact devices, sensing schemes based on indirect absorption, such as the photothermal and photoacoustic effects can be employed, reaching limits of detection (LODs) down to the pptv range.^{12,13} For multi-gas sensing, the non-broadband nature of these very sensitive and selective devices once again results in bulkier designs.¹⁴ Integrated evanescent field sensing schemes based on mid-IR QCL spectroscopy and waveguides have been demonstrated. They offer very small footprints and broadband application going towards a Lab-on-a-Chip approach.¹⁵ However, the propagation losses in the mid-IR region, which are still in the range of 10 dB cm⁻¹ for most waveguides or 2.5 dB cm⁻¹ for more efficient Ge-on-Si systems,¹⁶ limit the optical path lengths for gas sensing applications.

By employing enrichment layers, the concentration of target analytes in the probed volume of the waveguide can be locally increased. Hence, the sensitivity of waveguide-based sensing schemes can be enhanced while reducing the pathlengths and, thus, propagation losses. One approach can be the preconcentration of analytes before interaction with the sensor, which has been demonstrated successfully for other sensing methods such as gas chromatography,¹⁷ sensors based on surface acoustic waves,¹⁸ or a combination of complementary sensors.¹⁹ In recent years, it has also been shown that the use of thin layers of various materials can significantly improve the sensitivity of evanescent field sensing schemes by acting as preconcentrators for VOCs. These materials include polymers for VOCs in water,²⁰ metal oxides,²¹ and mesoporous materials (e.g. mesoporous silica).²² Our recent report also showed a proof of concept using enrichment layers for Ge-on-Si systems, reaching low ppm LODs for toluene in water.²³

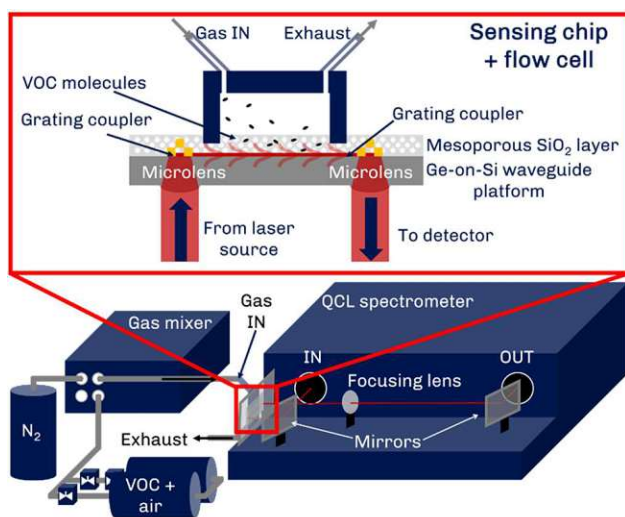


Figure 1: Schematic depiction of the multi-gas sensing platform and the enrichment concept and the gas sampling system as employed in this report. The sample VOC gas cylinder (VOC + air) and N₂ for the dilution are connected to the gas mixer supplying the sensing chip with sample gas mixtures at a constant flow.

In this contribution, we present a multi-gas sensor based on our previously presented platform, as outlined in Figure 1. In our approach, the QCL light is coupled into the Ge-on-Si optical waveguides from the backside of the chip using monolithically integrated microlenses and grating couplers. The waveguide is complimented by a mesoporous silica coating, which allows for the enrichment of target analytes from the gas phase. The hydrophobic nature of the coating excludes water vapor from the probed volume of the waveguide. This significantly reduces the strong water vapor interferences with the characteristic fingerprint bands of VOCs.²⁴ The waveguide platform is mounted in an external cavity-QCL-based mid-IR spectrometer with a tuning range between 1750 and 1350 cm⁻¹, covering the propagating wavelength range of 6.5-7.5 μm (1540-1335 cm⁻¹) of the waveguide. For the validation of the sensor, we chose three different aromatic VOCs, namely, toluene, p-xylene, and 1,2,4-trimethylbenzene. We applied vapor samples of the individual VOCs as well as different VOC mixtures to the sensor, demonstrating sub-ppmv limits of detection and high stability against water vapor traces. Deconvolution of the overlapping spectra was performed using least square fitting methods such as multivariate curve resolution alternate least squares (MCR-ALS), with different algorithms evaluated in respect to the real-time applicability. This was then showcased in a sensor use-case simulation, where we determined the response and stability of the sensor. Although improvements in the long-term stability of the sensor still need to be made, we believe that this work facilitates future advances of moving integrated photonic technologies further towards real world applicability.

Experimental Section

Materials

Ethanol (EtOH, Chem-Lab, 100 % p.a.), tetraethoxysilane (TEOS, Sigma Aldrich 99.5%), hydrochloric acid (HCl, VWR, 37%), cetyltrimethylammonium bromide (CTAB, Sigma Aldrich, 99%), hexamethyl-disilazane (HMDS, TCI Chemicals, >96.0%), toluene (VWR AnalaR NORMAPUR, 99.8%), p-xylene (Merck, 99%), 1,2,4-trimethylbenzene (Sigma Aldrich, p.s.) were used as received. Absolute acetone (Sigma-Aldrich, 99%) used for surface functionalization was dried over molecular sieves. Acetone and isopropyl alcohol (IPA) for rinsing the chips were used in technical quality.

Peak deconvolution using least-squares fitting

The nature of absorption spectra being linearly dependent on the concentration c of the analyte as described in the Beer-Lambert law (1) can be used for peak deconvolution using least-squares fitting (2). By assuming the total spectrum D of a multi-component mixture being the product of a loading matrix C , which is directly correlating to the concentration of the respective analytes, and a spectral matrix S^T , which consists of the pure component spectra, one can perform least squares fitting to keep the square of the residual matrix E minimal.

$$A = \epsilon \cdot c \cdot d \quad (1)$$

$$D = C \cdot S^T + E \quad (2)$$

For spectral analysis, there are plentiful methods that have been successfully applied in order to solve (2).^{25, 26} In this report, we compared two of those algorithms being non-negative least squares fitting (NNLS) and multivariate curve resolution alternating least squares (MCR-ALS). These algorithms were chosen in order to compare the performance of a very powerful algorithm such as MCR-ALS to the basic NNLS. NNLS is an extension of the basic ordinary least squares fitting (OLS) algorithm by means of the constraint of all elements of the loading matrix being larger than 0, needing pure component spectra as input to find the solution with the lowest residuals.

On the other hand, MCR-ALS is a very powerful soft-modeling technique that can be used without knowing the pure component spectra but requires more computational power and calculation time. It iteratively improves the loading and spectral matrices starting from an initial estimation until a threshold value for the standard deviation of the residual matrix is reached. In the used MATLAB toolbox,²⁷ the number of components was determined to be three to account for all three applied VOCs (four components were also tried to account for water, with no tangible improvement), with the initial estimate being generated using a method similar to the SIMPLISIMA algorithm.²⁸ We chose non-negative constraints for both the spectral and concentration matrices. For the comparison of the execution times, we used a desktop computer with an AMD Ryzen 5 3600 processor and 16 GB of RAM.

Fabrication of the integrated optics waveguide sensor

The sensor fabrication consists of three different parts: fabricating the grating couplers and waveguides, fabricating the microlenses, and applying the mesoporous coating.

After cleaving the sample from a 4-inch Ge-on-Si wafer, a photoresistive coating (MIR701) was spin-coated onto the sample. Using UV-lithography, we patterned the grating coupler and waveguide layout into the photoresist. This pattern was then transferred onto the 2 μm thick germanium layer in one etch step through reactive ion etching (RIE) with a mixture of CF_4 , SF_6 , and H_2 , etching 1 μm of Ge. We subsequently removed the remaining photoresist by rinsing with acetone, IPA, and deionized water and then using an oxygen plasma. Another UV-lithography step was used for a lift-off process so that a reflective layer of 1 μm of gold, deposited using e-gun evaporation, only covered the grating couplers.

Before defining the microlenses on the backside, we protected the top side with a thick layer of photoresist. Then, we polished the backside to minimize scattering effects. We applied a thick layer of AZ4562 (12 μm) to the backside and patterned it with UV-lithography, leaving cylinders with a diameter of 250 μm . These were then reflowed on a hotplate at 150°C, resulting in nearly spherical structures. These structures were transferred from the photoresist layer into the silicon using RIE with an SF_6 , O_2 gas mixture and finally covered with a 900 nm thick Si_xN_y antireflective coating using plasma-enhanced chemical vapor deposition (PECVD). Finally, we removed the photoresist from the top by again rinsing in acetone, IPA, and deionized water and freed the surface from any remaining residues using an oxygen plasma.

We prepared the sensing layer based on mesoporous silica with an ordered 3D hexagonal pore structure in accordance with our previously reported method.²⁹ Three films were spin-coated onto the waveguide

chip by using a sol solution with a molar ratio of 1:13:5:5·10⁻³:0.12 for TEOS:EtOH:H₂O:HCl:CTAB. Between each coating step, the layers were annealed at 110 °C overnight. After the deposition of the three layers, we performed surface functionalization and template removal as previously reported.²⁹

Laser-based mid-IR spectroscopy

For recording the IR spectra, we used the ChemDetect Analyzer (DRS Daylight Solutions, USA), a commercially available external cavity-quantum cascade laser-based mid-IR spectrometer with a tuning range between 1750 and 1350 cm⁻¹. During operation, the laser head was water cooled to 17 °C. We acquired the spectra using the proprietary ChemDetect software, with one spectrum consisting of 30 scans averaged over 15 s. The sensor chip was mounted in a custom-built waveguide mount we adapted from our previously reported add-on unit²³ for laser spectrometers to comply with the dimensions of the ChemDetect Analyzer. We determined the noise level and the transmittivity of the sensor by collecting 100% lines of the sensor flushed with N₂.

Sample preparation

The pure gas samples and gas mixtures were prepared using an adapted protocol from a previous report.²² For this, 400-600 μL of the liquid VOCs were injected into a PTFE tubing connected to the evacuated gas reservoir (2 x 10 L Festo CRVZS Series, connected with stainless steel tubing). After filling the reservoir with pressurized air to 7 bar, the filled gas cylinder was then connected to an MCQ GB100 gas mixer (MCQ instruments, Italy) via a pressure reducing valve to ensure a 1.5 bar operating pressure. N₂ was connected to the second inlet of the gas mixer to dilute the gas samples.

To determine the VOC concentrations of the diluted gas samples, the outlet of the gas mixer was connected to a 4 cm gas transmission cell mounted in a Vertex 70V FT-IR spectrometer (Bruker, Germany) equipped with a liquid nitrogen cooled mercury cadmium telluride (MCT) detector (InfraRed Associates, D* = 4 × 10¹⁰ cm Hz^{0.5} W⁻¹ at 9.2 μm). Using this setup, the transmission cell was flushed with dilutions of the gas samples (with 2 % steps between 0 % and 10 % and 10 % steps between 10 % and 100 %) and collected the spectra with the OPUS 8.1 software. They were recorded using a spectral resolution of 2 cm⁻¹, 32 scans per spectrum (double-sided, backward forward acquisition mode). During all measurements, the sample compartment was flushed with dry air. The VOC concentrations were obtained by deconvoluting the mixed spectra using a MATLAB R2021a script by applying an MCR-ALS algorithm to the collected spectra in the spectral range of the skeletal vibrations of the aromatic rings of the VOCs between 1400 and 1600 cm⁻¹. The corresponding concentrations were calculated by multiplying the loadings with the respective pure spectra and comparing the areas with reference spectra (1 ppm, 1 m path length) from the PNNL database (for 1,2,4-trimethylbenzene, the spectrum of 1,2,3-trimethylbenzene was used under the assumption of a similar total absorption in the analyzed region).

Sensor calibration

For the demonstration of the sensing capabilities, we applied several dilutions of VOC samples with concentrations between 0-800 ppmv (for the more volatile toluene) and 0-200 ppmv (for the less volatile p-xylene and 1,2,4-trimethylbenzene) to the sensing unit using a total flow rate of 500 mL min⁻¹. We tested the response of the sensor by applying a gas mixture of all three VOCs and determined the time it took for the equilibrium concentration and a subsequent sensor regeneration to be reached.

For the calibration of the sensor, we applied pure VOC samples and all possible combinations at a total flow rate of 500 mL min⁻¹ for 3 min, followed by a flushing step for another 3 min. We obtained the peak areas of the respective VOC components by deconvoluting the mixed spectra using a MATLAB R2021a script by applying an NNLS algorithm to the collected spectra in the spectral range of the skeletal vibrations of the aromatic rings of the adsorbed VOCs between 1490 and 1525 cm⁻¹ using Lorentzian functions as pure component spectra. We then calculated the calibration function by multiplying the loadings with the respective pure spectra and fitting the data using the Freundlich adsorption model.

Use case simulation

For the demonstration of the sensing capabilities in a more realistic experimental setup, we applied dilutions of a mixture containing all three VOCs with concentrations between 0-200 ppmv (for the more volatile toluene) and 0-100 ppmv (for the less volatile p-xylene and 1,2,4-trimethylbenzene) to the sensing unit using a total flow rate of 500 mL min⁻¹. To simulate a realistic application of the sensor, the concentrations of the dilution were increasing and decreasing over a time period of 66 min.

Next, we deconvoluted the mixed spectra by applying the same NNLS algorithm to the collected spectra in the spectral range of the skeletal vibrations of the aromatic rings of the adsorbed VOCs between 1490 and 1525 cm⁻¹ using Lorentzian functions as pure component spectra. Finally, we applied the calibration model to the deconvoluted spectra to obtain the measured concentrations of the respective VOC components.

Results and discussion

Evaluation of the sensing system

Figure 1 depicts a schematic of the sensing setup. The mounted chip is housed in a gas flow cell, which is fed with VOC mixtures from the outlet of the gas mixer. The two inlets of the gas mixer are connected to the VOC sample and N₂ used for dilution, respectively.

The transmittivity of the waveguide structure and the noise levels were determined by acquiring 100 % lines of the coated waveguide during N₂ flow. The single channel spectrum and 100 % lines are shown in Figure 2.

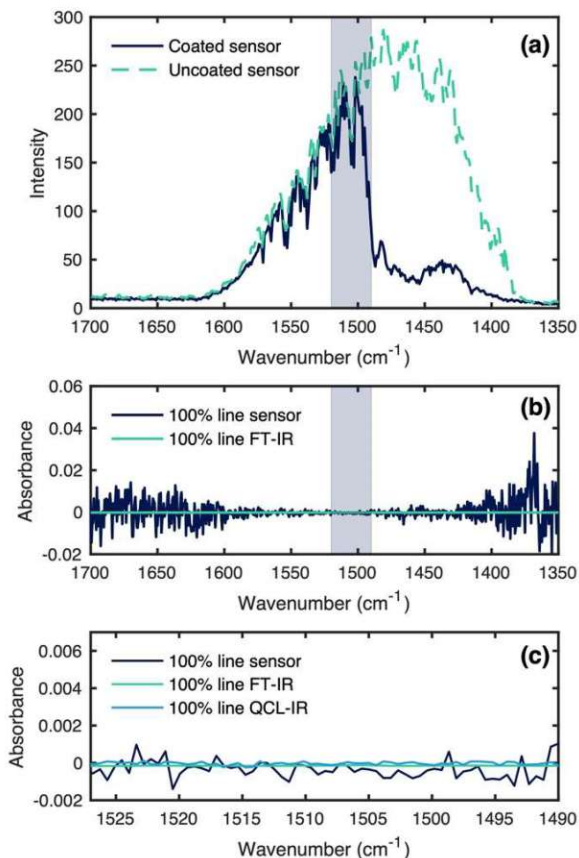


Figure 2: A: Single channel spectrum of the coated and uncoated waveguide, with the region of interest for VOC sensing marked, B: 100 % RMS lines of the sensor (blue) compared to a transmission cell in a FT-IR spectrometer, with the region of interest for VOC sensing marked, C: region of interest for VOC sensing shown zoomed out with 100 % RMS line of the QCL-IR spectrometer acquired in transmission.

The noise floor of the sensor was determined by evaluating the root mean square (RMS) noise of the 100 % lines in the spectral range from 1530 to 1490 cm^{-1} , resulting in a noise floor of 4.80×10^{-4} . This equates to about 46 times the noise of a 4 cm gas transmission cell in a high-end FT-IR spectrometer and 6 times the noise of the QCL-IR spectrometer in transmission mode using the same settings. The noise floor of the waveguides depends on the intensity of the signal reaching the detector and, thus, needs to be considered in relation to anticipated waveguide losses. The measured propagation losses at 1490 cm^{-1} equate to 4 dB (2.5 dB cm^{-1} , 1.6 cm waveguide length). Further losses are added at the microlenses and the grating coupler. Using a grating pitch of 1.87 μm in the simulations and combining these losses (microlenses + grating coupler), an optical interfacing efficiency of 10 % was calculated for 1490 cm^{-1} .²³ Other losses to be considered may be caused by absorptions by the mesoporous layer, as can be seen in Figure 2-A. However, the IR transmittance only decreases below 1490 cm^{-1} , and the losses caused by the silica cladding can be disregarded for VOC sensing. Nonetheless, the new QCL-based spectrometer allowed us to improve the noise level by a factor of 42 compared to our previous report.²³ The improvements of the noise floor can be attributed to the dynamic adjustment of the QCL spectrometer's laser power for lower transmission applications together with a generally more stable emission as well as the implementation of a more efficient and compact optical setup.

The characterization of the sensing layers confirmed the 3D hexagonal pore structure and a layer thickness of 1.71 μm , which covers the evanescent field of the waveguides. The results of the characterization are featured in the Supporting Information and are in accordance with our previous publications.^{29, 30}

Sensor calibration

For the initial calibration of the sensor, we applied several dilutions of samples of the individual VOC and all possible mixtures with concentrations between 0-800 ppmv (for the more volatile toluene) and 0-200 ppmv (for the less volatile p-xylene and 1,2,4-trimethylbenzene) to the sensing unit at a total flow rate of 500 mL min^{-1} . In Figure 3, the spectra of adsorbed p-xylene, toluene, and 1,2,4-trimethylbenzene are displayed in comparison to their gas phase spectra. The bands correspond to the respective skeletal ring vibrations in liquid phase at 1497 cm^{-1} (toluene), 1507 cm^{-1} (1,2,4-trimethylbenzene), and 1517 cm^{-1} (p-xylene). This is due to the formation of a condensed phase of adsorbed molecules and the interaction with other molecules, leading to broadening effects of the absorption bands, as can be seen in Figure 3-bottom. In addition, we found out that water vapor traces did not spectroscopically interfere with the recorded spectra. (Figure S6) This can be attributed to the hydrophobic surface functionalization of the mesoporous enrichment layer, which excludes water from the probed volume of the sensor.

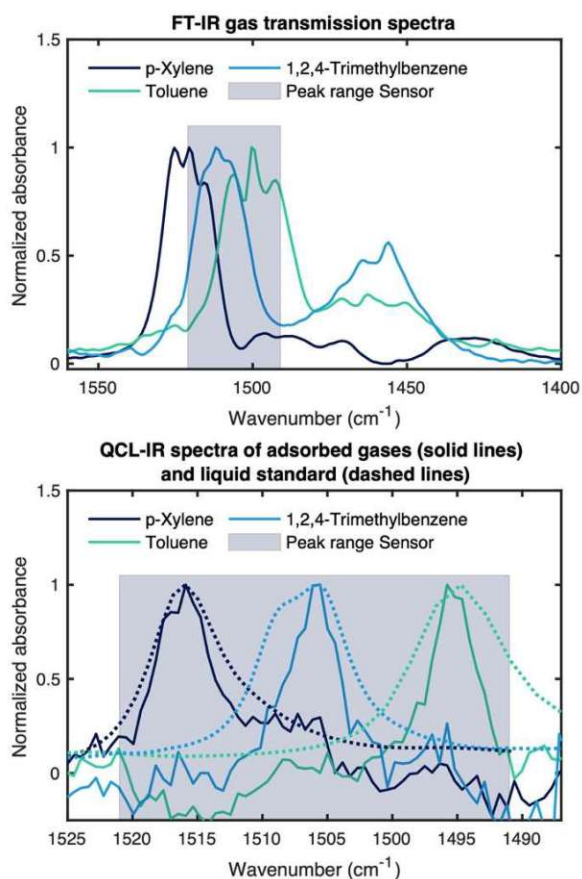


Figure 3: Top: Normalized FT-IR transmission spectra of gaseous *p*-xylene (dark blue), toluene (turquoise), and 1,2,4-Trimethylbenzene (light blue). Bottom: Normalized QCL-IR spectra of adsorbed *p*-xylene (87 ppmv, 1517 cm^{-1} , dark blue), toluene (263 ppmv, 1497 cm^{-1} , turquoise), and 1,2,4-Trimethylbenzene (57 ppmv, 1507 cm^{-1} , light blue) in the spectral region of their respective skeletal ring vibrations, dashed line spectra refer to the liquid standards measured for each respective VOC. The peak range of the sensor is featured as a grey box for scale in top and bottom, respectively.

The sensor response was derived from band areas as function of application time (Figure 4) to determine the optimal measurement time. The time needed to reach equilibrium (with the $t_{90\%}$ taken as metric, where 90 % of the enrichment has been reached) was 12 min and the regeneration time (with the $t_{10\%}$ taken as metric, where the signal has been fallen to 10 % of the full enrichment) was 60 min. This slow enrichment as compared to literature can be explained by the applied multiple coatings and a larger sensor area. Both result in a much greater pore volume in which the analytes can undergo diffusion in addition to a simple adsorption process (Figure 4-bottom) while not being covered by the single propagating waveguide. To ensure reasonable sensor response times, we chose an enrichment time of 3 min (shown as light blue in Figure 4-bottom) as a compromise between speed and performance.

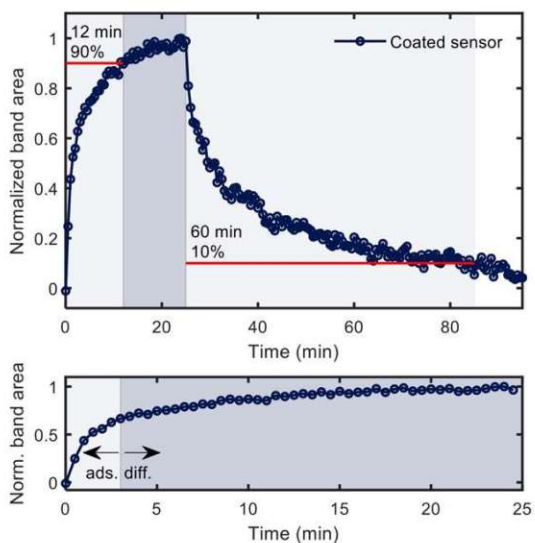


Figure 4: Sensor response during enrichment and regeneration for the enrichment of 198 ppmv 1,2,4-Trimethylbenzene (top), zoom into the initial enrichment, which is dominated by adsorption at the beginning and dominated by diffusion after 3 min (bottom).

The resulting QCL-IR spectra were fed into the non-negative least squares (NNLS) algorithm for deconvolution. The resulting pure component spectra were then integrated and plotted against the respective VOC concentration (Figure 5). The non-linear response was attributed to the prevailing adsorption mechanism, which is controlled by van der Waals interactions between the hydrophobic surface functionalization and the target analytes (as well as between the analytes themselves). We used the Freundlich adsorption model (3) to describe the system with the signal q_e , the concentration c , and the slope determined by the two constants K_F and n_F . The fit results can be found in Table S1.

$$q_e = K_F \cdot c^{\frac{1}{n_F}} \quad (3)$$

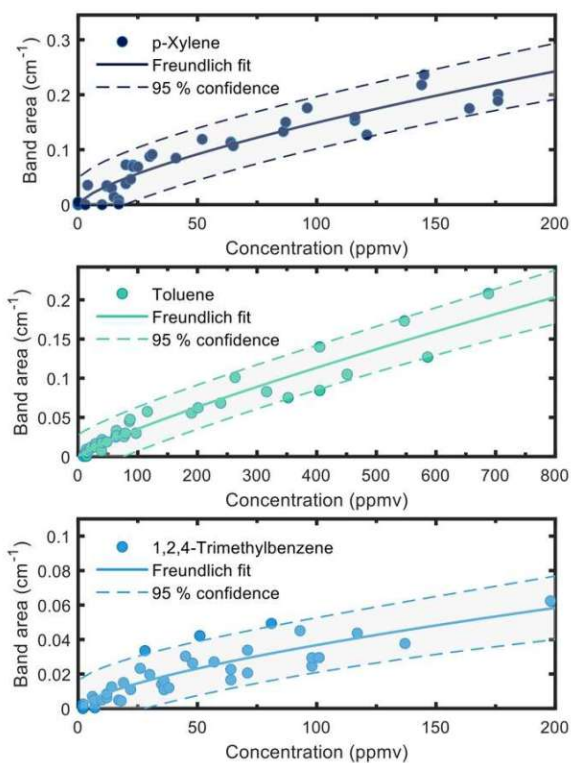


Figure 5: Sensor calibration for the three respective VOCs. Fitting was performed using the Freundlich adsorption isotherms (solid lines) with the 95 % confidence of the fit marked (dashed lines).

In Table 1, the performance parameters for FT-IR spectroscopy (4 cm pathlength) and the sensor are compared, at the concentration of the respective LODs (marked in grey), as well as 5 ppmv, 10 ppmv, 25 ppmv, and 50 ppmv. We approximated (4) the LODs as the concentration at which the signal equates to three times the noise σ .^{31, 32} This yields sub-ppmv LODs for the less volatile p-xylene and 1,2,4-trimethylbenzene, while for the more volatile toluene, the LOD is 2.1 ppmv. We calculated the signal-to-noise ratios (SNR) for each VOC at the displayed concentrations as the ratio of the respective signals divided by the RMS noise (5). The enrichment factors are calculated as the ratio of the signals (q_e) divided by the ratio of the pathlengths ($L = 4$ cm for the FT-IR and $L = 86 \mu\text{m}$ for the sensor) and is shown in (6). In a first approximation it is assumed that the absorption coefficients of the gas spectra of the analytes in the 4 cm cell are comparable with those of the adsorbed analyte in the waveguide.

In comparison to the high-end FT-IR spectrometer used for calibration of the gas-phase with a 4 cm pathlength, the mesoporous coating combined with the waveguide platform can perform at the same order of magnitude as the FT-IR concerning its SNR. Specifically, for p-xylene at a concentration of 5 ppmv, the SNR is 37 for the sensing platform, while the SNR of the FT-IR is 104. This shows the high potential of our integrated approach, considering the noise being 42 times higher for the sensor while also having an active pathlength 460 times smaller than the FT-IR spectrometer. The still successful monitoring can be attributed to the high enrichment factor of 7500 for p-xylene at this concentration (5 ppmv). It is further important to note that these values were recorded under dry conditions. In real-world scenarios, water vapor bands would strongly interfere during gas phase transmission measurements in this spectral region with the VOC bands and add significant noise levels.

Table 1: Performance parameters for FT-IR spectroscopy and the sensor for each respective VOC, with the LOD (marked in grey) for p-xylene being 0.1 ppmv, for toluene being 2.1 ppmv, while the LOD for 1,2,4-trimethylbenzene was determined to be 0.9 ppmv. SNR = signal-to-noise ratio.

| | c (ppmv) | p-Xylene | Toluene | Trimethylbenzene |
|--------------------------------|----------|----------|---------|------------------|
| SNR FT-IR | LOD | 3 | 25 | 9 |
| | 5 | 104 | 56 | 52 |
| | 10 | 208 | 112 | 104 |
| | 25 | 519 | 279 | 260 |
| | 50 | 1038 | 558 | 519 |
| SNR QCL-IR | LOD | 3 | 3 | 3 |
| | 5 | 37 | 6 | 9 |
| | 10 | 60 | 11 | 15 |
| | 25 | 114 | 23 | 27 |
| | 50 | 186 | 42 | 43 |
| Enrichment factor QCL-IR | LOD | 22108 | 2549 | 6924 |
| | 5 | 7543 | 2252 | 3844 |
| | 10 | 6128 | 2024 | 3038 |
| | 25 | 4657 | 1758 | 2226 |
| | 50 | 3783 | 1580 | 1759 |

$$\text{LOD} = \left(\frac{3 \cdot \sigma}{K_F} \right)^{n_F} \quad (4)$$

$$\text{SNR}(c) = \frac{q_e(c)}{\sigma} \quad (5)$$

$$\text{Enrichment factor} = \frac{q_{e,QCL}(c)}{q_{e,FTIR}(c)} \cdot \frac{L_{FTIR}}{L_{QCL}} \quad (6)$$

Evaluation of different chemometric models

In order to decide which algorithm to use for the deconvolution of the acquired multi-analyte QCL-IR spectra, we evaluated MCR-ALS and NNLS in respect to the real-time applicability. The parameters used to showcase the differences between the two algorithms were speed (measured in time of execution of the respective algorithms), stability (measured in the ability to react to additional components), and accuracy (measured in the respective root mean errors of the spectral fit and the prediction as well as the R^2 of the predictive fit). In Figure 6, deconvoluted spectra of a VOC mixture derived with NNLS and corresponding residues are shown, demonstrating a good fit quality. Additional details describing the deconvolution of the spectra are given in the ESI.

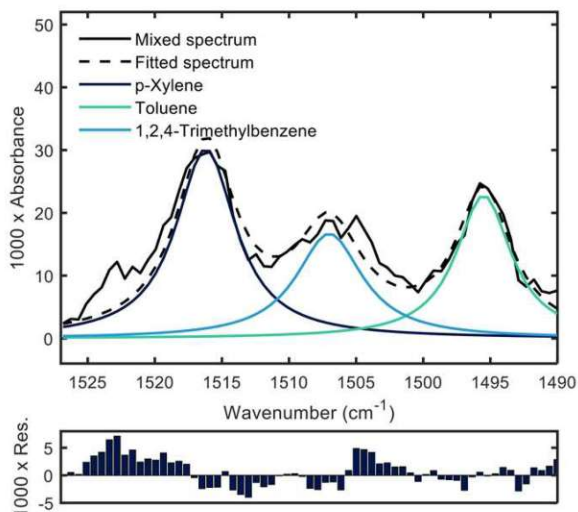


Figure 6: VOC spectra of a mixture of 164 ppmv p-xylene, 405 ppmv toluene, and 93 ppmv 1,2,4-trimethylbenzene acquired with the QCL based VOC sensor fitted by three Lorentzian curves (top). Sum spectrum of the three fits in dashed line. Residual plot of the fit (bottom).

Table 2 compares performance parameters for the two chosen methods. The simpler NNLS algorithm is significantly faster than MCR-ALS, requiring only a fifth of the execution time. Both methods are faster than spectral acquisition (15 s/spectrum). However, the NNLS algorithm lacks versatility when faced with additional analytes, unlike MCR-ALS, which can quickly detect and react to new analytes. MCR-ALS provides better spectral fits with lower root mean square errors of the fit (RMSEF) due to iterative improvement, while NNLS shows slightly better root mean square errors of the prediction (RMSEP) and R^2 , possibly indicating overfitting with MCR-ALS. Similar indications of overfitting with the MCR-ALS algorithm can be seen when comparing the predictive fits of the MCR-ALS model with the NNLS model, as shown in Figure 7. In this figure, the slopes for the NNLS are all very close to $k = 1$, whereas for the predictive fits for the MCR-ALS model, the slopes deviate significantly from the $k = 1$ optimum, indicating overfitting. Therefore, we chose NNLS for sensor calibration as the added features of the more powerful MCR-ALS algorithm were not considered necessary for the calibration.

Table 2: Performance parameters for spectral evaluation performed with NNLS and MCR-ALS.

| | | NNLS | MCR-ALS |
|-----------|---|-----------------|-----------------|
| accuracy | 1000 x RMSEF | 1.7 | 1.0 |
| | RMSEP (ppmv) | 34.8 | 37.7 |
| | R^2 of fit | 0.947 | 0.938 |
| speed | execution time (s) | 0.74 ± 0.02 | 3.49 ± 0.06 |
| stability | ability to react to additional analytes | ~ | ✓ |

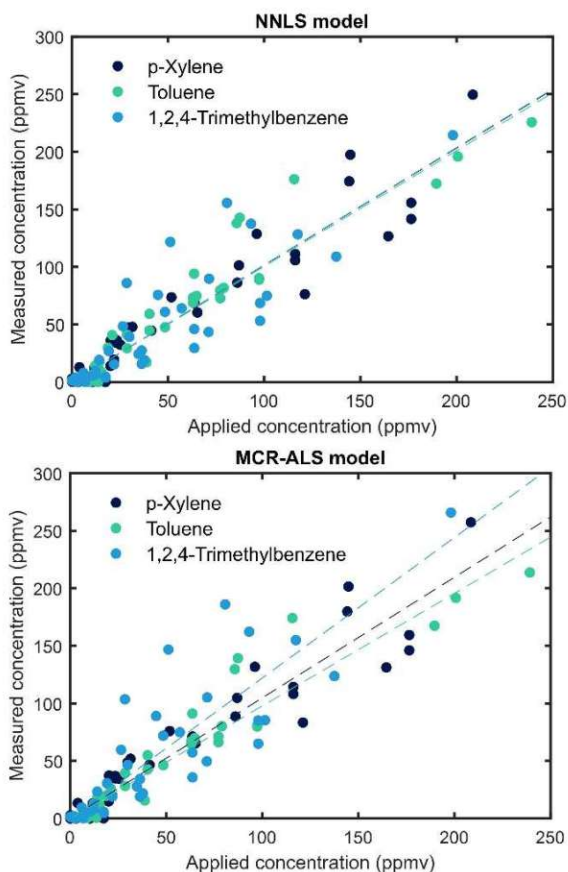


Figure 7: Predictive fit for the NNLS (top) and MCR-ALS (bottom) models.

Use-case simulation

To simulate the response and stability of our sensor, we applied a gas mixture with variable concentrations of all three VOCs to the sensor over a time period of 66 min at a total flow rate of 500 mL min^{-1} . The results of this use case simulation and a comparison of the results generated by the sensing platform and spectra acquired in standard transmission are shown in Figure 8.

The capabilities and limitations of the sensing concept become apparent when looking at the sensor response shown in Figure 8: On the one hand, the response of the sensor is quick and accurate and stable results can be gathered during the first 30 min. Further, the overlap of the spectra is reduced due to the absorption bands created by adsorbed gases being more similar to their liquid counterparts. On the other hand, a drift is noticeable when conducting longer measurements. This is probably due to extended diffusion in the thick, porous layers, which combined with longer exposure times than in the calibration experiments lead to a slow increase of signal over the course of the measurement. Regardless of this, the quick response of our platform to changing concentrations shows promise for the use as at-line contaminant sensing in PAT environments.

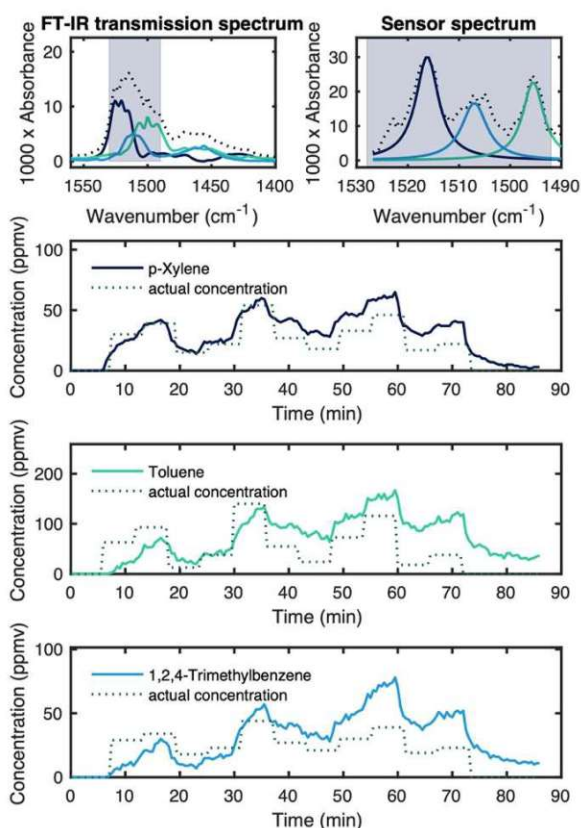


Figure 8: VOC spectra of the mixture used for the use case simulation in an FT-IR transmission setup (top left) and acquired with the QCL based VOC sensor (top right). Spectral region used for the chemometric evaluation marked in blue. Results of the use case simulation for each respective VOC (bottom).

Conclusion and outlook

In this work, we presented a highly sensitive QCL-IR based multi-gas sensor, utilizing a Ge-on-Si optical waveguide sensing platform, grating couplers and monolithically integrated microlenses. We successfully deposited a functionalized mesoporous silica coating on the waveguide chip, increasing the sensitivity by up to 22,000 times. The full measurement setup has a footprint of $29 \times 23 \times 11 \text{ cm}^3$ and delivers results in 3 min. We demonstrated the sensing capabilities of the presented system by analyzing three different aromatic VOCs (toluene, p-xylene, 1,2,4-trimethylbenzene) and their respective mixtures, achieving sub-ppmv levels of detection and stability to water vapor traces. We explored deconvolution of the overlapping VOC spectra and subsequent quantification of the respective pure component peak areas using different chemometric methods including non-negative least squares fitting and multivariate curve resolution alternating least squares. Lastly, we performed a use case simulation of the sensor, with the sensor reacting rapidly to changing concentrations of the three VOCs. In this experiment, the capabilities of the presented technique were demonstrated in a more realistic scenario, with long-term stability of the sensor signal still not optimal due to diffusion in the sensing layer covering the whole chip. To improve on that, our future work will focus on patterning the mesoporous layer, improving the response time and long-term stability of the sensor. Furthermore, next-generation waveguide designs with even lower propagation losses or other schemes based on dispersion spectroscopy that have shown high potential in transmission configuration³³ can be combined with our approach, leading to even higher sensitivities comparable to established techniques.

AUTHOR INFORMATION

Supplemental material

All supplemental material mentioned in the text is available in the online version of the journal. In the electronic supporting information, additional information can be found regarding the synthesis and characterization of functionalized silica sensing layers, the sensor calibration, the stability of the sensor to water vapor traces, as well as an evaluation and statistical comparison of different chemometric models.

Declaration of competing interests

The authors declare that they have no conflict of interests.

Acknowledgements

This work is partly funded by the ACTPHAST4R project, which have received funding from the European Union's Horizon 2020 research and innovation program under the grant agreement No. 825051. This project is an initiative of the Photonics Public Private Partnership. X-ray diffraction was performed at the interfaculty X-ray center of TU Wien. The authors acknowledge TU Wien Bibliothek for financial support through its Open Access Funding Programme.

References

1. A. Kansal, Sources and reactivity of NMHCs and VOCs in the atmosphere: A review. *J. Hazard. Mater.* **2009**, *166* (1): 17-26.
2. E. David; V.-C. Niculescu, Volatile Organic Compounds (VOCs) as Environmental Pollutants: Occurrence and Mitigation Using Nanomaterials. *Int. J. Environ. Res. Public Health.* **2021**, *18* (24).
3. C. Jia; S. Batterman; C. Godwin, VOCs in industrial, urban and suburban neighborhoods, Part 1: Indoor and outdoor concentrations, variation, and risk drivers. *Atmos. Environ.* **2008**, *42* (9): 2083-2100.
4. S.J. Maisey; S.M. Saunders; N. West; P.J. Franklin, An extended baseline examination of indoor VOCs in a city of low ambient pollution: Perth, Western Australia. *Atmos. Environ.* **2013**, *81*: 546-553.
5. M. Khatib; H. Haick, Sensors for Volatile Organic Compounds. *ACS Nano.* **2022**, *16* (5): 7080-7115.
6. B. Szulczyński; J. Gebicki, Currently Commercially Available Chemical Sensors Employed for Detection of Volatile Organic Compounds in Outdoor and Indoor Air. *Environments.* **2017**, *4* (1).
7. C.K. McGinn; Z.A. Lampert; I. Kymissis, Review of Gravimetric Sensing of Volatile Organic Compounds. *ACS Sens.* **2020**, *5* (6): 1514-1534.
8. E.L. Schymanski; H.P. Singer; J. Slobodnik; I.M. Ipolyi, et al., Non-target screening with high-resolution mass spectrometry: critical review using a collaborative trial on water analysis. *Anal. Bioanal. Chem.* **2015**, *407* (21): 6237-6255.
9. R. Selvaraj; N.J. Vasa; S.M.S. Nagendra; B. Mizaikoff, Advances in Mid-Infrared Spectroscopy-Based Sensing Techniques for Exhaled Breath Diagnostics. *Molecules.* **2020**, *25* (9).
10. L. Bizet; R. Vallon; B. Parvitte; M. Brun, et al., Multi-gas sensing with quantum cascade laser array in the mid-infrared region. *Appl. Phys. B.* **2017**, *123* (5): 145.
11. A. D'Arco; T. Mancini; M.C. Paolozzi; S. Macis, et al., High Sensitivity Monitoring of VOCs in Air through FTIR Spectroscopy Using a Multipass Gas Cell Setup. *Sensors.* **2022**, *22* (15).
12. D. Pinto; H. Moser; J.P. Waclawek; S. Dello Russo, et al., Parts-per-billion detection of carbon monoxide: A comparison between quartz-enhanced photoacoustic and photothermal spectroscopy. *Photoacoustics.* **2021**, *22*: 100244.
13. J. Hayden; M. Giglio; A. Sampaolo; V. Spagnolo; B. Lendl, Mid-infrared intracavity quartz-enhanced photoacoustic spectroscopy with pptv – Level sensitivity using a T-shaped custom tuning fork. *Photoacoustics.* **2022**, *25*: 100330.
14. L. Dong; A.A. Kosterev; D. Thomazy; F.K. Tittel, Compact portable QEPAS multi-gas sensor. *Proc. SPIE.* **2011**, *7945*: 79450R.
15. B. Hinkov; F. Pilat; L. Lux; P.L. Souza, et al., A mid-infrared lab-on-a-chip for dynamic reaction monitoring. *Nat. Commun.* **2022**, *13* (1): 4753.
16. Y.-C. Chang; V. Paeder; L. Hvozda; J.-M. Hartmann; H.P. Herzig, Low-loss germanium strip waveguides on silicon for the mid-infrared. *Opt. Lett.* **2012**, *37* (14): 2883-2885.
17. I. Lara-Ibeas; A. Rodríguez-Cuevas; C. Andrikopoulou; V. Person, et al., Sub-ppb Level Detection of BTEX Gaseous Mixtures with a Compact Prototype GC Equipped with a Preconcentration Unit. *Micromachines.* **2019**, *10* (3).
18. F. Bender; N. Barié; G. Romoudis; A. Voigt; M. Rapp, Development of a preconcentration unit for a SAW sensor micro array and its use for indoor air quality monitoring. *Sens. Actuators, B.* **2003**, *93* (1): 135-141.
19. Y. Wang; Z. Chen; Q. Chen; E. Tian, et al., Preconcentrating sensor systems toward indoor low-concentration VOC detection by goal-oriented, sequential, inverse design strategy. *Build. Environ.* **2024**, *254*: 111372.
20. M. Karlowatz; M. Kraft; B. Mizaikoff, Simultaneous Quantitative Determination of Benzene, Toluene, and Xylenes in Water Using Mid-Infrared Evanescent Field Spectroscopy. *Anal. Chem.* **2004**, *76* (9): 2643-2648.
21. A. Prasanth; S.R. Meher; Z.C. Alex, Metal oxide thin films coated evanescent wave based fiber optic VOC sensor. *Sens. Actuators, A.* **2022**, *338*: 113459.
22. B. Baumgartner; J. Hayden; B. Lendl, Mesoporous silica films for sensing volatile organic compounds using attenuated total reflection spectroscopy. *Sens. Actuators, B.* **2020**, *302*: 127194.

23. N.T. Benítez; B. Baumgartner; J. Missinne; S. Radosavljevic, et al., Mid-IR sensing platform for trace analysis in aqueous solutions based on a germanium-on-silicon waveguide chip with a mesoporous silica coating for analyte enrichment. *Opt. Express*. **2020**. 28 (18): 27013-27027.
24. K. Eslami Jahromi; Q. Pan; A. Khodabakhsh; C. Sikkens, et al., A Broadband Mid-Infrared Trace Gas Sensor Using Supercontinuum Light Source: Applications for Real-Time Quality Control for Fruit Storage. *Sensors*. **2019**. 19 (10).
25. E.V. Thomas; D.M. Haaland, Comparison of multivariate calibration methods for quantitative spectral analysis. *Anal. Chem.* **1990**. 62 (10): 1091-1099.
26. S. Vijayakumar; J. Rowlette; A. Schwaighofer; B. Lendl, Laser-Based Mid-Infrared Spectroscopy for Monitoring Temperature-Induced Denaturation of Bovine Serum Albumin and De-/Stabilization Effects of Sugars. *Anal. Chem.* **2023**. 95 (15): 6441-6447.
27. J. Jaumot; A. de Juan; R. Tauler, MCR-ALS GUI 2.0: New features and applications. *Chemom. Intell. Lab. Syst.* **2015**. 140: 1-12.
28. W. Windig; J. Guilment, Interactive self-modeling mixture analysis. *Anal. Chem.* **1991**. 63 (14): 1425-1432.
29. B. Baumgartner; J. Hayden; A. Schwaighofer; B. Lendl, In Situ IR Spectroscopy of Mesoporous Silica Films for Monitoring Adsorption Processes and Trace Analysis. *ACS Appl. Nano Mater.* **2018**. 1 (12): 7083-7091.
30. B. Baumgartner; J. Hayden; J. Loizillon; S. Steinbacher, et al., Pore Size-Dependent Structure of Confined Water in Mesoporous Silica Films from Water Adsorption/Desorption Using ATR-FTIR Spectroscopy. *Langmuir*. **2019**. 35 (37): 11986-11994.
31. G.L. Long; J.D. Winefordner, Limit of detection. A closer look at the IUPAC definition. *Anal. Chem.* **1983**. 55 (7): 712A-724A.
32. J. Mocak; A.M. Bond; S. Mitchell; G. Scollary, A statistical overview of standard (IUPAC and ACS) and new procedures for determining the limits of detection and quantification: Application to voltammetric and stripping techniques. *Pure Appl. Chem.* **1997**. 69 (2): 297-328.
33. A. Dabrowska; S. Lindner; A. Schwaighofer; B. Lendl, Mid-IR dispersion spectroscopy – A new avenue for liquid phase analysis. *Spectrochim. Acta, Part A*. **2023**. 286: 122014.

A.3. Publication III: Experimental Demonstration of the high alignment-tolerant Behavior of a mid-Infrared Waveguide Platform for evanescent Field Sensing

Experimental Demonstration of the High Alignment-Tolerant Behavior of a Mid-Infrared Waveguide Platform for Evanescent Field Sensing

Felix Frank, Mattias Verstuyft, Nuria Teigell Beneitez, Jeroen Missinne, Gunther Roelkens, Dries van Thourhout, and Bernhard Lendl*

Cite This: <https://doi.org/10.1021/acsaom.4c00280>

Read Online

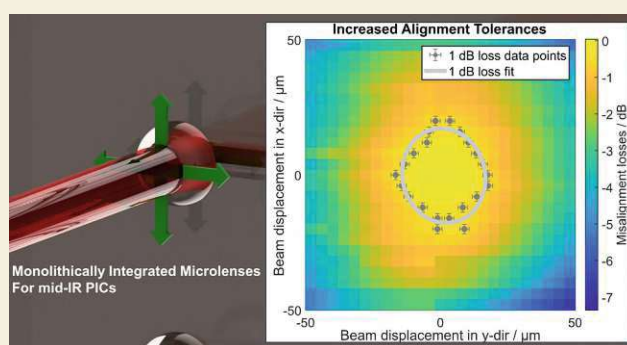
ACCESS |

Metrics & More

Article Recommendations

ABSTRACT: Alignment tolerant coupling interfaces are an important feat for mid-IR waveguides when moving closer to real-world sensing applications, as they allow for an easy and fast replacement of waveguides. In this work, we demonstrate the alignment tolerant behavior of a germanium-on-silicon trenched waveguide platform with monolithically integrated microlenses using backside coupling of an expanded beam for evanescent field sensing between 6.5 and 7.5 μm . The chip with a propagation loss of approximately 5 dB/cm was mounted and aligned, using active alignment, in a sample holder that could be moved in all three dimensions to induce misalignments with a precision of the manual actuator of 1.3 μm . Using this setup, the in-plane 1 dB alignment tolerances were measured to be $\pm 16 \mu\text{m}$, while the 1 dB alignment tolerances in the longitudinal direction were found to be larger than $\pm 150 \mu\text{m}$. Without the addition of the microlenses, we expect an in-plane 1 dB alignment tolerance of $\pm 3 \mu\text{m}$ based on simulations. Additionally, it could be demonstrated that the integration of the microlenses significantly improves the stability of the broadband grating couplers in regard to misalignment-induced intensity changes in the obtained transmission spectra.

KEYWORDS: mid-infrared, waveguide, photonic integrated circuit, silicon photonics, alignment tolerances



INTRODUCTION

Silicon photonics (or group IV photonics) has evolved into a mature and widely adopted technology in the field of integrated photonics. This has led to the establishment of highly reliable large-scale sites for the production of photonic circuits in a compact and cost-efficient way for established materials such as silicon on insulator (SOI). Recently, the use of germanium (Ge) and silicon (Si) hybrid materials has increased, especially in the field of mid-infrared (IR) spectroscopy, where the use of SOI is limited by the low-loss transmission range of 1.2–6 μm .¹ Germanium, on the other hand, is a close to perfect material for the use in photonic systems in the mid-IR range, as it is transparent in nearly the entirety of the mid-IR region and has a high refractive index of 3.97 at 5 μm (compared to 3.47 for Si),^{2,3} but does not offer the same mature fabrication sites compared to SOI. Subsequently, the first mentions of the high theoretical efficiency of germanium-on-silicon (GOS) materials were found in the mid-2000s,¹ followed by the demonstration of early devices some years later, proving their low loss properties in the mid-IR.^{4–6} Most early works focused on growing Ge ribs onto the surface of either SOI wafers or etching rib waveguides into

Ge-on-insulator wafers.^{7,8} Further investigations based on these rib structures have then isolated the mode confinement in the interlayer between Ge and Si as one of the major reasons for the propagation loss of these waveguides.⁹ This is due to the mismatch of the lattice constant of 4% between Ge (5.66 Å) and Silicon (5.43 Å) which results in imperfect crystal growth in the Ge through dislocation and threading defects.¹⁰ Another source of loss for Ge grown on Si is due to unintended background doping of the Ge, resulting in high propagation losses due to free-carrier absorption.¹¹

To minimize these losses, new strategies were proposed, such as going to GOS wafers and etching the waveguide structures into the top germanium layer. By doing this, a layer of Ge between the waveguide and the Ge–Si interface, limiting the

Received: June 21, 2024

Revised: July 30, 2024

Accepted: August 4, 2024

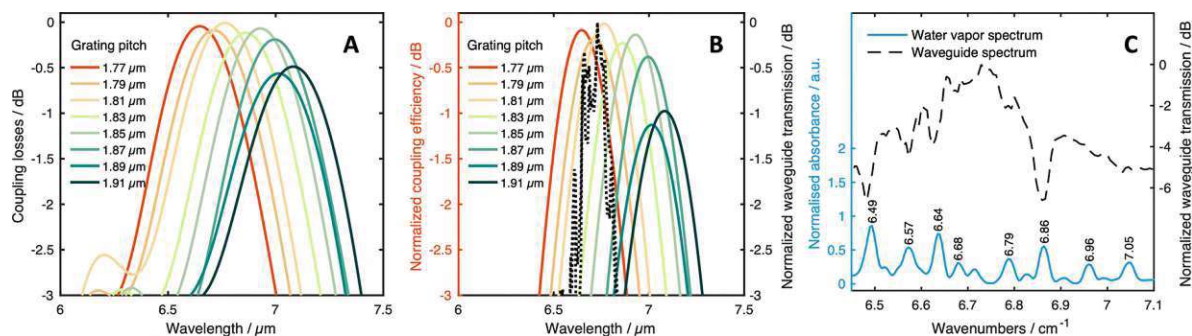


Figure 1. (A) Simulations of the normalized coupling losses of the gratings for different grating pitches. (B) Simulations for the normalized coupling efficiency (in- and out-coupling) and the waveguide transmission spectrum (black dotted line). (C) Water vapor spectrum and waveguide transmission spectrum between 6.45 and 7.15 μm showing the influence of water vapor in the recorded transmission spectrum.

propagation losses caused by the mode confinement in the Ge–Si interlayer.¹² By properly tailoring the deposition parameters during the Germanium growth, free carriers can also be suppressed.¹³

Using this technique, propagation losses of ~ 1 dB/cm could be demonstrated in the mid-IR (for wavelengths of 10 μm ¹³ and 5–8 μm ,¹⁴ respectively), moving closer to practical sensing application of these waveguides.

Looking beyond the inherent propagation losses, which can be minimized by design and fabrication of the waveguide structures, the second considerable source of loss when operating waveguides are coupling losses. This is especially true for silicon photonics, as its compatibility with current optical fiber components is not optimal, making high-efficiency coupling still challenging.¹⁵ Conceptually, two main strategies are chosen to couple light into waveguide structures, edge-coupling and vertical coupling. Edge coupling shows very high coupling efficiency and a relatively high bandwidth, while traditional grating couplers struggle to achieve both feats at the same time.^{16,17} On the other hand, edge couplers need to be placed at the edge of the chip, whereas grating couplers can be placed anywhere on the chip, giving more flexibility in design, and making fabrication significantly easier. In addition, they generally exhibit wider alignment tolerances than edge couplers, which is crucial for bringing integrated waveguide optics closer to industrial applications.^{17,18} By integrating monolithic back-side microlenses, the alignment tolerances can be improved even further, which has been first demonstrated for the NIR with 1 dB alignment tolerances of ± 10 μm .^{19,20} By using an expanded beam for coupling, which is focused onto the gratings by means of silicon lenses, this concept has also been applied to the mid-IR.^{20,21} Building on these findings, we demonstrated an integrated circuit platform using trenched GOS waveguides employing back-side coupling with monolithically integrated microlenses and broadband grating couplers with a 3 dB bandwidth of ~ 500 nm at the cost of a decreased coupling efficiency of 30%, and slightly increased simulated back reflection of $\sim 20\%$ in our previous work. However, no impairment of the laser operation was observed due to back-reflections. We further combined these waveguides with functional mesoporous layers for analyte enrichment in the evanescent field to increase sensitivity, reaching limits of detection of 7 ppm for toluene in water.²²

In this work, we focused on the experimental demonstration of the alignment tolerances of our previously reported waveguide platform to showcase its potential for a range of practical applications. We mounted the chip on an xyz-stage with

manual adjusters, with a scanning range of 100 $\mu\text{m} \times 100 \mu\text{m}$ for in-plane alignments and $\pm 150 \mu\text{m}$ for out-of-plane alignments. Using this setup, we looked at relevant properties for PICs when going toward practical applications, demonstrating the advantages of monolithically integrated microlenses in the mid-IR. First, we compared the experimental alignment tolerances of the entire PIC waveguide platform to the simulated alignment tolerances of the grating. We then investigated the stability of the transmission spectrum for different alignments, showing that spectral shifts caused by grating coupler misalignments can be significantly reduced. The results of this experimental demonstration can serve as a catalyst for further research in the emerging field of mid-IR photonics, bringing mid-IR waveguides closer to application.

RESULTS AND DISCUSSION

Experimental Determination of the Alignment Tolerances

To determine the alignment tolerances of the waveguide platform, we swept the in-plane directions systematically. Initially, the setup was actively aligned using the detector feedback to achieve optimal alignment, which is further referred to as 'reference point'. This optimal alignment was achieved for a grating pitch of 1.79 μm . Simulations of the normalized coupling losses, the normalized coupling efficiency and the transmission spectrum of the waveguide suggesting alignment at a grating pitch of 1.79 μm are shown in Figure 1. The influence of water vapor on the transmission spectrum is shown in Figure 1C, as the dips in transmission at 6.64, 6.68, 6.71, 6.79, and 6.85 μm can be assigned to the water vapor absorption bands. As we were using an expanded beam concept, the angular tolerance of the chip needs to be considered. For this, a chip holder as described in our previous report²² was used to keep the chip in place and limit angular misalignments. Similarly, potential misalignments between the microlens and the grating couplers must be considered, as they can impose angular misalignments. This, however, can be limited by precise fabrication, and can be neglected from a practical standpoint.

Subsequently, we performed a scan of a 100 $\mu\text{m} \times 100 \mu\text{m}$ area centered at the reference point, with 4 μm increments in both the y - and z -directions, capturing a spectrum at each point. This involved taking a reference spectrum, followed by sweeping in y -direction while maintaining a fixed position in the z -direction. To assess the out-of-plane alignment tolerances, we acquired spectra in-axis relative to the reference point, utilizing the entire 300 μm fine travel range of the manual adjuster (schematic depiction of the waveguide chip and the scanned

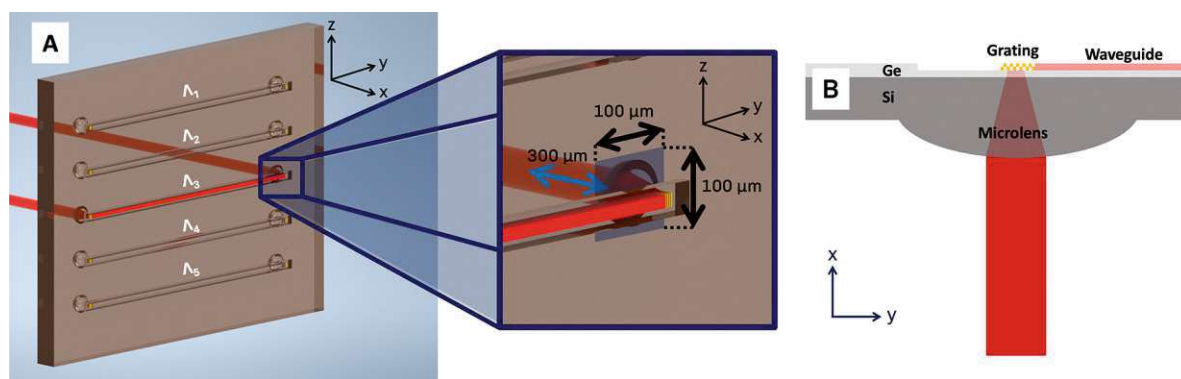


Figure 2. (A) Schematic depiction of the waveguide chip (Λ_n denoting different grating pitches for each waveguide) and the scanned area (blue area marked on the chip, in-plane movement marked with black arrows, out-of-plane movement marked with blue arrows). (B) Schematic depiction of the cross-section of the waveguide, demonstrating the vertical coupling concept of the integrated microlenses and grating couplers.

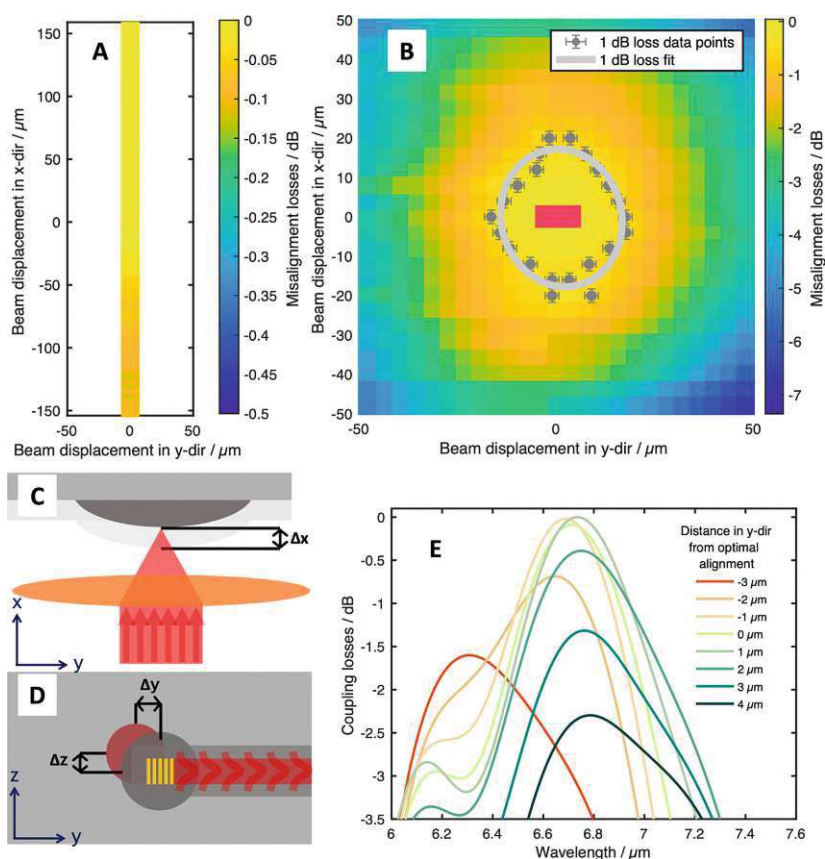


Figure 3. (A, B) Experimental alignment tolerances of the waveguide platform in regard to misalignments in x - and y -directions (A) and y - and z -directions (B). Each measurement series for the respective misalignment in z -direction was fitted with a Gaussian curve, with the 1 dB loss marked by the gray data points and the 1 dB loss fit for total beam marked by the gray ellipse. Area covered by the simulations in E marked with pink box. (C) Schematic depiction of misalignments in x -direction. (D) Schematic depiction of misalignments in y - and z -directions of the laser (red circle) relative to the microlenses (gray circle) and the grating couplers (yellow structure). (E) Simulated transmission spectra for different misalignment distances in y -direction relative to the center of the grating coupler for a grating pitch of $1.79 \mu\text{m}$.

area shown in Figure 2). Each spectrum was obtained by averaging 1000 individual spectra, with a total integration time of 1 s.

For the out-of-plane scans (x -axis), in which the focus of the beam was changed by moving the chip in longitudinal direction relative to the fixed focusing lens, no significant misalignment losses could be found, with the whole fine travel range ($\pm 150 \mu\text{m}$) of the manual adjuster leading to maximum losses $< 0.2 \text{ dB}$, as seen in Figure 3A. This was to be expected as the calculated

beamwidth at $150 \mu\text{m}$ longitudinal misalignment is only $43 \mu\text{m}$ (compared to a beam waist of $7.5 \mu\text{m}$ and a radius of curvature of the lens of $530 \mu\text{m}$). To determine the 1 dB alignment tolerances, the single channel spectra of the reference point and sample points were fitted with Gaussian profiles to mitigate the influence of slightly changing water vapor concentrations. The losses were determined as the ratio of the maximum of the fitted sample spectra compared to the maximum of the reference point. In Figure 3B, the mapping of all in-plane spectra.

For each sweep in the x - and y -dimensions, the data points were fitted with another Gaussian profile, and the 1 dB loss misalignment points were determined (shown as gray points, error bars show the influence of noise). The 1 dB alignment tolerance of the platform was determined as the mean distance of the 1 dB loss misalignment points to the reference point, which equated to $16.4 \mu\text{m}$ (compared to $<3 \mu\text{m}$ for the simulated values for the grating couplers). This is approximately half of the simulated 1D-behavior of $\sim 30 \mu\text{m}$, but slightly better than the experimental 1D hollow-core fiber results presented in our previous report.²² Adding to this, it also has to be said that the simulations do not take into account the change of the incidence angle for lateral misalignments, which may add slightly to the worse performance when comparing the experimental results to the simulations, although the angular dependence of the coupling efficiency of the employed grating couplers is rather low. The better experimental alignment tolerances may be attributed to a better focusing of the IR beam using free space optics, as hollow-core fibers with an output beam diameter of $130 \mu\text{m}$ were used for in-coupling in our previous report.

Experimental Determination of Misalignment Induced Changes of the Transmission Spectra

In Figure 4, transmission spectra at different alignment positions can be seen. In contrast to the single line spectra used for Figure 3, these spectra are calculated as transmission spectra referenced to the power spectrum of the spectrometer. Looking at the spectra, apart from the obvious decrease in coupling efficiency when moving away from the center, it can be noted that the

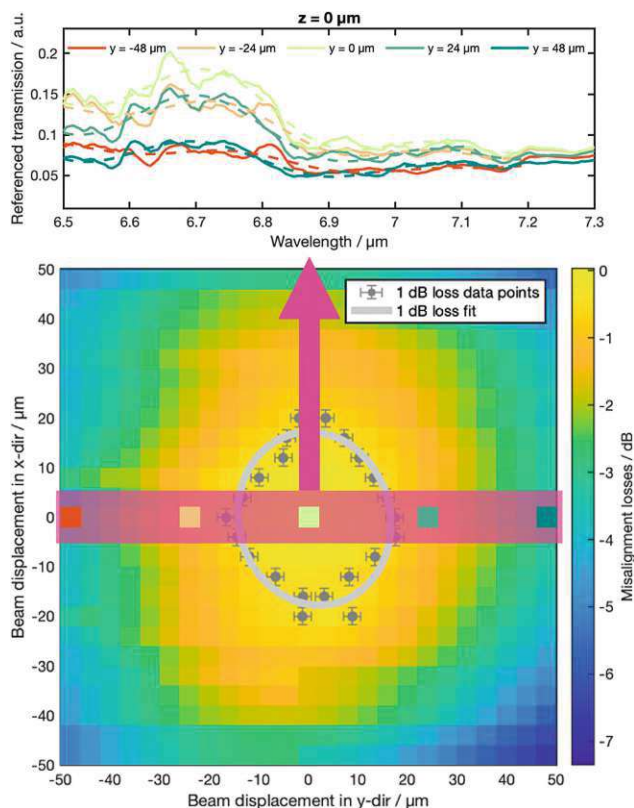


Figure 4. (A) Referenced transmission spectra (solid lines) and Fourier fits (dotted lines) at different misaligned points in y -direction. (B) Locations of the spectra are shown in the 1 dB loss map.

transmission spectrum changes, especially when moving in the y -direction (perpendicular to the orientation of the grating).

To investigate any spectral shifts induced by misalignments, two approaches were chosen: The first one was identifying the wavelength with the highest transmission, while the second approach studied parameter concerned the change of the transmission spectrum shape. For that, the calculated chip transmission spectra (Figure 4A, solid lines) were fitted with a two term Fourier function (Figure 4A, dotted lines) in the spectral range of the spectrometer between 6.5 and $7.2 \mu\text{m}$. The use of a Fourier fit was due to the dip in transmission at $6.85 \mu\text{m}$ caused by strong water vapor bands (seen in Figure 1C) to still obtain a satisfying fit. The maxima of these function were then mapped and are shown in Figure 5. Looking at this map, the

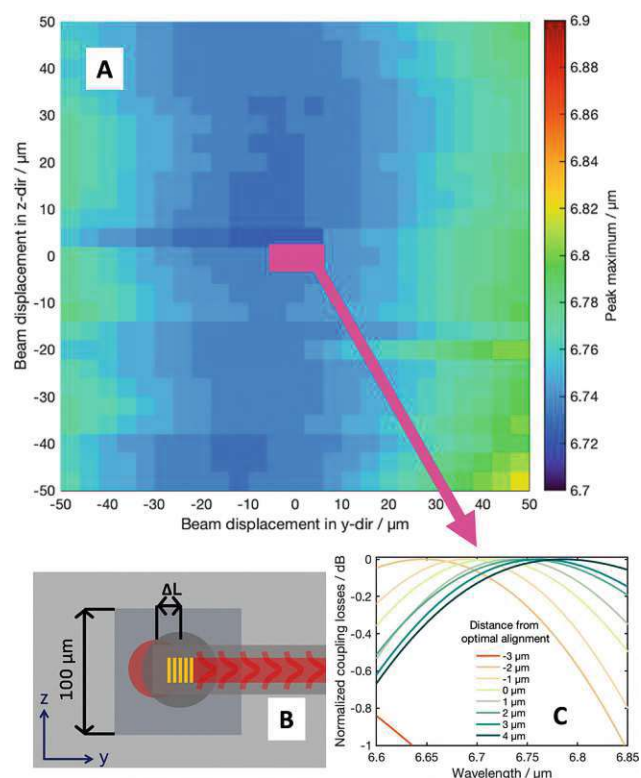


Figure 5. (A) Experimental peak maximum of the referenced spectra. The borders of the color bar refer to the two simulated peak maxima of the grating couplers for different alignments. The pink area shows the region of the simulation for the grating couplers. (B) Schematic depiction of misalignments of the laser (red circle) relative to the microlenses (gray circle) and the grating couplers (yellow structure). (C) Normalized simulated transmission spectra for different misalignment distances in y -direction relative to the center of the grating coupler for a grating pitch of $1.79 \mu\text{m}$.

maximum of the peak does not seem to shift in the scanned $100 \mu\text{m} \times 100 \mu\text{m}$ area. Comparing this to the simulations of the shift of the grating coupler (Figure 5C), it can be seen that integrating the microlenses leads to a much more stable peak maximum for the waveguide transmission spectra, as the simulations for the grating couplers suggest wavelength shifts at lateral misalignments of approximately $3 \mu\text{m}$. Considering industrial applications, where not only the coupling losses, but also the wavelength range, needs to be stable in an environment, where slight misalignments are inevitable, this demonstrates the capabilities of the presented waveguide platform in that concern.

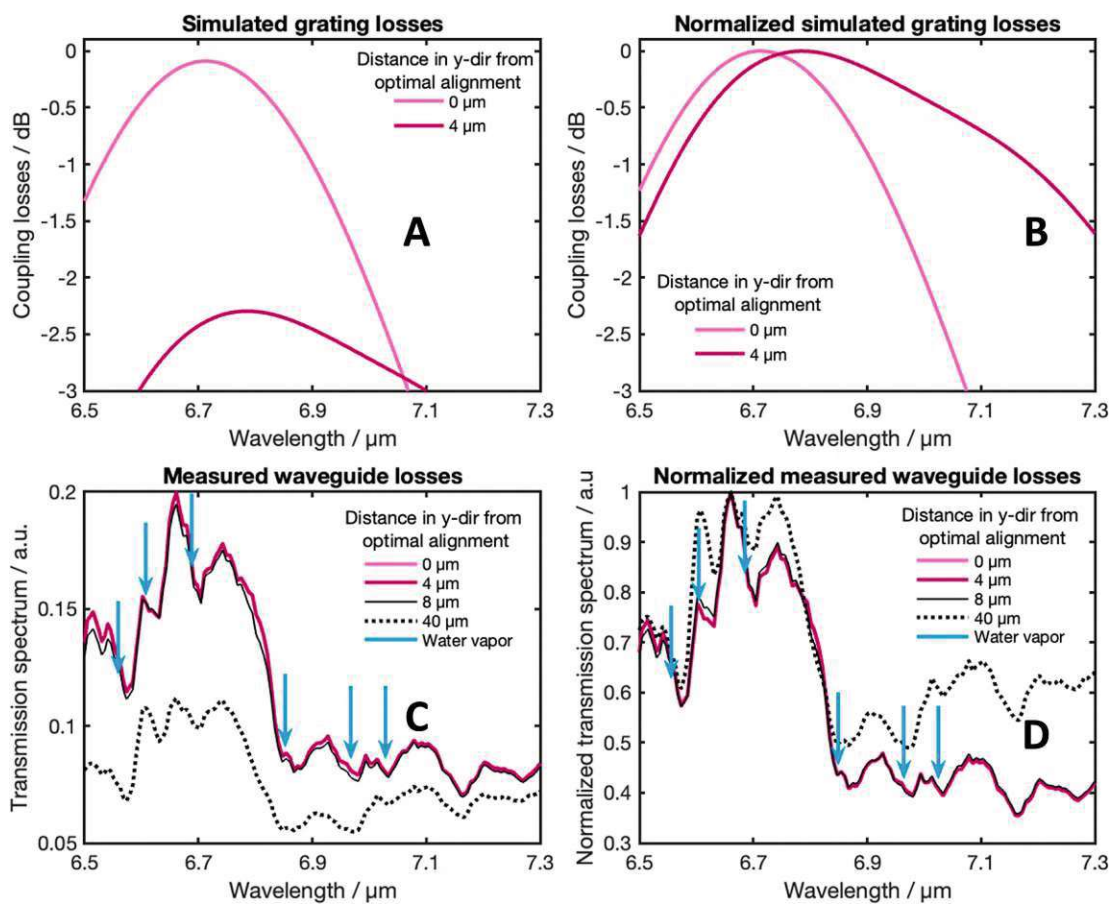


Figure 6. (A) Simulated grating losses for an optimal alignment and a misalignment of $\Delta x = 4 \mu\text{m}$. (B) Normalized simulated grating losses for an optimal alignment and a misalignment of $\Delta x = 4 \mu\text{m}$. (C) Measured waveguide transmission spectra for an optimal alignment and misalignments of $\Delta x = 4, 8,$ and $40 \mu\text{m}$. Water vapor band positions are shown with red lines. (D) Normalized measured waveguide transmission spectra for an optimal alignment and misalignments of $\Delta x = 4, 8,$ and $40 \mu\text{m}$. Water vapor band positions are shown with blue arrows.

As the peak maximum did not change significantly across the scanned area, we adopted a different approach to detect more subtle variations in the spectral features of the waveguide transmission spectra. In Figure 6, we compare the simulated grating losses for different misalignments with the corresponding measured spectra. Two important observations emerge from this comparison: First, the alignment-tolerant behavior of the waveguide is showcased in the transmission spectra, as a misalignment of $4 \mu\text{m}$ does not result in a significant change in the transmission. In contrast, the simulation predicts a similar decrease in transmission for a $4 \mu\text{m}$ misalignment as it was observed for a $40 \mu\text{m}$ misalignment in the measured data. Second, the normalized measured transmission spectra exhibit broadening toward higher wavelengths. Notably, strong water vapor bands exist in the region between 6.8 and $7 \mu\text{m}$, making this broadening most evident between 7 and $7.3 \mu\text{m}$. Consequently, we calculated the ratio of transmission spectra at 6.65 and $7.1 \mu\text{m}$ as a measure of the misalignment-induced changes in waveguide transmission. Figure 7 presents a map of this ratio. Upon closer examination, we observe a slight red shift in the transmission spectra near the edge of the grating couplers, suggesting peak shifts. However, this shift does not align with lateral misalignments of less than $4 \mu\text{m}$, as predicted by the simulations. Hence, the high margin of error for in-plane misalignments, especially perpendicular to the propagating direction of the waveguide further showcases the increased

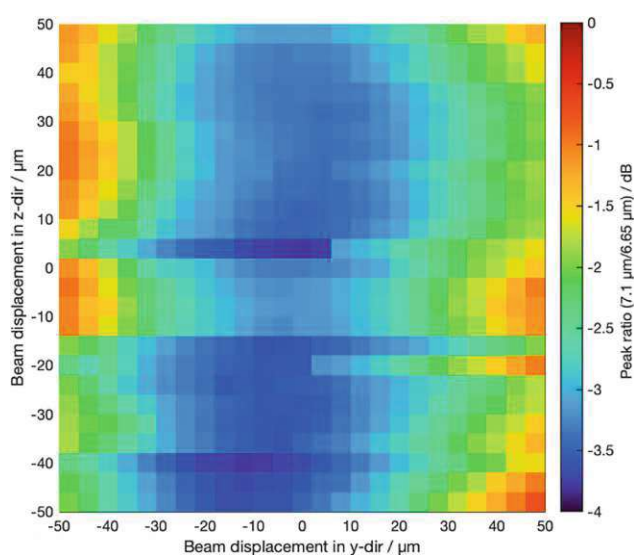


Figure 7. Experimental ratio of the peak maximum at $6.65 \mu\text{m}$ and the growing peak shoulder at $7.1 \mu\text{m}$ of the grating couplers.

alignment tolerance of the microlens system when comparing it to a simulation only including the grating couplers.

EXPERIMENTAL SECTION

The fabrication of the waveguide chips can be divided into the fabrication of the waveguide structures with grating couplers and the subsequent fabrication of the microlenses on the backside and is described in detail in our previous report.²² The sensing chips consist of trenched rib waveguides with a width of $3.3\ \mu\text{m}$ (at a trench width of $8\ \mu\text{m}$), a distance of $16\ \text{mm}$ between the grating couplers, and an etching depth of $1\ \mu\text{m}$ on a $2\ \mu\text{m}$ GOS platform. The grating couplers support TE polarization and have 8 different grating pitches for each waveguide on a chip (between 1.77 and $1.91\ \mu\text{m}$) and are designed to feature a high bandwidth and low angular dependency. In order to focus the incident laser beam and to collimate the emitted output beam, microlenses were etched into the backside of the chip, aligned directly below the grating coupler. The radius of curvature of the microlenses is in line with our previous report at $530\ \mu\text{m}$.²²

For the testing of the waveguide platform, the chip was mounted on an xyz -stage equipped with manual adjusters (DS-4F, mks|Newport) with $1.33\ \mu\text{m}$ graduations and a $300\ \mu\text{m}$ fine travel range. The light source was a micro-opto-electro-mechanical system (MOEMS) external cavity quantum cascade laser (EC-QCL) developed in the European Union funded H2020 Project AQUARIUS. The laser was operated with a $570\ \text{kHz}$ pulse repetition rate and a $100\ \text{ns}$ pulse length and emitted between 6.36 and $7.45\ \mu\text{m}$. The used detector was a thermoelectrically cooled high speed MCT detector integrated ($D^* \geq 4.0 \times 10^9\ \text{cm}\ \sqrt{\text{Hz/W}}$). The whole system is depicted in Figure 8.

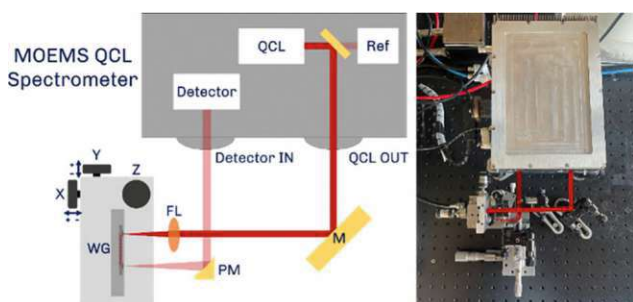


Figure 8. Schematic depiction of the setup to test the alignment tolerances of the waveguide platform (left); image of the setup (right).

Inside the spectrometer, the beam is split into the output beam and the reference beam using a 99/1 beamsplitter. The inherently linearly polarized QCL beam was adjusted to match the required propagating mode of the waveguide platform (designed for TE polarization). The collimated output beam is then directed on the focusing lens (FL), focusing the beam onto the integrated microlenses of the waveguide (WG) chip. After propagation, the out-coupled beam is collimated and directed toward the detector using an off-axis parabolic mirror (PM). The difference in path length between the reference beam and the beam used for sensing has to be noted, as the measurements were performed in air, and the presence of water vapor (having many absorption lines of their fundamental ro-vibrational transitions in the $6\text{--}7.5\ \mu\text{m}$ wavelength range) led to additional noise which had to be considered in the evaluation of data by accounting for small fluctuations in water vapor concentration.

CONCLUSION

We experimentally investigated the benefits of monolithically integrated microlenses for the backside coupling on our germanium-on-silicon trenched waveguide platform in a free space setup. For this, the chip was mounted on an xyz -stage and an area of $100\ \mu\text{m} \times 100\ \mu\text{m}$ was scanned in-plane centered at the point of maximum transmission. These measurements revealed a mean in-plane $1\ \text{dB}$ alignment tolerance of the waveguide platform of $\pm 16.4\ \mu\text{m}$, compared to a simulated grating bandwidth of $\pm 3\ \mu\text{m}$. Out-of-plane measurements

performed in a $\pm 150\ \mu\text{m}$ longitudinal 1D scan showed no significant losses. Further, the spectral features of the transmission spectra were investigated, showing that the spectral shifts caused by misalignments on the grating coupler can be reduced significantly. It was proven experimentally that employing a waveguide platform design with integrated microlenses leads to a very alignment tolerant system, going a step closer toward industrial application of GOS photonic sensing systems.

AUTHOR INFORMATION

Corresponding Author

Bernhard Lendl – Institute of Chemical Technologies and Analytics, TU Wien, 1060 Wien, Austria; orcid.org/0000-0003-3838-5842; Email: bernhard.lendl@tuwien.ac.at

Authors

Felix Frank – Institute of Chemical Technologies and Analytics, TU Wien, 1060 Wien, Austria; orcid.org/0000-0002-7584-5812

Mattias Verstuyft – Photonics Research Group, Ghent University-imec, 9052 Gent, Belgium

Nuria Teigell Beneitez – Photonics Research Group, Ghent University-imec, 9052 Gent, Belgium

Jeroen Missinne – Center for Microsystems Technology, Ghent University-imec, 9052 Gent, Belgium; orcid.org/0000-0002-3470-620X

Gunther Roelkens – Photonics Research Group, Ghent University-imec, 9052 Gent, Belgium; orcid.org/0000-0002-4667-5092

Dries van Thourhout – Photonics Research Group, Ghent University-imec, 9052 Gent, Belgium; orcid.org/0000-0003-0111-431X

Complete contact information is available at:

<https://pubs.acs.org/10.1021/acsaoam.4c00280>

Author Contributions

The manuscript was written through contributions of all authors. All authors have given approval to the final version of the manuscript.

Notes

The authors declare no competing financial interest.

ACKNOWLEDGMENTS

This work was carried out in the context of the ACTPHAST4R Project, which has received funding from the European Union's Horizon 2020 Research and Innovation Program under Grant Agreement No. 825051. Further funding from the HYDROPTICS Project, which has received funding from the European Union's Horizon 2020 Research and Innovation Program under Grant Agreement No. 871529, is also acknowledged. The authors acknowledge TU Wien Bibliothek for financial support through its Open Access Funding Programme.

REFERENCES

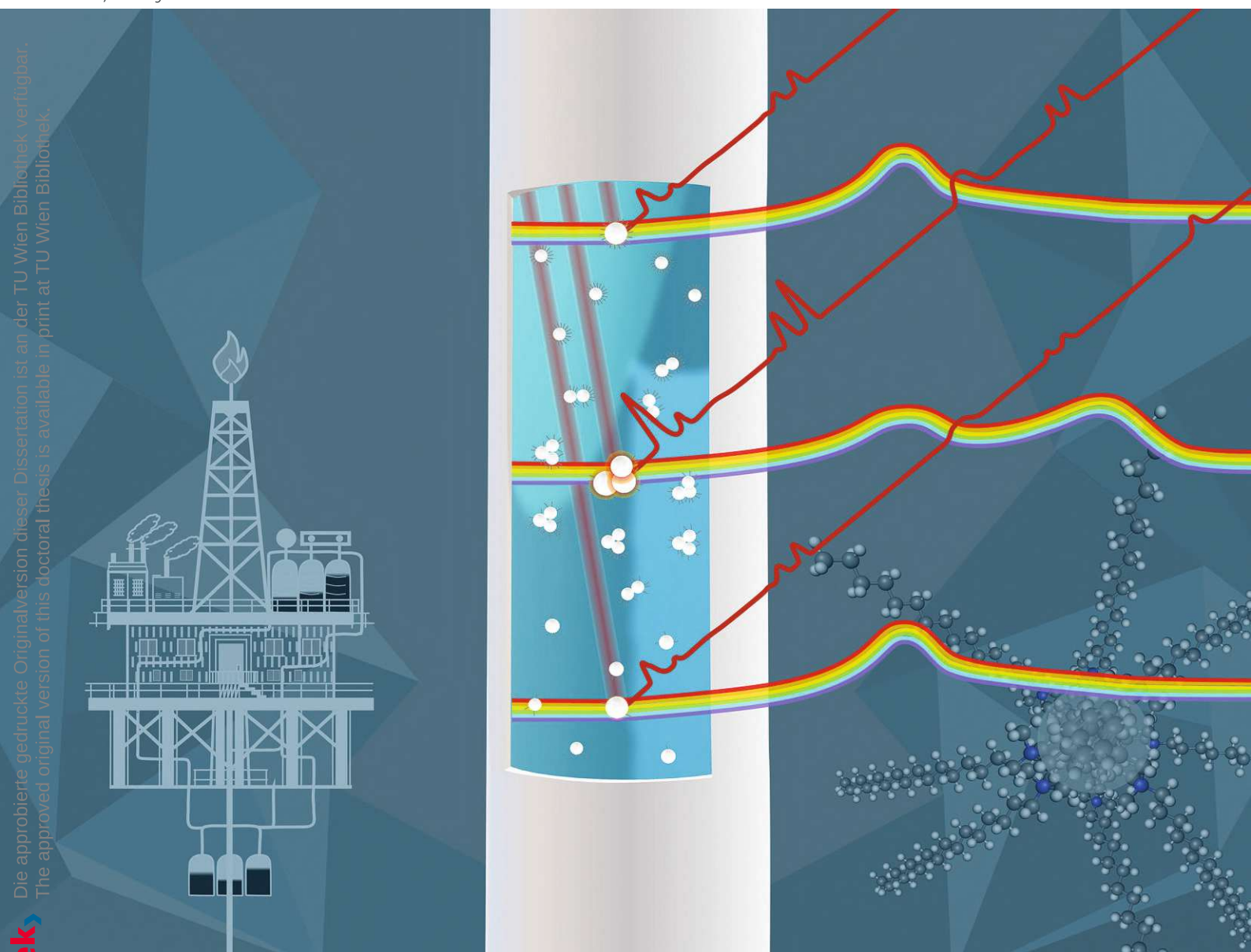
- (1) Soref, R. A.; Emelett, S. J.; Buchwald, W. R. Silicon waveguided components for the long-wave infrared region*. *J. Opt. A-Pure appl. Opt.* **2006**, *8* (10), 840.
- (2) Amotchkina, T.; Trubetskoy, M.; Hahner, D.; Pervak, V. Characterization of e-beam evaporated Ge, YbF₃, ZnS, and LaF₃ thin films for laser-oriented coatings. *Appl. Opt.* **2020**, *59* (5), A40–A47.

- (3) Shkondin, E.; Takayama, O.; Panah, M. E. A.; Liu, P.; Larsen, P. V.; Mar, M. D.; Jensen, F.; Lavrinenko, A. V. Large-scale high aspect ratio Al-doped ZnO nanopillars arrays as anisotropic metamaterials. *Opt. Mater. Express* **2017**, *7* (5), 1606–1627.
- (4) Chang, Y.-C.; Paeder, V.; Hvozdar, L.; Hartmann, J.-M.; Herzig, H. P. Low-loss germanium strip waveguides on silicon for the mid-infrared. *Opt. Lett.* **2012**, *37* (14), 2883–2885.
- (5) Roelkens, G.; Dave, U.; Gassenq, A.; Hattasan, N.; Hu, C.; Kuyken, B.; Leo, F.; Malik, A.; Muneeb, M.; Ryckeboer, E.; Uvin, S.; Hens, Z.; Baets, R.; Shimura, Y.; Gencarelli, F.; Vincent, B.; Loo, R.; Van Campenhout, J.; Cerutti, L.; Rodriguez, J.-B.; Tournié, E.; Chen, X.; Nedeljkovic, M.; Mashanovich, G.; Shen, L.; Healy, N.; Peacock, A. C.; Liu, X.; Osgood, R.; Green, W. Silicon-based heterogeneous photonic integrated circuits for the mid-infrared. *Opt. Mater. Express* **2013**, *3* (9), 1523–1536.
- (6) Shen, L.; Healy, N.; Mitchell, C. J.; Penades, J. S.; Nedeljkovic, M.; Mashanovich, G. Z.; Peacock, A. C. Mid-infrared all-optical modulation in low-loss germanium-on-silicon waveguides. *Opt. Lett.* **2015**, *40* (2), 268–271.
- (7) Kang, J.; Takenaka, M.; Takagi, S. Novel Ge waveguide platform on Ge-on-insulator wafer for mid-infrared photonic integrated circuits. *Opt. Express* **2016**, *24* (11), 11855–11864.
- (8) Younis, U.; Luo, X.; Dong, B.; Huang, L.; Vanga, S. K.; Lim, A. E.-J.; Lo, P. G.-Q.; Lee, C.; Bettiol, A. A.; Ang, K.-W. Towards low-loss waveguides in SOI and Ge-on-SOI for mid-IR sensing. *J. Phys. Commun.* **2018**, *2* (4), No. 045029.
- (9) Marris-Morini, D.; Vakarin, V.; Ramirez, J. M.; Liu, Q.; Ballabio, A.; Frigerio, J.; Montesinos, M.; Alonso-Ramos, C.; Le Roux, X.; Serna, S.; Benedikovic, D.; Chrastina, D.; Vivien, L.; Isella, G. Germanium-based integrated photonics from near- to mid-infrared applications. *Nanophotonics* **2018**, *7* (11), 1781–1793.
- (10) Wietler, T. F.; Bugiel, E.; Hofmann, K. R. Relaxed germanium films on silicon (110). *Thin Solid Films* **2008**, *517* (1), 272–274.
- (11) Nedeljkovic, M.; Penades, J. S.; Mittal, V.; Murugan, G. S.; Khokhar, A. Z.; Littlejohns, C.; Carpenter, L. G.; Gawith, C. B. E.; Wilkinson, J. S.; Mashanovich, G. Z. Germanium-on-silicon waveguides operating at mid-infrared wavelengths up to 8.5 μm . *Opt. Express* **2017**, *25* (22), 27431–27441.
- (12) Malik, A.; Muneeb, M.; Radosavljevic, S.; Nedeljkovic, M.; Penades, J. S.; Mashanovich, G.; Shimura, Y.; Lepage, G.; Verheyen, P.; Vanherle, W.; Van Opstal, T.; Loo, R.; Van Campenhout, J.; Roelkens, G. Silicon-based Photonic Integrated Circuits for the Mid-infrared. *Procedia Eng.* **2016**, *140*, 144–151.
- (13) Gallacher, K.; Millar, R. W.; Griškevičiūtė, U.; Baldassarre, L.; Sorel, M.; Ortolani, M.; Paul, D. J. Low loss Ge-on-Si waveguides operating in the 8–14 μm atmospheric transmission window. *Opt. Express* **2018**, *26* (20), 25667–25675.
- (14) Montesinos-Ballester, M.; Vakarin, V.; Liu, Q.; Le Roux, X.; Frigerio, J.; Ballabio, A.; Barzaghi, A.; Alonso-Ramos, C.; Vivien, L.; Isella, G.; Marris-Morini, D. Ge-rich graded SiGe waveguides and interferometers from 5 to 11 μm wavelength range. *Opt. Express* **2020**, *28* (9), 12771–12779.
- (15) Marchetti, R.; Lacava, C.; Carroll, L.; Gradkowski, K.; Minzioni, P. Coupling strategies for silicon photonics integrated chips [Invited]. *Photonics Res.* **2019**, *7* (2), 201–239.
- (16) Taillaert, D.; Bienstman, P.; Baets, R. Compact efficient broadband grating coupler for silicon-on-insulator waveguides. *Opt. Lett.* **2004**, *29* (23), 2749–2751.
- (17) Marchetti, R.; Lacava, C.; Khokhar, A.; Chen, X.; Cristiani, I.; Richardson, D. J.; Reed, G. T.; Petropoulos, P.; Minzioni, P. High-efficiency grating-couplers: demonstration of a new design strategy. *Sci. Rep.* **2017**, *7* (1), 16670.
- (18) Lee, J.-M.; Kim, K.-J.; Kim, G. Enhancing alignment tolerance of silicon waveguide by using a wide grating coupler. *Opt. Express* **2008**, *16* (17), 13024–13031.
- (19) Mangal, N.; Snyder, B.; Van Campenhout, J.; Van Steenberge, G.; Missinne, J. Expanded-Beam Backside Coupling Interface for Alignment-Tolerant Packaging of Silicon Photonics. *IEEE J. Sel. Top. Quantum Electron.* **2020**, *26* (2), 1–7.
- (20) Missinne, J.; Benítez, N. T.; Mangal, N.; Zhang, J.; Vasiliev, A.; Campenhout, J. V.; Snyder, B.; Roelkens, G.; Steenberge, G. V. Alignment-tolerant interfacing of a photonic integrated circuit using back side etched silicon microlenses. *Proc. SPIE* **2019**, 1092304.
- (21) Mangal, N.; Snyder, B.; Van Campenhout, J.; Van Steenberge, G.; Missinne, J. Monolithic integration of microlenses on the backside of a silicon photonics chip for expanded beam coupling. *Opt. Express* **2021**, *29* (5), 7601–7615.
- (22) Benítez, N. T.; Baumgartner, B.; Missinne, J.; Radosavljevic, S.; Wacht, D.; Hugger, S.; Leszcz, P.; Lendl, B.; Roelkens, G. Mid-IR sensing platform for trace analysis in aqueous solutions based on a germanium-on-silicon waveguide chip with a mesoporous silica coating for analyte enrichment. *Opt. Express* **2020**, *28* (18), 27013–27027.

A.4. Publication IV: In-situ study of the interactions between metal surfaces and cationic surfactant corrosion inhibitors by surface-enhanced Raman spectroscopy coupled with visible spectroscopy

Analyst

rsc.li/analyst



Die approbierte gedruckte Originalversion dieser Dissertation ist an der TU Wien Bibliothek verfügbar.
The approved original version of this doctoral thesis is available in print at TU Wien Bibliothek.

TU
WIEN
Bibliothek
Your knowledge hub

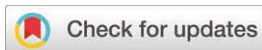
ISSN 0003-2654

 ROYAL SOCIETY
OF CHEMISTRY

PAPER

Felix Frank, Bernhard Lendl *et al.*

In situ study of the interactions between metal surfaces and cationic surfactant corrosion inhibitors by surface-enhanced Raman spectroscopy coupled with visible spectroscopy


 Cite this: *Analyst*, 2024, **149**, 5372

In situ study of the interactions between metal surfaces and cationic surfactant corrosion inhibitors by surface-enhanced Raman spectroscopy coupled with visible spectroscopy†

 Felix Frank,^a Daniela Tomasetig,^a Peter Nahrungbauer,^a Wolfgang Ipsmiller,^b Gerd Mauschitz,^b Karin Wieland^{b,c} and Bernhard Lendl^{b,*a}

Cationic surfactants are widely used as corrosion inhibitors for industrial tubings and pipelines. They protect the surface of steel pipes through a film-forming mechanism, providing both anodic and cathodic inhibition. To improve the efficiency of the corrosion protection, it is essential to understand the interactions between the surfactants and metal surfaces. To achieve this, surface enhanced Raman spectroscopy (SERS) can serve as a powerful tool due to its surface sensitivity and potential to detect trace amounts of analytes in complex media. In this contribution, we have investigated the behaviour of *in situ* prepared AgNPs in the presence of benzalkonium chloride as a model corrosion inhibitor using SERS coupled to visible spectroscopy and combined with light scattering methods. By combining these experimental methods, we were able to correlate the aggregation of silver particles with the concentration of added surfactant in the resulting mixture. Using this insight, we also established a SERS method for the detection of benzalkonium chloride traces in water. For this, we utilised the quenching of the SERS response of methylene blue by competitive adsorption of methylene blue and the surfactant on SERS active AgNPs. We believe that our approach can serve a variety of applications to improve the industrial water treatment. For example, the modelling of the interaction of different surfactants with SERS can be used for process intensification, and ultimately, to move towards the digital twinning of corrosion processes for more efficient corrosion inhibition. Furthermore, the ability to adapt our sensing protocol for on-line corrosion inhibitor monitoring allows a fast response to process changes, hence, enabling resource-efficient, continuous process control.

 Received 17th June 2024,
 Accepted 24th August 2024

DOI: 10.1039/d4an00861h

rsc.li/analyst

1 Introduction

In water treatment for large industrial plants, corrosion of pipelines is one of the most important cost factors, as excessive corrosion leads to shorter maintenance intervals and, thus, increased costs. A prominent method for the surface protection of steel materials in pipelines is the application of corrosion inhibitors whose working principle is based on a film forming mechanism. Inhibitors showing this behaviour include various organic compounds such as acetylenic alco-

hols, aromatic aldehydes and various nitrogen-containing heterocyclic compounds, as well as long-chain quaternary ammonium compounds (quats). The films formed by these compounds can inhibit both anodic dissolution of pipeline metal and cathodic hydrogen evolution.^{1,2} However, their efficiency and inhibition potential can vary greatly with changing operating conditions, which can increase the likelihood of corrosion-related failures and unscheduled downtime.³ With respect to quats, their interactions with the metal surface have been extensively studied, while the exact mechanisms responsible for corrosion inhibition are still not fully understood.^{4,5} As a result, many industrial facilities rely on formulations that have previously shown successful results, rather than actively dosing to respond to changes in the process. This leads to two important research problems. On the one hand, it is essential to learn more about the interactions at the metal-water interface in order to accurately model these processes forming the foundation of moving toward digital twinning of pipelines for corrosion protection purposes, which has the

^aInstitute of Chemical Technologies and Analytics, TU Wien, Getreidemarkt 9, 1060 Wien, Austria. E-mail: bernhard.lendl@tuwien.ac.at

^bInstitute of Chemical, Environmental and Bioscience Engineering, TU Wien, Getreidemarkt 9, 1060 Wien, Austria

^cCompetence Center CHASE GmbH, Ghegastrasse 3, 1030 Wien, Austria

†Electronic supplementary information (ESI) available: Additional explanation of the experimental parameters and considerations for the comparison of different volumetric ratios. See DOI: <https://doi.org/10.1039/d4an00861h>

potential to actively respond to process changes in real time and provide optimal inhibition performance.⁶ On the other hand, until a more efficient method of corrosion inhibitor formulation is established, it is necessary to accurately monitor corrosion inhibitor levels as frequently as possible or financially feasible. By doing this, a consistent dosage and effective treatments can be maintained. Traditionally, inhibitors are measured by taking water samples and measuring them off-line with time-consuming, labor- and resource-intensive colorimetric assays or by titration. With both approaches, a two-phase titration⁷ based on the method proposed by Epton⁸ as well as the colorimetric approach,⁹ inhibitor concentrations in the mg L^{-1} -range can be detected, with measurement times depending on the sample and the trained operator. Raman spectroscopy is a non-destructive and molecule specific method that can accurately measure water samples, as water is a weak Raman scatterer. This results in low interferences of water with the Raman spectrum, making the technique an excellent candidate for the monitoring of aqueous process streams.^{10,11} However, the inelastically scattered light representing the spontaneous Raman spectrum is weak, resulting in generally low sensitivities.¹² Therefore, it is often not applicable for monitoring process chemicals that are present at trace levels, such as corrosion inhibitors. Surface-enhanced Raman spectroscopy (SERS) is a powerful technique that enhances the inherently weak Raman signal by several orders of magnitude using metallic nanostructures in close proximity to the target analyte.¹³ The enhancement is attributed to the localised surface plasmon resonance (LSPR) of the metal, which results in an enhanced electromagnetic field near the surface that enhances both incident and scattered light.¹⁴ SERS is widely used for the detection of various analytes such as drugs, pesticides or explosives at low concentrations with a wide range of applications ranging from biomedical sensing to environmental monitoring, food safety, materials or forensic science.^{15–19} In addition to the greatly enhanced sensitivity, the advantages of SERS include ease of sample preparation and speed of analysis.²⁰ On the other hand, some of the disadvantages of SERS include reproducibility and applicability in real-life scenarios.^{21,22}

Moreover, the surface sensitivity of SERS enables detailed analysis of adsorption processes and surface reactions.²³ This was exploited in this study investigating the interaction of quats with AgNPs, using their similar negative surface (zeta) potentials compared to stainless steel²⁴ to simulate the film forming mechanism²⁵ on the nanoscale. The postulation that the interaction between the surfactants and the silver and stainless steel surfaces, respectively, can be compared, is based on the assumption that no chemical reaction happens between the surfactants and the respective surfaces and the attraction is purely of electrostatic and hydrophobic nature. We studied their aggregation at different quat concentrations using an excitation laser centered on the shifted extinction band observed for aggregated particles (785 nm, hypothesis of interactions shown in Fig. 1). This allowed us to obtain a SERS signal dependent on the aggregation-induced shift of the visible (VIS)

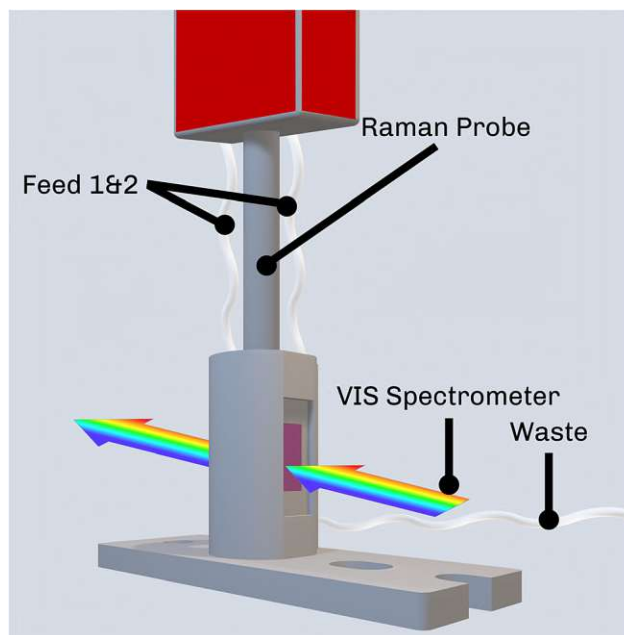


Fig. 1 Hypothesis of the interaction between cationic surfactants and AgNPs. The aggregation of the particles leads to the promotion of hot-spots and a shift in the extinction spectrum towards the Raman laser line, both enhancing the SERS spectrum of the adsorbed surfactant molecules.

extinction spectrum. We explored this *in situ* using a custom flow cell that allows both SERS and VIS spectroscopy. These results were then correlated with data obtained on particle aggregate size and zeta potential from dynamic light scattering (DLS) to provide a more comprehensive view of the interactions between the metal surface and the quats. Finally, we used this system to establish a detection protocol for quats in water with good sensitivity in the typical application range of the corrosion inhibitors ($10\text{--}50 \text{ mg L}^{-1}$). This method makes use of the competitive adsorption of methylene blue (MB) and quats on the AgNPs by looking at the quenching of the MB SERS signal at higher quat concentrations. In conclusion, this work not only provides valuable insight into the processes behind corrosion inhibition moving a step closer to efficient process intensification but also demonstrates the potential of SERS for corrosion inhibitor monitoring in water treatment.

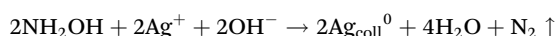
2 Materials and methods

2.1 Used reagents

Silver nitrate (AgNO_3 , Sigma-Aldrich, >99.0%), Hydroxylammonium chloride ($\text{NH}_2\text{OH}\cdot\text{HCl}$, Sigma-Aldrich, 99.999%), Sodium hydroxide (NaOH , Sigma-Aldrich, >98% anhydrous), Benzyltrimethylhexadecylammonium chloride (BAC-16, Sigma-Aldrich) and Methylene blue (MB, Sigma-Aldrich, p.a.) were used as received, Nitric acid (HNO_3 , Sigma-Aldrich, 70%) was diluted to a 2 M solution with deionised water for cleaning purposes.

2.2 Studies of the interaction between AgNPs and BAC-16

For the SERS measurement, a custom-made aluminium flow cell equipped with optical grade windows designed to fit into the sample compartment of a Cary 50 Bio UV-VIS spectrometer (Agilent, USA) with a total usable liquid volume of 12 mL was used. The measurement setup is depicted schematically in Fig. 2. The SERS-active AgNPs were prepared by reducing silver nitrate with hydroxylamine using a modified version of the procedure proposed by Leopold and Lendl.²⁶ For this, a 1.11 M AgNO₃ stock solution and solution of the reducing agent containing 15 mM NH₂OH·HCl and 30 mM NaOH were prepared. The mechanism of the reaction can be summed up with the following reaction equation:



With the Leopold and Lendl method, monodisperse particles with a median particle radius of 53 nm and an extinction maximum at 430 nm can be synthesised (Fig. 3). Further, no citrate is used for the synthesis of the nanoparticle which could interfere with the BAC-16 bands as would be the case for particles synthesised with the method proposed by Lee and Meisel, as the reaction only produces gaseous side products.^{27,28} For the BAC-16 surfactant, a concentration series ranging from 0.02 mg L⁻¹ to 100 mg L⁻¹ was prepared freshly.

For the study of the interaction between the AgNPs and the surfactants, four measurement series with different AgNP : BAC-16 ratios (1 : 9, 2 : 8, 5 : 5, 8 : 2) were carried out using the mixtures listed in Table 1, with the concentrations referring to the samples before mixing (corrected concen-

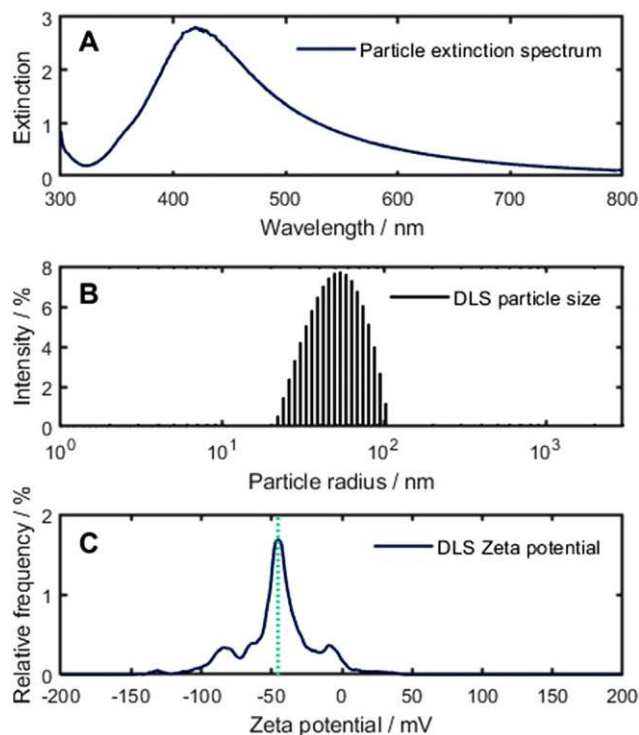


Fig. 3 (A) Extinction spectrum of the pristine AgNPs. (B) DLS particle size distribution for the pristine AgNPs. (C) Zeta potential for the pristine AgNPs, maximum of the potential function (−45 mV) marked with green dotted line.

trations after mixing are displayed in Table S2†). Each single measurement was performed according to the following sequence (illustrated in more detail in the Fig. S1†):

First, the stock solutions for the synthesis of the AgNPs were injected into the measurement cell in a 9 : 1 volumetric ratio (AgNO₃ to reducing agent) under stirring using a Cimarec i Mini Stirrer (Thermo Fisher Scientific, USA). In order to prevent AgNP formation in the tubings, injection happened using two separate feed lines (Feed 1 & 2 in Fig. 2) for the AgNO₃ and the reducing agent, respectively. After 1 min of stirring, the BAC-16 solution was added. 9 min after initial mixing (referring to the addition of BAC-16 to the AgNP colloid), extinction spectra between 350 nm and 800 nm were recorded to ensure the quality of the colloid. Raman measurements were performed 10 min after initial mixing using a WP 785 Raman spectrometer (Wasatch Photonics, USA) with an excitation wavelength of 785 nm fibre-coupled to a WP RP 785 Raman probe (Wasatch Photonics, USA) with an outside diameter of 12.7 mm and a sapphire ball probe tip. The Raman spectra were recorded using the WP Enlighten software, with 10 averages and the exposure time adjusted to prevent detector saturation while maximising the signal. Between individual measurements, the measurement cell, ports, and Raman probe were rinsed with deionised water multiple times until no additional bands compared to the blank were visible in the Raman spectrum. Additionally, the cell was cleaned with a 2 M

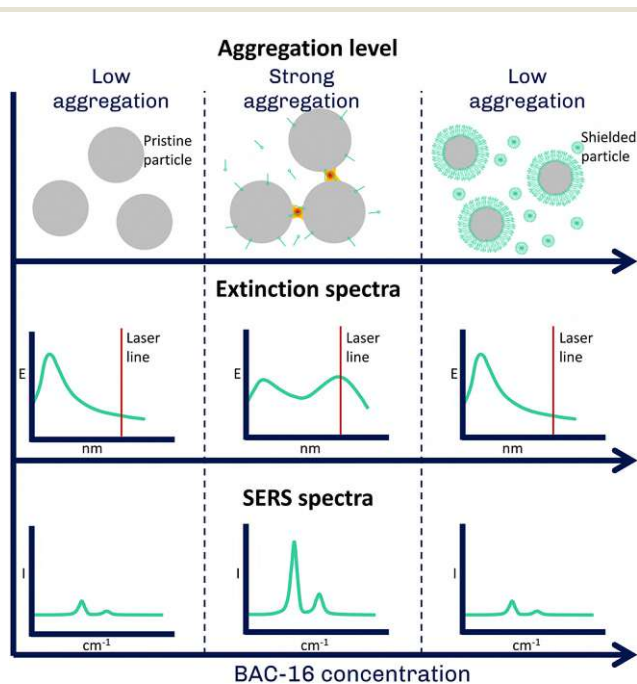


Fig. 2 Schematic depiction of the measurement setup accommodating the Raman probe used for SERS inside the sample compartment of the UV-VIS spectrometer.

Table 1 Experimental parameters for the VIS-SERS measurements. BAC-16 concentrations refer to the samples before mixing

| Ratios | V (AgNO ₃)/mL | V (NH ₂ OH)/mL | V (BAC-16)/mL | c (BAC-16)/mg L ⁻¹ | | | | | | | | |
|--------|---------------------------|---------------------------|---------------|-------------------------------|------|-----|-----|---|---|---|----|-----|
| 1 : 9 | 0.9 | 0.1 | 9 | 0.02 | 0.05 | 0.2 | 0.5 | 1 | 2 | 4 | | |
| 2 : 8 | 1.8 | 0.2 | 8 | 0.02 | 0.05 | 0.2 | 0.5 | 1 | 2 | 4 | | |
| 5 : 5 | 4.5 | 0.5 | 5 | 0.02 | 0.05 | 0.2 | 0.5 | 1 | 2 | 4 | 10 | 100 |
| 8 : 2 | 7.2 | 0.8 | 2 | | | 0.2 | 0.5 | 1 | 2 | 4 | 10 | 100 |

HNO₃ solution after each measurement series to avoid the accumulation of Ag on the walls of the flow cell. In order to show the time dependence of the interaction, additional VIS/SERS measurements were performed in 5 min intervals for a total of 45 min.

2.3 Further characterisation of the AgNPs

To give further context on the aggregation of the AgNPs, dynamic light scattering (DLS) was performed on the colloid-surfactant system. For these experiments, the stock solutions for the synthesis of the AgNPs as mentioned above were injected into a glass vial in a 1 : 9 volumetric ratio (AgNO₃ to reducing agent) under stirring, resulting in a total of 0.5 mL. After stirring for 90 seconds, 4.5 mL of the surfactant solutions were added and stirred for another eight minutes. Afterwards, 1 mL of the mixture were injected into a polycarbonate cuvette and the DLS measurement started. The DLS measurements were performed on a Litesizer 500 (Anton Paar, Austria) at 25 °C, with temperature stabilisation and calibration of the instrument set at 30 s (total time after particle synthesis was 10 minutes for each measurement). The particle size distribution functions were calculated using ISO 22412²⁹ and the narrow analysis model in the Kalliope software package (Anton Paar, Austria).

2.4 Trace sensing of BAC-16 using surface-enhanced Raman spectroscopy

For the trace sensing of BAC-16 with SERS, we made use of the competitive adsorption of methylene blue and BAC-16 on the AgNPs. For these measurements, the sequence of the interaction studies was slightly adapted: First, the stock solutions for the synthesis of the AgNPs as mentioned above were injected into the measurement cell in a 1 : 9 volumetric ratio (AgNO₃ to reducing agent) under stirring, resulting in a total of 2 mL. This colloidal suspension was then diluted with 7 mL of deionised water. After one minute of stirring, 0.9 mL of the 1 mg L⁻¹ MB solution were added. Finally, 0.1 mL of the BAC-16 solution were added after another half a minute. Raman spectra were recorded 10 min after initial mixing of the AgNPs and the MB solution in the same way as for the interaction studies. Between individual measurements, the measurement cell, ports, and Raman probe were rinsed multiple times with deionised water until no additional bands compared to the blank were visible in the Raman spectrum. After each measurement series, the cell was cleaned as mentioned before.

3 Results and discussion

3.1 Evaluation of the surface-enhanced Raman spectra

The pre-treatment of the SERS spectrum involved a baseline correction to remove the fluorescence background. This was done in Matlab R2023b using an adaptation of the iterative algorithm of Lieber and Mahadevan-Jansen (50 iterations, smoothing parameter of the cubic spline set to 0.00001).³⁰ Afterwards, the bands were referenced to the sapphire band of the Raman probe at 752 cm⁻¹ unless stated otherwise. Finally, band heights of the processed Raman spectra were determined and used for data evaluation. Here, we focused on the aromatic C–H in-plane deformation vibration as well as the C–N deformation of the quaternary amine overlapping at 1003 cm⁻¹ and the symmetrical C–N vibration at 1390 cm⁻¹ for MB.^{28,31}

To correlate the experiments with different colloid to surfactant volumetric ratios (Table 1), the concentrations were standardised to reflect the number of BAC-16 molecules per AgNP. For this, two simplifications regarding the particle size were made: First, all particles were assumed to have a particle radius of 53 nm (the median size of the pristine particles) as an average for the unimodal particle size distribution. Additionally, for aggregated silver particles, the surface of the particle aggregates equals the sum of the single particles.

Considering this, the BAC-16 concentrations can be used to estimate the number of BAC-16 molecules per AgNP in suspension to compare the SERS concentration series of different volumetric ratios to each other. The calculation behind this estimation is based on the stoichiometric reduction of the silver with a concentration of 1.11 mmol L⁻¹, which combined with the particle radius and the density and molar mass of silver results in a AgNP concentration (c_{AgNP}) of 1.65×10^{10} particles per mL suspension before mixing with BAC-16 (calculation described in detail in the ESI†). The number of BAC-16 molecules per AgNP (C_{BAC}^*) can then be calculated using the BAC-16 concentration before mixing with the AgNP colloid (c_{BAC} , in mol mL⁻¹) and the volumetric ratio ($x:y$) with the following equation:

$$C_{\text{BAC}}^* = \frac{c_{\text{BAC}} \cdot N_{\text{A}} \cdot y}{c_{\text{AgNP}} \cdot x} \quad (1)$$

3.2 In situ study of the interaction between AgNPs and BAC-16

In Fig. 4, the normalised SERS signal (band at 1003 cm⁻¹ divided by the highest SERS signal for each measurement

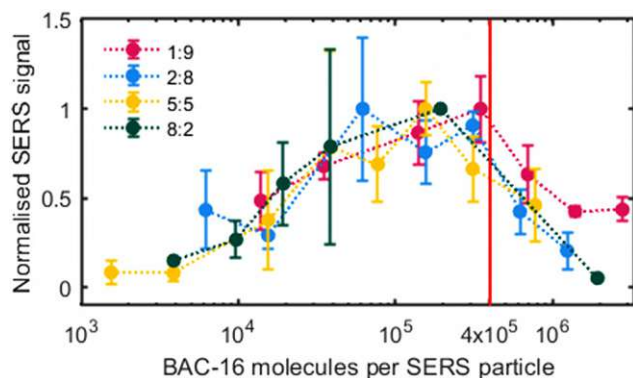


Fig. 4 Normalised SERS signal 10 min after initial mixing for different volumetric ratios (*in situ* synthesised particle/BAC-16 solution) vs. BAC-16/particle ratio.

series) for the studied AgNP-BAC-16 surfactant system is shown, which is plotted against the number of BAC-16 molecules per AgNP in suspension (as introduced in the previous section 3.1).

Upon examining the data, it becomes apparent that a positive correlation exists between the SERS response and the BAC-16 concentration when the concentration is below a threshold of about 4×10^5 BAC-16 molecules per AgNP. However, this trend reverses at higher BAC-16 concentrations, resulting in a decrease in the SERS response. This unusual behaviour, where an increase in the analyte concentration results in a decreased SERS response, suggests a change in the surface enhancement on the silver particles. Similar results have been reported by other researchers in this field, correlating the decrease of the SERS response at higher BAC-16 concentrations with the critical micellar concentrations (CMC) of the surfactants.³² Trying to give a more complete picture of the interactions causing this trend, we focused on studying the aggregation of the AgNPs responsible for the surface enhancement.

For the time dependent extinction spectra (Fig. 5A), a significant shift can be observed between the mixture (2 : 8 AgNP to BAC-16 ratio, 0.5 mg L^{-1} BAC-16) at 0 min (extinction spectrum recorded right after mixing) and 5 min. For these two spectra, the maximum of the second higher wavelength band shifts from 660 nm to around 800 nm. After that, the system stabilises and the extinction decreases over the whole wavelength range. Considering this trend, all SERS experiments were evaluated using the SERS spectrum recorded 10 min after initial mixing.

In Fig. 5B and C, the dependence of the SERS spectra on the BAC-16 concentration is shown for a 2 : 8 AgNP to BAC-16 ratio 10 min after initial mixing. Here, the trend also shown in Fig. 4 can be seen for a single measurement series, with the maximum SERS response being present for a BAC-16 concentration of 0.5 mg L^{-1} (equivalent to 2.5×10^5 BAC-16 molecules per AgNP). Correlating this with the extinction spectra for these respective concentrations in Fig. 5D and E, an interesting

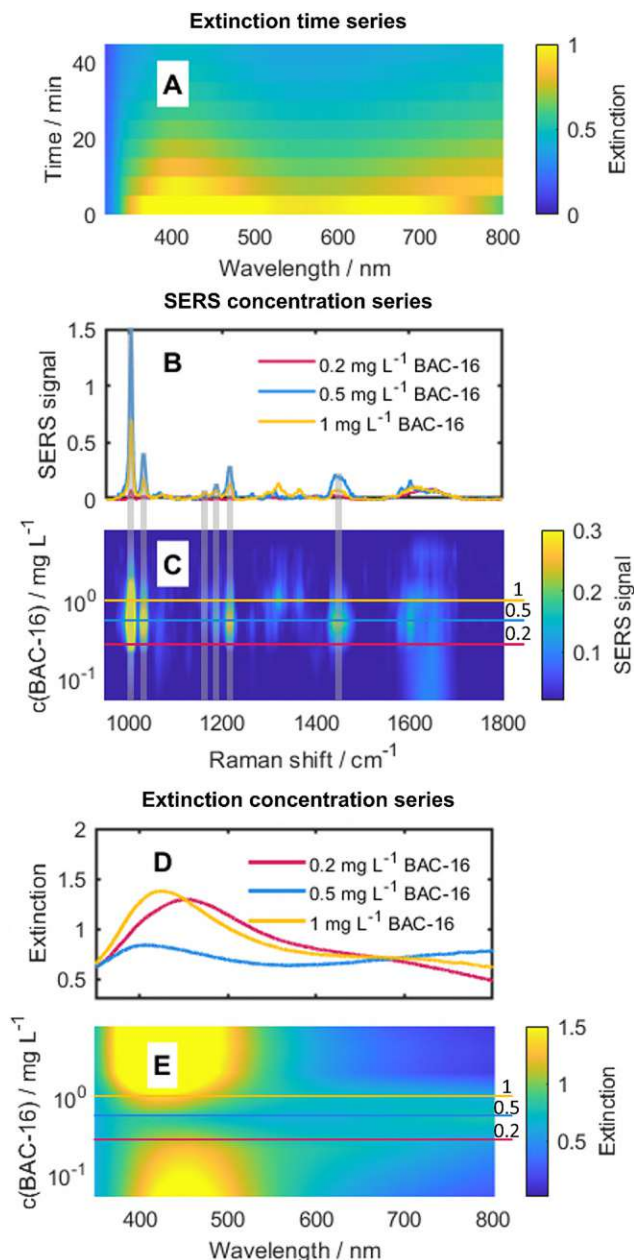


Fig. 5 (A) Time dependence of the extinction spectra of the particles for the interaction with 0.5 mg L^{-1} BAC-16. (B) Exemplary SERS spectra for three different BAC-16 concentrations 10 min after initial mixing. (C) Concentration dependence of the SERS spectra of BAC-16 10 min after initial mixing. (D) Exemplary extinction spectra for three different BAC-16 concentrations 10 min after initial mixing. (E) Concentration dependence of the extinction spectra of the system at different BAC-16 concentrations 10 min after initial mixing. All concentrations refer to a particle/BAC-16 ratio of 2 : 8 (see Table 1).

trend can be found, as the extinction peak broadening primarily happens in the same concentration range in which the highest SERS response can be made out. For all other concentrations, the extinction spectrum closely resembles the spectrum of pristine silver particles (Fig. 3), featuring a single band with a maximum close to 430 nm.

A reason for the broadening of the peaks in the extinction spectra can be found in the aggregation of AgNPs at certain concentrations.³³ As the Stokes (or hydrodynamic) radius of a group of aggregated particles increases, the light scattering behaviour changes. This phenomenon can be explained by the Mie theory, which describes the scattering behaviour of particles with diameters in the same order of magnitude as the wavelength of the incident light.³⁴ The Mie theory can be used to simulate the theoretical extinction spectra of colloidal metal suspensions or, in turn, estimate the particle size of AgNPs considering their extinction spectra.³⁵ For the calculations in this work, a Matlab script by Andrea Baldi based on the Mie theory was used.³⁶ It uses the relative permittivity of a material to compute the extinction cross-section for spherical particles. The permittivity data necessary for these calculations were taken from the work of Johnson and Christy.³⁷ In Fig. 6, top, the calculated extinction spectra of AgNP with radii between 40 nm and 150 nm are shown, while in Fig. 6, bottom, the simulated extinction spectrum for a colloid with the same particle size distribution as measured for the AgNPs is compared with the measured extinction spectrum. The maxima of both extinction spectra appear at comparable wavelength indicating a consistency between the calculated extinction spectrum of the suspension of the measured particle size distribution with the measured extinction spectrum. The deviation in the shapes of the spectra can be explained by the non-spherical shape of real particles.

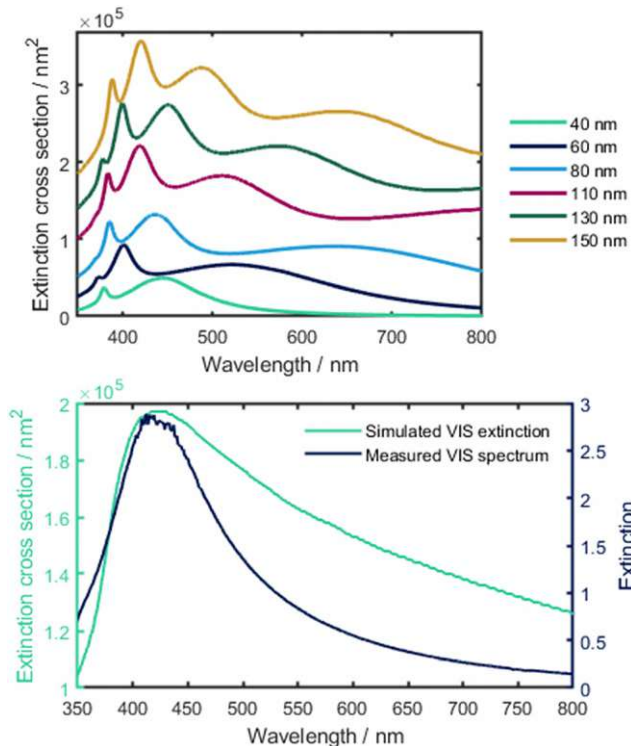


Fig. 6 Top: calculated extinction spectra of different sized AgNPs based on the Mie theory. Bottom: simulated VIS extinction using the particle size distribution vs. Measured extinction spectrum.

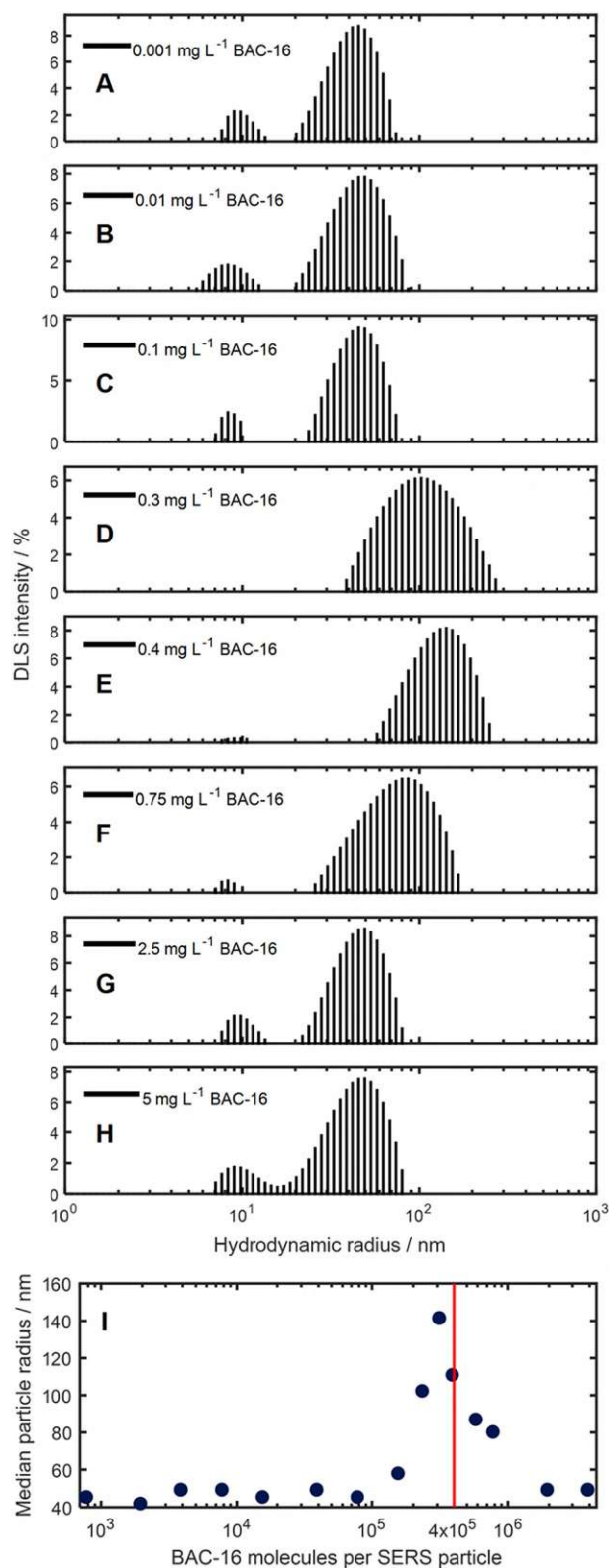


Fig. 7 (A–H) Particle size distributions for freshly synthesised AgNPs mixed with different concentrations of BAC-16 after 10 min. (I) Median particle size for these AgNPs and BAC-16 mixtures, referenced to the BAC-16/particle ratio.

To get actual information on the promotion of particle aggregation at certain BAC-16 concentrations, we investigated their respective particle size distributions obtained through DLS experiment as a function of BAC-16 concentration. The results of these measurements are shown in Fig. 7. For the AgNP DLS signal, a shift of the median particle radii from 46 nm to 142 nm can be seen for the concentrations between 0.1 and 2.5 mg L⁻¹, with the maximum at a concentration of 0.4 mg L⁻¹ (equivalent to a BAC-16/particle ratio of 3.1×10^5). This correlates well with the data gathered from both SERS and VIS, where the threshold, after which the surface enhancement decreases, was determined to be around 4×10^5 BAC-16 molecules per AgNP. The promotion of aggregation determined with DLS can be explained by the formation of micellar encapsulation structures around the AgNPs. A monolayer of BAC-16 increases the van der Waals attraction between encapsulated particles, while for a bilayer, electrostatic repulsion forces lead to a shielding of particles, inhibiting aggregation.

Beside the aggregation-induced shift in the hydrodynamic radius, for some measurements, a small second peak at 10 nm can be detected. This is thought to be an artifact due to the formation of some small BAC-16 covered AgNPs after addition of BAC-16, leading to smaller BAC-16 capped AgNPs.^{38,39} However, they can be disregarded for the analysis, as this size region does not contribute significantly to the extinction spectra broadening.

The data from the zeta potential measurements of the particles at higher BAC-16 concentrations could not be translated

by the models of the Kalliope software, possibly due to interferences of the BAC-16 micelle formation, while the measurements at lower BAC-16 concentrations led to similar results as obtained for the pristine AgNPs (shown in Fig. 3, bottom).

3.3 Trace sensing of BAC-16 using surface-enhanced Raman spectroscopy

As the direct quantification of BAC-16 is not feasible with the SERS system due to particle shielding at higher surfactant concentrations, a protocol for an indirect measurement of BAC-16 is proposed using a tracer molecule at a constant concentration, whose SERS intensity is reduced upon increasing BAC-16 concentration. For such a tracer, a molecule with a good SERS response and high sensitivity was required. Hence, we chose MB as it fulfils these criteria and its SERS response is well studied.⁴⁰ A calibration curve was created to determine the range at which the MB SERS signal shows a steep concentration dependency. The results of these measurements are presented in Fig. 8. When looking at the data, the non-linear nature of the SERS response is observed. As the region of interest was determined in the concentration range below 1 mg L⁻¹ (highlighted in red in Fig. 8, bottom), 1 mg L⁻¹ MB was chosen for the tracer.

Using the 1 mg L⁻¹ MB tracer, a sensing protocol was devised for a concentration range of 10–50 mg L⁻¹ BAC-16, which represents typically applied corrosion inhibitor dosages. For other

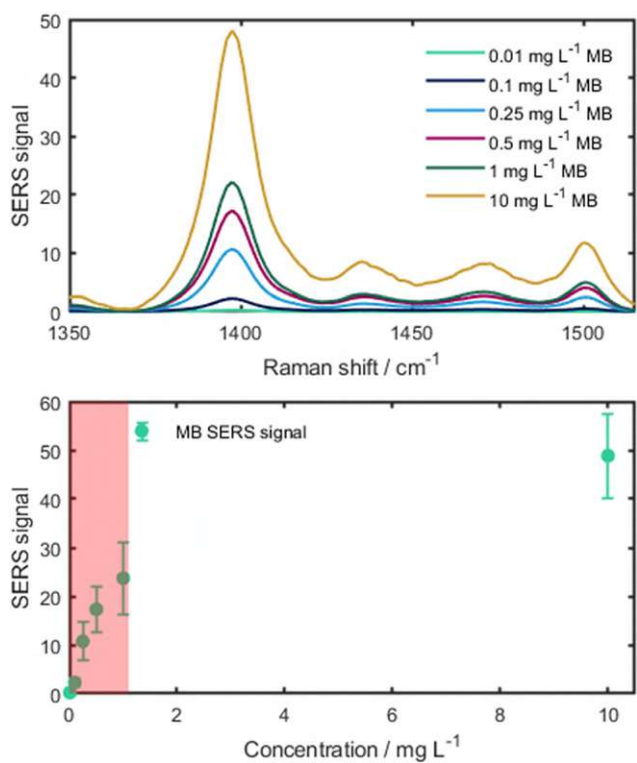


Fig. 8 Top: SERS spectra of different MB concentrations. The pure MB SERS spectra were normalised by the integration time. Bottom: calibration curve of MB showing the region of interest (in red).

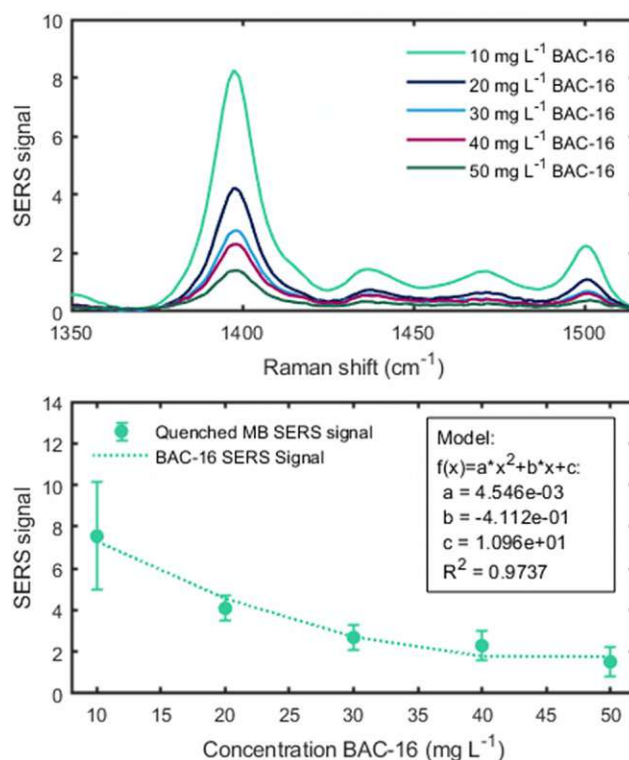


Fig. 9 Top: average ($n = 5$) SERS spectra of 1 mg L⁻¹ MB at different BAC-16 concentrations. Bottom: quenched SERS signal of the MB ($n = 5$) depending on the BAC-16 concentration for a volumetric ratio of 1 : 0.05 : 0.45 : 3.5 (colloid to BAC-16 to MB to H₂O).

applications, the method can also be scaled by changing the volume ratios of BAC-16 and the deionised water used for dilution. By doing this, the smallest measureable concentration range of this method equates to 150–750 $\mu\text{g L}^{-1}$ BAC-16. The results of the BAC-16 measurements are depicted in Fig. 9, showing a good fit for a second order polynomial function.

4 Conclusion and outlook

In this report, we presented an *in situ* study of the interactions of BAC-16, a representative of cationic surfactants commonly used in corrosion inhibition with metal surfaces. We utilised SERS-active AgNPs as a model system for the protected metal surfaces in the corrosion inhibition process due to similar negative surface potentials. As the aggregation of the AgNPs leads to a broadening of the extinction spectrum and an increase of the surface enhancement, we chose an off-centered laser with an excitation wavelength of 785 nm. We designed and applied a custom flow cell to accommodate both SERS and VIS spectroscopy, showing a maximum of the SERS signal between 1×10^5 and 4×10^5 surfactant molecules per AgNP. We further correlated this with DLS measurements, giving insight into the shielding of the particles by means of their hydrodynamic radius at different surfactant concentrations.

Finally, we used these insights to devise a sensing protocol for BAC-16 in water, utilizing the particle shielding at higher BAC-16 concentrations for the SERS quenching of a MB tracer. With this indirect protocol, we could quantify BAC-16 in the concentration range of 10–50 mg L^{-1} . Upon adapting the mixing ratio of the sample and water in the assay, the application range of the calibration function can be shifted, allowing quantification of BAC-16 traces down to 150 $\mu\text{g L}^{-1}$. This study combines both points of emphasis of corrosion inhibition research with the understanding of the inhibition processes and the quantification of corrosion inhibitors in water samples. We, therefore, believe that this work can serve as a stepping stone for future research in this field with the aim to optimise the use of corrosion inhibitors in industrial processes.

Author contributions

FF: conceptualisation, methodology, investigation, data curation, formal analysis, validation, writing – original draft, visualization. DT: investigation, writing – review & editing. PN: investigation, writing – review & editing. WI: investigation. GM: investigation. KW: methodology, writing – review & editing. BL: conceptualisation, validation, writing – review & editing, funding acquisition, supervision.

Data availability

Data for this article, including the raw data and evaluation scripts are available at Zenodo at <https://doi.org/10.5281/zenodo.11547084>.

Conflicts of interest

There are no conflicts to declare.

Acknowledgements

This work is part of the HYDROPTICS project, which has received funding from the European Union's Horizon 2020 research and innovation program under the grant agreement no. 871529. This project is an initiative of the Photonics Public Private Partnership. His work was further supported by the COMET Centre CHASE, funded within the COMET-Competence Centers for Excellent Technologies Programme by the BMK, the BMDW, and the Federal Provinces of Upper Austria and Vienna. The COMET Programme is managed by the Austrian Research Promotion Agency (FFG).

References

- 1 N. F. Atta, A. Fekry and H. M. Hassaneen, *Int. J. Hydrogen Energy*, 2011, **36**, 6462–6471.
- 2 S. M. Wilhelm, *Corrosion*, 1992, **48**, 691–703.
- 3 M. Schwingenschlögl, PhD thesis, TU Wien, 2023.
- 4 J. Wang, T. Zhang, X. Zhang, M. Asif, L. Jiang, S. Dong, T. Gu and H. Liu, *J. Mater. Sci. Technol.*, 2020, **43**, 14–20.
- 5 L. Guo, S. Zhu and S. Zhang, *J. Ind. Eng. Chem.*, 2015, **24**, 174–180.
- 6 C. D. Taylor, *Corros. Eng., Sci. Technol.*, 2015, **50**, 490–508.
- 7 V. W. Reid, G. F. Longman and E. Heinerth, *Tenside, Surfactants, Deterg.*, 1968, **5**, 90–96.
- 8 S. R. Epton, *Nature*, 1947, **160**, 795–796.
- 9 E. Jurado, M. Fernández-Serrano, J. Núñez-Olea, G. Luzón and M. Lechuga, *Chemosphere*, 2006, **65**, 278–285.
- 10 K. Wieland, M. Masri, J. von Poschinger, T. Brück and C. Haisch, *RSC Adv.*, 2021, **11**, 28565–28572.
- 11 D. I. Ellis, R. Eccles, Y. Xu, J. Griffen, H. Muhamadali, P. Matousek, I. Goodall and R. Goodacre, *Sci. Rep.*, 2017, **7**, 12082.
- 12 E. Smith and G. Dent, *Modern Raman spectroscopy: a practical approach*, John Wiley & Sons, 2019.
- 13 S. M. Asiala and Z. D. Schultz, *Analyst*, 2011, **136**, 4472–4479.
- 14 S. Schlücker, *Angew. Chem., Int. Ed.*, 2012, **53**, 4756–4795.
- 15 J. Fei, L. Wu, Y. Zhang, S. Zong, Z. Wang and Y. Cui, *ACS Sens.*, 2017, **2**, 773–780.
- 16 J. Ando, M. Asanuma, K. Dodo, H. Yamakoshi, S. Kawata, K. Fujita and M. Sodeoka, *J. Am. Chem. Soc.*, 2016, **138**, 13901–13910.
- 17 S. Pang, T. Yang and L. He, *TrAC, Trends Anal. Chem.*, 2016, **85**, 73–82.
- 18 A. Chou, E. Jaatinen, R. Buividas, G. Seniutinas, S. Juodkazis, E. L. Izake and P. M. Fredericks, *Nanoscale*, 2012, **4**, 7419–7424.

A.5. Publication V: In-situ study of the adsorption of phosphate species and phosphate derivatives in the confined spaces of mesoporous titania

This prepared manuscript has not been submitted to a journal at the time of submitting this thesis, therefore, the unsubmitted document without journal formatting is included.

Mesoporous titania for the detection of phosphate species and phosphate derivatives using attenuated total reflection infrared spectroscopy

Felix Frank¹, Bettina Baumgartner², Dominik Wacht¹, Mauro David³, Gottfried Strasser³, Borislav Hinkov³ and Bernhard Lendl^{1*}

¹ Institute of Chemical Technologies and Analytics, TU Wien, Getreidemarkt 9, 1060 Wien, Austria

² Homogeneous, Supramolecular and Bio-Inspired Catalysis, Van 't Hoff Institute for Molecular Sciences, University of Amsterdam, Netherlands

³ Institute of Solid State Electronics, TU Wien, Gusshausstraße 25-25a, 1040 Wien, Austria

KEYWORDS. Mid-IR spectroscopy, mesoporous materials, functional coating, sensing, water quality

ABSTRACT: The widespread use of inorganic (as fertilizers) and organic phosphates (as herbicides) in agriculture leads to significant runoff and potential pollution of freshwater resources. To combat this, many efforts have been made in establishing sensing methods of trace contaminant amounts and designing removal agents, limiting the effects of phosphate pollution on the environment. The high reactivity of mesoporous titania, particularly its free Ti-OH groups, towards phosphates makes it an ideal candidate for both adsorptive sensing and remediation applications. In this context, understanding the adsorption of phosphates in the confined spaces of the mesoporous titania is detrimental for efficient processes. For that reason, we used an attenuated total reflection infrared (ATR-IR) spectroscopy configuration with a mesoporous layer applied onto the internal reflection element to study the adsorption of different phosphate species in-situ. With this setup, we studied the interaction of phosphates with titania surfaces in the confined spaces of the mesopores. Here, we looked at the kinetics of the phosphate adsorption as well as at the characteristic spectral features of the adsorbed phosphates and compared them to literature and non-porous titania. Finally, we also quantified the enrichment potential of mesoporous titania for phosphates, potentially opening up sensing applications making use of emerging photonic waveguide technologies to move towards an integrated lab-on-a-chip approach.

INTRODUCTION

Phosphorus is an essential element for the development and survival of life. Especially plants and algae flourish with high concentrations of ortho-phosphates, which they can accumulate. Thus, fertilizers containing inorganic phosphates are widely used in agriculture. Phosphates also find application in detergents, where they mitigate water hardness by forming coordination compounds. However, the overuse of phosphates in agriculture, industry, and households has resulted in nutrient accumulation in global aquatic ecosystems. This has triggered eutrophication in numerous aquatic environments, leading to the formation of algal and cyanobacterial mats, a reduction in oxygen levels, and consequently, a significant loss of biodiversity. [1, 2]

In recent years, attention has been drawn to another phosphate species, namely organophosphorus herbicides, with glyphosate (N-phosphonomethyl glycine) being the most notable. To date, glyphosate remains the most extensively used herbicide globally. Its high toxicity and classification as a probable carcinogen by the International

Agency for Research on Cancer (IARC) necessitate the development of innovative sensing and remediation methods to control public exposure levels.

Mesoporous oxides have emerged as a promising solution for the removal of contaminants from water, including phosphates.[3, 4] Their high surface area,[5] ordered pore structure,[6] and tunable functionalities[7, 8] show high potential for adsorption and catalytic processes. For instance, mesoporous aluminum oxide and iron(III) oxide have successfully been used for herbicide removal from water samples.[9] Similarly, ammonium-functionalized mesoporous MCM-48 silica have demonstrated efficient removal of phosphates and nitrates from aqueous solutions.[10] Titanium oxide is particularly interesting for the removal of contaminants in water due to the potential of photodegradation of adsorbed contaminants. This has been shown for glyphosate [11] as well as for other pesticides.[12, 13]

Mid-infrared (mid-IR) spectroscopy is a powerful technique to study adsorption processes due to the

excitation of molecule-specific fundamental vibration modes by mid-IR radiation (2.5-25 μm). The resulting absorption spectra can be used to extract both qualitative and quantitative information for analytes in complex matrices. Attenuated total reflection infrared (ATR-IR) spectroscopy is a surface-sensitive technique that can be used in the study of adsorption processes and catalytic conversions. By covering the volume probed by the evanescent field in ATR-IR spectroscopy by a thin layer of mesoporous oxides, it is possible to study the interactions and structures of adsorbents in the confined spaces of the mesopores.[14] Combining this configuration with multi-bounce internal reflection elements also makes it possible to perform trace contaminant sensing with tunable selectivities making use of the adsorptive enrichment of target analytes in mesoporous silica. This has been demonstrated for aromatic compounds as well as for nitrates in water, and similarly for phosphates using other mesoporous materials.[15-17]

In contrast to mesoporous silica, mesoporous zirconia offers advantageous properties such as a broader IR-transparency and a better stability in alkaline conditions, with similar versatility.[18] The even greater IR-transparency and similar stability of mesoporous titania are particularly appealing for the detection of phosphate species, which also have a high selectivity for other metal oxides such as goethite. Mid-IR techniques have been used to study this, revealing absorption bands in the 8.3-10 μm range for various phosphate species.[19-21]

In this work, we demonstrate the use of mesoporous titania layers (Figure 1) with tunable selectivities as a tool to study the adsorption of different phosphate species in confined spaces. The layer is applied by a simple, reproducible sol-gel soft templating process onto a Germanium IRE. To improve adhesion and stability in the aqueous phase, we protected the surface of the IRE with a thin layer of sputtered titania. The high reproducibility of the mesoporous layer was evaluated using small angle X-ray diffraction (SA-PXRD) and grazing incidence small angle X-ray scattering (GI-SAXS) to confirm the defined mesoporous structure and to estimate the pore size as by the d-spacing of the mesoporous structure. To determine the layer thickness, we performed profilometry.

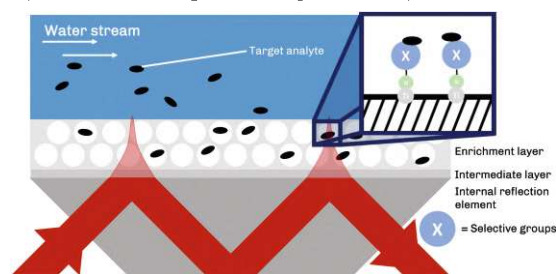


Figure 1. Evanescent field (light red) sensing scheme using a mesoporous titania sensing layer.

Using this platform, we studied the adsorption of orthophosphates (o-phosphates) into the mesoporous titania and compared it to non-porous titania. In a first step, we applied the o-phosphates at various pH values to identify possible changes in binding modes, while also

demonstrating the high chemical stability of the titania layers. Then, we explored the kinetics of monobasic phosphate adsorption into the confined spaces. We further expanded to glyphosate as an organic phosphate derivative, also investigating its surface binding modes and adsorption isotherms. Finally, we assessed the layer in terms of its potential application for infrared sensors to monitor phosphate species in water. By this, we conclude with a comprehensive overview of the use of mesoporous titania in infrared spectroscopy, possibly opening the door for further developments using advances in photonic technology going towards cheaper miniaturized sensing approaches.

EXPERIMENTAL SECTION

Used reagents.

Solvents: Ethanol (EtOH, Chem-Lab, 100 % p.a.), chloroform (CHCl_3 , VWR, anhydrous ≥ 99.5 % stabilized with isoamylene), acetone (VWR, ≥ 99.8 %)

Titania precursors or reference materials: Titanium(IV)chloride (TiCl_4 , Merck, 97 % p.s.), Pluronic® F-127 (F-127, Sigma-Aldrich, BioReagent), titanium oxide (Degussa P25)

Analytes: Phosphoric acid (H_3PO_4 , 85 % in H_2O , 99.99 % trace metal basis), sodium dihydrogen phosphate (NaH_2PO_4 , Fluka, 99 % p.a.), sodium hydrogen phosphate (Na_2HPO_4 , Sigma-Aldrich, ≥ 98.0 %), sodium phosphate (Na_3PO_4 , Sigma-Aldrich, ≥ 98.0 %), glyphosate (GLP, Sigma-Aldrich, analytical standard)

Passivation of Germanium ATR prisms. The samples were sputtered with titanium dioxide (KJ Lesker, 99.9 %) on a LS 320 S sputter system (Von Ardenne, Germany). The residual pressure in the chamber prior to the inlet of the Argon gas was 8×10^{-5} mbar. During sputtering, the equilibrium chamber pressure was 2×10^{-5} mbar. After cleaning of the samples and of the target, the deposition was performed at a deposition rate of 2.27 nm min^{-1} . The thickness of the deposited film was determined with an alpha-SE ellipsometer and the corresponding CompleteEASE software (J.A. Wollam Co., United States) at an angle of incidence at 70° .

Synthesis of Mesoporous Titania. The mesoporous titania layers were prepared using an ethanolic titania stock solution $\text{TiOEt}_{x,y} \text{HCl}$ adapted from the procedure reported by Faustini et al.[22] This solution was prepared by mixing TiCl_4 with EtOH to reach a molality of 2.432 mmol Ti per g solution. The sol was prepared by suspending 0.0766 g of the surfactant Pluronic® F-127 in 0.38 g deionized water, 1.85 g EtOH and 0.5 g of the prepared titania stock solution. The used chemicals equate to a molar ratio of 1:33.0:17.3:0.005 for Ti:EtOH:H₂O:F-127. The mixture was stirred vigorously at room temperature until the surfactant dissolved completely. The stirring then continued for another 30 min. Before coating, the passivated germanium IREs were cleaned with EtOH using a lab wipe. 50 μL of the prepared sol was then spin-coated onto the passivated ATR prisms at 2000 rpm and 30 % relative humidity for 25 s. Annealing of the layer was performed at 60°C for 1 day, followed by 110°C , 150°C and 185°C for 2 days each. To

remove the remaining surfactant, the coated ATR sensors were calcined at 350 °C for 30 min.

Characterization of Mesoporous Titania. Small-angle x-ray diffractometry (SA-XRD) data and grazing-incidence small-angle x-ray scattering (GI-SAXS) data were collected using an Empyrean multipurpose diffractometer, equipped with a GalliPIX 3D area detector and the Data Collector software (all from PANalytical, Netherlands). The measurements were conducted in Bragg Brentano geometry (SA-XRD) and in a standard GI-SAXS configuration, respectively, both with the Cu anode operating at 45 kV and 40 mA. The diffractograms were recorded between 1 and 5° 2 θ with a step size of 0.0143° and an integration time of 98 s/step in continuous scan mode. The GI-SAXS measurements were performed in a 2 θ range between -3.5 and 3.5°, following the guideline provided by PANalytical. The small-angle x-ray diffractograms were evaluated using the Data Viewer software by PANalytical whereas the 2D-scattering patterns received in the GI-SAXS experiments were evaluated using the XRD2DScan software by PANalytical. The layer thickness was determined using a Dektak XTL Stylus profilometer (Bruker, Germany) by measuring the indent of three scratches at different positions. Contact angles were measured on a DSA 30 contact angle goniometer (Kruss, Germany) equipped with a video camera. Static contact angles were determined by placing 3 μ L water droplets on the sample's surface. The shape of the droplets was analyzed by the Young-Laplace method in the software of the goniometer.

Optical Setup. The Ge ATR crystals (20 mm \times 10 mm \times 0.5 mm) used for coating were diced from undoped double side polished wafers. Narrow facets with a defined angle of 45° were polished using a MULTIPREP™ polishing system (ALLIED High Tech Products, USA). Using this ATR crystal configuration, 20 active bounces can be achieved, with a depth of penetration of 584 nm for each bounce between 1200 and 1000 cm⁻¹ (averaging the respective single depths of penetration at the two wavenumbers, with $n_{Ge} = 4.00$, $n_{sample} = n_{water} = 1.33$). [23] The measurement setup comprises a custom built ATR mount and aluminium flow cell previously reported by Baumgartner et al. [15] Liquid handling was performed using a peristaltic pump (Ismatec, Germany), and 1/16" PTFE tubings (0.75 mm I.D.). The measurement setup is designed for seamless integration into a Vertex 80V FTIR spectrometer (Bruker, Germany) equipped with a liquid nitrogen cooled mercury cadmium telluride (MCT) detector (InfraRed Associates, $D^* = 4 \times 10^{10}$ cm Hz^{0.5} W⁻¹ at 9.2 μ m). The collection of the spectra was done with the OPUS 8.1 software, which were recorded using a spectral resolution of 4 cm⁻¹, 32 scans per spectrum (double-sided, backward forward acquisition mode). During all measurements, the sample compartment was flushed with dry air. For sensing experiments, spectra were recorded every 10 s, else using the same settings as for the characterization of the enrichment layer. The noise floor of

the sensor was determined by evaluating the RMS noise of 100 % lines, measuring the water flushed flow cell with a sample compartment flushed with dry air. Calculating the RMS noise between 1200 and 1000 cm⁻¹ resulted in a noise floor of 1.518×10^{-4} A.U., averaging the RMS noises of all used sensors. The evaluation of the spectra collected during the sensing experiments was done using an in-house Matlab R2021a script.

RESULTS AND DISCUSSION

Evaluation of the Sensing System. The employed Germanium crystal exhibits a broad IR-transparency in the mid-IR region, with IR-transparency down to wavenumbers of 900 cm⁻¹, which is necessary for the sensing of phosphates in water (Figure 2-A, spectral region between 1300 and 900 cm⁻¹ marked in blue). This behavior also does not change significantly when passivating the crystal (Figure 2-A, black line) with a 20 nm sputtered TiO₂ thin layer, which was necessary in order to utilize the ATR prism for liquid sensing, due to the water soluble GeO₂ layer forming on top of the crystal. [24, 25] Within the spectral region between 1300 and 900 cm⁻¹, absorption bands of various phosphate species can be found, which heavily depend on their chemical environments (Figure 2-B,C, further studies on the adsorption of phosphates on P25 nanoparticles shown in the ESI). This is also seen when comparing these spectra to literature [20], where the phosphate bands have their maxima (dependent on the pH of the solution) at 1105 and 1022 cm⁻¹, which equates to a shift of 50 cm⁻¹ compared to monobasic phosphate.

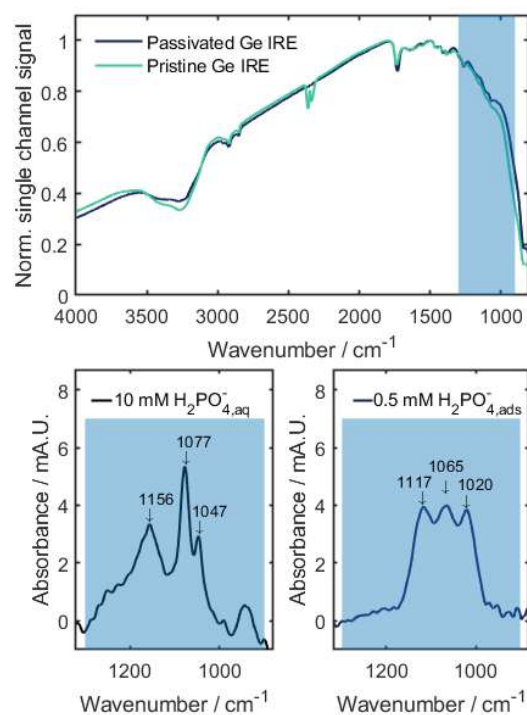


Figure 2. Normalized single channel signal of the passivated (blue line) and pristine (green line) Germanium ATR crystals, region of interest for phosphate sensing marked in red (A). ATR-FTIR spectra of 10 mM NaH₂PO₄ in solution (B) and

0.5 mM NaH_2PO_4 , adsorbed onto P25 titania nanoparticles (C).

Synthesis and Characterization of Mesoporous Titania Sensing Layers. The coating sol for the sensing layers was created using a facile soft templating method, performing in-situ hydrolysis of an ethanolic titania stock solution ($\text{TiEt}_x \cdot \gamma\text{HCl}$) while using the amphiphilic block copolymer Pluronic® F-127 as template. The amorphous titania layer with an average thickness of 205 nm (for the four prepared sensors) was then applied to the passivated germanium ATR crystals by spin-coating the sol and removing the surfactant by pyrolysis at 350 °C. The successful removal of the template was confirmed by the absence of the characteristic organic absorption bands between 3000 and 2800 cm^{-1} . The remaining bands in the range of 1650 to 1350 cm^{-1} can be attributed to chemisorbed CO_2 and H_2O due to the hydrophilic nature of the mesoporous layer.[26] The hydrophilicity was confirmed by contact angle measurements, where a contact angle of 28.5° could be determined (between the layer surface and water). The sensor crystal shows transparency in the region of interest for phosphate sensing of adsorbed phosphate onto titania films between 1200 and 1000 cm^{-1} . This equates to an average root mean square noise of 1.52×10^{-4} A.U. for all prepared sensors in this spectral region (Figure 3). The ordered mesoporous structure of the sensing layer was confirmed using X-ray techniques (Figure 4). SA-XRD was performed after heat treatment and after pyrolysis of the template, revealing two reflexes which hint at a body centered cubic structure (Im3m) which was confirmed by GI-SAXS and compared with literature.[27] The pore size could be approximated by interpreting the d-spacing of the mesopores and by assuming the two peaks as the (100) and (111) reflexes. This leads to a d-spacing of the unit cell of 6.9 nm, which correlates with the pore size with the actual pore size being slightly smaller as the wall thickness is included in the d-spacing.

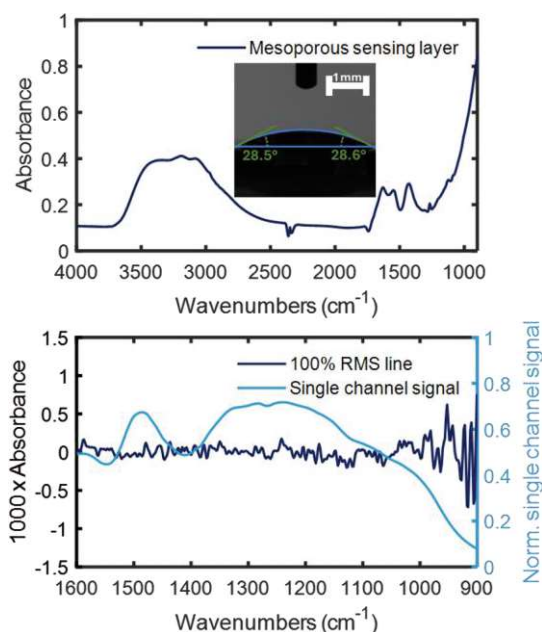


Figure 3. Top: FTIR spectrum of the mesoporous sensing layer. Spectrum was recorded using a passivated Ge ATR as background. Inset demonstrates the high hydrophilicity of the mesoporous titania with a contact angle of 28.5° between the surface and water. Bottom: 100 % RMS line of the coated sensor crystal (black line), associated normalized single channel signal of the coated sensor crystal (blue line).

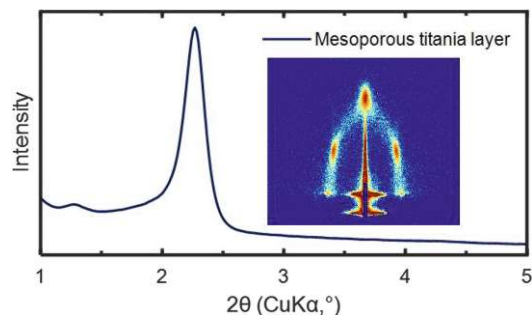


Figure 4. Top: Small angle X-ray diffraction pattern of the mesoporous sensing layer measured in Bragg-Brentano geometry. Inset shows grazing incidence small angle X-ray scattering pattern.

Adsorption Studies of Inorganic Phosphate Species.

The dependence of the phosphate absorption bands on the pH value was studied by applying a 50 mg L^{-1} solution of ortho-phosphates at different pH values between 2 and 11. Each solution was applied for 30 min to come close to equilibrium adsorption. In Figure 5, the spectra of four ortho-phosphate solutions with different pH are shown.

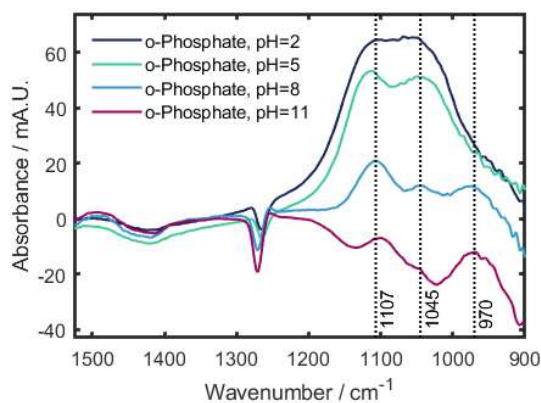


Figure 5. Exemplary spectra of adsorbed ortho-phosphates at different pH values. The background spectrum was recorded of deionized water on the mesoporous film.

These spectra follow a pattern, with three peaks (1097 cm^{-1} , 1045 cm^{-1} , and 970 cm^{-1}) at higher pH values and two strong peaks (1107 cm^{-1} and 1045 cm^{-1}) at lower pH values. Connor and McQuillan[20] reported comparable behavior for high pH values, but for low pH values in confined spaces, the band at 1045 cm^{-1} does not appear to shift to lower wavenumbers the same way as reported in literature. This may be explained with the findings of Gong[28], who reported the presence of some electrostatically bound phosphates at 1008 cm^{-1} and correlated this with the shift of the band at 1045 cm^{-1} in the report of Connor and McQuillan. On the contrary, no peak

shift or second peak can be identified for the adsorption in confined spaces. This indicates that all o-phosphate is chemisorbed onto the surface of the mesoporous titania. Here, both reports propose a bridging bidentate surface complex $(\text{TiO})_2\text{PO}_2$, which is consistent with the other bands observed in our spectra.

The dependence of the phosphate absorption bands on the concentration was studied by applying different concentrations monobasic phosphate in water in a range of 1 to 150 mg L^{-1} . To also describe the kinetics of the adsorption of phosphate into the mesoporous titania, adsorption data for three different interaction times (2 min, 6 min, and 9 min) were collected. In **Figure 6**-top, exemplary spectra of different concentrations adsorbed ortho-phosphate after 6 min of interaction are shown. The location of their absorption peaks with maxima located at wavenumbers at 1107 cm^{-1} and 1050 cm^{-1} are in accordance with literature for non-porous titania at a pH of 5.3-6.8[20]. This was confirmed by measuring the pH of downstream solution, which revealed a pH of 4.7-5.8 (depending on the phosphate concentration).

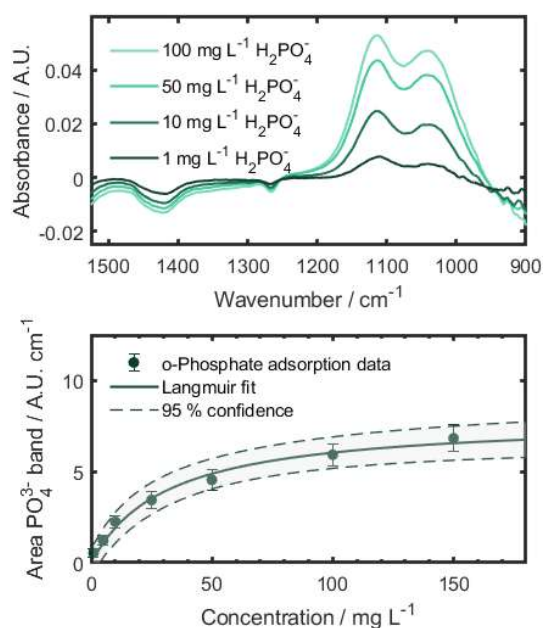


Figure 6. Top: Exemplary spectra of different concentrations of adsorbed monobasic ortho-phosphate. The background spectrum was recorded of deionized water on the mesoporous film. Bottom: Langmuir fit for the data set received for monobasic ortho-phosphate with 95 % confidence interval of the fit function represented by the grey area. Error bars show standard deviations for 4 independent samples.

In line with the perceived mechanism of monolayer adsorption[20], the adsorption data was described with the Langmuir model in order to receive a calibration function. In the equation (1) describing this model, q_e (A.U. cm^{-1}) denotes the band area of the adsorbed analyte, while q_m (A.U. cm^{-1}) being the maximum band area associated to the adsorbed analyte, and K_L (L mg^{-1}) being the Langmuir constant. In **Figure 6**-bottom, the Langmuir fit for the

adsorption data at 6 min with 95 % confidence intervals is shown. The Langmuir fitting parameters for all three interaction times are shown in **Table 1**.

$$q_e = \frac{q_m K_L c}{1 + K_L c} \quad (1)$$

Table 1. Langmuir isotherm parameters received by fitting the phosphate adsorption data for each timeframe.

| o-Phosphate | q_m (A.U. cm^{-1}) | K_L (L mg^{-1}) | χ^2 |
|-------------|---------------------------------|------------------------------|----------|
| 2 min | 4.45 | 0.0238 | 0.156 |
| 6 min | 7.93 | 0.0321 | 0.461 |
| 9 min | 9.81 | 0.0331 | 0.701 |

The kinetic data was described with both the Elovich model (2), which has shown an adequate fit for phosphates onto metal oxides in literature, as well as with the intraparticle diffusion (ID) model (3), which is also often used for the modeling of adsorption kinetics in porous materials.[29, 30] In these equations, q_t (cm^{-1}) is the phosphate band area at a certain time t (min), q_{ref} (cm^{-1}) is the phosphate band area at the reference time t_{ref} (min), which was chosen to be 9 min, while R_E and k_p were the constants for the respective models.

$$\frac{q_t}{q_{ref}} = R_E \ln\left(\frac{t}{t_{ref}}\right) + 1 \quad (2)$$

$$q_e = k_p t^2 \quad (3)$$

The kinetic data is shown in **Figure 7**. For the studied data, the Elovich constant was determined to be 0.43 ± 0.02 , which refers to a slow adsorption process[30] and is in line with literature data.[20] Comparing the two models, the Elovich model seems to be inaccurate for shorter interaction times. This is due to the slow adsorption of phosphate onto titania[31], which leads to a larger intercept on the time axis caused by the logarithmic nature of the Elovich equation. Extrapolating for longer interaction times, the two models once again differ, with the Elovich model expecting a flatter increase in adsorbed phosphate than the ID model. Considering the fact that the Elovich model has shown to describe the adsorption well for long interaction times,[20] it can be said that for the phosphate adsorption onto mesoporous titania, the ID model can be used to describe the initial kinetic behavior, while the Elovich model works well to describe the kinetic behavior for extended time periods.

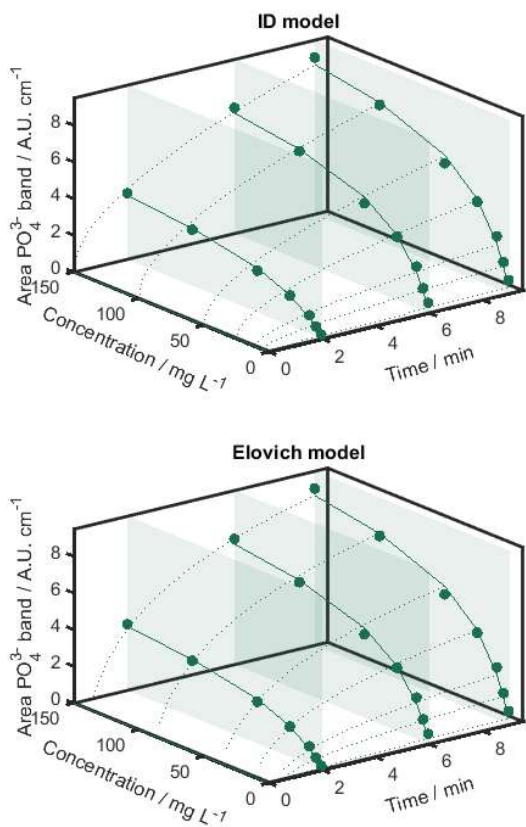


Figure 7. Top: Kinetic modeling of the adsorption data using the ID model (dotted lines). Langmuir functions (solid lines) are added for each interaction time (green plane). Bottom: Kinetic modeling of the adsorption data using the Elovich model (dotted lines). Langmuir functions (solid lines) are added for each interaction time (green plane).

Adsorption Studies of Organic Phosphate Species. As a model analyte for organic phosphate species, GLP was used due to its widespread use and suspected carcinogenicity. In the United States, the environmental protection agency (EPA) issued a maximum contaminant level of 0.7 mg L^{-1} for drinking water.[32] The dependence of the GLP absorption bands on the concentration was studied by applying different concentrations of GLP in water in a range of 5 to 250 mg L^{-1} for 30 min. Sampling was performed with a peristaltic pump, which provided a steady supply of 1.5 mL min^{-1} of the solution to the sensing layer. In **Figure 8**-top, exemplary spectra of different concentrations of adsorbed GLP are shown.

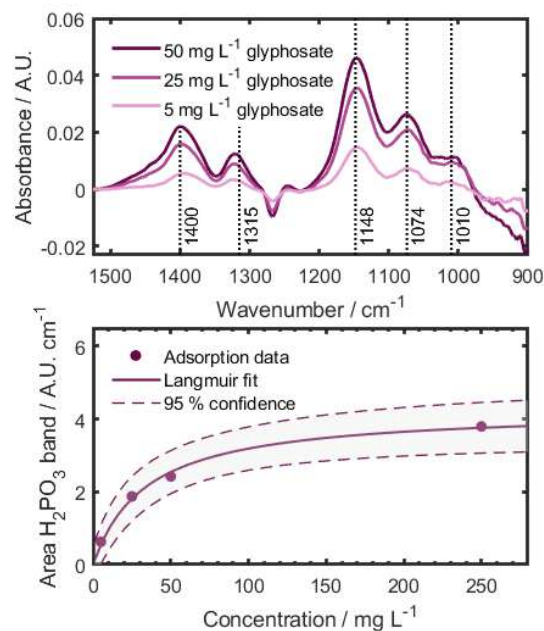


Figure 8. Top: Exemplary spectra of different concentrations of adsorbed GLP. The background spectrum was recorded of deionized water on the mesoporous film. Bottom: Langmuir fit for the data set received for GLP with 95 % confidence interval of the fit function represented by the grey area.

The band positions of GLP adsorbed onto mesoporous titania are similar to those observed for GLP adsorbed onto goethite. The bands at 1400 cm^{-1} and 1315 cm^{-1} can be assigned to the symmetric stretching vibration of the deprotonated carboxyl group and a combination vibration of the amine and the methylene groups, respectively and are equivalent to the bands observed for GLP in aqueous solutions and to those observed for GLP adsorbed onto goethite.[33, 34] For GLP adsorbed onto goethite, the remaining bands showed disagreements between DFT-calculated band positions hinting on the formation of different complexes between the GLP molecules and the iron oxide surface.[35] Based on that, the band at 1148 cm^{-1} can be assigned to the stretching vibration of the P=O of the phosphonate group for a binuclear bidentate complex. The two other bands at 1074 cm^{-1} and 1010 cm^{-1} may be assigned to the symmetric and asymmetric stretching vibration of the P-(O-Ti)₂ bonds. Due to the nature of the chemisorption of GLP onto the titania surfaces, the concentration data was fitted with the Langmuir model. In **Figure 8**-bottom, the resulting fit is shown. The Langmuir fitting parameters are shown in **Table 2**.

Table 2. Langmuir isotherm parameters received by fitting the GLP adsorption data.

| GLP | $q_m (\text{A.U. cm}^{-1})$ | $K_L (\text{L mg}^{-1})$ | χ^2 |
|--------|-----------------------------|--------------------------|----------|
| 30 min | 4.27 | 0.02946 | 0.0204 |

Evaluation of Mesoporous Titania for Sensing Applications. For sensing applications, an enrichment layer has to fulfil several criteria: IR-transparency, sensitivity, rapid response, and stability. Consequently, the potential of

the mesoporous titania layer for sensing applications has to be evaluated based on these parameters.

By combining the mesoporous titania with a germanium IRE, a broad IR-transparency between 4000-950 cm^{-1} could be achieved, which covers the whole region of interest for phosphates.

The sensitivity can be described by two parameters: the limit of detection (LOD) and the enrichment factor n_{Enrich} . Evaluating the sensing system regarding its LOD uses the fitting parameters as calibration function. Applying the standard definition of the LOD [36, 37] to the sensing system, it can be calculated by the concentration equivalent to a band area 3 times the noise floor of the sensing system, which is equivalent to a significance of 99 % for the signal in comparison to the noise floor. The resulting equation is shown in (4) for a Langmuir fit. In this equation, σ is denoting the noise, which is calculated from the 100 % lines in the peak area (1200-1000 cm^{-1} for the o-phosphate and GLP).

$$\text{LOD} = \frac{3\sigma}{(q_m - 3\sigma)K_L} \quad (4)$$

To estimate the enrichment factors of the demonstrated sensing system, ATR-FTIR measurements with uncoated Ge IREs (20 active bounces) were performed with the respective analytes. The enrichment factor was then determined as the ratio of adsorbed and applied analyte concentrations. Further information on the exact methodology is found in the supporting information. In **Table 3**, the sensitivity parameters for the mesoporous titania platform are shown for each respective analyte, showing good enrichment (two to three orders of magnitude) and sub-mg L^{-1} LODs.

Table 3. Sensing parameters of merit for the respective analytes (o-phosphate enrichment factor calculated for an enrichment time of 9 min).

| Analyte | LOD (mg L^{-1}) | n_{Enrich} | σ (A.U. cm^{-1}) |
|-------------|----------------------------|---------------------|-----------------------------------|
| o-Phosphate | 0.36 | 4900 | 0.030 |
| GLP | 0.73 | 1600 | 0.030 |

For the adsorption of phosphates, a rapid response is connected to the sensitivity of the method by the kinetics, necessitating a compromise between speed and LOD. As shown in **Figure 7**, the slow kinetics of the phosphate chemisorption makes an equilibrium approach as demonstrated for organic contaminants on other mesoporous oxides [15] not feasible for the adsorption of phosphate species onto titania.

When looking at the stability of mesoporous titania for the enrichment of phosphate species, a reasonable regeneration of a sensor based on mesoporous titania is not possible due to the strong covalent bonds of the phosphates to the surface titania. Therefore, a possible application would be cheap single-use concepts based on photonic waveguides. [38, 39]

CONCLUSION AND OUTLOOK

In this work, we present a platform for the in-situ measurement of adsorption processes based on mesoporous titania and ATR-IR spectroscopy. In our approach, a mesoporous titania layer is coated onto a germanium IRE covered with a sputtered layer of titania to increase adhesion and protect the water-soluble surface oxide of the IRE. Defined mesoporosity was confirmed by means of X-ray characterization techniques.

We studied the adsorption kinetics and the pH-Value dependence of the band positions of adsorbed o-phosphates, showing similar adsorption bands in confined spaces as for titania surfaces. For GLP as model substance for organic phosphate derivatives, adsorption studies were performed to find out the nature of the bond of GLP to the surface titania. Here, the position of absorption bands could be correlated to a binuclear bidentate complex structure.

Finally, we evaluated these layers regarding their applicability as sensing layers. For phosphate species, their high affinity to the titania surfaces shows a very high enrichment. However, the regeneration of the sensing layers is not feasible due to the strong complexation of the surface bonds. Still, recent advances in photonic waveguide technology open up the possibility of cheap miniaturized single-use sensors.

AUTHOR INFORMATION

Corresponding Author

*E-mail: bernhard.lendl@tuwien.ac.at

Notes

The authors declare no competing financial interest.

ACKNOWLEDGMENTS

In the supporting information, extra details can be found on the phosphate adsorption on non-porous titania, the protection of the germanium IRE, the synthesized titania layers, and the adsorption experiments in the mesoporous titania.

ACKNOWLEDGMENTS

This work is part of the M3NIR project, which has received funding from the European Union's Horizon research and innovation program under grant agreement No. 101093008. Additional support from the BROMEDIR project, which has received funding from the European Union's Horizon research and innovation program under grant agreement No. 101092697, is acknowledged. This project is an initiative of the Photonics Public Private Partnership. X-ray diffraction was performed at the interfaculty X-ray center of TU Wien. Diced double-side polished Germanium-wafers were provided by the IMEC research group at Ghent University. The faceting was performed in the sample preparation lab of the interfaculty electron microscopy service center USTEM of TU Wien.

REFERENCES

- Correll, D. L., The Role of Phosphorus in the Eutrophication of Receiving Waters: A Review. *J. Environ. Qual.* **1998**, *27*, (2), 261-266.
- Abelson, P. H., A Potential Phosphate Crisis. *Science* **1999**, *283*, (5410), 2015.
- Zhang, P.; He, M.; Teng, W.; Li, F.; Qiu, X.; Li, K.; Wang, H., Ordered mesoporous materials for water pollution treatment: Adsorption and catalysis. *Green Energy Environ.* **2023**.
- Diagboya, P. N. E.; Dikio, E. D., Silica-based mesoporous materials; emerging designer adsorbents for aqueous pollutants removal and water treatment. *Microporous Mesoporous Mat.* **2018**, *266*, 252-267.
- Zhao, D.; Feng, J.; Huo, Q.; Melosh, N.; Fredrickson, G. H.; Chmelka, B. F.; Stucky, G. D., Triblock Copolymer Syntheses of Mesoporous Silica with Periodic 50 to 300 Angstrom Pores. *Science* **1998**, *279*, (5350), 548-552.
- Yang, P.; Zhao, D.; Margolese, D. I.; Chmelka, B. F.; Stucky, G. D., Generalized syntheses of large-pore mesoporous metal oxides with semicrystalline frameworks. *Nature* **1998**, *396*, 152-155.
- Vinu, A.; Hossain, K. Z.; Ariga, K., Recent Advances in Functionalization of Mesoporous Silica. *J. Nanosci. Nanotechnol.* **2005**, *5*, (3), 347-371.
- Krishna, N. V.; Anuradha, S.; Ganesh, R.; Kumar, V. V.; Selvam, P., Sulfonic Acid Functionalized Ordered Mesoporous Silica and their Application as Highly Efficient and Selective Heterogeneous Catalysts in the Formation of 1,2-Monoacetone-D-glucose. *ChemCatChem* **2018**, *10*, (24), S610-S618.
- Pirozzi, D.; Sannino, F., Design of a multi-stage stirred adsorber using mesoporous metal oxides for herbicide removal from wastewaters. *J. Environ. Chem. Eng.* **2014**, *2*, (1), 211-219.
- Hamoudi, S.; Saad, R.; Belkacemi, K., Adsorptive Removal of Phosphate and Nitrate Anions from Aqueous Solutions Using Ammonium-Functionalized Mesoporous Silica. *Ind. Eng. Chem. Res.* **2007**, *46*, (25), 8806-8812.
- Garcia-Muñoz, P.; Dachtler, W.; Altmayer, B.; Schulz, R.; Robert, D.; Seitz, F.; Rosenfeldt, R.; Keller, N., Reaction pathways, kinetics and toxicity assessment during the photocatalytic degradation of glyphosate and myclobutanil pesticides: Influence of the aqueous matrix. *Chem. Eng. J.* **2020**, *384*, 123315.
- Kralova, M.; Levchuk, I.; Kasperek, V.; Sillanpaa, M.; Cihlar, J., Influence of synthesis conditions on physical properties of lanthanide-doped titania for photocatalytic decomposition of metazachlor. *Chinese J. Catal.* **2015**, *36*, (10), 1679-1684.
- Zhang, Y.; Han, C.; Zhang, G.; Dionysiou, D. D.; Nadagouda, M. N., PEG-assisted synthesis of crystal TiO₂ nanowires with high specific surface area for enhanced photocatalytic degradation of atrazine. *Chem. Eng. J.* **2015**, *268*, 170-179.
- Baumgartner, B.; Hayden, J.; Loizillon, J.; Steinbacher, S.; Grosso, D.; Lendl, B., Pore Size-Dependent Structure of Confined Water in Mesoporous Silica Films from Water Adsorption/Desorption Using ATR-FTIR Spectroscopy. *Langmuir.* **2019**, *35*, (37), 11986-11994.
- Baumgartner, B.; Hayden, J.; Schwaighofer, A.; Lendl, B., In Situ IR Spectroscopy of Mesoporous Silica Films for Monitoring Adsorption Processes and Trace Analysis. *ACS Appl. Nano Mater.* **2018**, *1*, (12), 7083-7091.
- Baumgartner, B.; Freitag, S.; Gasser, C.; Lendl, B., A pocket-sized 3D-printed attenuated total reflection-infrared filterometer combined with functionalized silica films for nitrate sensing in water. *Sens. Actuators B Chem.* **2020**, *310*, 127847.
- Frank, F.; Baumgartner, B.; Lendl, B., Metal-organic frameworks combined with mid-infrared spectroscopy for the trace analysis of phosphates in water. *Sens. Actuators B Chem.* **2024**, *399*, 134778.
- Wacht, D.; David, M.; Hinkov, B.; Detz, H.; Schwaighofer, A.; Baumgartner, B.; Lendl, B., Mesoporous Zirconia Coating for Sensing Applications Using Attenuated Total Reflection Fourier Transform Infrared (ATR FT-IR) Spectroscopy. *Appl. Spectrosc.* **2021**, *76*, (1), 141-149.
- Fattakhova-Rohlfing, D.; Zaleska, A.; Bein, T., Three-dimensional titanium dioxide nanomaterials. *Chem. Rev.* **2014**, *114*, (19), 9487-558.
- Connor, P. A.; McQuillan, A. J., Phosphate Adsorption onto TiO₂ from Aqueous Solutions: An in Situ Internal Reflection Infrared Spectroscopic Study. *Langmuir* **1999**, *15*, (8), 2916-2921.
- Tejedor-Tejedor, M. I.; Anderson, M. A., The protonation of phosphate on the surface of goethite as studied by CIR-FTIR and electrophoretic mobility. *Langmuir* **1990**, *6*, (3), 602-611.
- Faustini, M.; Grenier, A.; Naudin, G.; Li, R.; Grosso, D., Ultraporous nanocrystalline TiO₂-based films: synthesis, patterning and application as anti-reflective, self-cleaning, superhydrophilic coatings. *Nanoscale* **2015**, *7*, (46), 19419-25.
- Ramer, G.; Lendl, B., Attenuated Total Reflection Fourier Transform Infrared Spectroscopy. In *Encyclopedia of Analytical Chemistry*, Meyers, R. A.; Meyers, R. A., Eds. John Wiley & Sons: 2013.
- Onsia, B.; Conard, T.; De Gendt, S.; Heyns, M. M.; Hoflijck, I.; Mertens, P. W.; Meuris, M.; Raskin, G.; Sioncke, S.; Teerlinck, I.; Theuwis, A.; Van Steenberghe, J.; Vinckier, C., A Study of the Influence of Typical Wet Chemical Treatments on the Germanium Wafer Surface. *Sol. St. Phen.* **2005**, *103-104*, 27-30.
- David, M.; Doganlar, I. C.; Nazzari, D.; Arigliani, E.; Wacht, D.; Sistani, M.; Detz, H.; Ramer, G.; Lendl, B.; Weber, W. M.; Strasser, G.; Hinkov, B., Surface Protection and Activation of Mid-IR Plasmonic Waveguides for Spectroscopy of Liquids. *J. Light. Technol.* **2024**, *42*, (2), 748-759.
- Mino, L.; Cesano, F.; Scarano, D.; Spoto, G.; Martra, G., Molecules and heterostructures at TiO₂ surface: the cases of H₂O, CO₂, and organic and inorganic sensitizers. *Res. Chem. Intermediat.* **2019**, *45*, (12), S801-S829.

27. Gonzalez Solveyra, E.; Fuertes, M. C.; Soler-Illia, G. J. A. A.; Angelomé, P. C., 2D-SAXS In Situ Measurements as a Tool To Study Elusive Mesoporous Phases: The Case of 60 nm TiO₂. *J. Phys. Chem. C* **2017**, 121, (6), 3623-3631.
28. Gong, W., A real time in situ ATR-FTIR spectroscopic study of linear phosphate adsorption on titania surfaces. *Int. J. Miner. Process.* **2001**, 63, (3), 147-165.
29. Bolan, N. S.; Barrow, N. J.; Posner, A. M., Describing the effect of time on sorption of phosphate by iron and aluminium hydroxides. *J. Soil Sci.* **1985**, 36, (2), 187-197.
30. Wu, F.-C.; Tseng, R.-L.; Juang, R.-S., Characteristics of Elovich equation used for the analysis of adsorption kinetics in dye-chitosan systems. *Chem. Eng. J.* **2009**, 150, (2), 366-373.
31. Nooney, M. G.; Campbell, A.; Murrell, T. S.; Lin, X.-F.; Hossner, L. R.; Chusuei, C. C.; Goodman, D. W., Nucleation and Growth of Phosphate on Metal Oxide Thin Films. *Langmuir* **1998**, 14, (10), 2750-2755.
32. EPA National Primary Drinking Water Regulations. <https://www.epa.gov/ground-water-and-drinking-water/national-primary-drinking-water-regulations#Organics> (02.Dec.2024),
33. Sheals, J.; Persson, P.; Hedman, B., IR and EXAFS Spectroscopic Studies of Glyphosate Protonation and Copper(II) Complexes of Glyphosate in Aqueous Solution. *Inorg. Chem.* **2001**, 40, (17), 4302-4309.
34. Waiman, C. V.; Avena, M. J.; Regazzoni, A. E.; Zanini, G. P., A real time in situ ATR-FTIR spectroscopic study of glyphosate desorption from goethite as induced by phosphate adsorption: Effect of surface coverage. *J. Colloid Interface Sci.* **2013**, 394, 485-489.
35. Yan, W.; Jing, C., Molecular Insights into Glyphosate Adsorption to Goethite Gained from ATR-FTIR, Two-Dimensional Correlation Spectroscopy, and DFT Study. *Environ. Sci. Tech.* **2018**, 52, (4), 1946-1953.
36. Long, G. L.; Winefordner, J. D., Limit of detection. A closer look at the IUPAC definition. *Anal. Chem.* **1983**, 55, (7), 712A-724A.
37. Mocak, J.; Bond, A. M.; Mitchell, S.; Scollary, G., A statistical overview of standard (IUPAC and ACS) and new procedures for determining the limits of detection and quantification: Application to voltammetric and stripping techniques. *Pure Appl. Chem.* **1997**, 69, (2), 297-328.
38. Benítez, N. T.; Baumgartner, B.; Missinne, J.; Radosavljevic, S.; Wacht, D.; Hugger, S.; Leszcz, P.; Lendl, B.; Roelkens, G., Mid-IR sensing platform for trace analysis in aqueous solutions based on a germanium-on-silicon waveguide chip with a mesoporous silica coating for analyte enrichment. *Opt. Express.* **2020**, 28, (18), 27013-27027.
39. Frank, F.; Verstuyft, M.; Teigell Beneitez, N.; Missinne, J.; Roelkens, G.; van Thourhout, D.; Lendl, B., Experimental Demonstration of the High Alignment-Tolerant Behavior of a Mid-Infrared Waveguide Platform for Evanescent Field Sensing. *ACS Applied Optical Materials* **2024**.

A.6. Publication VI: Development of a particle analysis system for the process water of the petrochemical industry using hyperspectral imaging, white-light imaging, and fluorescence imaging

Development of a particle analysis system for the process water of the petrochemical industry using hyperspectral imaging, white-light imaging, and fluorescence imaging

Thomas Arnold^a, Martin De Biasio^a, Tibor Bereczki^a, Barbara Oliveira^a, Felix Frank^b,
Stephan Freitag^c, and Bernhard Lendl^b

^aSilicon Austria Labs GmbH, Villach, Austria

^bTU Wien, Institute of Chemical Technologies and Analytics, Vienna, Austria

^cUniversity of Natural Resources and Life Sciences Vienna, Department of Agrobiotechnology (IFA-Tulln), Institute of Bioanalytics and Agro-Metabolomics, Austria

ABSTRACT

The process water of the petrochemical industry contains particles and oil droplets which need to be removed by the water treatment process before the water can safely be reinjected into the well. For the detection and analysis of the particles and oil droplets a particle analysis system based on hyperspectral imaging, fluorescence imaging and white-light imaging has been developed. The particle and droplet size range for this application varies from 5 μm to 150 μm . Currently used particle analyzers use monochrome cameras with backlight illumination. The thereby obtained monochromatic image is used to derive shape and size of the particles and droplets, but no chemical information. The shape information is used to differentiate between solid particles and oil droplets. The solid particles appear black in the images and therefore a more detailed analysis of their material is not possible. The combination of different imaging systems presented in this work allow for a more detailed and robust analysis of the particles and oil droplets in the process water. The fluorescence imaging system is used for a reliable detection of the oil droplets. The white-light imaging system and hyperspectral imaging system acquire high quality color information of particles and oil droplets. This information is vital for the process water treatment during oil production. An ultrasound particle manipulation system is used to guide the particles and oil droplets into the focal plane of the imaging systems. The alpha version of the particle analysis system and the initial results of measurements on solid particles and oil droplets in aqueous suspension are presented.

Keywords: particle analysis, oil droplets, petrochemical industry, hyperspectral imaging, fluorescence imaging

1. INTRODUCTION

In oil production plants, large amounts of brine with high oil contents as well as suspended sedimental particles are produced as byproducts. In order to reuse the water safely for reinjection into the oil well in order to reduce water demand, these process waters are thoroughly cleaned in multi-step processes in water treatment facilities. For process control, information on the type and quantity of suspended particles and residual dissolved and dispersed oil is needed. For the detection of these suspended particles and oil droplets with sizes larger than 1 μm in the ppm-range, plane-focused imaging systems in process pipes and bypass lines are currently employed. These plane-focused imaging systems are optionally complemented by light scatter-based optical counting sensors. A quantitative analysis of particles and oil droplets is done by standard image processing techniques like particle detection/tracking coupled to a counting algorithm. The overall particle load is calculated from this data assuming a given flow profile and is monitored over time. This method suffers from the poor contrast of suspended droplets, which negatively affects the reliability of the measurements and may result in underestimating the actual particle load as well as not being able to deliver qualitative information on the particles.

Further author information: (Send correspondence to Thomas Arnold: E-mail: thomas.arnold@silicon-austria.com)

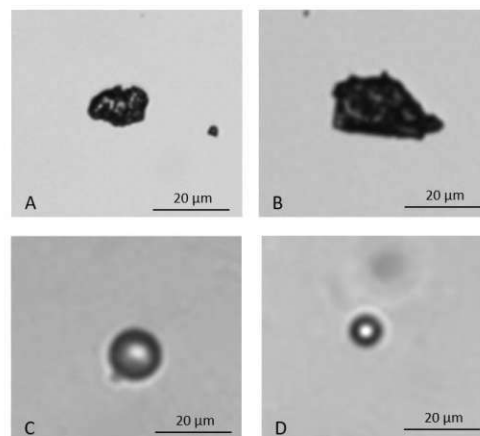
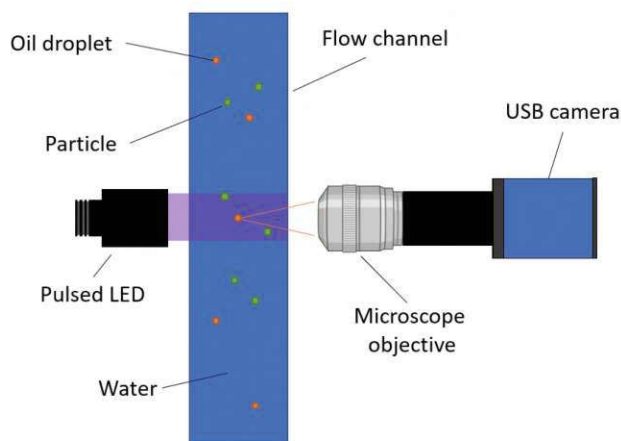


Figure 1. (left) Schematic of a visual particle analyzer with pulsed LED backlight and microscope optics. (right) Monochrome images with backlight illumination from solid particles (A, B) and oil droplets (C,D).

In Fig. 1, a schematic of a visual particle analyzer as well as example images of oil droplets and solid particles are shown. Out-of-focus particles are detected by the imaging system and removed from the analysis. Computer vision algorithms are used to differentiate between solid particles and oil droplets based on their shape. Solid particles are more likely to have sharp edges, while oil droplets assume various rounded shapes. Apart from the inherently low selectivity of the approach, the reliability is limited.

To increase both the contrast and the selectivity, a combination of white-light imaging, fluorescence imaging, and VIS/NIR-hyperspectral imaging is used in this work. The wavelength range is limited to transparent regions of the process solutions. Thus, the VIS/NIR region from 400 nm to 1000 nm is used. The research also includes fluorescence imaging, which is attributed a high potential to be able to both selectively and sensitively detect oil droplets within relevant time frames. An encountered challenge in current sensing schemes for particles in process water is the particles not being in the focal plane of the imaging systems as well as the long-term stability of the optical system, which is often impaired by formation of deposits on surfaces. To mitigate these problems, a flow cell with ultrasound particle manipulation is employed to guide the particles into the focal plane of the imaging systems and to decrease the contamination of the measurement window.

2. MATERIALS AND METHODS

2.1 White-light Imaging (WLI) and Fluorescence Imaging (FLI)

A WLI system uses visible light to illuminate a sample and capture the information of the sample with a RGB color camera. A RGB color camera is a monochrome camera that utilizes a Bayer filter mask in front of the detector pixels to provide 3 broadband color channels. In each of the channels the sensor integrates the signals and provides three color values for each pixel. This type of camera and the filter settings are matched to the color perception of the human eye. For this work a reflected light microscopy system was designed. The system illuminates the sample with a white LED ring light and uses a color RGB camera to acquire the reflected light. This system provides high spatial resolution and RGB color information. Compared to the particle analyzer shown in Fig. 1 the color information can be used to distinguish between different particle materials. The acquired WLI images are close to what the human eye can see. On the other hand a fluorescence imaging system uses a narrow band illumination to excite a fluorescent dye or intrinsic fluorescence of a sample and a monochrome camera with a long-pass filter to collect the emitted fluorescence signal. Each pixel in a fluorescence image shows the detected intensity of the fluorescence signal. In Fig. 2, a schematic of the developed imaging system that is a combination of WLI and FLI systems is shown alongside with two example images acquired with the two imaging systems.

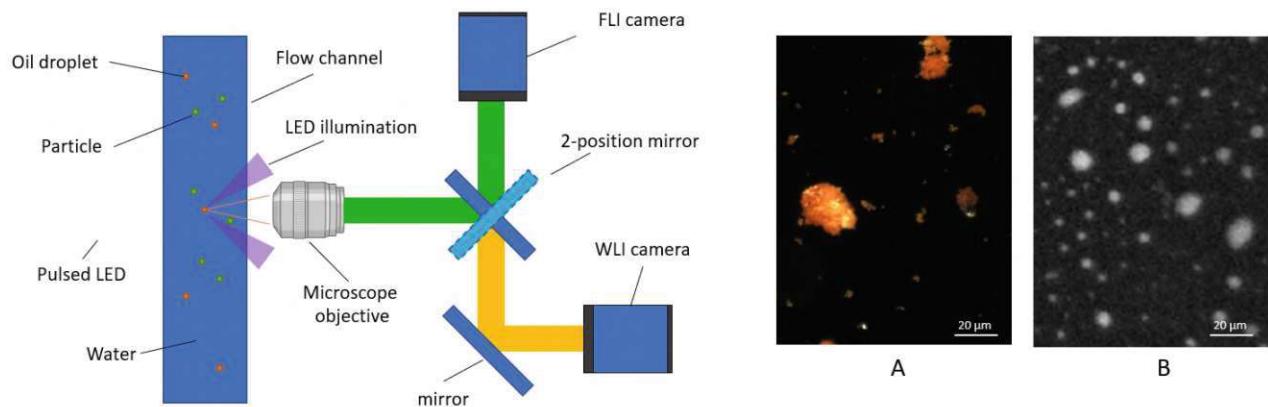


Figure 2. (left) Schematic of a white-light imaging and fluorescence imaging particle analyzer with LED ring light and microscope optics. (right) Color image of particles (A) and monochrome image of oil droplets (B).

2.2 Hyperspectral Imaging (HSI)

HSI is the combination of imaging with spectroscopy and comprises the acquisition, processing, and classification of hyperspectral images.¹ Compared to a RGB camera that captures three broadband channels, a spectral imaging system captures up to several hundred narrow band channels.² The increased spectral information makes chemometric analyses possible. The most prominent approaches to acquire hyperspectral data can be separated in spectral or spatial scanning approaches. For high throughput industrial applications, spatial scanning HSI is more suitable. Instead of recording a two-dimensional image like spectral scanning HSI, a line across the sample perpendicular to the direction of the relative movement is projected into an imaging spectrograph. The spectral information for each pixel along this observation line is projected along the second axis of the two-dimensional detector chip. The spectral encoding can be provided by an imaging spectrograph (see Fig. 3). Since the spatial information along the line is retained, the images contain the spatial information along the first axis and the full spectral wavelength information along the second axis.³ The spectral and the first spatial dimension are simultaneously acquired, while the second spatial dimension is recorded sequentially due to the movement of the sample relative to the HSI sensor. The HSI data acquisition process produces a three-dimensional data set with two spatial dimensions and one spectral dimension. For each image pixel, a reflectance spectrum is available.

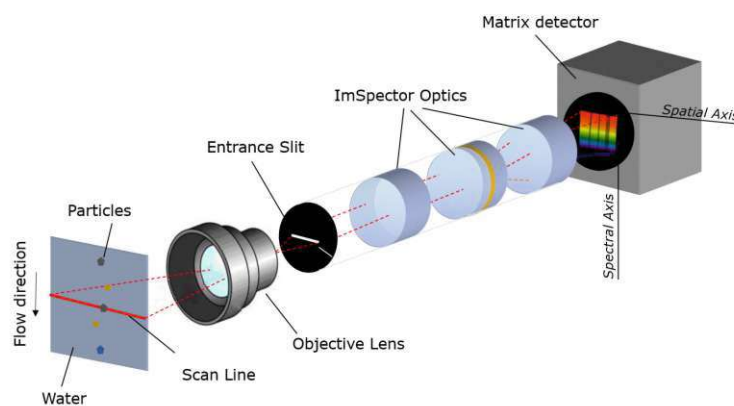


Figure 3. ImSpector imaging spectrograph (Specim, FI).

2.3 Ultrasound Particle Manipulation

Ultrasound (US) particle manipulation is a technique that uses US waves to manipulate particles in a medium. This can either be used in an effort to guide particles (acoustophoresis) or to immobilize (trap) particles in flow for a variety of applications, including separation, concentration, and sorting of particles. US particle manipulation has been successfully applied in research for the handling of bacteria,⁴ microplastic particles,⁵ and cells.⁶ When using an US standing wave (USW) to manipulate particles, a piezo-element as transducer generates an initial US wave, which is then reversed by a reflector. If the resonance condition is met, the superposition of the initial and reflected waves result in an USW. The acoustic radiation force F_z^{rad} in the USW is consequently acting on the suspended particles as a function of the properties of the particles such as size (a), compressibility ($\tilde{\kappa}$), and density ($\tilde{\rho}$), as well as the acoustic energy input E_{ac} .

$$F_z^{rad} = 4\pi \cdot \phi(\tilde{\kappa}, \tilde{\rho}) \cdot ka^3 \cdot E_{ac} \cdot \sin(2kz) \quad (1)$$

As a consequence of F_z^{rad} , particles are driven either in the nodal or anti-nodal planes of the USW, respectively, depending on their acoustic contrast ϕ (i.e, material properties). The frequency of the USW is usually defined by the width of the cavity in which manipulation shall take place. In microfluidics, the frequency of the sound waves used typically ranges in the small megahertz region, equating to a US distance of 150–750 μm between nodal planes (equating to half the wavelength for frequencies of 1–5 MHz). We chose a half wavelength resonator configuration based on a design shown in,⁴ including temperature stabilization. In such a geometry, only one nodal plane is formed, which was used as the focal plane for the imaging system, ensuring a maximum number of particles to be detected.

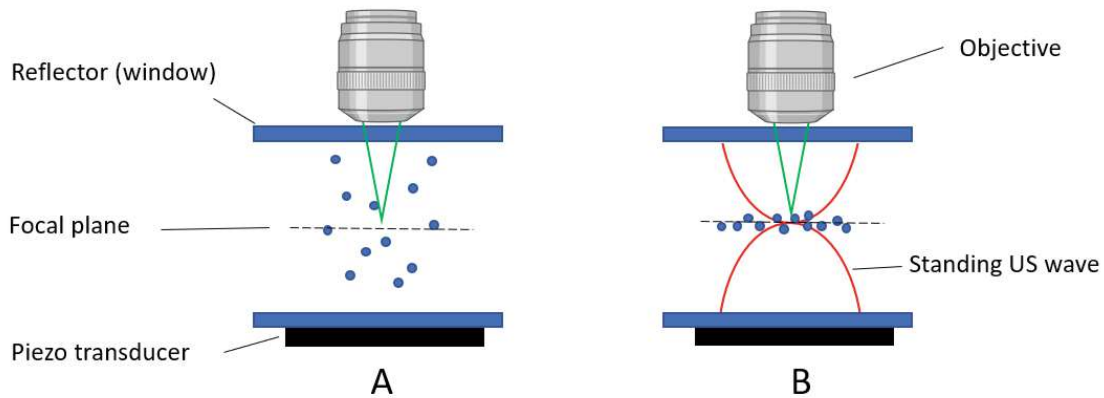


Figure 4. (A) Schematic of a half wavelength resonator acoustofluidic cell with deactivated US particle manipulation (B) Principle with activated US particle manipulation.

In Fig. 4, a schematic of a half wavelength resonator acoustofluidic cell as employed in our system is illustrated. The particles are pushed into the single nodal plane of the USW which coincides with the focal plane of the imaging systems, thus, improving contrast and sensitivity of the imaging.

2.4 Imaging Modules

The imaging systems are built-in in 19" industrial housings and mounted in a 19" rack together with an industrial PC. This allows the system to be moved to a project partner or measurement site. A Python control software was developed to control the data acquisition and data analysis.

White light imaging and fluorescence imaging module The fluorescence imaging system consists of a LED illumination with a center wavelength at 340nm and a FWHM of 12 nm. A 10 X long working distance microscope objective (Mitutoyo, GER) is used to collect the fluorescence light from the sample. The light is focused with a field lens with a focal length of 200 mm (Thorlabs, GER) and redirected by a mirror to a fluorescence emission filter (440 nm) onto a monochrome 5 MP CMOS camera (Ximea, GER). The white-light imaging system uses the same microscope objective and field lens as the fluorescence imaging module. The optical paths of the two systems are selectable by a rotating mirror. The illumination of the WLI module consists of white LEDs which are incorporated in the ring light of the FLI system. The WLI system uses a 5 MP CMOS RGB camera (Ximea, GER) as detector.

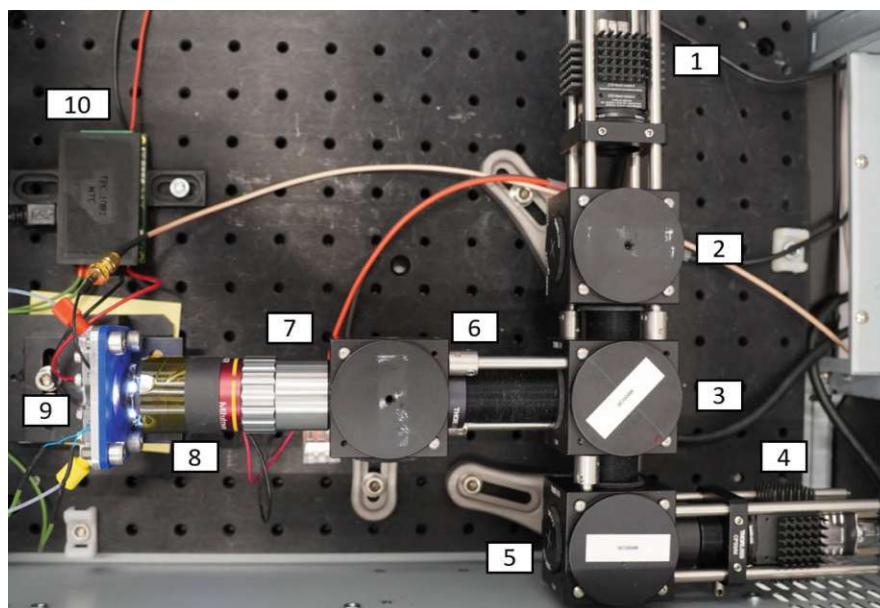


Figure 5. Laboratory setup of fluorescence microscopy system:[1] FLI camera, [2] emission filter, [3] 2-position mirror, [4] WLI camera, [5] mirror, [6] field lens, [7] microscope objective, [8] LED ring light, [9] flow cell, [10] TEC controller.

The main components of the white-light imaging and fluorescence imaging modules are shown in Fig. 5. A ring light illumination was chosen to have more flexibility and to get rid of the beam splitter that would have been needed with a confocal illumination. This increases the fluorescence signal that reaches the detector.

Hyperspectral imaging module The hyperspectral imaging module has already been presented in our previous contribution.⁷ The HSI module uses the same type of flow cell with US particle manipulation as the other presented measurement modules. The heat introduced by the halogen illumination and US particle manipulation of the HSI module made it necessary to incorporate a thermoelectric temperature stabilization of the flow cell. Also, the fiber illumination that originally used two fiber bundles was replaced by a fiber with 8 fiber bundles to achieve a smaller illuminated spot on the sample. Moreover, the CMOS camera was replaced by a much more sensitive scientific CMOS camera (Ximea, GER).

Laboratory setup To be able to test the developed modules without the liquid handling system of the HYDROPTICS sensor platform, a laboratory liquid handling system was established. A review of liquid-liquid separation methods as implemented in the HYDROPTICS sensor platform can be found in.⁸

In Fig. 6, this liquid handling system is shown as used for laboratory testing of the WLI/FLI module. It comprises a peristaltic pump (Ismatec, GER) and a magnetic stirrer used to keep the particles in the sample container in a steady suspension. Further, the sonicamp (usePAT, AUT), an US driver used for driving the acoustofluidic flow

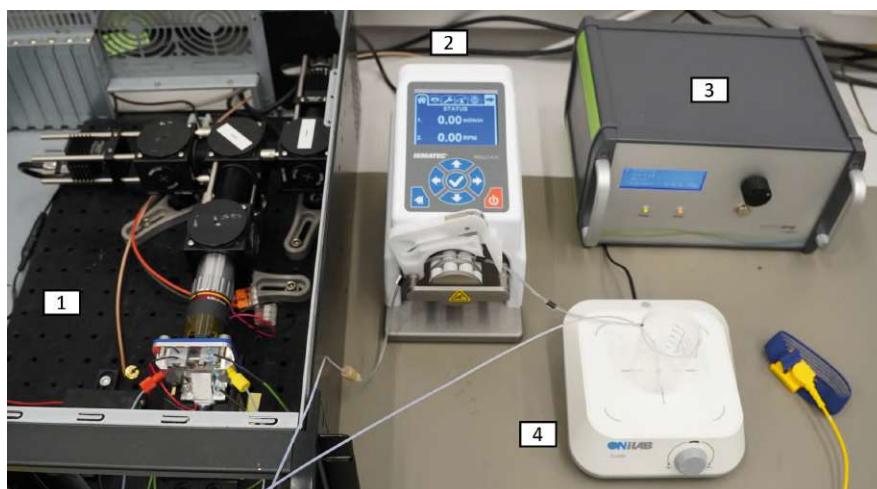


Figure 6. Laboratory setup: [1] WLI/FLI module, [2] peristaltic pump, [3] amplifier for ultrasonic particle manipulation, [4] magnetic stirrer with sample container.

cell is shown. This system makes it possible to operate the developed particle imaging modules under laboratory conditions. Different types of calibration particles or beads can be pumped through the flow cells. In case of process water samples, the residual oil content is removed with cyclohexane before the samples get introduced in the measurement system to avoid contamination.

3. MEASUREMENTS

First measurements carried out on dry particle samples and in aqueous NaCl suspension were already presented in an earlier contribution.⁷ After considerable extension and improvements of the initially presented imaging modules, new measurements on calibration particles have been carried out with the newly designed flow cells with US particle manipulation. The US particle manipulation is a key component of the measurement systems, as it significantly enhances the contrast by moving the particles into the focal plane of the imaging system.

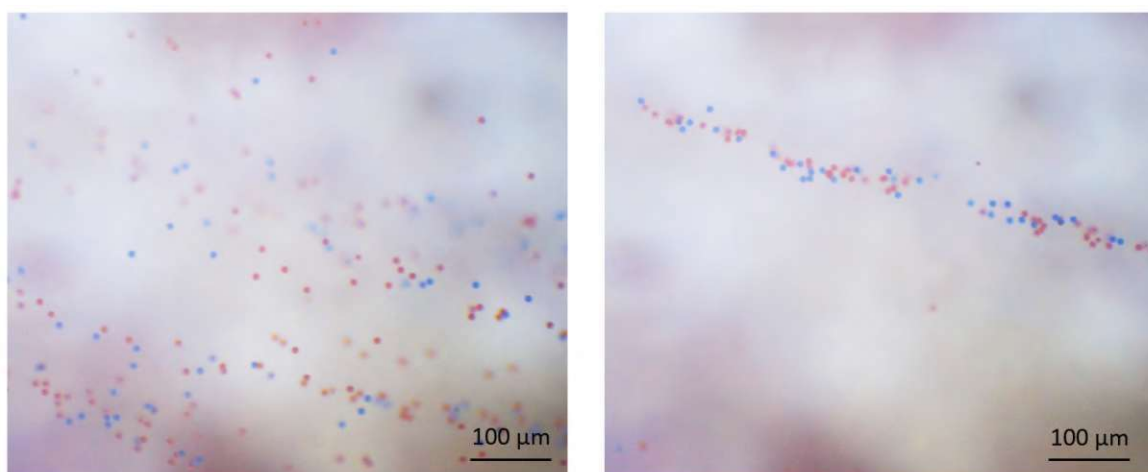


Figure 7. Pictures of red and blue colored 10 μm polystyrene beads without US particle manipulation (left), and with US particle manipulation (right).

The effects of US particle manipulation are shown in Fig. 7. The two images were taken from red and blue

colored polystyrene beads with a nominal diameter of $10\ \mu\text{m}$. The image on the left shows the beads moving through the field of view of the WLI system without US particle manipulation. A large number of particles are not in focus and therefore have to be rejected for the calculation of the particle size distribution. In the image on the right the US particle manipulation forces the particles into the nodal planes of the USW. The particles are moving in a narrow line and only a few particles are not in focus of the WLI system. This is especially important for the hyperspectral imaging system which is a line scanning system and relies on a constant movement of the particles through the scan line of the system. By choosing the correct design properties of the flow cell such as distance between US transducer and reflector, operating frequency, power and flow speed of the medium the particle manipulation can be used to guide particles, catch particles or wipe particles from the measurement window. The dark shadows in the background of the images in Fig. 7 result from the fact that the flow channel was not coated and consisted of bare aluminum. This will be optimized in future versions of the flow cell.

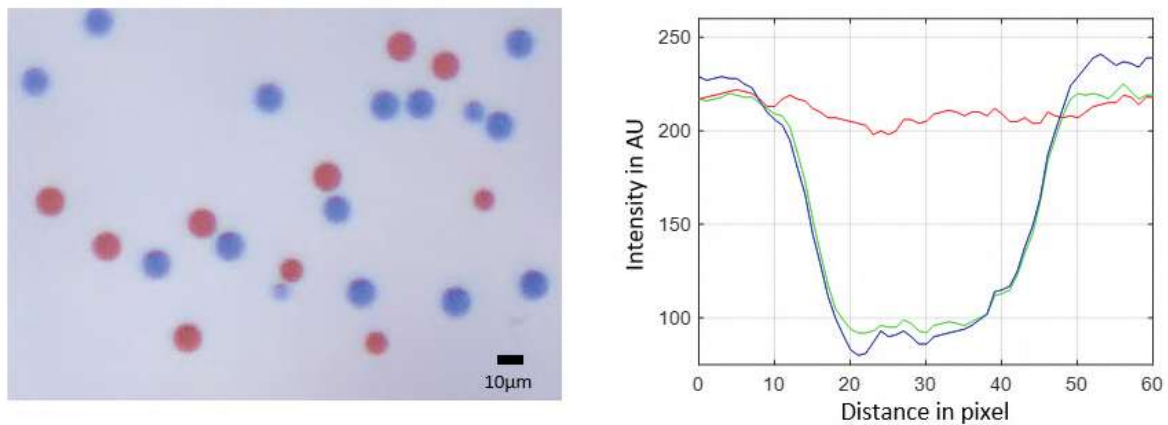


Figure 8. (left) WLI image of red and blue polystyrene beads, (right) RGB profiles of cross-section of a red polystyrene bead.

In Fig. 8, a close-up of the red and blue colored polystyrene beads is shown. From this image, it is already visible that there are size variations of the beads, which was verified with a laboratory microscope. The RGB line profiles show a profile through the center of a red colored bead. It shows that the color information is consistent and a $10\ \mu\text{m}$ bead is represented by a distance of approx. 40 pixels. This shows that after doubling the optical magnification of the measurement systems, the spatial resolution of $0.25\ \mu\text{m}/\text{pixel}$ is high enough for the targeted particle size range of $5\ \mu\text{m}$ to $150\ \mu\text{m}$.

4. SUMMARY & OUTLOOK

The presented work shows the newest developments of our measurement system which is able to measure solid particles and oil droplets in process water of the petrochemical industry. It provides white-light imaging, fluorescence imaging and hyperspectral imaging data with high spatial and spectral resolutions. The combination of these imaging systems with a flow cell with US particle manipulation improves the determination of particle and oil droplet size distributions. The color information and spectral signatures of the particles can be used to identify the materials of the particles to give more information about the performance of the water treatment process. In future work the imaging modules and flow cells will be finalized and tested in the field of the water treatment of the petrochemical industry. State of the art machine learning techniques will be applied to identify the different types of particles based on their spectral fingerprint. The final system will be part of the HYDROPTICS sensor platform for the petrochemical industry.

5. ACKNOWLEDGMENT

This work has been supported by Silicon Austria Labs (SAL), owned by the Republic of Austria, the Styrian Business Promotion Agency (SFG), the federal state of Carinthia, the Upper Austrian Research (UAR), and the Austrian Association for the Electric and Electronics Industry (FEEL). Financial support was provided by the European Union's Horizon 2020 research and innovation programme within the research project HYDROPTICS under the grant agreement no.: 871529.

REFERENCES

- [1] Boldrini, B., Kessler, W., Rebner, K., and Kessler, R. W., "Hyperspectral imaging: A review of best practice, performance and pitfalls for in-line and on-line applications," *Journal of Near Infrared Spectroscopy* 20(5) (2012).
- [2] Leitner, R., DeBiasio, M., and Arnold, T., "High-sensitivity hyperspectral imager for biomedical video diagnostic applications," *Proceedings of SPIE - The International Society for Optical Engineering* (2010).
- [3] DeBiasio, M., Arnold, T., and Leitner, R., "UAV-based Multi-spectral Imaging System for Environmental Monitoring," *Technisches Messen* 11(78), 503–507 (2011).
- [4] Freitag, S., Baumgartner, B., Radel, S., Schwaighofer, A., Varriale, A., Pennacchio, A., D'Auria, S., and Lendl, B., "A thermoelectrically stabilized aluminium acoustic trap combined with attenuated total reflection infrared spectroscopy for detection of escherichia coli in water," *Lab on a Chip* 21(9): 1811-1819 (2021).
- [5] Wieland, K., Tauber, S., Gasser, C., Rettenbacher, L. A., Lux, L., Radel, S., and Lendl, B., "In-line ultrasound-enhanced raman spectroscopy allows for highly sensitive analysis with improved selectivity in suspensions," *Analytical Chemistry* 91(22): 14231-14238 (2019).
- [6] Olm, F., Lim, H. C., Schallmoser, K., Strunk, D., Laurell, T., and Scheduling, S., "Acoustophoresis enables the label-free separation of functionally different subsets of cultured bone marrow stromal cells," *Cells. Cytometry*, 99: 476-487 (2020).
- [7] Arnold, T., DeBiasio, M., Bereczki, T., Baumgart, M., and Horn, A., "Development of inspection system for the detection and analysis of solid particles and oil droplets in process water of the petrochemical industry using hyperspectral imaging and fluorescence imaging," *Proc. SPIE DCS* (2022).
- [8] Dimitrijevic, D., Bösenhofer, M., and Harasek, M., "Liquid-liquid phase separation of two non-dissolving liquids - a mini review," *MDPI, Processes*, 11(4), 1145; (2023).

A.7. Curriculum Vitae

Felix Frank

| | |
|---------------|------------|
| Contact | [REDACTED] |
| Nationality | [REDACTED] |
| Date of Birth | [REDACTED] |

Education

| | |
|-----------------|---|
| 05/2020-12/2024 | PhD Candidate at Institute of Chemical Technologies and Analytics, TU Wien. Topic: Combining Nanoscale Materials with Vibrational Spectroscopy Supervisor: Prof. Bernhard Lendl |
| 11/2017-04/2020 | MSc in 'Technical Chemistry' with specialisation in High Performance Materials, TU Wien. Master Thesis: Gas Permeance Characteristics of Microporous Polymer-Derived Ceramics Supervisor: Prof. Thomas Konegger |
| 10/2014-11/2017 | BSc in 'Technical Chemistry', TU Wien Bachelor Thesis: Recovery of Tungsten-Containing Materials Supervisor: Prof. Christian Edtmaier |
| 09/2005-05/2013 | Secondary Education at Sacré Coeur Wien |

Work experience

| | |
|-----------------|--|
| 05/2020-12/2024 | Project Assistant at the Institute of Chemical Technologies and Analytics, TU Wien |
|-----------------|--|

Awards and Fellowships

| | |
|------|---|
| 2023 | Poster Prize at ANAKON 2023, AT |
| 2022 | Poster Prize at Spring SciX 2022, UK |
| 2019 | Merit Grant of TU Wien |
| 2018 | Merit Grant of TU Wien |
| 2013 | Hans-Riegel-Fachpreis for best Highschool Thesis |
| 2013 | VCÖ Prize for best Highschool Thesis |
| 2012 | Fellowship of BMUKK for attendance of Forum Alpbach |

Peer-reviewed Publications

ORCID: 0000-0002-7584-5812

1. **F. Frank**, B. Baumgartner, D. Wacht, M. David, C.I. Doganlar, G. Strasser, B. Hinkov, B. Lendl, In-situ study of the adsorption of phosphate species and phosphate derivatives in the confined spaces of mesoporous titania, Submitted manuscript
2. **F. Frank**, B. Baumgartner, M. Verstuyft, N.T. Beneitez, J. Missinne, G. Roelkens, D. van Thourhout, B. Lendl, Integrated optics waveguides and mesoporous oxides for the monitoring of volatile organic compound traces in the mid-infrared, Applied Spectroscopy, Accepted
3. **F. Frank**, D. Tomasetig, P. Nahrungbauer, W. Ipsmiller, G. Mauschwitz, K. Wieland, B. Lendl, In-situ study of the interactions of metal surfaces with cationic surfactant corrosion inhibitors with surface-enhanced Raman spectroscopy coupled with visible spectroscopy
<https://doi.org/10.1039/D4AN00861H>
4. **F. Frank**, M. Verstuyft, N.T. Beneitez, J. Missinne, G. Roelkens, D. van Thourhout, B. Lendl, Experimental demonstration of the high alignment-tolerant behavior of a mid-infrared waveguide platform for evanescent field sensing
<https://doi.org/10.1021/acsaom.4c00280>
5. **F. Frank**, B. Baumgartner, B. Lendl, Metal-organic frameworks combined with mid-infrared spectroscopy for the trace analysis of phosphates in water
<https://doi.org/10.1016/j.snb.2023.134778>.

Conference proceedings

1. T. Arnold, M. de Biasio, T. Bereczki, B. Oliveira, **F. Frank**, S. Freitag, B. Lendl, Development of a particle analysis system for the process water of the petrochemical industry using hyperspectral imaging, white-light imaging, and fluorescence imaging.
<https://doi.org/10.1117/12.2663912>.

Conference Contributions as presenting author

1. **F. Frank**, B. Baumgartner, M. Verstuyft, N.T. Beneitez, D. Wacht, M. David, E. Traxler, B. Hinkov, D. van Thourhout, B. Lendl, Mesoporous materials and mid-infrared spectroscopy for the trace monitoring of contaminants in process analytical technology, Talk, SciX 2023, Reno, NV, USA
2. **F. Frank**, M. Verstuyft, B. Baumgartner, N.T. Beneitez, D. van Thourhout, B. Lendl, A new sensitive multi-analyte VOC sensor based on an integrated optics waveguide coated with a functionalised mesoporous sensing layer and QCL-IR spectrometry, Poster, ICAVS 12, Krakow, PL

3. **F. Frank**, B. Baumgartner, L. Riedlsperger, B. Lendl, Making the case for adsorption enhanced attenuated total reflection spectroscopy using metal-organic frameworks, Poster, ANAKON 2023, Wien, AT (awarded with a poster prize)
4. **F. Frank**, B. Baumgartner, B. Lendl, Pushing the limits of adsorption enhanced attenuated total reflection spectroscopy using metal-organic frameworks for trace analysis of phosphates in water, Poster, Junganalytikerforum 2022, Tulln, AT
5. **F. Frank**, B. Baumgartner, B. Lendl, Swipe and wipe: The next generation phosphate sensing platform based on $\text{NH}_2\text{-MIL-88B(Fe)}$ and mid-infrared attenuated total reflection spectroscopy, Poster, Spring SciX, 2022, Liverpool, UK (awarded with a poster prize)
6. **F. Frank**, B. Baumgartner, M. David, C.I. Doganlar, G. Strasser, B. Hinkov, G. Ramer, B. Lendl, Development of a micromolar sensitivity dipstick mid-IR ATR sensor for phosphate in water, Poster, ICAVS 11, online